

Contents

1	Introduction	1
2	Spectroscopy on classically modulated atoms	5
2.1	The magneto-optical trap	5
2.1.1	The basic MOT theory	6
2.1.2	Characterization of the MOT by absorption spectroscopy	7
2.2	Double-optical resonance	10
2.3	The polarization interferometer	13
2.4	Spectroscopy on a modulated magneto-optical trap	15
2.4.1	Experimental setup	16
2.4.2	FM absorption spectroscopy	17
2.4.3	FM polarization rotation spectroscopy	19
2.4.4	Diode laser phase noise	20
3	Squeezed states of light	23
3.1	Basic properties of the squeezed states	24
3.2	Squeezing from the optical parametric oscillator	26
3.3	Polarization squeezed light	29
3.4	Experimental squeezing setup	32
3.5	Sub-shot noise polarization spectroscopy	36
4	Mapping the quantum state of light onto atoms	39
4.1	The fundamental equations	40
4.1.1	The Hamiltonian	41
4.1.2	The field propagation equation	43
4.2	Fluctuations in the collective spin \hat{F}'_z	46
4.2.1	Direct calculation of $(\Delta\hat{F}'_z)^2$ for uncorrelated atoms	50
4.3	Fluctuations in $\hat{F}'^2_x - \hat{F}'^2_y$ and $\hat{F}'_x\hat{F}'_y + \hat{F}'_y\hat{F}'_x$	51
4.4	Comments on the applied linearization approach	54
5	Spin squeezed states and entanglement	57
5.1	Definition of spin squeezed states	57
5.2	Realization of spin squeezed states	60
5.3	Generation of spin squeezed states by mapping light onto atoms	61
6	Theory for the atomic state readout	65
6.1	Probing excited state atoms in double-optical resonance	66
6.2	The readout of atomic fluctuations	69
6.2.1	Correlated atoms and small optical depth.	70
6.2.2	Uncorrelated atoms and large optical depth	73
6.3	Inhomogeneous broadening of the atomic noise spectrum	75

7	Quantum noise of uncorrelated atoms	79
7.1	The setup for detection of atomic quantum noise	80
7.2	Measurements and results	82
7.2.1	The spectrum of atomic spin noise	83
7.2.2	Atomic noise versus optical depth	84
7.2.3	Atomic noise versus probe power	87
7.2.4	A quantum spin noise limited experiment	88
8	Spin squeezing in a cold atomic ensemble	91
8.1	The spin squeezing setup	92
8.1.1	The atomic sample and laser sources	93
8.1.2	The quantum pump	93
8.1.3	The probe and the lock-in detection scheme	94
8.2	DC absorption measurements	96
8.3	Atomic spin noise - coherent excitation	99
8.4	Atomic spin noise - excitation with classical noise	103
8.5	Atomic spin noise - excitation with nonclassical light	106
8.5.1	Spin antisqueezing - $\theta = \pi/2$	106
8.5.2	Spin squeezing - $\theta = 0$	108
8.6	Analysis of the spin squeezing data	108
8.7	The limiting factors - radiation trapping and probe shot noise	111
8.7.1	The degree of spin squeezing and radiation trapping	111
8.7.2	Fluctuations in the spin squeezing data	113
9	Future prospects for spin squeezed atoms	117
9.1	The atomic fountain	118
9.2	Spin squeezing in a fountain	120
10	Résumé	123
10.1	Introduction	123
10.2	Spectroscopy on classically modulated atoms	123
10.3	Squeezed states of light	124
10.4	Mapping the quantum state of light onto atoms	124
10.5	Spin squeezed states and entanglement	125
10.6	Theory for the atomic state readout	125
10.7	Quantum noise of uncorrelated atoms	125
10.8	Spin squeezing in a cold atomic ensemble	126
10.9	Future prospects for spin squeezed atoms	126
A	Circular birefringence for two different transitions	129
B	Correlation functions of Langevin forces	131
B.1	Langevin forces used in the F_z' calculations	132
B.2	Langevin forces used in the $\hat{F}_x'^2 - \hat{F}_y'^2$ calculations	133
C	The ground state fluctuations in light-atom mapping	135
C.1	Correlation functions of ground state variables	137
D	Proof of entanglement in spin squeezed states	139
E	The uncertainty in a spectral density measurement	141

Preface

This thesis is presented for the Faculty of Science at the University of Aarhus as part of the requirements for the Ph.D.-degree in physics.

The work presented in this thesis has been carried out in the Quantum Optics Laboratory at the Institute of Physics and Astronomy, Aarhus University. The work is based on the cesium magneto-optical trap (MOT) and the tunable squeezed light source. These tools were just about to be finished when I joined the Quantum Optics group in 1996. The MOT is constructed by Nicolaj Jørgensen and John Erland, and Jens Lykke Sørensen is responsible for the first squeezing setup. With these two toys available we could soon start the first real experiments, which included spectroscopy on a MOT exposed to classical modulation, sub-shot noise polarization spectroscopy on cold atoms, and observation of the quantum noise of uncorrelated atoms. These experiments were carried out together with Jens Lykke Sørensen. I learned a lot of useful (and some useless) techniques from working with Jens on these experiments. Christian Schori joined the group in 1998, and he participated in the spin squeezing experiment, which constitutes the main results of this thesis. The thesis also includes the theory behind the spin squeezing experiments, and I appreciate the discussions with Alexander Kozhokin about some of the more subtle theoretical aspects.

A new project was started during the last year of my Ph.D. study in collaboration with the group of Christophe Salomon at École Normale Supérieure in Paris. A part of my time has been spent on the construction of the setup for this new experiment on spin squeezing in an atomic fountain. I appreciate the patient answers from Sébastien Bize, Paris, on all my (some times stupid) questions about atomic fountains. I have also had the pleasure of working with Brian Julsgaard on the initial part of this experiment.

I have, during my studies, shared the lab with Peter Lodahl, Lasse Leick, Jens Peter Christensen, Jacob Skovborg Andersen, Mikkel Andersen, and Peter Møller Nielsen. These guys have not been directly involved in the work presented in this thesis, but they have contributed to the general discussions in the lab, and their great sense of humor has made life easier on the days that gave more questions than answers.

Finally, I am truly grateful for the enthusiasm and patience of my thesis adviser Eugene Polzik. I am sure that without his optimism and intuition, we would never have had such fruitful results.

Publications and presentations

The work presented in this thesis have resulted in the following publications

1. J. L. Sørensen, J. Hald, N. Jørgensen, J. Erland, and E. S. Polzik, *Squeezing with $\chi^{(2)}$ for atomic physics and spectroscopy*, Quantum Semiclass. Opt. **9**, 239 (1997). [3]
2. J. L. Sørensen, J. Hald, and E. S. Polzik, *Fundamental noise of an atomic spin measurement*, J. Mod. Opt. **44**, 1917 (1997). [2, 3, 7]
3. J. L. Sørensen, J. Hald, and E. S. Polzik, *Spectroscopy on a modulated magneto-optical trap*, Opt. Lett. **23**, 25 (1998). [2]
4. J. Hald, J. L. Sørensen, L. Leick, and E. S. Polzik, *Quantum noise of cold atomic spins illuminated with non-classical light*, Optics Express **2**, 93 (1998). [3, 4, 7]
5. J. L. Sørensen, J. Hald, and E. S. Polzik, *Quantum noise of an atomic spin polarization measurement*, Phys. Rev. Lett. **80**, 3487 (1998). [3, 7]
6. E. S. Polzik, J. L. Sørensen, and J. Hald, *Subthreshold tunable OPO: a source of nonclassical light for atomic physics experiment*, Appl. Phys. B **66**, 759 (1998). [3, 4]
7. E. S. Polzik, J. Hald, and J. L. Sørensen, *Spectroscopy with non-classical light and non-classical atoms*, AIP Conf. Proc. **467**, 267 (1999). [3, 8]
8. J. Hald, J. L. Sørensen, C. Schori, and E. S. Polzik, *Spin squeezed atoms: a macroscopic entangled ensemble created by light*, Phys. Rev. Lett. **83**, 1319 (1999). [8]
9. E. S. Polzik, J. Hald, and J. L. Sørensen, *From entangled photons to entangled atoms*, in *Quantum Communication, Computing, and Measurement 2*, P. Kumar, G. M. D'Ariano, and O. Hirota, Eds., (Plenum, New York, 2000), pp. 423-432. [8]

The numbers in square brackets refer to the chapters in this thesis which include the results presented in the actual publication.

The work have been presented at the following meetings

- *New Frontiers in Laser-Atom Interactions*, Nordic-European Summer School, Sandbjerg Manor, Denmark, June 1997
- *The Fifth French-Israeli Symposium on Nonlinear & Quantum Optics*, Eilat, Israel, February 1998
- *European Quantum Electronics Conference*, Glasgow, Scotland, September 1998
- *International Workshop on the Physics of Quantum Information*, Helsinki, Finland, September 1998
- *14th International Conference on Laser Spectroscopy*, Innsbruck, Austria, June 1999

Chapter 1

Introduction

The main theme in this thesis is noise in measurements on quantum systems. In particular, we will consider the noise in measurements on atoms and on light. The contributions to the measured noise can be classified as shown in the scheme in Fig. 1.1. In this thesis we will present experimental work within each of the six boxes in the figure. We will start with the simplest experiments within the "upper right" triangle in Fig. 1.1 and work our way down to the "lower left" triangle, with the demonstration of spin squeezed atoms as the prime topic.

The variables of the electromagnetic field are typically measured with an arrangement of photodetectors, whereas the atomic variables can be measured in several different ways. Throughout this thesis we will use spectroscopy with a probe beam of light to read out information about the atoms. The probe field interacts with our atomic sample and subsequently carries information about the atoms. The noise in the transmitted probe field is a sum of the light noise originally present in the probe and the atomic noise added by the atom-light interaction.

The noise of the measured variables can be grouped into classical noise and quantum noise contributions. When we talk about classical noise, we will not distinguish between a modulation we apply on purpose and the unavoidable classical/technical noise like e.g. acoustic noise. In other words, we use the term classical noise for any classical time dependent oscillations/fluctuations. The classical noise can be explained without using quantum mechanics. For example, if a classical electromagnetic field is modulated in amplitude, it will have classical intensity noise at the frequency of modulation. The rms value of this modulation is proportional to the intensity of the field; if we attenuate the intensity of the field by a factor of two, the rms value drops by a factor of two¹. The classical atomic noise is seen if we somehow apply an external modulation to the atomic sample. The modulated atoms will, through the atom-light interaction, result in a modulated atomic contribution to the probe signal. The rms value of the atomic noise is proportional to the number of atoms interacting with the probe field. This classical atomic noise is often considered to be "the signal" in atomic spectroscopy. In chapter 2 we describe a spectroscopy experiment where the signal is induced by classical modulation of the atoms. However, as we will also see in chapter 2, the distinction between signal and noise is decided by the actual experiment; the classical atomic noise considered to be a signal in one experiment may in a different experiment be a noise source that we would rather be without.

The quantum noise contribution is the noise level basically dictated by the Heisenberg uncertainty relation for noncommuting quantum operators. But even the quantum fluctuations can be divided further into two groups. One group contains the fluctuations from systems of uncorrelated particles. In the other group, the quantum noise is manipulated by the use of quantum correlated or entangled particles. These particles can in our experiments be either atoms or photons.

The quantum state of light corresponding to uncorrelated photons is the coherent state. In a photon picture the photon distribution in the coherent state is described by a stochastic Poisson process. In

¹This holds for an applied amplitude modulation as well as for the amplitude modulation caused by e.g. acoustic noise.

		Atomic noise	Light noise
Classical noise		FM Spectroscopy signal	Technical noise
Quantum noise	Uncorrelated particles	Atomic quantum noise	Coherent light Shot noise
	Quantum correlated particles	Spin squeezed atoms	Squeezed light

Figure 1.1: Classification of atom and light noise. The two main groups are classical and quantum noise. The quantum noise can be divided further into noise from uncorrelated particles and noise from quantum correlated particles. The gray "upper right" triangle covers the most simple experiments whereas the experiments in the "lower left" triangle confront the experimentalist with a real challenge.

other words, all photons arrive at random to the photon detector. As a result the rms fluctuations are proportional to the square root of the average number of photons measured in a given measurement time. The different scaling for classical noise and quantum noise of uncorrelated photons makes it easy to characterize the actual light source. Just double the optical power and see if the noise increases by a factor of 2 (predominantly classical noise) or a factor of $\sqrt{2}$ (predominantly quantum noise). The coherent state is the most classical state of light, and the output of many lasers approaches the coherent state at high detection frequencies. At low frequencies the technical (e.g. acoustic) noise gives a huge classical noise contribution on top of the coherent state quantum fluctuations. By band pass filtering of the photocurrent produced by the photodetector, we can reach the coherent state quantum noise (also called shot noise) at frequencies above, typically, a few MHz. Today the signal-to-noise ratio in atomic spectroscopy is often fundamentally limited by the shot noise of the probe light. The experiment in chapter 2 is such an example.

The physics becomes more challenging when we go from the "upper right" triangle to the "lower left" triangle in the scheme in Fig. 1.1. The quantum noise of quantum correlated particles is interesting from two different viewpoints. One of them is the viewpoint of a spectroscopist. Systems of correlated particles can have fluctuations in collective observables below the *standard quantum limit* (SQL) set by the fluctuations of uncorrelated particles. Quantum correlations can therefore be utilized in ultra sensitive spectroscopy with a noise level below the SQL. This holds in ordinary spectroscopy where the limiting factor often is the shot noise of the probe field. But also the atomic quantum noise of uncorrelated atoms can be a limiting factor. This is seen in the state of the art atomic clocks based on fountains of cold atoms. The frequency stability of the clock is today limited by the atomic quantum noise (or projection noise) from uncorrelated atoms [1]. The other viewpoint comes from quantum information, where an essential part is control and manipulation of quantum states of systems composed of several qubits. Our experiment on quantum correlated atoms involves manipulation of a quantum system of many atoms. Although we do not have control at the qubit level, the scheme we use for correlating our atoms may be extended in that direction. The measurement of reduced quantum noise is, within this context, our evidence for successful manipulation and generation of multi-atom quantum correlations.

The first experiment within the "lower left" triangle was generation of squeezed light by R. E. Slusher *et al.* in 1985 [2]. In the squeezed light the photons are pair-wise correlated so that e.g. the amplitude of the field has fluctuations below the shot noise level. Still, Heisenberg's uncertainty relation must be fulfilled and the conjugate variable (the phase of the field) will have increased fluctuations. In chapter 3 we describe our source of squeezed light together with an experiment on sub-shot noise polarization spectroscopy of classically modulated atoms.

The rms quantum noise of uncorrelated atoms scales with the square root of the number of atoms

being probed. Thus, just as with classical and quantum light noise, we can distinguish between classical and quantum atomic noise by the dependence on the number of probed atoms. The first experiment, where the atomic noise was observed and the \sqrt{N} scaling was indicated, utilized up to a few hundred trapped ions and was carried out by W. M. Itano *et al.* in 1993 [3]. A much more reliable measurement of the \sqrt{N} dependence was measured by our group in a polarization spectroscopy setup with cold trapped atoms in 1998 (chapter 7 and Ref. [4]). Subsequently, the atomic quantum noise has been observed in the atomic fountain clock [1] and in atomic QND measurements [5].

The most challenging experiment is the observation of a change in the atomic noise properties caused by quantum correlated atoms. In Ref. [6] we report on the observation of reduced fluctuations in a collective atomic spin component due to quantum correlated atoms. The effect is analogous to squeezing of light where correlations reduce the fluctuations in a given observable below the quantum fluctuations of uncorrelated photons. The analogy also goes into the terminology; the prepared quantum correlated atomic ensemble is said to be spin squeezed. The detection of reduced quantum noise in spin squeezed atoms is the main topic in this thesis. The spin squeezed atoms are generated by mapping the quantum state of squeezed light onto certain atomic spin components. This mapping of quantum correlations from one quantum system to another quantum system links our experiment to the notion of quantum information. We could consider the correlated photons to be the quantum information carriers and the atoms to be the storage medium for quantum information [7]. In this thesis we consider mapping of squeezed light, but other nonclassical states of light may be used too, as proposed theoretically in Ref. [8].

The initial theory behind the spin squeezing experiment is given in Ref. [9]. In chapter 4 we extend this theory to atoms with nonzero ground state angular momentum and for an arbitrary polarization squeezed excitation field. This extension is found to be nontrivial and brings the theory closer to the experimental realization. Chapter 5 introduces the concept of spin squeezed states, and the results of chapter 4 are related to the notion of spin squeezing. In chapter 6 we present the theory for the readout of atomic fluctuations using a coherent state probe of light. Note that the theoretical chapters include the coherent field excitation and the quantum noise of uncorrelated atoms as a special case. We therefore choose to present the full theory before the two experimental chapters on quantum noise of uncorrelated atoms (chapter 7) and quantum noise of spin squeezed atoms (chapter 8).

The future prospects for spin squeezed atoms are discussed in chapter 9. A new project based on an atomic fountain (similar to the fountains used in frequency standards [1]) is currently under construction in our laboratory. The new experiment involves spin squeezing in the atomic ground state and quantum memory. The ideas and advantages behind this new experiment are presented.

The final chapter is a résumé of the thesis with emphasis on the main results and conclusions from each chapter.

Chapter 2

Spectroscopy on classically modulated atoms

In this chapter we investigate the classical contributions to the signal and noise when atoms are probed by a beam of light. Although the main theme in this thesis is the quantum noise in atom-light interactions, it is instructive first to consider the classical counterparts. In particular, we consider the polarization and intensity noise of a probe field after interaction with a classically modulated atomic ensemble. The measured probe noise induced by this classical modulation is usually referred to as the signal in atomic spectroscopy. However, the distinction between "signal" and "noise" is not unique. What in one experiment is considered to be a signal, may in other experiments be a noise source. We will see such an example at the end of this chapter. The classical noise is described by a semi-classical theory involving classical electromagnetic fields and mean values of atomic observables. In the following chapters we will extend this theory to include quantized fields as well as quantum fluctuations of the atomic observables.

We begin this chapter with an introduction to our atomic sample. We use cesium atoms, which are cooled and trapped in a magneto-optical trap (MOT). The MOT is an important tool in our experiments, and the working principles of the MOT are important for the understanding of the experiments presented later on. The MOT parameters relevant for our experiments are mainly the density of atoms and the overall number of trapped atoms. These two parameters are measured by absorption spectroscopy with a weak probe field. We continue with a section on double-optical resonance, which is a technique used extensively throughout this thesis. We use double-optical resonance with a weak probe on the upper transition to probe certain properties of the atoms in the intermediate state. In this chapter, we also introduce the polarization interferometer (PI). This device is used along with the double-optical resonance technique for probing atoms. When the PI is employed, we get access to certain intermediate state atomic spin components. We complete this chapter with our experiments concerning spectroscopy on classically modulated atoms.

2.1 The magneto-optical trap

The atomic samples used in the experiments presented in this thesis are cesium atoms trapped and cooled in a magneto-optical trap (MOT). Cesium is very convenient for interaction with squeezed light due to the atomic transitions frequencies. Some of the best sources for production of squeezed light are based on the sub-threshold OPO with KNbO_3 as the non-linear material (see chapter 3). The non-critical phase matching of a-cut KNbO_3 can be achieved for the 850nm-920nm wavelength range by adjusting the crystal temperature between 0°C and 130°C . Thus, both the $6S_{1/2} \rightarrow 6P_{3/2}$ (852nm) and the $6P_{3/2} \rightarrow 6D_{5/2}$ (917nm) transitions in Cs are covered by the KNbO_3 based squeezing source. Furthermore, the relatively simple level structure of cesium makes cooling and trapping in a MOT quite

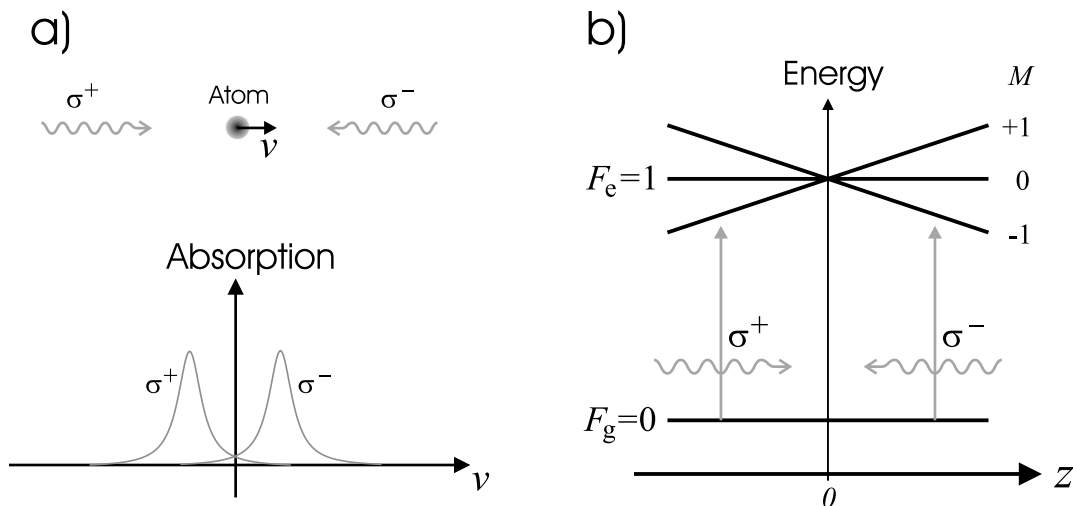


Figure 2.1: a) The 1D absorption profiles for σ^+ and σ^- polarized counterpropagating laser fields versus the atomic velocity. The net effect is a damping force on the atoms. b) The 1D position dependent energy levels are the result of the magnetic field gradient. At positive z the σ^- field is resonant and pushes atoms back to $z = 0$. The σ^+ field is resonant at negative z . The net effect is a "spring force" on the atoms.

easy, and the trapping transition at 852nm can be reached by inexpensive diode lasers. Since the first demonstration of magneto-optical trapping in 1987 [10], the MOT properties (e.g. temperature, density and overall number of atoms) have been studied extensively. Densities on the order of 10^{12}cm^{-3} and temperatures as low as $4\mu\text{K}$ have been achieved for a small Cs MOT with a trap diameter below $50\mu\text{m}$ [11]. The small, dense and cold MOT was the first step in generation of Bose-Einstein condensation in a dilute Rb gas [12]. The MOT has also been used in a number of quantum optics experiments where the demands on temperature and density are less stringent. In these experiments, as well as in ours, the basic requirements to the atomic sample are a Doppler width much smaller than the natural linewidth and enough atoms for efficient light-atom interaction. A standard MOT is used because it is robust and easy to operate. Very large traps (1.1cm diameter) containing a large number of atoms ($3 \cdot 10^{10}$) can be obtained by the use of large and powerful laser beams [13]. The fluorescence photons in the large traps experience multiple scattering before escaping the atomic cloud. This radiation trapping heats the atoms, and the temperature can reach the mK level [14, 15]. However, the Doppler width is still small compared to the natural linewidth.

2.1.1 The basic MOT theory

The theory behind the MOT is most easily explained in one dimension. Two forces are needed to cool and trap atoms; a damping force, which always acts in the direction opposite to the atomic velocity, and a "spring force", which acts towards the center of the trap. The damping force is provided by two counterpropagating, red-detuned and circularly polarized laser beams (Fig. 2.1a). If an atom is moving towards one of the laser beams, it will, because of the Doppler shift, absorb more photons from the counterpropagating laser beam than from the copropagating beam. Each photon absorption is accompanied by a momentum kick in the laser beam direction and followed by a spontaneous emission together with a momentum kick in a random direction. After many absorption/emission cycles, the atomic velocity is reduced by this cooling method known as Doppler cooling.

The spring force requires Zeeman degeneracy of the atomic excited state and a magnetic field gradient.

We consider for simplicity a $F_g = 0 \rightarrow F_e = 1$ transition, where F_g and F_e are the total atomic angular momentum in the ground- and excited state. The position dependent splitting of the Zeeman levels due to the magnetic field gradient is shown in Fig. 2.1b. At positive z positions the σ^- polarized field is close to resonance with the $|F_g, 0\rangle \rightarrow |F_e, -1\rangle$ transition, whereas the σ^+ field is far from resonance with the $|F_g, 0\rangle \rightarrow |F_e, +1\rangle$ transition¹. The situation is opposite at negative z . Atoms at positive (negative) z positions mostly absorb photons from the σ^- (σ^+) field and they are hence pushed towards $z = 0$.

In real life things are a bit more complicated. First of all, atoms are trapped and cooled in three dimensions. This is easily achieved by using three pairs of counterpropagating laser fields - one pair for each dimension. A pair of coils in the anti-Helmholtz configuration provides the necessary magnetic field gradients in all three dimensions with zero magnetic field in the center. Most atoms have Zeeman degenerate ground states ($F_g > 0$). The Doppler cooling mechanism still works with a minimum temperature given by the Doppler limit $T_D = \hbar\gamma/2k_B$, where γ is the linewidth of the cooling transition. It is possible to go below T_D when the polarization gradients of the overall excitation field and the degeneracy of the ground state is taken into account [16, 11].

2.1.2 Characterization of the MOT by absorption spectroscopy

The basic component of the vapor cell MOT is a vacuum chamber with viewports for three pairs of counterpropagating laser beams in three dimensions. A cesium cell with a valve is connected to the chamber so that the cesium pressure inside the vacuum chamber can be adjusted by opening/closing the valve. The atoms are trapped from the low velocity tail of the Maxwell distribution of atoms at room temperature. An ion-pump is used to keep the pressure of gases other than Cs at around 10^{-9} torr. The typical Cs pressure is 10^{-8} torr. A pair of coils in an anti-Helmholtz configuration provides a quadrupole magnetic field with a maximum field gradient at the center of about 10 gauss/cm.

Besides the chamber we also need the lasers. In all experiments presented in this thesis we use the same vacuum chamber for the MOT, whereas different lasers are used for the cooling and trapping. In the first experiments we use a diode laser (SDL 5401), which is stabilized by optical feedback from a grating. The construction of the MOT based on diode lasers is described in detail in Ref. [17]. The diode laser is inexpensive and easy to operate. However, the large excess phase noise of the diode laser [18, 19] is found to be a major obstacle in observation of the quantum noise of independent atoms [20]. In the measurements on atomic noise, we substitute the diode laser for trapping with a much more quiet Ti:Sapphire laser. Besides having better noise properties, the Ti:Sapphire laser also produces more power, and that improves the number of atoms trapped in the MOT. In the first setup we use only five laser beams although the standard MOT geometry consists of six laser beams as described above. Two beams are counterpropagating and the other three beams are in the plane perpendicular to the first two beams and at an angle of 120° to each other. This geometry is not efficient in terms of laser power since three of the beams cannot be reused by simple retroreflection. When we modified the trap to utilize the Ti:Sapphire laser, the configuration was changed to a standard six beam MOT with retroreflection of the three beams. At the same time the size of the beams was increased from about 6mm to 25mm in diameter. The increase in beam size is required for optimum trapping with the larger power provided by the Ti:Sapphire laser [13]. The diode laser gives us about 15-20mW for trapping, whereas we have 150-200mW optical power for trapping when the Ti:Sapphire laser is used. At the end of this chapter we show a picture of the MOT vacuum chamber and the surrounding optics for the six-beam configuration, (Fig. 2.8, page 22).

The relevant atomic levels in cesium are shown in Fig. 2.2a. Trapping and cooling take place on the closed transition $6S_{1/2}F = 4 \rightarrow 6P_{3/2}F = 5$. The splitting between $6P_{3/2}F = 5$ and $6P_{3/2}F = 4$ is around 250MHz ($50\gamma/2\pi$), and there is a small probability ($\sim 10^{-4}$) of exciting atoms on the $6S_{1/2}F = 4 \rightarrow 6P_{3/2}F = 4$ transition. Atoms can subsequently decay to the other ground state $6S_{1/2}F = 3$. A repumping laser on $6S_{1/2}F = 3 \rightarrow 6P_{3/2}F = 4$ pumps atoms in the $F = 3$ ground state back into the

¹ σ^+ and σ^- do not refer to the helicity of the fields (quantization along the direction of field propagation). Instead, we describe the polarizations of the two fields using a common quantization axis.

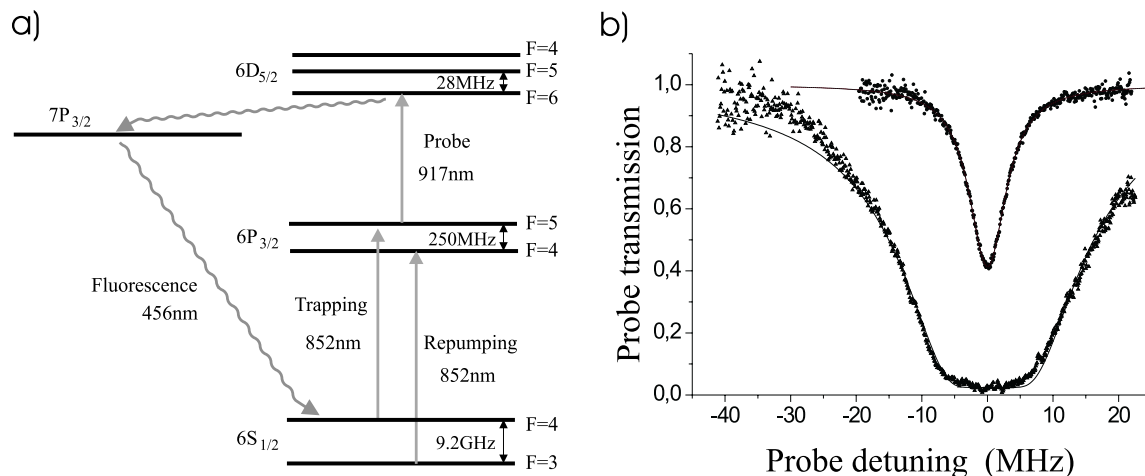


Figure 2.2: a) The relevant energy levels in Cs and the three fields interacting with the atoms (trapping, repumping and probe field). The decay from $6D$ to $7P$ has a branching ratio of only 0.4%, but this is enough to observe the blue fluorescence at 456nm when a strong probe field is present, see Fig. 2.8 page 22. b) Absorption spectra for a weak 852nm probe scanned across the atomic resonance in the "dark". Narrow profile (dots): reduced atomic density. Broad profile (triangles): maximum trap density. Solid lines: Fit to Eq. (2.1).

cooling cycle. In all experiments we use a diode laser (SDL 5401) for repumping with around 30mW of available power. The laser frequencies are locked close to the atomic transitions by an electronic feedback loop, utilizing an error signal obtained from standard FM saturation spectroscopy methods [21, 22]. The repumping laser is locked at exact resonance, whereas the trapping laser is detuned between 5 and 15MHz to the red. The tuning of the trapping laser is made possible by an acousto-optical modulator (AOM) in the probe path of the saturation spectroscopy setup. The RF frequency of the AOM supply sets the frequency of the trapping laser relative to the atomic transition frequency.

Initially we had a single Ti:Sapphire laser (Microlase MBR-110) pumped by an Ar-ion laser (Spectra-Physics 2080). This laser was used for probing the atoms in the MOT on the $6P_{3/2} \rightarrow 6D_{5/2}$ transition at 917nm (Fig. 2.2a). When we realized that the phase noise of the diode laser prevented us from observing the quantum noise of independent atoms, we decided to build a second Ti:Sapphire laser. The construction of this laser is described in detail in Ref. [23]. Both Ti:Sapphire lasers are pumped by the same Ar-ion laser. In the first atomic quantum noise experiment we use the home-made Ti:Sapphire laser for trapping and the MBR-110 for probing. In the spin squeezing experiment we find it more advantageous to change the role of the two lasers. However, the trapping parameters in terms of beam size, power and detuning are similar in the two experiments.

The most relevant MOT parameter for our experiments is the optical depth α for a probe of light. α describes the efficiency at which the probe interacts with the atomic sample, and it is defined through the transmission as $T = \exp(-\alpha)$. Depending on the type of experiments, we either require α to be large or small compared to 1. It also depends on the experiment whether it is the optical depth on the 852nm transition or on the 917nm transition which is of importance. In the experiment on modulated MOT spectroscopy (section 2.4) we do not need a large α because of the high efficiency of the modulation technique. In the squeezed probe experiment (chapter 3) α should be small since large absorption will deteriorate the squeezing. In the first experiment where the atomic quantum noise is observed (chapter 7) it is an advantage to have large α on the probe transition because the quantum noise (variance) scales linearly with the number of atoms. Finally, in the spin squeezing experiment (chapter 8) we need a large optical depth on the pump transition (852nm) in order to efficiently map the quantum correlations of

light onto the atoms.

Here we consider the optical depth on the $6S_{1/2}F = 4 \rightarrow 6P_{3/2}F = 5$ (852nm) transition when a Ti:Sapphire laser is used for trapping. We turn off the trapping beams in order to probe the atoms without the influence of the strong trapping beams. In the following "dark" period we measure the absorption of a weak probe scanned across resonance with a rate of 0.4MHz/ μ s. The probe field comes from the laser used for trapping, and it is scanned in frequency by the use of two AOMs. We turn off the current in the coils generating the quadrupole magnetic field at the time when the trapping beams are turned off. The measured absorption spectra for maximum α and a somewhat reduced α are shown in Fig. 2.2b (dots and triangles). The optical depth is reduced by attenuation of the repumping field. Without any excess broadening, the absorption spectrum is given by

$$T(\Delta) = \exp(-\alpha(\Delta)) = \exp\left(-\frac{\sigma_0 \rho l}{1 + 4\Delta^2/\gamma^2}\right) \quad (2.1)$$

$$\sigma_0 = \frac{2F + 3}{2F + 1} \frac{\lambda^2}{2\pi}$$

$\Delta = \omega_{atom} - \omega_{field}$ is the atom-laser detuning, ρ is the density of atoms, l is the diameter of the atomic cloud, γ is the natural linewidth and σ_0 is the resonant absorption cross section. The expression for σ_0 is valid for an $F \rightarrow F' = 1$ transition with unpolarized atoms and arbitrary polarization of the probe field, see chapter 6, Eq. (6.16). Fitting the small α data in Fig. 2.2b to Eq. (2.1) with ρ and γ as free parameters gives $\gamma_{fit}/2\pi = 5.42$ MHz. An average over six independent absorption measurements gives $\gamma_{fit}/2\pi = 5.58 \pm 0.05$ MHz. We can deduce the density of trapped atoms by fitting the large α measurements in Fig. 2.2b to Eq. (2.1). For a large resonant optical depth α_0 we can approximate Eq. (2.1) by $T(\Delta) \simeq \exp(-\alpha_0 \gamma^2/\Delta^2)$, and we can no longer fit γ and α_0 independently. We therefore fit the large α measurements to the absorption spectrum in Eq. (2.1) with $\gamma/2\pi$ fixed at 5.58MHz. The fit is shown in the figure as a solid line², and it gives a resonant optical depth of $\alpha_0 = 23 \pm 3$. The discrepancy between the fit and the measurements at detunings below -20MHz is explained by the probe moving off the trap when the AOM frequency is scanned very far. Only the data between ± 22 MHz are used in the fit. The diameter of the trap is estimated from fluorescence pictures taken with a CCD camera. The measured diameters in the horizontal and vertical plane agree within 10%, and the maximum FWHM diameter observed is 6.2 ± 0.5 mm [23]. For large traps the density is almost constant within the trap [15], and we can estimate the density and overall number of trapped atoms as

$$\rho = \frac{\alpha_0}{\sigma_0 l} = (2.6 \pm 0.4) \cdot 10^{10} \text{cm}^{-3} \quad (2.2)$$

$$N = \frac{4\pi l^3 \rho}{24} = (3.2 \pm 0.9) \cdot 10^9$$

The measured density is in agreement with previous results for a large Cs MOT with similar parameters [13]. When we use the diode laser for trapping, the MOT is somewhat smaller with a diameter of about 1.5mm and a density near $3 \cdot 10^9 \text{cm}^{-3}$.

The measured linewidth $\gamma_{fit}/2\pi$ is about 7% larger than the known natural linewidth of 5.23MHz [24]. Several possible contributions to the excess broadening exist: power broadening by the probe, Doppler broadening from nonzero temperature, optical pumping, magnetic broadening, and nonzero laser linewidth (about 100kHz). In the following we discuss the importance of each contribution.

The power broadened linewidth is given by $\gamma\sqrt{1 + 2s_0}$, where we have defined the resonant saturation parameter as $s_0 = \sigma_0 \Phi/\gamma\pi w^2$ with Φ as the probe photon flux and $2w$ as the probe diameter. s_0 can be written in terms of a saturation intensity as $s_0 = I/I_{sat}$ with $I_{sat} = 5.50 \text{mW/cm}^2$. For a $2\mu\text{W}$ probe with a beam radius of 0.7mm, we deduce a power broadened linewidth of 1.02γ .

²We explain the 2.5% transmission at $\Delta = 0$ by a small fraction of non-resonant light in the probe. This is possible if a small part of the travelling soundwave in the AOM is reflected on the crystal surface. The -1 order of the reflected wave will be diffracted into the same spatial mode as the +1 order diffraction of the main soundwave.

The finite temperature of the atoms adds Doppler broadening to the measurement with a FWHM linewidth of $\delta\nu_D = 243\sqrt{T/T_D}$ kHz. The Doppler limit for Cs is given by $T_D = \hbar\gamma/2k_B = 125\mu\text{K}$. The temperature in a MOT with powerful trapping beams scales as [15, 11]

$$T = A + BN^{1/3} \frac{\gamma\sqrt{s_0^t}}{\Delta} \quad (2.3)$$

s_0^t is the total saturation parameter for the trapping beams. The constants A and B are in our notation given by $A=30\mu\text{K}$ and $B=0.36\mu\text{K}$. Using 6 trapping beams with a $2.5\pm 0.2\text{cm}$ diameter and $60\pm 5\text{mW}$ in each beam gives an average saturation parameter in the center of $s_0^t = 27\pm 5$. With $\Delta/2\pi = 12\pm 2\text{MHz}$ we get a MOT temperature of $T = 1.2\pm 0.3\text{mK}$. The Doppler width is then found to be $\delta\nu_D \simeq 0.75\text{MHz}$. For the small α measurement in Fig. 2.2b, the number of atoms are somewhat smaller. The trap size is measured to be about 4mm and with $\alpha_0 \simeq 1$ we get $N \simeq 6 \cdot 10^7$ and $\delta\nu_D \simeq 0.4\text{MHz}$. Addition of the independent contributions from Doppler broadening and laser linewidth gives $\delta\nu = (\delta\nu_D^2 + \delta\nu_L^2)^{1/2} \simeq \delta\nu_D$.

Optical pumping by the weak probe beam can decrease the observed linewidth. When the σ^+ polarized probe approaches resonance it will start to optically pump atoms into the $|F=4, m=4\rangle$ state. The absorption cross section on the $|4, 4\rangle \rightarrow |5, 5\rangle$ transition is almost 3 times larger than σ_0 from Eq. (2.1), and consequently the absorption is increased at resonance. This problem can be circumvented by optically pumping of all atoms into $|4, 4\rangle$ before doing the spectroscopy. However, optical pumping is not that easy in the presence of a magnetic field perpendicular to the circularly polarized probe field. The typical time scale for optical pumping is given by the inverse excitation rate $(s_0\gamma)^{-1} \simeq 1.5\mu\text{s}$. The pumping is destroyed by Larmor precession of the atomic spin around the direction of the magnetic field. The Larmor period for the $6S_{1/2} F=4$ state in a 1gauss field (the typical residual field from ion-pump, earth field etc.) is $2.7\mu\text{s}$. With the Larmor period comparable to the optical pumping time we neglect the effect of optical pumping.

The magnetic broadening has two contributions. In a homogeneous magnetic field, the different $|F=4, m\rangle \rightarrow |F'=5, m+1\rangle$ transitions have different resonance frequencies because the gyromagnetic ratios for the upper and lower state are unequal. The predominant contribution with a magnetic field gradient present is the different Zeeman splittings for different atoms/positions. We can estimate the gradient contribution to the magnetic broadening by the product of the field gradient (10gauss/cm), the diameter of the trap (4mm), and the ratio of the Larmor frequency to the magnetic field (0.37MHz/gauss), and we get $\delta\nu_B \simeq 1.5\text{MHz}$. The measured linewidth for small α_0 is found to increase by 1.2MHz to $6.80\pm 0.10\text{MHz}$ when the magnetic field gradient is present during the probe absorption measurement. The measurements in Fig. 2.2b are taken after the trapping beams and the current to the coils are turned off. However, the chamber itself has the shape of a torus and is made of stainless steel. It is possible that a current is induced in the chamber when the gradient coils are shut down. A measurement with a small probe coil close to the chamber indicates that this is in fact the case, although a careful measurement at the center of the chamber was never done.

If we add the Doppler broadening to the power broadened natural linewidth we get a Voigt profile with $\gamma_{\text{Lorentz}}/2\pi = 5.3\text{MHz}$ and $\gamma_{\text{Gauss}}/2\pi = 0.4\text{MHz}$. However, this profile is still well fitted with a pure Lorentzian lineshape with $\gamma = 5.3\text{MHz}$. We believe that the observed excess broadening is caused mainly by the residual magnetic field gradient together with the bias field from ion-pump, earth magnetic field etc. The difference in excess broadening for the small and large α_0 measurements in Fig. 2.2b is expected to be small compared to 5.58MHz, and its effect on the measured maximum optical depth α_0 is within the stated uncertainty.

2.2 Double-optical resonance

We now consider the probing of excited state Cs atoms on the $6P_{3/2} F=5 \rightarrow 6D_{5/2} F=6$ transition at 917nm (Fig. 2.2a). The atoms are excited to the $F=5$ state by the rather strong trapping fields, and we

probe the atoms while the MOT is running. Closely related experiments on excited state spectroscopy on cold trapped atoms can be found in Ref. [25, 26].

The experimental situation can be described by a three-level atom interacting with two near-resonant laser fields if we neglect the Zeeman degeneracy of the atomic states. The theory for this system, known as *double-optical resonance* or *cascade two-photon transitions*, is derived for arbitrary intensities and detunings for the two fields in Ref. [27]. We will use the terms *pump field* or *excitation field* for the laser field exciting atoms on the lower transition ($6S_{1/2}F = 4 \rightarrow 6P_{3/2}F = 5$) and *probe field* for the field interacting with atoms on the upper transition ($6P_{3/2}F = 5 \rightarrow 6D_{5/2}F = 6$). It is possible to arrive at rather simple analytical expressions for this system under the constraints of a weak probe. The results in Ref. [28] can be used to derive the following expression for the complex probe susceptibility

$$\chi = \chi_r + i\chi_i = \frac{13\rho\lambda^3}{11 \cdot 8\pi^2} \frac{s_0}{2s_0 + 1 + 4\Delta^2/\gamma^2} \frac{-(i\gamma_{21} - \Delta')\gamma'}{(i\gamma_{21} - \Delta')(i\gamma'/2 - \Delta - \Delta') - s_0\gamma^2/4} \quad (2.4)$$

The susceptibility is defined through the relation $\mathbf{P} = \varepsilon_0\chi\mathbf{E}$, where \mathbf{P} and \mathbf{E} are the polarization density and the probe electric field. s_0 is the resonant saturation parameter for the pump field. We use a prime on the variables related to the probe transition. γ, γ' are the spontaneous decay rates for the two states, $\gamma_{21} = (\gamma + \gamma')/2$, and Δ, Δ' are the detunings of the two fields. We use $\gamma'/2\pi = 3.1\text{MHz}$ for the $6D_{5/2}$ state natural linewidth [29]. λ is the probe wavelength and ρ is the density of atoms. Note that the second fraction in (2.4) is the intermediate state population. The optical depth on the probe transition is given by

$$\alpha'_i(\Delta') = 2\pi \frac{l\chi_i(\Delta')}{\lambda} \quad (2.5)$$

In the limit of a weak resonant pump field ($s_0 \ll 1$), the expression for the probe optical depth in Eq. (2.5) is identical to the optical depth for the probing of ground state atoms if, in Eq. (2.1), we substitute the density of atoms in the intermediate state for ρ . For large s_0 the absorption line splits up into an AC Stark doublet [28].

In Fig. 2.3a we plot the measured probe transmission $T = \exp(-\alpha'(\Delta'))$ versus the probe detuning. The measurement is carried out while the MOT is on and the trapping beams excite atoms to the intermediate level. We use a powerful Ti:Sapphire for trapping with a value for the average saturation parameter similar to the value in the previous section; $s_0 = 27 \pm 5$. However, we cannot neglect the interference of the fields in the 3D configuration with circularly polarized laser beams. We can write one pair of counterpropagating trapping fields as

$$\begin{aligned} \vec{E}_{\sigma^+}(z, t) &= E_0 (\cos(kz - \omega t + \phi_1) \mathbf{e}_x - \sin(kz - \omega t + \phi_1) \mathbf{e}_y) \\ \vec{E}_{\sigma^-}(z, t) &= E_0 (\cos(-kz - \omega t + \phi_2) \mathbf{e}_x + \sin(-kz - \omega t + \phi_2) \mathbf{e}_y) \end{aligned} \quad (2.6)$$

Here $\mathbf{e}_{x,y}$ are the unit polarization vectors along the x - and y axis. The other four beams are given by similar expressions. Adding the six fields and calculating the intensity gives for all phases ϕ_i set to zero

$$\left| \vec{E}_{total} \right|^2 = E_0^2 (6 + 4 [\cos(kz) \sin(ky) - \cos(kx) \sin(kz) + \cos(ky) \sin(kx)]) \quad (2.7)$$

We see that the total intensity has a strong position dependence. Since the relative phases ϕ_i are not stabilized, we calculate the probability distribution for the total intensity assuming uniform distributions of all phases and positions. This is easily done in a Monte Carlo simulation, and one finds that the average intensity is indeed the sum of the intensities in each of the six beams. The maximum intensity is twice the average, and the minimum intensity is zero. We make the further assumption that the atomic density is proportional to the local field intensity. This is explained by the dipole force of the red-detuned trapping field [26]. The probability for an atom to be at a position with field intensity x (normalized to the average

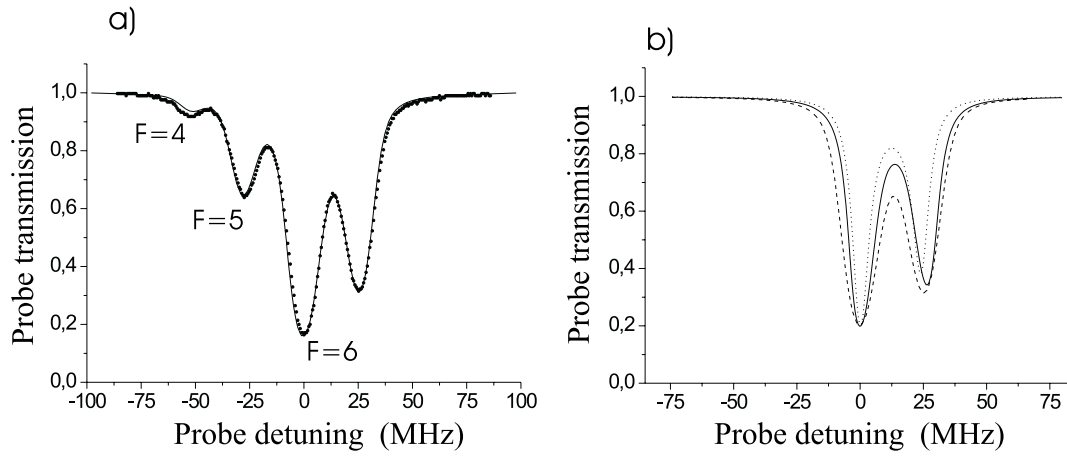


Figure 2.3: a) Dots: the measured probe transmission spectrum in double-optical resonance. Line: theoretical spectrum, Eq. (2.11). Three hyperfine components are seen together with AC Stark splitting of the $F = 6$ component. b) Theoretical transmission spectra for a single hyperfine component. Dotted line: without any broadening; based on $\alpha'_i(\Delta')$ Eq. (2.5). Solid line: including polarization gradient effects; $\alpha'_{ii}(\Delta')$ Eq. (2.8). Dashed line: including magnetic broadening; $\alpha'_{iii}(\Delta')$ Eq. (2.9). All three spectra are normalized to the same maximum absorption. Note the different detuning scale in a) and b).

intensity) is termed $P(x)$. The probe optical depth including polarization gradient effects is then given by

$$\alpha'_{ii}(\Delta') = \frac{2\pi l}{\lambda} \int_0^2 \chi_i(\Delta', \bar{s}_0 \cdot x) P(x) dx \quad (2.8)$$

\bar{s}_0 is the average saturation parameter.

Besides the spatially dependent intensity, we also have the magnetic field gradient, which broadens the line. It is not possible to model the magnetic broadening accurately without including the Zeeman sublevels in the theory. The measurements from the previous section show that the width of the $6S_{1/2}F = 4 \rightarrow 6P_{3/2}F = 5$ transition with the magnetic field gradient present is 6.8MHz for a Lorentzian fit. In a Voigt fit with the Lorentzian width set to 5.3MHz, this corresponds to a inhomogeneous Gaussian broadening of 3.7MHz. A simple way of including the magnetic broadening consists of averaging α'_{ii} over a Gaussian distribution of detunings with identical width for the pump and probe transition. We then obtain

$$\alpha'_{iii}(\Delta') = \frac{1}{\sqrt{\pi}} \int_{-\infty}^{\infty} \alpha'_{ii}(\Delta' + by, \Delta + by) e^{-y^2} dy \quad (2.9)$$

$$b/2\pi = \frac{\delta\nu_{Gauss}}{2\sqrt{\ln 2}}$$

$\delta\nu_{Gauss}$ is the FWHM Gaussian width. We use $\delta\nu_{Gauss} = 5.2\text{MHz}$ to account for the larger trap size in the measurement in Fig. 2.3a (about 6mm).

The last complication is the small hyperfine splitting in the $6D_{5/2}$ state. The strength of the $(J_1, F_1) \rightarrow (J_2, F_2)$ transition with an unpolarized F_1 state (equal population in all Zeeman sub-levels) is for arbitrary F_2 proportional to [30]

$$(2F_2 + 1) \left\{ \begin{array}{ccc} F_2 & 1 & F_1 \\ J_1 & I & J_2 \end{array} \right\}^2 \quad (2.10)$$

I is the nuclear spin ($I = 7/2$ for ^{133}Cs) and $\{\cdot\}$ is the 6j symbol. We find the relative strengths of the dipole allowed transitions $6P_{3/2}F = 5 \rightarrow 6D_{5/2}F = 6, 5, 4$ to be $1 : \frac{77}{325} : \frac{21}{650}$. The hyperfine splitting in the $6D_{5/2}$ state is given by [31] $\delta_F = \frac{1}{2}A(F(F+1) - J(J+1) - I(I+1))$ with $A/2\pi = -4.69\text{MHz}$ [29]. The final expression for the measured probe absorption spectrum is given by

$$T(\Delta') = \exp(-\alpha'_{iv}(\Delta')) \quad (2.11)$$

$$\alpha'_{iv}(\Delta') = \alpha'_{iii}(\Delta' - \delta_6) + \frac{77}{325}\alpha'_{iii}(\Delta' - \delta_5) + \frac{21}{650}\alpha'_{iii}(\Delta' - \delta_4)$$

In Fig. 2.3a we show, as a solid line, the theoretical absorption spectrum from Eq. (2.11) with the parameters $\gamma/2\pi = 5.2\text{MHz}$, $\gamma'/2\pi = 3.1\text{MHz}$, $\bar{s}_0 = 20$, $\Delta/2\pi = 4.2\text{MHz}$, $\delta\nu_{Gauss} = 5.2\text{MHz}$, $l = 6.2\text{mm}$, $\lambda = 917\text{nm}$ and $\rho = 2.0 \cdot 10^{10}\text{cm}^{-3}$. The parameters ρ , \bar{s}_0 , and Δ are chosen for the best agreement between theory and experiment. A careful measurement of the experimental detuning is not carried out for the actual measurement, but we estimate it to be in the range of $5 - 10\text{MHz}$. An increase in Δ in the theoretical graph will increase the asymmetry between the two components of the $F = 6$ AC Stark doublet. The small "theoretical" detuning indicates that the measured asymmetry is smaller than expected theoretically. A similar observation is found in section 2.4.2 and in Ref. [26]. Equation (2.5) is valid when radiative decay is the only source to atomic decoherence. The asymmetry in the AC Stark doublet will typically be reduced in the presence of excess atomic decoherence [28]. It is therefore not unlikely that the discrepancy between the estimated experimental detuning and the theoretical detuning can be caused by a too simple implementation of e.g. the magnetic field, the Zeeman degenerate atoms, and the neglected trap dynamics. Otherwise the agreement between measurement and theory is good, and it confirms the atomic density measured in section 2.1.2. The hyperfine splitting in $6D_{5/2}$ and the AC Stark splitting of the $6P_{3/2}F = 5$ state are almost identical, and this results in overlapping lines. This explains why we only see four absorption lines and not all six lines from the AC Stark doublets for each hyperfine component. For comparison we show in Fig. 2.3b the theoretical curves corresponding to the incomplete expressions in Eq. (2.5), (2.8) and (2.9).

2.3 The polarization interferometer

We proceed with a simple description of the polarization interferometer (PI), and we explain which atomic variables we can probe by utilizing the PI. In chapter 6, we give a more complete description of atomic measurements with the PI, which is necessary for a complete understanding of the spin squeezing experiment. For now the following simple analysis using classical fields will be sufficient.

The polarization interferometer consists of two polarizing beamsplitters (PBS) and a half-wave retarder in between, (see the setup in Fig. 2.4, page 16, which involves the PI). The first polarizer is used to give a probe light beam a well defined polarization. In chapter 3, this polarizer is also used to mix the coherent state probe with a squeezed vacuum field for spectroscopy below the standard quantum limit. The wave plate rotates the polarization of the light by 45° before the second polarizer splits the beam into two components with intensities I_1 and I_2 . The optical power in each of the two output arms is detected with two photodetectors, and the difference (i_-) between the resulting two photocurrents (i_1, i_2) is measured. i_- is obviously proportional to the difference in the optical intensities, $I_1 - I_2$. The intensities in the two output arms are identical without anything else in the interferometer. If we now place an anisotropic medium between the two polarizers, the probe polarization may be rotated further giving a nonzero current i_- . The anisotropic medium will, of course, be our sample of cold and trapped cesium atoms.

We can use the Jones formalism to describe the effect of the anisotropic medium on the two circular components of the probe polarization [32]. The general expression for the change in the complex amplitudes of the two orthogonal circular polarizations after propagating a small distance dz , is given

by

$$d\mathbf{E} = (\underline{\mathbf{A}} - \frac{\sigma\rho}{2}\mathbf{1})\mathbf{E}dz \quad (2.12)$$

Here $\mathbf{E} = (E^+, E^-)^T$ are the circularly polarized field amplitudes, $\mathbf{1}$ is the identity matrix, σ is the atomic cross section averaged over polarizations, ρ is the density of atoms being probed, and $\underline{\mathbf{A}}$ is given by

$$\underline{\mathbf{A}} = \frac{1}{l} \begin{pmatrix} -\xi^+ - i\eta^+ & -\xi^{+-} - i\eta^{+-} \\ -\xi^{-+} - i\eta^{-+} & -\xi^- - i\eta^- \end{pmatrix} \quad (2.13)$$

l is the geometrical length of the anisotropic medium. $\underline{\mathbf{A}}$ describes the anisotropic properties of the medium. The solution to Eq. (2.12) is given by

$$\mathbf{E}(z) = \exp(\underline{\mathbf{A}}z) \exp(-\sigma\rho z/2)\mathbf{E}(0) \simeq (\mathbf{1} + \underline{\mathbf{A}}z) \exp(-\sigma\rho z/2)\mathbf{E}(0) \quad (2.14)$$

Here it is assumed that the expansion is valid for all $z \leq l$; that is, the anisotropy is assumed to be small. On the other hand, the sample may be optically thick since a large common absorption for both polarizations is included in the $\sigma\rho$ term. A common phase shift is not relevant in our experiments, but it may of course be included together with $\sigma\rho$.

We now have to i) relate the coefficients in $\underline{\mathbf{A}}$ to the detected signal i_- and ii) relate the coefficients to certain atomic properties. Once this is accomplished, we can use the polarization interferometer to measure properties of the atomic sample placed inside the interferometer. For a probe with linear polarization along the x -axis (horizontal) and propagating along the z -axis, we have $E^\pm(0) = E_0 = \sqrt{I_0/(2\varepsilon_0 c)}$ with I_0 as the incident probe intensity. Propagating $\mathbf{E}(l)$ through the half wave retarder, the polarizing beamsplitter and deducing the resulting photocurrents $i_{1,2} \propto I_{1,2}$ is a trivial calculation with the final lowest order (in \mathbf{A}_{ij}) result

$$\begin{aligned} i_- &= 2\theta i_+ \\ 2\theta &= \{\eta^- - \eta^+ + \eta^{-+} - \eta^{+-}\} \\ i_+ &= i_0 e^{-\alpha} \end{aligned} \quad (2.15)$$

The product $\sigma\rho l$ is now identified as the optical depth α . i_+ is the sum of the two detected photocurrents. The interpretation of Eq. (2.15) is quite simple. The term $\eta^- - \eta^+$ is twice the polarization rotation angle in the presence of optical activity (circular birefringence) with different refractive indices for the two circularly polarized components. The refractive indices have a dispersion-like profile as a function of probe frequency, and we expect the $\eta^- - \eta^+$ term to contribute off resonance. Transforming the calculation above into a basis of linear polarization oriented at $\pm 45^\circ$ to the x -axis shows that $\eta^{-+} - \eta^{+-}$ is the difference in absorption for the $+45^\circ$ and -45° polarizations (linear dichroism). The absorption coefficients have a Lorentzian profile, and consequently the $\eta^{-+} - \eta^{+-}$ contribution will peak for a resonant probe. It is seen that the PI is sensitive only to deviations from an isotropic atomic sample. For a perfect isotropic ensemble of atoms we have $i_- = 0$.

The PI is very similar to a Mach-Zehnder interferometer, except that the two modes in the PI have different polarizations instead of different paths. The circular birefringence in the PI correspond to different phase shifts in the two arms of a Mach-Zehnder interferometer. The linear dichroism, which mixes the two circularly polarized modes in the PI, has no counterpart in a Mach-Zehnder with spatially separated modes.

There are some advantages in the use of a PI instead of the conventional crossed-polarizers setup [33], where the transmission of two nearly crossed polarizers with the sample in between is observed. For small θ the balanced detection in the PI will substantially suppress possible technical (classical) noise in

the probe laser, but still all photons of the probe are detected. This is of great importance when squeezed light is applied to the setup, see chapter 3. In terms of signal-to-noise ratio, the PI performs equally to the crossed-polarizer setup when the noise in the detected differential photocurrent i_- is limited by the intrinsic quantum noise of the probe. In the PI it is easy to switch to the sum of the two photocurrents, which gives access to the probe absorption; the same signal as one would measure with just a single detector behind the atomic sample.

In chapter 6, we will calculate, in detail, the relation between atomic observables and the optical activity and linear dichroism. For now, we just state the results [34]

$$\begin{aligned}\eta^- - \eta^+ &\propto \frac{\Delta/\gamma}{1 + 4\Delta^2/\gamma^2} \langle \hat{F}_z \rangle \\ \eta^{-+} - \eta^{+-} &\propto \frac{1}{1 + 4\Delta^2/\gamma^2} \langle \hat{F}_x \hat{F}_y + \hat{F}_y \hat{F}_x \rangle\end{aligned}\quad (2.16)$$

Δ is the probe detuning and γ is the linewidth of the probed atomic transition. $\langle \hat{F}_z \rangle$ is the mean value of the z -component of the atomic spin in the lower state of the probe transition. $\langle \hat{F}_z \rangle$ is proportional to the atomic orientation. $\langle \hat{F}_x \hat{F}_y + \hat{F}_y \hat{F}_x \rangle$ is proportional to the mean value of the difference in atomic alignment along the axes at $+45^\circ$ and -45° . A nonzero value for $\langle \hat{F}_z \rangle$ can be generated if the atoms are optically pumped by a circularly polarized pumping field. In the same way we have nonzero $\langle \hat{F}_x \hat{F}_y + \hat{F}_y \hat{F}_x \rangle$ if the atoms are optically pumped with a field linearly polarized along $+45^\circ$ or -45° with respect to the x -axis.

Equation (2.16) can also be used for double-optical resonance experiments with a weak resonant pump and a probe field used to probe atoms in the intermediate state. When the pump field is strong enough to induce AC Stark splitting of the intermediate state, the line shapes in (2.16) should be modified to be proportional to χ_r and χ_i from equation (2.4).

2.4 Spectroscopy on a modulated magneto-optical trap

We now apply the results of the previous two sections to do very sensitive spectroscopy on a magneto-optical trap (MOT). The experiments in this section can be seen as the classical counterpart to the atomic quantum noise and spin squeezing experiments (chapter 7 and 8). In the latter, we measure the probe noise induced by quantum fluctuations of the atoms. In the present experiments we use a similar setup to measure the probe noise induced by classical modulation of the atoms. The probe noise induced by classical modulation is in the context of spectroscopy considered to be our spectroscopic signal. The experiments in this section are also the subject of Ref. [35].

Similar to more traditional gas samples, trapped atoms require modulation techniques, e.g. frequency modulation of the probe, for increased sensitivity [22, 36]. This is because of the low frequency amplitude noise of most lasers, which reduce the signal-to-noise ratio (S/N) obtainable at low frequencies or at DC. Frequency modulation (FM) is usually generated with an electro-optical modulator or by current modulation of a diode laser. In both methods the frequency modulation is usually accompanied by residual amplitude modulation [37]. Therefore, in FM detection with a modulated probe, the noise level is set by the residual amplitude modulation and not the fundamental quantum noise (shot noise) of the probe field. Quantum-limited spectroscopy can be achieved by utilizing techniques for suppression of the amplitude modulation [38, 36]. In the present experiment we use the approach of sample modulation instead. Since MOT's are sustained with light, modulation of this trapping light is a natural way of modulating the trapped atoms. In fact, usually the trapping laser is locked to an atomic transition by means of a FM spectroscopy signal from a gas cell, and hence the trapping light is frequency modulated anyway. The idea uses the atomic third order nonlinearity to convert frequency modulation of the pump/trapping beams into amplitude modulation of the probe. Although we, in this experiment, find the classical modulation of atoms useful, we will in the end of this section show how unintentional classical noise in the atomic sample can be a limiting factor in observation of atomic quantum fluctuations.

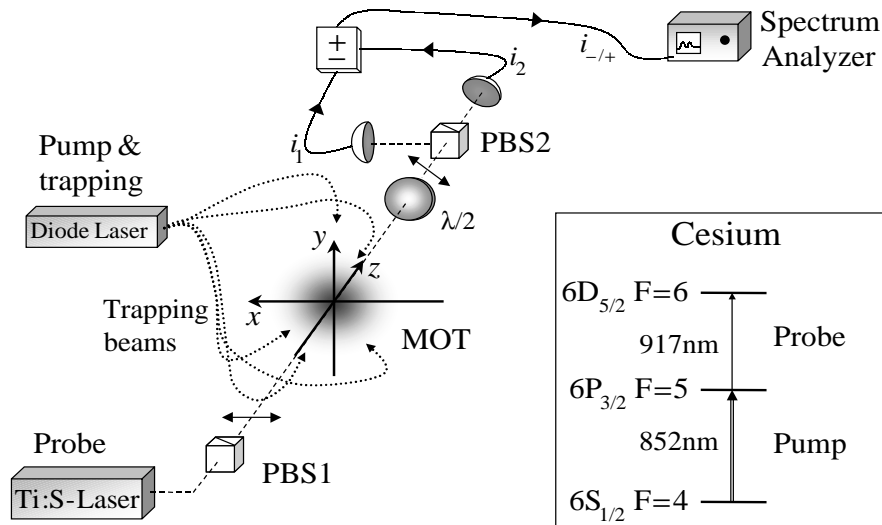


Figure 2.4: The setup used for spectroscopy on a magneto-optical trap sustained by classically modulated trapping fields. We use a polarization interferometer, which gives polarization sensitive spectroscopy in the differential photocurrent i_- and absorption spectroscopy in the sum i_+ . The inset shows the Cs levels used for the double-optical resonance interaction.

2.4.1 Experimental setup

The setup in Fig. 2.4 includes the polarization interferometer described in the previous section. The two high-quality polarizers (PBS1, PBS2) are of the Glan-Thompson type with an extinction ratio better than 10^{-5} . The intensities in the two output arms are detected with two photodetectors, and the emerging photocurrents can be either added or subtracted in a hybrid junction. The photodiodes have a specified quantum efficiency of more than 99%, and the detectors are optimized for detection at 3.0MHz with a peaked response. The bandwidth (FWHM) of the response is 640kHz. The signal after the hybrid junction is fed into a spectrum analyzer (SA, Anritsu MS710A) used at zero span (fixed frequency $\Omega/2\pi = 3.0\text{MHz}$). When the differential current (i_-) is detected, the setup works as a polarization interferometer and is sensitive to polarization rotations and hence to atomic spin orientation and alignment. When the sum current (i_+) is detected, we simply measure the absorption caused by the trapped atoms.

In this experiment we use a diode laser for trapping. The laser drive current is frequency modulated at 3.0MHz to produce FM of the output. The FM is used both for locking of the laser to the Cs transition as well as for modulating the trap. We use five trapping beams with circular polarizations. The two horizontal trapping beams are counter-propagating with a relatively small angle ($\sim 15^\circ$) to the probe direction (z -axis). The atoms are probed on the 917nm $6P_{3/2} \rightarrow 6D_{5/2}$ transition utilizing a Ti:Sapphire laser (Microlase MBR-110). The noise of probe field is set by the intrinsic quantum noise for a coherent state (shot noise) in both phase and amplitude at the detection frequency Ω . The DC-absorption of the probe, when it is sent through the trapped atoms, is measured to be 3% at the two photon resonance during this experiment, (compare to Fig. 2.3).

2.4.2 FM absorption spectroscopy

An experimental trace of FM absorption with the probe scanned across resonance is shown in figure 2.5a (dots). The figure shows the noise or modulation of the photocurrent i_+ measured by the spectrum analyzer as a function of the atom-probe detuning. The frequency scale is obtained from the known hyperfine splitting (see Eq. (2.11)), and we choose zero detuning at the largest double-peaked structure. We can explain the main features in the measured signal by a simple steady-state three-level theory based on Eq. (2.4). For the modulated pump frequency/detuning we have $\Delta(t) = \Delta_0 + M \cos(\Omega t)$, where M is the frequency modulation index. For small absorption and modulation depth, we can write the transmitted probe power as

$$P_t(t) = P_0 e^{-\alpha(\Delta)} \simeq P_0 \left(1 - \frac{2\pi l}{\lambda} \chi_i(\Delta) \right) \simeq P_0 \left(1 - \frac{2\pi l}{\lambda} \left[\chi_i(\Delta_0) + \frac{\partial \chi_i}{\partial \Delta} M \cos(\Omega t) \right] \right) \quad (2.17)$$

χ_i is the imaginary part of the probe susceptibility in double-optical resonance, see Eq. (2.4). The SA gives the rms power or the spectral density of the photocurrent component oscillating at frequency Ω . The photocurrent is given by $i_+(t) = egP_t(t)/h\nu$, where e is the elementary charge, g is the detector gain, and we take the detector quantum efficiency to be unity. Hence, the observed signal is given by

$$(i_+)_{\Omega}^2 = \frac{1}{2} \left(MP_0 \frac{eg2\pi l}{hc} \frac{\partial \chi_i}{\partial \Delta} \right)^2 \quad (2.18)$$

$(i_+)_{\Omega}^2$ as function of probe detuning is plotted in Fig. 2.5b (dotted line). For the plot we use the parameters $s_0 = 17$ and $\Delta/2\pi = 8.9\text{MHz}$. The theoretical curve is scaled so that the improved theory below agrees with the experiment. We see that the qualitative shape of the theoretical curve is in agreement with the experimental data for a single hyperfine component. In both experiment and theory the absorption signal is split into an AC Stark doublet. One component of the doublet is single peaked and the other component consists of a double peak.

The pump modulation method is not inferior to the usual probe modulation with respect to the signal size. In Ref. [22] it is shown that the probe modulation signal is given by: $(i_+)_{\Omega,probe}^2 = \frac{1}{2} (geP_0\lambda M\delta/(hc\Omega))^2$, where δ is the difference in absorption of the upper and lower sidebands of the modulated probe. For our parameters, we find that the ratio $(i_+)_{\Omega}^2 / (i_+)_{\Omega,probe}^2$ is on the order of one. The size of the signals obtained from the two methods are nearly the same, but the physics behind is different. In probe modulation the two RF-sidebands experience different absorption/phase shift when they propagate through the medium. As a result the beat notes between the carrier and the two sidebands no longer cancel and a signal is seen at frequency Ω . In pump modulation the modulated sample gives rise to a modulation of the transmitted intensity.

The current modulation of the trapping laser causes not only frequency modulation but also amplitude modulation. The amplitude modulation is measured to be around 5%. The estimated size of the AM signal is found to be around 1% of the FM signal. In other words, the atoms are much more sensitive to frequency modulation than to amplitude modulation of the saturating pump.

The noise equivalent power of the detection system is around $80\mu\text{W}$; at this optical power level the electronic noise is equal to the intrinsic quantum noise of the coherent state probe (shot noise). The shot noise of the coherent state probe adds a frequency independent noise power of $2egi_0\nu_{RB}$ to the measured rms power of the photocurrent. i_0 is here the average photocurrent and ν_{RB} is the resolution bandwidth of the spectrum analyzer ($\nu_{RB} = 100\text{kHz}$ in the experiment). In the experiment we use a rather weak non-saturating probe of $3\mu\text{W}$, and because of imperfect detectors we have only an insignificant contribution from shot noise to the off-resonant noise level. This, however, is a technical problem that can be overcome by using low-noise narrow band detectors, larger probe diameter, and increased probe power. The signal-to-noise ratio (S/N) in the experiment is about 30dB or 10^3 . For comparison the S/N in a DC-absorption measurement with the same measurement time is below 1. The S/N obtained with pump FM can in principle be increased further by reducing the bandwidth ν_{RB} and increasing the probe power P_0 and modulation index M .

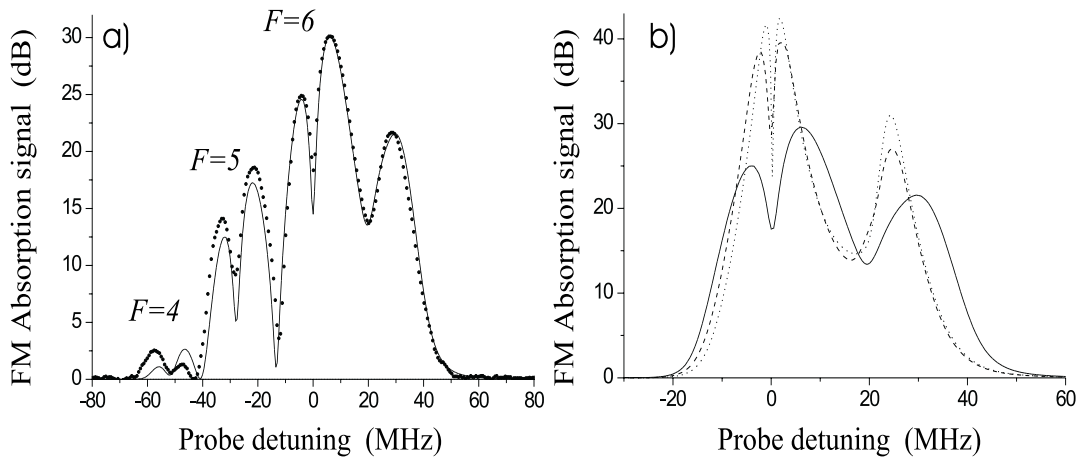


Figure 2.5: a) Dots: experimental FM absorption spectrum; shows three hyperfine components and AC Stark splitting. Solid line: complete theory. b) Dotted line: steady-state theory from Eq. (2.18). Dashed line: theory including finite atomic response time. Solid line: theory including polarization gradients and excess broadening (e.g. magnetic field gradient), but only one hyperfine component. The off-resonant noise level sets the reference for the dB scale. Note the different scales in a) and b).

A qualitative understanding of the shape of the signal can be given by the following argument, which is valid for a not too large s_0 ³. The absorption signal can be separated into a coherent part centered at $\Delta + \Delta' \simeq 0$ and an incoherent part centered at $\Delta' \simeq 0$ - these are the two resonance conditions obtained from Eq. (2.4). The coherent resonance condition depends in the same way on the pump and probe frequency, and we expect this part to contribute with the derivative of a Lorentzian as in ordinary probe FM spectroscopy. Hence the coherent signal from the SA has a double-peaked structure (squared dispersion profile). The resonance condition for the incoherent term does not depend on Δ , but this term is still modulated through the Δ dependence of the intermediate state population. This is more like AM spectroscopy, which does not alter the Lorentzian line shape, and we get an incoherent single-peak structure.

In the experiment the 3.0MHz modulation frequency is comparable to the natural linewidth of 5.2MHz for the $6P_{3/2}$ state. Such a high modulation frequency allows to reach shot-noise limited sensitivity, but makes the validity of Eq. (2.18) questionable. The atoms can no longer follow the modulation adiabatically when they are modulated at frequencies comparable to γ owing to the finite atomic response time. This effect can also be seen in a frequency-domain picture. The FM of the pump introduces sidebands on the pump displaced at $\pm\Omega$ with respect to the pump carrier frequency. If the modulation is faster than γ , the sidebands are shifted more than one linewidth away from resonance (the pump carrier is always quasi-resonant). These non-resonant sidebands do not have a large effect on the atoms, and the effect goes down when Ω is increased further.

To investigate the effect of fast pump modulation, we solve numerically the semi-classical Bloch equations for a three-level atom interacting with two classical fields. The differential equation for the time evolution of the density matrix for the three-level atom can be found in Ref. [28]. The differential equation is integrated numerically with a fourth order Runge-Kutta algorithm with the phase of the classical pump-field modulated at 3MHz with a phase modulation index of 0.5. The calculation gives the time dependent probe susceptibility $\chi(t) = \chi_r(t) + i\chi_i(t) \propto \rho_{32}(t)$ with ρ_{32} as the density matrix element for the optical coherence on the probe transition. The modulation in the measured photocurrent is proportional to the imaginary part $\chi_i(t)$ for small absorption; $i_+(t) = geP_0(h\nu)^{-1}(1 - 2\pi l\lambda^{-1}\chi_i(t))$.

³We are not really in the limit of small s_0 , but the qualitative explanation still describes the line shape well

The spectral density $(i_+)_{\Omega}^2$ measured by the spectrum analyzer is then proportional to the absolute square of the Fourier transform of $\chi_i(t)$ at frequency Ω

$$(i_+)_{\Omega}^2 = 2 \left| \int_{-\infty}^{\infty} i_+(t) e^{-i\Omega t} dt \right|^2 \propto \left| \int_{-\infty}^{\infty} \chi_i(t) e^{-i\Omega t} dt \right|^2 \quad (2.19)$$

We calculate the Fourier transform from the numerical solution to $\chi_i(t)$, and the resulting signal is plotted in Fig. 2.5b (dashed line). Compared to the curve from Eq. (2.18) we see that the fast modulation increases the linewidth by about 50% and reduces the S/N by 3dB. We checked that our numerical calculations give the same signal as Eq. (2.18) in the limit $\Omega \ll \gamma$.

Finally, we have to include the effects of polarization gradients, excess broadening from e.g. the magnetic field gradient and the small hyperfine splitting of the $6D_{5/2}$ state into the calculations. When these effects are modelled in the numerical calculation of $\chi(t)$ in the same way as in section 2.2, we get the theoretical curve shown as a solid line in Fig. 2.5a (and in Fig. 2.5b for just the $F = 6$ hyperfine component). For this theoretical curve we used the parameters $s_0 = 17$, $\Delta/2\pi = 8.9\text{MHz}$, $M_{phase} = 0.5$ and $\delta\nu_B = 5.2\text{MHz}$. The parameters for the theoretical curve are chosen for the best agreement between theory and experiment. The pump detuning measured in the experiment is $12 \pm 1\text{MHz}$ and, just as in section 2.2, the theory fits with a pump detuning a little smaller than the experimental value. The broadening $\delta\nu_B$ is somewhat larger than expected for the small trap diameter (around 1.5mm) in this experiment. Part of that can be the diode trapping laser linewidth, which is larger than the linewidth of the Ti:Sapphire laser used in section 2.2. The saturation parameter s_0 is close to the experimental value of $s_0 = 19$ for a total trapping power of 15mW and 6mm beam diameter. The modulation index is measured by injecting a part of the trapping beam into an optical resonator and comparing the transmission modes for the carrier and the sidebands. The measurement gives $M_{phase} = 0.5$ although with a large uncertainty ($\sim 50\%$) because of extrapolation down to the modulation frequency and depth used in the experiment. All the theoretical curves are scaled so that the final result fits the experimental data.

The discrepancy between theory and experiment at the $F = 5$ hyperfine component can be due to partly polarized atoms caused by an anisotropic trapping field. The ratio between the line strengths as given by Eq. (2.10) is only valid for unpolarized atoms. The shape for the smallest hyperfine component $F = 4$ show a clear disagreement with the theory. The reason for that is unknown, but perhaps it is related to the fact that the $6P_{3/2}F = 5 \rightarrow 6D_{5/2}F = 4$ transition is modelled as a closed transition in the theory.

2.4.3 FM polarization rotation spectroscopy

We now turn to the polarization rotation signal obtained from the differential photocurrent i_- . i_- gives information about the deviations from an isotropic distribution of atoms as explained in section 2.3. The measured rms power $(i_-)_{\Omega}^2$ as a function of probe detuning is, for balanced trap intensities, plotted in Fig. 2.6a. These data are taken under the exact same conditions as the FM absorption measurements in Fig. 2.5a. The intensities in the horizontal trapping beams, which are at a small angle to the probe beam, are adjusted to maximize the FM absorption and to minimize the FM polarization rotation. In this way the sample is made as isotropic as possible, and consequently the polarization rotation signal in Fig. 2.6a is rather small.

We can make the sample anisotropic by using unequal intensities in the two horizontal trapping beams. The trapping field then contains mainly one circular polarization, and the atoms in the $6P_{3/2}$ state will acquire a nonzero orientation ($\langle F'_z \rangle \neq 0$). According to Eq. (2.16) and the text below this equation, we expect the polarization rotation spectrum to be described by the real part of the probe susceptibility χ_r and to be proportional to $\langle F'_z \rangle$. In Fig. 2.6b (solid line) we show the FM polarization rotation spectrum measured for unbalanced trapping intensities. The corresponding FM absorption spectrum has a signal 7dB smaller than the FM absorption spectrum measured with balanced intensities. This shows that the larger signal in Fig. 2.6b, as compared to Fig. 2.6a, is *not* caused by improved trapping conditions

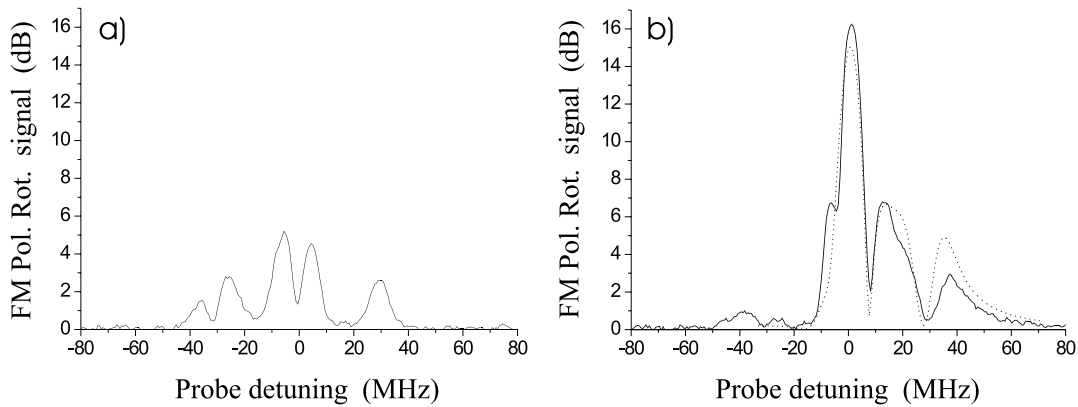


Figure 2.6: a) Experimental FM polarization rotation signal for balanced trap intensities. b) Solid line: experimental FM polarization rotation signal for unbalanced intensities (induced orientation). Dotted line: theoretical calculation.

(more trapped atoms). The unbalanced trap does not work as well as the balanced trap, but it is clearly anisotropic.

We obtain a theoretical FM polarization rotation spectrum by using the same calculation as for the FM absorption spectrum in Fig. 2.5a, except we use $\chi_r(t) \propto \text{Re}(\rho_{32}(t))$ instead of $\chi_i(t)$ in the Fourier transform for $(i_-)_{\Omega}^2$. That is

$$(i_-)_{\Omega}^2 = 2 \left| \int_{-\infty}^{\infty} i_-(t) e^{-i\Omega t} dt \right|^2 \propto \left| \int_{-\infty}^{\infty} \chi_r(t) e^{-i\Omega t} dt \right|^2 \quad (2.20)$$

All the parameters of the calculation are identical to the FM absorption calculation except that we scale the signal to fit the experimental polarization rotation data, and we only include one hyperfine transition ($6P_{3/2}F = 5 \rightarrow 6D_{5/2}F = 6$). It can be shown that the polarization rotation signals from the other two hyperfine components are insignificant. The argument is simple, but it depends on results from the subsequent chapters, and it is therefore given in Appendix A. The calculated spectrum is shown as the dotted line in Fig. 2.6b, and we see a fine qualitative agreement in the shape of the theoretical and experimental spectra. The detuning scale in Fig. 2.6b is identical to the scale in Fig. 2.5a, and we see that the FM polarization rotation signal at positive frequencies (around 50MHz) goes to zero more slowly than the FM absorption signal. This is a signature of the fact that the polarization rotation signal, caused by circular birefringence, is related to a dispersion profile.

The small FM polarization rotation signal in Fig. 2.6a looks a little like the FM absorption spectrum in Fig. 2.5a. This can either be caused by an imperfectly balanced polarization interferometer or because of alignment anisotropy, which gives a spectrum like FM absorption according to the comments below Eq. (2.16).

The agreement between theory and experiment for FM polarization rotation is not quite as good as for FM absorption spectroscopy. The polarization rotation is caused by an anisotropic atomic sample with unequal populations in the different Zeeman levels. Since each Zeeman level is independently affected by magnetic and electric fields, we expect that the three-level calculation is less successful for the FM polarization rotation spectrum.

2.4.4 Diode laser phase noise

Diode lasers are today inexpensive and compact devices with enough power for many atomic physics experiments. Although the tunability is limited to a few nm, it is possible to purchase lasers for most

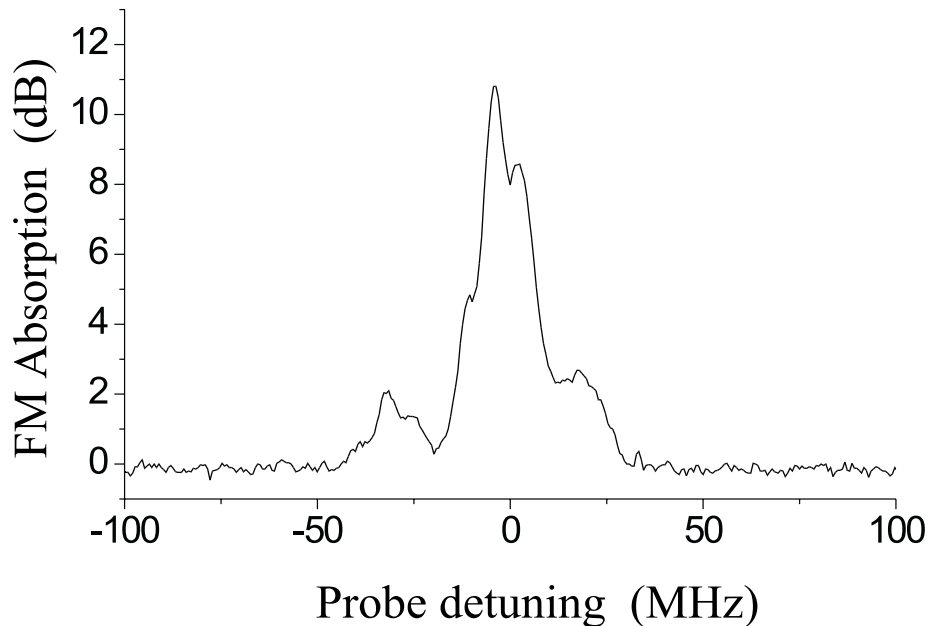


Figure 2.7: FM absorption spectroscopy using the intrinsic diode laser phase noise and no external modulation.

near infrared wavelengths including the Cs D2 line at 852nm. The intensity of the diode laser output is usually very stable, and it is even possible to reduce the fluctuations below the standard quantum limit (shot noise) [39]. On the other hand, the phase fluctuations are usually far above the standard quantum limit and extend into the GHz regime [18, 19]. The phase fluctuations are caused by the spontaneous emissions into the lasing mode, and the bandwidth of the excess fluctuations is set by the laser cavity linewidth. The very short cavity and large output coupler for the diode laser result in the very large bandwidth of phase fluctuations, even when the diode laser is externally stabilized by the grating feedback.

The diode laser phase noise can be utilized for FM spectroscopy without applying any external phase modulation as demonstrated in Ref. [40, 41]. In our setup we also observe a FM absorption signal when the SA detection frequency is different from the modulation frequency of the diode laser drive current. In Fig. 2.7 we show a FM absorption spectrum using the intrinsic phase noise of the diode laser and no external modulation.

The intrinsic phase noise is an essential problem in measurements of the excited state atomic quantum noise when the readout is performed with a probe field (see sections 7 and 8). If a diode laser is used for the pump field, the spectroscopic signal from the phase noise will surpass the atomic quantum noise. This problem is recognized in Ref. [20], and the solution is to use a Ti:Sapphire laser for the pump field. The noise of the Ti:Sapphire laser is found to be at the standard quantum limit in both amplitude and phase at frequencies above 2MHz and for the optical power of a few mW. The phase noise is checked by sending the field through an optical resonator, which converts phase noise into amplitude noise. The amplitude noise is measured directly with a photodetector and a spectrum analyzer.

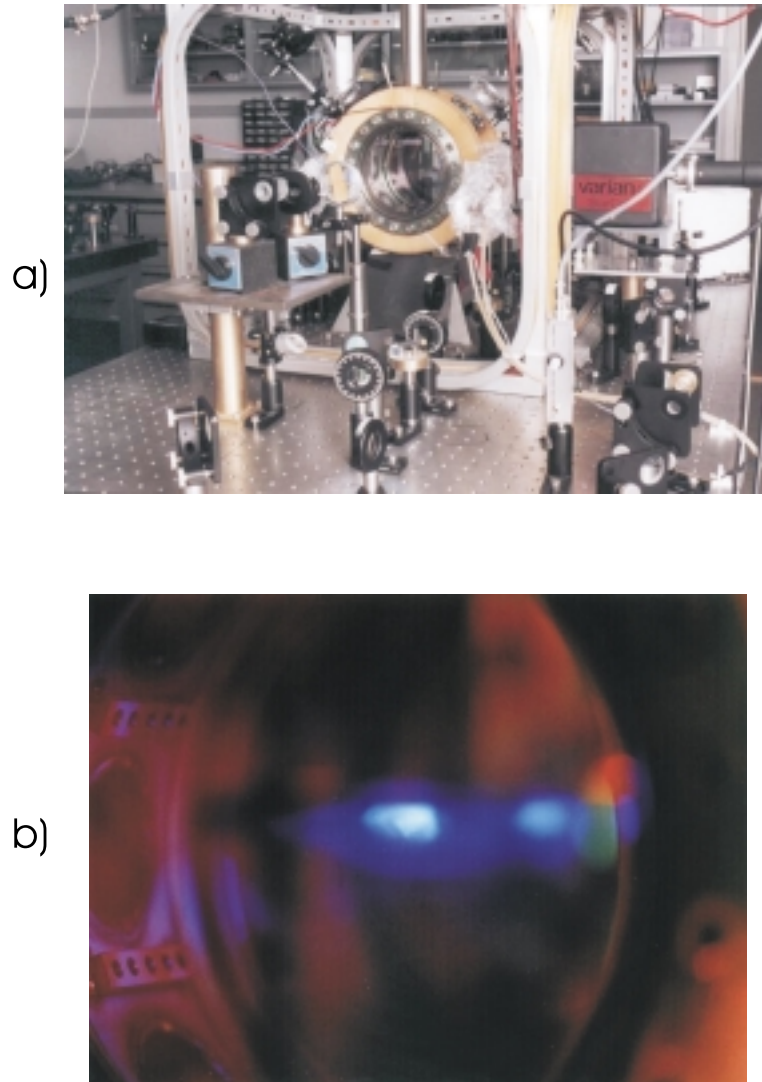


Figure 2.8: a) The MOT setup with the vacuum chamber in the middle and surrounded by the optics for a six-beam configuration. The "yellow rings" on the chamber are the anti-Helmholtz coils. The larger rectangular coils are used to produce a bias field. b) The blue fluorescence of the trap in double-optical resonance. Atoms in $6D_{5/2}F = 6$ decay with a small probability to $7P_{3/2}$ and subsequently to the ground state on a 456nm transition (see also Fig. 2.2, page 8). The picture is shown with the true colors. The blue spot to the right is a reflection from a viewport.

Chapter 3

Squeezed states of light

The squeezed states of light are one of the most important ingredients in the experiments presented in this thesis. Squeezing can be used for improved sensitivity in atomic spectroscopy, as demonstrated later in this chapter, but we also use the squeezed light as a source of quantum correlations. In the spin squeezing experiment, the quantum correlated photons constituting the squeezed light are mapped onto a cold ensemble of atoms and thereby producing quantum correlated atoms.

The Heisenberg uncertainty relation for noncommuting observables can be used to define a *standard quantum limit* (SQL) for quantum fluctuations. For the quantized electromagnetic field we introduce the two quadrature phase amplitudes \hat{X} and \hat{Y} as the real and imaginary part of the field annihilation operator \hat{a} for a single field mode. \hat{X} and \hat{Y} are noncommuting with $[\hat{X}, \hat{Y}] = i/2$, and they therefore obey the uncertainty relation

$$(\Delta\hat{X})^2(\Delta\hat{Y})^2 \geq \frac{1}{16} \quad (3.1)$$

$(\Delta\hat{X})^2$ is the usual quantum mechanical variance of \hat{X} . For the coherent state of light, which is a good approximation for the output of many lasers far above threshold, the two quadratures have identical minimum fluctuations. The coherent state fluctuations can also be explained in a photon picture, where the photon distribution is described as a stochastic Poisson process. The level of quantum noise or fluctuations for the coherent state defines the standard quantum limit or the shot noise level. The coherent states, which include the vacuum state, are the most classical states of light [42].

It is not prohibited by quantum mechanics to redistribute the fluctuations in the two quadratures. The squeezed states are defined as having the fluctuations in one quadrature below the standard quantum limit. The squeezed states are so-called nonclassical states as they cannot be expanded on the set of coherent states with a positive-definite weighting function. In other words, we cannot consider the squeezed states to be a classical distribution over the (almost) classical coherent states. The noise reduction in one quadrature is a consequence of the quantum correlations present in the squeezed field.

Several methods for generation of squeezed light have been explored since the first demonstration in 1985, which utilized four-wave mixing in atomic sodium [2]. The most efficient process today is the optical parametric oscillator (OPO) operating below threshold. The best measured squeezing is obtained in a monolithic OPO made of MgO:LiNbO₃ with 7.0dB noise reduction in one quadrature at the 1064nm Nd:YAG laser wavelength [43]. However, the phase of the squeezing is not actively stabilized in this experiment, which means that the quadrature being squeezed changes with time. 6.2dB of squeezing with a stabilized phase is measured in Ref. [44]. This experiment is also based on MgO:LiNbO₃ at 1064nm. 6.0dB of noise reduction with stabilized phase is reported in Ref. [45] with KNbO₃ as the nonlinear material and at 852nm. When the KNbO₃ based squeezing source is driven by a Ti:Sapphire laser, the wavelength of squeezing can be tuned by tuning of the laser frequency. Noncritical temperature phase matching and hence squeezing can be obtained in the 850nm-920nm wavelength range by adjusting

the a-cut KNbO_3 temperature between 0°C and 130°C . The tunability is an important requirement when the squeezed light is used for atomic physics, and this is not fulfilled by the $\text{MgO}:\text{LiNbO}_3$ based squeezing source driven by a Nd:YAG laser.

A completely different source of squeezed light is the diode laser with amplitude noise below the shot noise level. This can be achieved by e.g. suppression of pump noise using a stable current source [39] or by injection locking to a stable master laser [46]. In the latter experiment they observe 4.5dB noise reduction. However, the squeezing of diode lasers always takes place in the amplitude of the field, and the observed squeezing to date for collimated laser output is below the OPO performance.

The main goal in a large group of atomic physics experiments utilizing a squeezed state of light has been to demonstrate improved sensitivity in spectroscopy owing to the reduced quantum noise of the probe light [47, 45, 48, 49, 50]. Only a few atomic physics experiments use the properties of the squeezed light directly in the atom-light interaction. These experiments include the two-photon excitation of Cs atoms using squeezed vacuum [51], detection of quantum correlations at ultrahigh frequencies using atoms as nonlinear mixers [52], squeezed excitation in cavity QED [53], and our experiment on generation of spin squeezed atoms by squeezed light excitation (Ref. [6] and chapter 8 in this thesis). A large number of theoretical publications on atom-squeezed light interaction exist with the most important listed in Ref. [53]. However, these calculations often require the squeezed vacuum to occupy a large solid angle in order to minimize atomic interaction with other unsqueezed vacuum modes. Efficient interaction with a single squeezed mode can also be achieved with the atom sitting in a cavity pumped by squeezed light. This was attempted in Ref. [53] but only with a limited success.

Other fascinating experiments with continuous squeezed light includes quantum teleportation [54], QND measurements [55], and quantum state reconstruction [56, 57].

The electromagnetic field is basically described as a harmonic oscillator (one oscillator for each field mode). The squeezed states are based on the properties of the harmonic oscillator, and therefore other quantized harmonic oscillators can be squeezed as well. The motion of an ion in a harmonic potential can be squeezed as demonstrated in Ref. [58]. The two conjugate variables are the ion position and momentum. Squeezing of the atomic motion in a harmonic dipole trap is demonstrated in Ref. [59]. Note that this squeezed state of many atoms does not involve any multi-particle entanglement, and it is not the same as the spin squeezed atomic states discussed later in this thesis. The squeezed state in Ref. [59] is a pure single atom effect.

In this chapter, we continue with a section about the basic properties of the squeezed states followed by a brief review of the OPO as a squeezing source and a section on polarization squeezing. In the last two sections we describe our experimental squeezing setup and present our experimental results on squeezed probe polarization spectroscopy.

3.1 Basic properties of the squeezed states

An introduction to the squeezed states can be found in many textbooks (e.g. Ref. [42, 60, 61, 62]). Squeezing is a fundamental concept in this thesis, and a short introduction here is instructive and will furthermore introduce some of the notation used later on. The starting point is the general expression for the quantized electric field specified by the polarization \mathbf{e} and spatial mode u

$$\hat{\mathbf{E}}(\mathbf{r}) = i \int_{-\infty}^{\infty} \zeta_{\omega} [\mathbf{e}u(x, y) \hat{a}(k) e^{ikz} - \mathbf{e}^* u^*(x, y) \hat{a}^\dagger(k) e^{-ikz}] dk \quad (3.2)$$

$k = \omega/c$ and $\zeta = \sqrt{\hbar\omega/4\pi\epsilon_0}$. The continuous annihilation and creation operators fulfil $[\hat{a}(k), \hat{a}^\dagger(k')] = \delta(k - k')$. The integral can often be truncated at finite limits given by $k_0 \pm \pi/L$. L should be chosen so that the field amplitude remains approximately constant on length scales shorter than L . We will use this truncation in the next chapter, where the quantum field is absorbed in a gas of atoms.

The polarization is usually described in a basis of either linear or circular polarizations, and \mathbf{e} is the corresponding unit vector. $\hat{\mathbf{E}}(\mathbf{r})$ is time dependent in the Heisenberg picture through the Heisenberg

equation for the annihilation operators. The spatial mode is most often the lowest order Gaussian mode. If the beam diameter $2w$ is (almost) constant over the dimensions of interest we have

$$u(x, y) = \sqrt{\frac{2}{\pi w^2}} e^{ik(x^2+y^2)/2R} e^{-(x^2+y^2)/w^2} \quad (3.3)$$

$$\int \int dx dy |u(x, y)|^2 = 1 \quad \int \int dx dy |u(x, y)|^4 = \frac{1}{\pi w^2}$$

R is the radius of curvature of the Gaussian mode.

In some situations it is convenient to work with discrete annihilation and creation operators defined as

$$\hat{a}_{k_n} = \sqrt{L/2\pi} \int_{k_n - \frac{\pi}{L}}^{k_n + \frac{\pi}{L}} \hat{a}(k) dk \quad (3.4)$$

$$[\hat{a}_{k_n}, \hat{a}_{k_n}^\dagger] = 1 \quad , \quad k_n = n \frac{2\pi}{L}, \quad n: \text{integer}$$

The discrete operators are used in e.g. optical resonators where L is chosen as the resonator length, and $k_n = n2\pi/L$ ensures the periodic boundary conditions required for the resonating field. The discrete operators can also be used for free propagating fields, where we find the usual single mode description in the limit where L goes to infinity. The physical problem can often be described by the use of only one discrete mode, and for the rest of this chapter we take \hat{a} as the discrete annihilation operator for a single mode field. The field is normalized so that $n = \langle \hat{a}^\dagger \hat{a} \rangle$ is the overall photon number in the mode. The photon flux¹ for the free propagating field is given by $\Phi = \langle \hat{a}^\dagger \hat{a} \rangle c/L$.

It is convenient to introduce the Hermitian quadrature phase operators \hat{X}, \hat{Y} , which can be measured in the experiment, instead of the non-Hermitian operators \hat{a} and \hat{a}^\dagger . \hat{X}, \hat{Y} , and their commutator are given by

$$\hat{X} = \frac{\hat{a} + \hat{a}^\dagger}{2}, \quad \hat{Y} = \frac{\hat{a} - \hat{a}^\dagger}{2i}, \quad [\hat{X}, \hat{Y}] = i/2 \quad (3.5)$$

We can rewrite a single mode of $\hat{\mathbf{E}}$ in terms of the two quadrature phase operators, where we for simplicity assume $R \gg w$ and linear polarization ($\mathbf{e} = \mathbf{e}^*$)

$$\hat{\mathbf{E}}(\mathbf{r}, t) = 2\zeta u(x, y) \mathbf{e} \left[\hat{X}_0 \sin(\omega t - kz) - \hat{Y}_0 \cos(\omega t - kz) \right] \quad (3.6)$$

Here we write the free field time evolution explicitly, and we use the notation $\hat{X}_0 = \hat{X}(t=0)$, $\hat{Y}_0 = \hat{Y}(t=0)$. The equal uncertainties in the two quadratures for a coherent state can be illustrated in a phasor diagram as shown in Fig. 3.1a. The mean value of the complex field amplitude is represented by an arrow, and the fluctuations are shown as a "noise circle" on top of the arrow. The orientation of the vector or phasor in the diagram is set by the phase θ of the field. The phasor can be rotated by choosing e.g. a different time reference. The fluctuations in the X and Y quadratures are for all coherent states given by the minimum equal uncertainties $(\Delta \hat{X})^2 = (\Delta \hat{Y})^2 = 1/4$.

For a squeezed field the fluctuations in one quadrature are reduced below the standard quantum limit of $1/4$, whereas the conjugate quadrature is antisqueezed so that the Heisenberg uncertainty relation is still fulfilled. The squeezed state is represented in the phasor diagram by a noise ellipse as shown for two examples in Fig. 3.1b,c. When the phase between the squeezing ellipse and the mean field is 0° or 180° , we have reduced phase fluctuations as shown in Fig. 3.1b. With a phase difference of $\pm 90^\circ$, the fluctuations in the absolute amplitude are reduced below the standard quantum limit; Fig. 3.1c. The

¹"Photon flux" does not have an unambiguous meaning in the literature. We use the definition $\Phi = P/h\nu$ where P is the optical power in the mode and $h\nu$ is the photon energy.

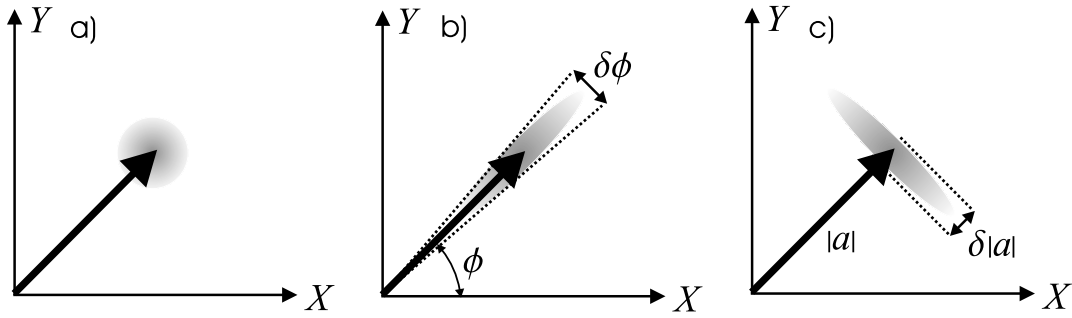


Figure 3.1: a) Phasor diagram representing the coherent state. b) Squeezed state with reduced phase fluctuations ($\delta\phi$). c) Squeezed state with reduced amplitude fluctuations ($\delta|a|$).

squeezing in Fig. 3.1b,c is found in the new quadratures X' and Y' corresponding to a rotation of the phasor diagram by about 45° .

It is also possible to have a squeezed state with zero mean amplitude. This state is termed *squeezed vacuum*, and it can be given a nonzero amplitude by mixing it with a coherent field on e.g. a highly asymmetric beamsplitter. The orientation of the squeezing ellipse relative to the coherent mean field is then set by the relative phase of the two modes combined on the beamsplitter.

Mathematically, the squeezed vacuum state is generated from the ordinary vacuum by applying the unitary squeeze operator [42]

$$\hat{S}(z) = \exp\left(\frac{1}{2}[z^*\hat{a}^2 - z\hat{a}^{\dagger 2}]\right), \quad z = re^{i\theta} \quad (3.7)$$

The parameter θ sets the orientation of the squeezing ellipse for the squeezed vacuum state $\hat{S}(z)|0\rangle$ and r sets the degree of squeezing or noise reduction. The variances of the quadrature phase operators in the state $\hat{S}(z)|0\rangle$ are

$$\begin{aligned} (\Delta\hat{X})^2 &= \frac{1}{4}(e^{2r}\cos^2\theta + e^{-2r}\sin^2\theta) \\ (\Delta\hat{Y})^2 &= \frac{1}{4}(e^{2r}\sin^2\theta + e^{-2r}\cos^2\theta) \end{aligned} \quad (3.8)$$

We see that for e.g. $\theta = 0$ the Y -quadrature is squeezed whereas the X -quadrature is antisqueezed. The exponent in the squeeze operator looks very similar to the Hamiltonian for a $\chi^{(2)}$ nonlinear process. In the following section we will see that squeezing can, in fact, be generated by the $\chi^{(2)}$ parametric process.

3.2 Squeezing from the optical parametric oscillator

We move on with a brief introduction to the most successful source of squeezed light, the optical parametric oscillator (OPO). A more thorough treatment of squeezing in the OPO can be found in Ref. [63]. The OPO consists of an optical resonator with a nonlinear crystal as sketched in Fig. 3.2. The OPO is pumped with a nonresonant strong coherent (classical) pump field at frequency 2ω . The pump field is coupled through the nonlinear medium to modes at frequency ω_{\pm} with $\omega_+ + \omega_- = 2\omega$. Here we only consider the degenerate mode ($\omega_{\pm} = \omega$), which is assumed to be resonant in the cavity. The Hamiltonian for the parametric process is given by

$$\hat{H} = \hbar\omega\hat{a}^\dagger\hat{a} - i\hbar g(\hat{a}^2\hat{b}^\dagger - \hat{a}^{\dagger 2}\hat{b}) \quad (3.9)$$

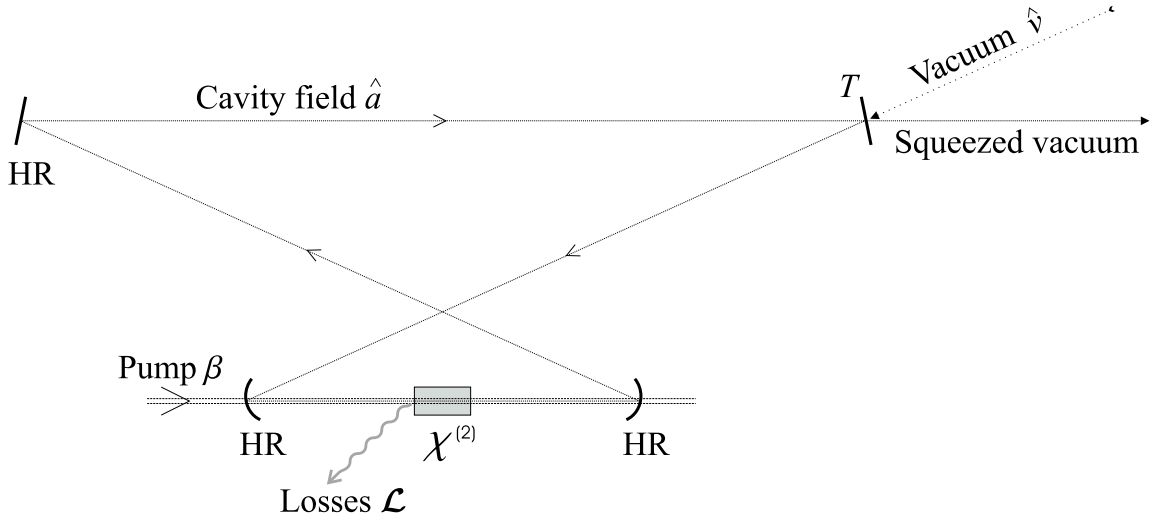


Figure 3.2: A sketch of the resonator with the $\chi^{(2)}$ nonlinear crystal which constitutes the OPO. HR: High reflector for cavity field \hat{a} at frequency ω . T : Output coupler transmission. \mathcal{L} : cavity losses except for T .

g is a real nonlinear coupling strength. \hat{a} is the discrete annihilation operator for the resonant cavity mode at frequency ω . \hat{b} is the annihilation operator for the pump field, which we, for the classical pump, can substitute by its mean value β . The chosen phase of the nonlinear term in H is found to be convenient below, but it can in principle be changed by changing the complex phase on β . The nonlinear part of H describes parametric down conversion, where one pump photon is annihilated and two photons at frequency ω are generated, as well as the opposite process of second harmonic generation. The first process will dominate because of the strong pump and the weak field at frequency ω .

The time evolution of \hat{a} is set by the Heisenberg equation together with the dissipation due to cavity losses and mirror transmissions. For simplicity we consider here the ideal cavity without losses, except for the output coupler with the transmission T . The equation for \hat{a} is

$$\begin{aligned} \frac{\partial}{\partial t} \hat{a} &= \frac{1}{i\hbar} [\hat{a}, \hat{H}] + \text{dissipation} \\ \Rightarrow \dot{\tilde{a}} &= 2g\beta\tilde{a}^\dagger - \Gamma\tilde{a} + \sqrt{2\Gamma c/l}\tilde{v} \end{aligned} \quad (3.10)$$

We have introduced the slowly varying operators given by $\tilde{a} = \hat{a}e^{i\omega t}$. The first term is the nonlinear coupling of the pump field and the cavity field. The second term is the decay of the cavity field through the output coupler, and the last term is the vacuum field coupled into the cavity through the output coupler. We assume that the cavity output coupler transmission is small so that we can write the amplitude reflection and transmission coefficients as $r = 1 - \Gamma l/c$ and $t = \sqrt{T} = \sqrt{2\Gamma l/c}$ with $r^2 + t^2 \simeq 1$. l is the cavity length and 2Γ is the rate at which photons leave the resonator through the coupler. The validity of Eq. (3.10) is discussed further in Ref. [64].

We can rewrite Eq. (3.10) and its Hermitian conjugate in terms of the slowly varying quadrature phase operators

$$\begin{aligned} \dot{\tilde{X}} &= -\Gamma\tilde{X} + 2g\beta\tilde{X} + \sqrt{2\Gamma c/l}\tilde{X}_v \\ \dot{\tilde{Y}} &= -\Gamma\tilde{Y} - 2g\beta\tilde{Y} + \sqrt{2\Gamma c/l}\tilde{Y}_v \end{aligned} \quad (3.11)$$

For simplicity we assume the pump field amplitude, β , to be real and positive and \tilde{X}_v, \tilde{Y}_v are the quadrature phase operators for the vacuum mode \hat{v} . A nonzero steady-state solution for the mean value

$\langle \tilde{X} \rangle$ is found for $\beta = \Gamma/2g$. This is the condition for parametric oscillation. β^2 is proportional to the pump power, and we can define the pump parameter as $\sigma = \sqrt{P/P_{th}} = 2g\beta/\Gamma$, where P_{th} is the threshold power.

We continue with the fluctuations for the sub-threshold OPO; i.e. for $\sigma < 1$. If we apply a Fourier transform to both sides of Eq. (3.11), we get

$$\begin{aligned}\tilde{X}(\Omega) &= \frac{\sqrt{2c/l\Gamma}\tilde{X}_v(\Omega)}{1 - \sigma + i\Omega/\Gamma} \\ \tilde{Y}(\Omega) &= \frac{\sqrt{2c/l\Gamma}\tilde{Y}_v(\Omega)}{1 + \sigma + i\Omega/\Gamma}\end{aligned}\quad (3.12)$$

We define our Fourier transform as $\tilde{X}(\Omega) = \int \tilde{X}(t) e^{-i\Omega t} dt$, and we use the same notation for an operator and its Fourier transform except for the argument. Equation (3.12) relates the intracavity quadrature phase operators to the vacuum coupled into the OPO through the output coupler. The output of the OPO, which is what we are really interested in, is obtained from the beamsplitter relation used on the output coupler; $\tilde{X}^{out}(\Omega) = t\tilde{X}(\Omega) - \tilde{X}_v(\Omega)$ and similar for \tilde{Y}^{out} . The first term is the intracavity field transmitted through the coupler, and the second term is the vacuum field reflected off the coupler assuming high reflectivity. The minus sign is required for a unitary beamsplitter. The quadrature phase operators \tilde{X}^{out} and \tilde{Y}^{out} are related to the number of photons in the mode, which depends on the quantization length L chosen for the free propagating field. It is convenient to introduce new operators that are independent of the quantization length and related to the photon flux. These operators are defined as $\tilde{\mathcal{X}}^{out}(\Omega) = \sqrt{c/L}\tilde{X}^{out}(\Omega)$ and $\tilde{\mathcal{Y}}^{out}(\Omega) = \sqrt{c/L}\tilde{Y}^{out}(\Omega)$.

The spectral density of fluctuations (or noise power) for the output quadrature phase operators is now given by²

$$\begin{aligned}(\tilde{\mathcal{X}}^{out})_{\Omega}^2 &= \frac{1}{2\pi} \int_{-\infty}^{\infty} \langle \tilde{\mathcal{X}}^{out}(\Omega') \tilde{\mathcal{X}}^{out}(\Omega) \rangle d\Omega' = \frac{R_+(\Omega)}{4} \\ (\tilde{\mathcal{Y}}^{out})_{\Omega}^2 &= \frac{R_-(\Omega)}{4} \\ R_{\pm}(\Omega) &= \left(1 \pm \xi \frac{4\sigma}{\Omega^2/\Gamma^2 + (\sigma \mp 1)^2} \right)\end{aligned}\quad (3.13)$$

We have used that the vacuum fluctuations in the \hat{v} -field are delta-correlated with $(\tilde{\mathcal{X}}_v)_{\Omega}^2 = 1/4$. This follows from the commutation relation for the free fields in the Heisenberg picture

$$\begin{aligned}[\tilde{a}(t), \tilde{a}^{\dagger}(t')] &\simeq \frac{L}{c} \delta(t - t') \\ [\tilde{a}(\Omega), \tilde{a}^{\dagger}(\Omega')] &\simeq \frac{L}{c} 2\pi \delta(\Omega + \Omega')\end{aligned}\quad (3.14)$$

These commutation relations follow from Eq. (3.4) and the Heisenberg equation for $\hat{a} = \tilde{a}e^{-i\omega t}$, and they become exact in the limit of small L .

ξ in Eq. (3.13) is a parameter used later on to include imperfections like losses in the squeezing path, cavity losses etc. For the ideal OPO considered so far we have $\xi = 1$. We see from Eq. (3.13) that the fluctuations in the $\tilde{\mathcal{Y}}$ quadrature at frequency Ω are reduced below the vacuum fluctuations (or shot noise) and hence the $\tilde{\mathcal{Y}}$ quadrature is squeezed. On the other hand, the $\tilde{\mathcal{X}}$ fluctuations are above the vacuum noise level and this quadrature is antisqueezed. The functions $R_{\pm}(\Omega)$ give the noise level of the

²The spectral density of i , which is measured by the spectrum analyzer, was introduced in Eq. (2.19) as $|i(\Omega)|^2$. However, this quantity is divergent if i is a stationary random process. If the process is truncated by setting $i(t) = 0$ for $|t| > T$, then we can define a spectral density by $(i)_{\Omega}^2 = \lim_{T \rightarrow \infty} \frac{\langle |i(\Omega)|^2 \rangle}{2T}$. This definition is equivalent to Eq. (3.13) with $\tilde{\mathcal{X}}^{out}$ instead of i [42].

squeezed and antisqueezed quadrature relative to the shot noise level. The mean values $\langle \tilde{\mathcal{X}}^{out} \rangle$, $\langle \tilde{\mathcal{Y}}^{out} \rangle$ are zero, and the OPO output is a squeezed vacuum state. The effect can be compared to the degenerate optical parametric amplifier, where a classical field is injected into the resonator through the output coupler. The output of the cavity is then either amplified or reduced in power, depending on the relative phase between the pump field and the injected field. With the subthreshold OPO we inject ordinary vacuum, and the OPO amplifies or reduces the vacuum fluctuations in a given quadrature, depending on the pump phase.

The squeezed vacuum from the OPO is not squeezing in a single mode. Instead we see from Eq. (3.13) that correlations between modes displaced by $\pm\Omega$ with respect to half the pump frequency are responsible for the noise reduction at frequency Ω . The physics behind the noise reduction is down conversion of a pump photon at frequency 2ω into a pair of photons at frequency $\omega \pm \Omega$. Energy conservation requires that the phases of photons at $\omega \pm \Omega$ add up to a phase set by the pump photon. The down converted photons are thus pair-wise phase locked at the quantum level, and the sum of their quadrature fluctuations will either add or cancel depending on the quadrature. The minimum squeezing bandwidth is set by the HWHM cavity bandwidth Γ . Even for a moderate pump parameter of $\sigma = 1/2$, the ideal OPO produces 89% or 9.5dB noise reduction at frequencies $\Omega \ll \Gamma$.

In the experiments we do not measure the quantum noise in terms of variances. Instead we measure the spectral density fluctuations of the relevant observable integrated over a narrow resolution bandwidth around a frequency Ω . We choose $\Omega/2\pi$ to be a few MHz so that we are free of the low frequency technical noise of the laser.

Any losses in the squeezing path will degrade the squeezing. Losses can be modelled by a beamsplitter that couples out quantum correlations and couples in vacuum fluctuations. Imperfect spatial mode matching of the OPO squeezed vacuum output and the coherent field will also reduce the observed noise reduction. These imperfections can be included in the ξ parameter as [63] $\xi = \xi_{he}^2 \xi_{qe} \xi_{pe} \xi_{ee}$. ξ_{he} is the homodyne efficiency or the visibility of the spatial mode matching of a coherent field and the squeezed vacuum. ξ_{qe} is the quantum efficiency of the detectors used to measure the field fluctuations. Silicon based photodiodes can have quantum efficiencies of more than 98% in our wavelength range (850nm-920nm). ξ_{pe} is the propagation efficiency from the OPO output to the detectors. ξ_{pe} is set by the losses on mirrors, windows, polarizing optics etc. Finally, ξ_{ee} is the OPO escape efficiency related to the OPO losses, \mathcal{L} , apart from the output coupler transmission T . ξ_{ee} is the probability that a photon in the cavity eventually escapes through the output coupler; $\xi_{ee} = T/(T + \mathcal{L})$. The extra cavity losses also modifies the cavity linewidth to $\Gamma = c(T + \mathcal{L})/2l$.

The intracavity photon number in the \hat{a} -mode is [63] $\langle \hat{a}^\dagger \hat{a} \rangle = \sigma^2/(2 - 2\sigma^2)$. For a typical pump parameter of $\sigma = 1/2$, an output coupler transmission of $T = 0.10$, and a cavity length of 50cm we get a power of about 2pW in the free propagating squeezed vacuum field at 850nm. This power level is many orders of magnitude smaller than the typical laser power used in atomic spectroscopy, and the squeezed vacuum photon flux can be neglected when the squeezed vacuum is combined with a coherent field.

3.3 Polarization squeezed light

In the discussions in the previous sections, only one polarization of the electromagnetic field was considered. However, it is possible to have the nonclassical correlations of squeezed light distributed over two orthogonal polarizations. This is easily seen if we take our squeezed light in one polarization (e.g. linearly polarized along x) and rotate our linear basis by 45° . In the new basis we need both the component at $+45^\circ$ and the component at -45° in order to fully describe our squeezed field polarized along x . Hence, in the new basis the correlations are distributed over two orthogonal polarizations.

In certain situations it is not only possible, but also necessary to describe the field using two orthogonal polarizations. An example is shown in Fig. 3.3; a strong coherent (classical) field polarized along x and a squeezed vacuum field polarized along y are overlapped in the same spatial mode propagating in the z direction. The overlapping is easily done on a polarizing beamsplitter (used to combine the fields rather

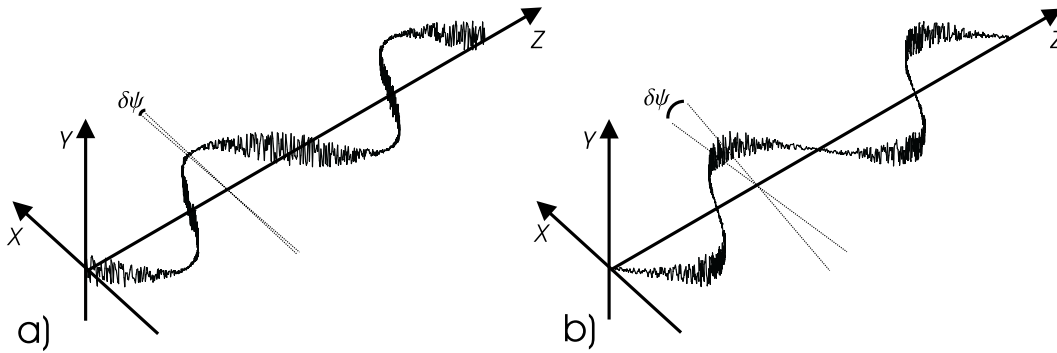


Figure 3.3: A picture of a classical field which is polarized along x and overlapped with a squeezed vacuum field polarized along y . a) The squeezed vacuum fluctuations are out of phase with the classical field. The direction of polarization is squeezed (small fluctuations $\delta\psi$). b) The squeezed vacuum fluctuations are in phase with the classical field. The ellipticity is squeezed and the direction of polarization is antisqueezed (large $\delta\psi$).

than splitting them). The interesting cases are when the relative phase between the squeezed vacuum fluctuations and the coherent field is either $\pm 90^\circ$ (Fig. 3.3a) or $0, 180^\circ$ (Fig. 3.3b). In the first situation we see, as illustrated in the figure, that the orientation of the electric field vector is well defined corresponding to small fluctuations in the direction of the linear polarization ($\delta\psi$ in the figure). Figure 3.3a thus represents a polarization squeezed state, where the fluctuations in the (linear) polarization direction is below the standard quantum limit (SQL). The SQL corresponds to ordinary vacuum fluctuations in the y -polarized mode. In the second situation we have large transverse fluctuations at the coherent field antinodes. The field polarization direction is then poorly defined and hence antisqueezed.

The interpretation of the squeezing in Fig. 3.3b is difficult in a linear basis. However, in a circular basis (σ^+ , σ^- polarizations) the well defined polarization direction corresponds to a well defined relative phase between the two circularly polarized components. Figure 3.3b represents a state with equal intensities in the two circular polarizations. Taken separately the intensities will fluctuate, but the intensity difference is very stable.

The fields described here look a lot like the twin-beams [65], where the intensity fluctuations in two modes are strongly correlated with the noise in the intensity difference below the SQL. The states discussed here are, however, not twin-beams. The individual intensities in the twin-beams do not have their noise level below the SQL. In the polarization squeezed states discussed here, the two intensities taken separately do fluctuate less than the SQL, but the maximum noise reduction within a single polarization is only 3dB. The noise in the difference can ideally be completely suppressed. The correct analogy is the 50/50 beamsplitter in an ordinary squeezed field. Correlations exist within each of the two beamsplitter outputs, but correlations also exist between the two outputs. In the polarization squeezed states the modes are separated in polarization (σ^+ , σ^-) and not spatially as with the 50/50 beamsplitter.

A more quantitative characterization of the polarization state can be given by introducing the Stokes parameters. The Stokes parameters are used to describe the polarization state of a classical field [32], but they can also be used for quantized modes of the field [66]. The four Stokes parameters are defined as

$$\begin{aligned}
\hat{S}_0 &= \hat{n} = \hat{a}_+^\dagger \hat{a}_+ + \hat{a}_-^\dagger \hat{a}_- \\
\hat{S}_1 &= 2\hat{S}_x = \hat{a}_+^\dagger \hat{a}_- + \hat{a}_-^\dagger \hat{a}_+ = \hat{a}_x^\dagger \hat{a}_x - \hat{a}_y^\dagger \hat{a}_y \\
\hat{S}_2 &= 2\hat{S}_y = i \left(\hat{a}_-^\dagger \hat{a}_+ - \hat{a}_+^\dagger \hat{a}_- \right) = \hat{a}_x^\dagger \hat{a}_{x'} - \hat{a}_{y'}^\dagger \hat{a}_y \\
\hat{S}_3 &= 2\hat{S}_z = \hat{a}_+^\dagger \hat{a}_+ - \hat{a}_-^\dagger \hat{a}_- \\
\hat{S}^2 &= \hat{S}_x^2 + \hat{S}_y^2 + \hat{S}_z^2 = \frac{\hat{n}}{2} \left(\frac{\hat{n}}{2} + 1 \right)
\end{aligned} \tag{3.15}$$

The indices $+-$, xy and $x'y'$ refer to the chosen basis (circular, linear $x-y$ and linear $\pm 45^\circ$) for the particular mode operator. $\hat{S}_0 = \hat{n}$ is the overall number of photons. In a basis of orthogonal linear polarizations along x and y , we see that \hat{S}_1 is the difference between the photon numbers in the two linearly polarized components. \hat{S}_2 is similar to \hat{S}_1 except that the linear basis $x'-y'$ is rotated $+45^\circ$ with respect to the $x-y$ basis. \hat{S}_3 is the difference between the photon numbers in the right- and left hand circularly polarized components of the field. Instead of the Stokes parameters directly, we will often concentrate on the parameters \hat{S}_x , \hat{S}_y and \hat{S}_z . These components fulfil the equal time angular momentum commutation relation $[\hat{S}_x, \hat{S}_y] = i\hat{S}_z$ together with the relations obtained by cyclic permutations of the indices. We can then consider \hat{S}_x , \hat{S}_y and \hat{S}_z as the three components of an angular momentum or spin for the field (Stokes spin). For completeness, we have included the expression for the square of the angular momentum operator (\hat{S}^2).

In the experiments we cannot measure the Stokes spin components directly since they depend on the chosen quantization length (L). Instead we measure the power of the field, which in units of photons per second corresponds to the observables $\hat{S}_{x,y,z} = \frac{c}{L} \hat{S}_{x,y,z}$.

A polarization squeezed state of light can be generated by combining a strong coherent field polarized along x ($\tilde{a}_x e^{i\theta}$) and the squeezed vacuum output of the OPO polarized along y (\tilde{a}_y) on a polarizing beamsplitter, (see PBS1 in Fig. 3.4). The photon flux in the coherent field is given by $\Phi = \frac{c}{L} |\langle \tilde{a}_x \rangle|^2$. θ is the relative phase between the two fields. Calculation of the Stokes parameters in the $x-y$ basis involves products like $e^{i\theta} \tilde{a}_x \tilde{a}_y^\dagger = e^{i\theta} (\langle \tilde{a}_x \rangle + \delta \tilde{a}_x) \tilde{a}_y^\dagger$. We define the fluctuating quantity $\delta \tilde{a}_x$ as $\delta \tilde{a}_x = \tilde{a}_x - \langle \tilde{a}_x \rangle$. By a strong coherent field we mean that $\langle \delta \tilde{a}_x^2 \rangle \ll \langle \tilde{a}_x \rangle^2$, and the operator product can be linearized to give $e^{i\theta} \langle \tilde{a}_x \rangle \tilde{a}_y^\dagger$. With this linearization it is straight forward to get

$$\hat{S}_y(\Omega) = \sqrt{\Phi} \left(\tilde{\mathcal{X}}^{out}(\Omega) \cos \theta + \tilde{\mathcal{Y}}^{out}(\Omega) \sin \theta \right) \tag{3.16}$$

$\tilde{\mathcal{X}}^{out}$, $\tilde{\mathcal{Y}}^{out}$ are the quadrature phase operators for the OPO output from Eq. (3.13). From the previous section we know that $\tilde{\mathcal{X}}^{out} \propto \tilde{\mathcal{X}}_v$ and $\tilde{\mathcal{Y}}^{out} \propto \tilde{\mathcal{Y}}_v$. Since the vacuum fluctuations are uncorrelated ($\langle \tilde{\mathcal{X}}_v \tilde{\mathcal{Y}}_v + \tilde{\mathcal{Y}}_v \tilde{\mathcal{X}}_v \rangle = 0$) we find that $\langle \tilde{\mathcal{X}}^{out}(\Omega) \tilde{\mathcal{Y}}^{out}(\Omega') + \tilde{\mathcal{Y}}^{out}(\Omega') \tilde{\mathcal{X}}^{out}(\Omega) \rangle = 0$, and the spectral density for \hat{S}_y is (together with the other Stokes components) found to be

$$\begin{aligned}
\langle \hat{S}_x \rangle &= \Phi/2, \quad \langle \hat{S}_y \rangle = \langle \hat{S}_z \rangle = 0 \\
\langle \hat{S}_x \rangle_\Omega^2 &= \frac{\Phi}{4} \\
\langle \hat{S}_y \rangle_\Omega^2 &= \frac{\Phi}{4} (R_+(\Omega) \cos^2 \theta + R_-(\Omega) \sin^2 \theta) \\
\langle \hat{S}_z \rangle_\Omega^2 &= \frac{\Phi}{4} (R_+(\Omega) \sin^2 \theta + R_-(\Omega) \cos^2 \theta) \\
R_\pm(\Omega) &= \left(1 \pm \xi \frac{4\sigma}{\Omega^2/\Gamma^2 + (\sigma \mp 1)^2} \right)
\end{aligned} \tag{3.17}$$

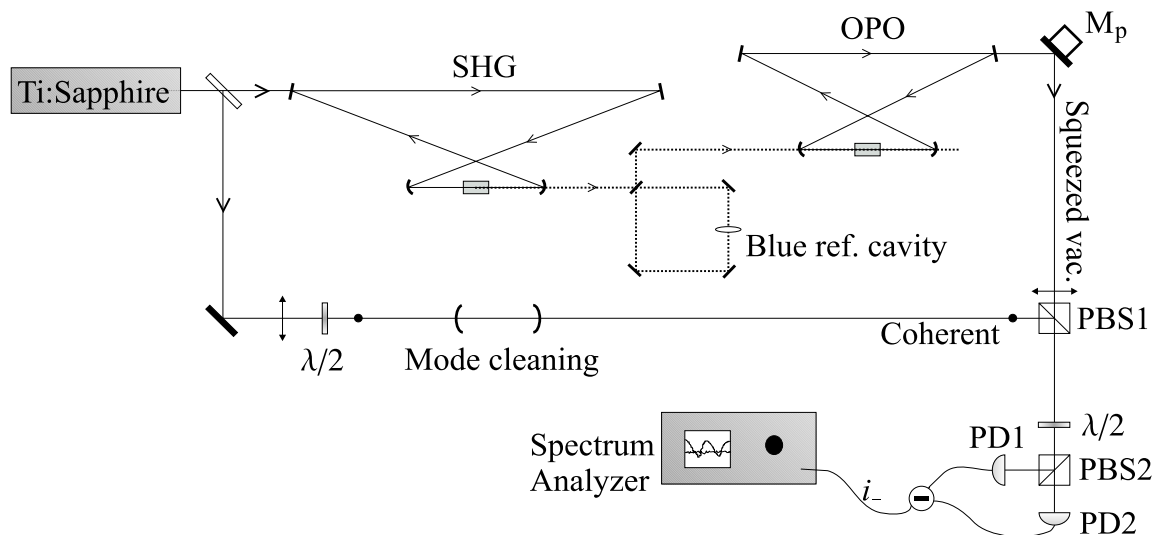


Figure 3.4: Schematic picture of the squeezing setup consisting of the cavity for second harmonic generation (SHG), the blue reference cavity, and the OPO producing the squeezed vacuum. Polarization squeezed light is generated at the polarizing beamsplitter PBS1 by adding a coherent field and the squeezed vacuum in orthogonal polarizations. The relative phase between the two fields is adjusted by the piezo-mounted mirror M_p . The spatial mode of the coherent field is cleaned in a mode cleaning cavity. The half-wave plate, PBS2 and the two photodetectors produce a differential photocurrent which is proportional to the Stokes spin \hat{S}_y . The quantum fluctuations in \hat{S}_y are analyzed on the spectrum analyzer.

We define a polarization squeezed state as a state with the fluctuations in one of the three Stokes spin components below the standard quantum limit set by the coherent state. The example in (3.17) is polarization squeezed for any θ as long as $\sigma > 0$. The situation in Fig. 3.3a corresponds to squeezed \hat{S}_y , whereas \hat{S}_z is squeezed in Fig. 3.3b. As discussed later in this thesis (chapter 5), a spin state with fluctuations in one component reduced below the standard quantum limit is a spin squeezed state.

3.4 Experimental squeezing setup

Our squeezed light source can run in the wavelength range between 850nm and 920nm. The 917nm wavelength is used in the squeezed probe polarization spectroscopy experiment discussed in the following section. In the spin squeezing experiment, which is the principal work in this thesis (Chapter 8), we run at 852nm. The construction of the squeezing source and its characterization around 917nm is discussed in great detail in Ref. [67]. A similar squeezing setup is presented in Ref. [47, 45]. In this section we give an overview of the setup and compare the parameters at 852nm and 917nm. Although the setup was completely rebuilt when we went from 917nm to 852nm, the geometry, mirrors, and crystals for the two main parts of the setup (doubling cavity and OPO) are identical for the two setups³. The parameters given below are for 852nm unless otherwise stated.

The setup is outlined in Fig. 3.4. A powerful Ti:Sapphire laser (Microlase MBR-110) drives the squeezing source. About 600mW of the IR laser output pumps a doubling cavity used for second harmonic generation. The doubling cavity is a four-mirror ring resonator with a $\chi^{(2)}$ nonlinear crystal between

³This rebuilding was not required by the change in wavelength, but we had to move and compress the squeezing setup in order to get room for a second Ti:Sapphire laser (home-made) on the optical table.

the two curved mirrors (radius of curvature 5cm). The nonlinear crystal is KNbO₃, which can be non-critically phase matched at around 5°C (130°C @ 917nm). The IR light is coupled into the resonator through an input coupler with a transmission of 10.7% (7.3% @ 917nm). The three other mirrors are all high reflectors at the IR wavelength, but transmit about 80% of the blue second harmonic field (slightly higher transmission at 917nm). Optimum focusing of the IR field in our 10mm long crystal requires a waist of about 15μm [68], and the cavity geometry is adjusted accordingly. The doubling cavity can give an output of up to 200mW blue light (300mW at 917nm). A doubling efficiency of 80% has been reached at 917nm, but the performance at 852nm is not quite as good. The mirrors and crystal are broadband coated but centered around 920nm. This partly explains the inferior performance at 852nm. Another limiting factor is the blue-light-induced infrared absorption (BLIIRA) present in KNbO₃ [69]. The blue light generated by the second harmonic process in the crystal induces losses for the IR pump field. The BLIIRA is smaller at large wavelength (higher phase matching temperature) [70], and this also contributes to the superior doubling efficiency at 917nm.

The OPO cavity is a ring resonator similar to the doubling cavity, except that the cavity length is shortened by using mirrors with 2.5cm radius of curvature. The short cavity is chosen because it increases the squeezing bandwidth (Eq. (3.13)). The OPO is pumped by the blue light from the doubling cavity and produces a squeezed vacuum field as described in the previous section. It is important that the spatial mode of the blue pump field is well matched to OPO cavity. However, the blue light is not resonated in the OPO, and hence the mode matching is not trivial. To circumvent this problem we pump the OPO with IR light through the output coupler and let the OPO generate blue light. This generated blue field is in the spatial mode that should be used for pumping the OPO. The blue OPO output is matched from one side to a blue reference cavity (see Fig. 3.4). We then match the blue output of the doubling cavity to the same reference cavity, but from the other side. Now the blue field reflected off the reference cavity goes into the correct mode for pumping the OPO. The estimated mode matching of the blue to the OPO is $mm^{852} = 0.72$ with 80% from the doubling cavity to the reference cavity and 90% from the OPO to the reference cavity. For 917nm we estimate $mm^{917} = 0.85$. The typical blue power used for pumping the OPO, when mode matching (0.72), blue transmission through curved mirror (0.80), and reflection and bulk losses in crystal (0.91) are taken into account, is about 70mW at 852nm. The effective pump power is about 130mW at 917nm.

The nonlinearity of the KNbO₃ crystal is specified in terms of the nonlinearity E_{NL} defined through the relation $P_{2\omega} = E_{NL}P_{\omega}^2$. $P_{2\omega}$ is the single pass generated second harmonic power for a pump power of P_{ω} . In the OPO we measure $E_{NL}^{852} = 1.6\%W^{-1}$ ($E_{NL}^{917} \simeq 0.5\%W^{-1}$). The inferior nonlinearity at 917nm is not well understood, but our measurements indicate that the nonlinearity suffers at the increased temperature. On the other hand, the cavity round trip losses at 852nm are somewhat higher; $\mathcal{L}^{852} = 2.2\% \pm 0.3\%$. \mathcal{L}^{852} includes about 1.3% BLIIRA at 70mW blue pump power, but excludes the output coupler transmission $T^{852} = 10.7\%$. The numbers for 917nm are $\mathcal{L}^{917} = 1.2\%$ including 0.7% BLIIRA. The pump threshold for the OPO can be calculated to be [71] $P_{th} = (T + \mathcal{L})^2 / (4E_{NL})$, and we find $P_{th}^{852} = 260\text{mW}$ and $P_{th}^{917} = 360\text{mW}$. The corresponding pump parameters are $\sigma^{852} = 0.52$ and $\sigma^{917} = 0.60$.

The imperfections quantified by the ξ -parameters are dominated by the escape efficiencies $\xi_{ee}^{852} = T^{852} / (T^{852} + \mathcal{L}^{852}) = 0.83$ and $\xi_{ee}^{917} = 0.86$. The other parameters are homodyne efficiency ($\xi_{he}^{852} = 0.96$, $\xi_{he}^{917} = 0.98$), detector quantum efficiency ($\xi_{qe}^{852} = 0.98$, $\xi_{qe}^{917} = 0.99$ - factory specifications), and propagation efficiency from the OPO to the detectors ($\xi_{pe}^{852} = 0.91$, $\xi_{pe}^{917} = 0.90$). The large propagation losses come from imperfect polarization optics, windows and mirrors⁴.

The length of the OPO is about 20cm and the corresponding HWHM cavity linewidths are $\Gamma^{852}/2\pi = \frac{c}{2l} \frac{T+\mathcal{L}}{2\pi} = 15\text{MHz}$ and $\Gamma^{917}/2\pi = 10\text{MHz}$. The bandwidth of the squeezing spectra is given by $\Gamma(1 + \sigma)$, which for our $\sigma \sim 0.5$ gives a squeezing bandwidth about 50% larger than the cavity linewidth.

From Eq. (3.13) we can calculate the expected squeezing/antisqueezing at our $\Omega/2\pi = 3\text{MHz}$ detection frequency. We get for the 852nm setup $R_{-}^{852}(\Omega) = 0.40$ (-4.0dB) and $R_{+}^{852}(\Omega) = 6.3$ (+8.0dB). For the

⁴One of the mirrors in the 852nm setup is the surface of a gold coated mechanical chopper wheel. The use of this chopper wheel is discussed in Chapter 8. Here we just note that the reflectivity was measured to be 95%.

917nm setup the numbers are: $R_-^{917}(\Omega) = 0.33$ (-4.8dB) and $R_+^{917}(\Omega) = 8.1$ (+9.1dB).

To generate the polarization squeezed light, we must overlap the squeezed vacuum output of the OPO with a coherent field in the orthogonal polarization. This is done on the polarizing beamsplitter PBS1 in Fig. 3.4. The spatial mode of the coherent field is cleaned in the mode cleaning cavity for better homodyne efficiency. The half-wave retarder, in front of the mode cleaning cavity, ensures that the coherent field and the squeezed vacuum have orthogonal polarizations on PBS1. The spatial modes of the fields are overlapped by injecting a coherent IR field into the OPO without the blue pump field. The transmission of this IR field is in the same spatial mode as the squeezed vacuum output. The overlap of the two modes on PBS1 is measured by mixing the two polarizations with a half-wave retarder and a second PBS. The interference fringe is monitored as the relative phase (or path length difference) is scanned by the mirror M_p mounted on a piezoelectric transducer (PZT) (Fig. 3.4).

The output of the Ti:Sapphire laser is frequency modulated at 20MHz with an electro-optical modulator. The modulation is used for locking the doubling cavity and the OPO at resonance by standard FM techniques [72]. A weak IR field used for locking is injected into the OPO through one of the high reflectors. The locking field and the generated squeezed vacuum field are counterpropagating in the resonator. Ideally, none of the locking field leaves the OPO in the same spatial mode as the squeezed vacuum. However, the normal cut KNbO₃ surfaces reflect a small fraction of the locking field into the opposite direction. Therefore, a very weak coherent field of about 50nW is present in the squeezed vacuum output. This coherent component can be neglected as long as the squeezed vacuum is mixed later on with a much stronger coherent field.

The mode cleaning cavity is locked in transmission on the side of a fringe. In this way a feedback to the cavity length ensures a constant intensity of the transmitted field. In the experiments later on, it is important with good long term stability. We use the mode cleaning cavity to obtain a clean spatial mode as well as to compensate for the slow intensity fluctuations of the Ti:Sapphire laser.

The noise properties of the polarization squeezed state, generated on PBS1, is analyzed in the polarization interferometer consisting of PBS1, PBS2 and the half-wave retarder in between (Fig. 3.4). The differential photocurrent i_- from the photodetectors PD1,2 is proportional to the Stokes spin component \hat{S}_y , defined with respect to the polarizations at PBS1, when the half wave retarder rotates the horizontal and vertical polarizations by 45°. The two photodetectors are the same 3.0MHz detectors as in section 2.4.1, except that the bandwidth is reduced to 180kHz. The noise equivalent power for both detectors is consequently reduced to about 25 μ W. The spectral density of the photocurrent fluctuations is given by

$$(i_-)_{\Omega}^2 = 4e^2g^2(\hat{S}_y)_{\Omega}^2 \quad (3.18)$$

e is the elementary charge, g is the detector gain, and we have assumed unity quantum efficiency. In practice, the spectral density is normalized to the coherent state fluctuations, and detailed knowledge about e^2g^2 is not necessary. Replacing the half-wave retarder with a correctly oriented quarter-wave retarder gives $i_- \propto \hat{S}_z$, whereas no retarder gives $i_- \propto \hat{S}_x$ (the last option is less interesting as it always gives the shot noise level, see Eq. (3.17)).

Fig. 3.5 shows the photocurrent fluctuations ($(i_-)_{\Omega}^2 \propto (\hat{S}_y)_{\Omega}^2$) measured with the 852nm setup. The measurement is carried out with the spectrum analyzer (SA, Anritsu MS710A) set at frequency $\Omega/2\pi = 3$ MHz and with zero span. The SA integrates the spectral density over a resolution bandwidth of 100kHz, and the sweep time is about 60ms. Curve a is the shot noise level with the squeezed vacuum path blocked. The laser output is checked to be shot noise limited at the actual detection frequency and power by doubling the power in the coherent field and observing a noise increase of 3dB, as expected for shot noise limited light. In curve b the relative phase between the coherent field and the squeezed vacuum is scanned by means of the PZT mounted mirror (M_p in Fig. 3.4). We observe the phase sensitive \hat{S}_y noise going below and above the shot noise level in accordance with Eq. (3.17). The electronic noise (detector noise) for these measurements is about 12dB below the sum of electronic noise and shot noise of light. We have subtracted the (small) electronic noise background in the graphs in Fig. 3.5. The nonlinearity of the horizontal axis in Fig. 3.5 is caused by phase drifts during the scan. The dotted line on top of curve b is a fit to Eq. (3.17) taking the dB scale, the known ratio Ω/Γ , and the slightly

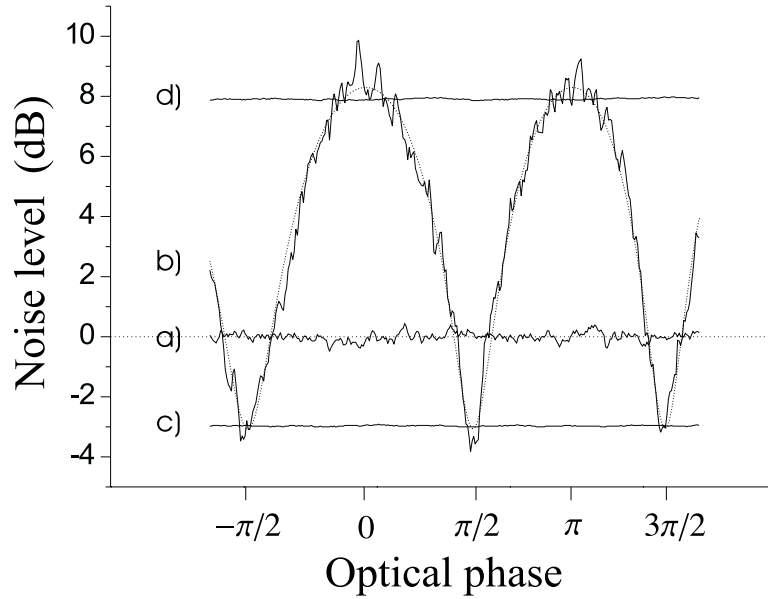


Figure 3.5: Noise in the differential photocurrent $(i_-)_{\Omega}^2 \propto (\hat{S}_y)_{\Omega}^2$ measured with the 852nm setup. a) The shot noise level. b) Phase sensitive noise with a scanned optical phase. The dotted line is a theoretical fit to Eq. (3.17) allowing for a slightly nonlinear scan and taking the dB scale into account. Parameters from the fit: $\sigma = 0.57$, $\xi = 0.56$. c) Squeezing with the phase actively stabilized. d) Antisqueezing with stable phase. Resolution bandwidth: 100kHz. Averaging time for c) & d): about 10 sec. The reference for the vertical dB scale is the coherent state shot noise.

nonlinear scan into account. The result of the fit gives $\sigma = 0.57$ and $\xi = 0.56$. This indicates that e.g. the propagation losses are somewhat higher than expected. One parameter that we did not measure is the direction of polarization for the squeezed vacuum output. If the KNbO_3 crystal is tilted in the OPO, the squeezed vacuum polarization and PBS1 will be misaligned and hence losses are introduced.

In order to have stable squeezing, it is important that the relative phase θ between the squeezed vacuum field and the coherent field is actively stabilized. This is done by dithering the phase at 2kHz using the PZT mounted mirror. The classical differential photocurrent is split into two parts; one goes to the SA used for monitoring the \hat{S}_y noise, and the other goes to a home-made SA. A lock-in amplifier with the output of the home-made SA as the signal input and the 2kHz modulation as the reference provides an error signal with zero crossings when the measured noise $(i_-)_{\Omega}^2$ is at a maximum or a minimum. A low frequency feedback loop to the same PZT mounted mirror compensates fluctuations in the phase θ . The home-made SA is build around a mixer, where the differential photocurrent goes into the RF input and an external function generator delivers the LO input (around Ω). The mixer output is subsequently squared electronically and then filtered by a low-pass filter. The principles behind the spectrum analyzer are discussed in more detail in Appendix E.

In Fig. 3.5 we show as curve c and d the observed polarization squeezing and antisqueezing at 852nm with the phase θ actively stabilized. All data in Fig. 3.5 correspond to the same parameters and are taken within a few minutes. The values for the squeezing and antisqueezing with stabilized phase are -3.0dB and +7.9dB - quite close to the minimum and maximum of -3.1dB and +8.2dB from the fit to curve b.

The squeezing at 852nm is clearly limited by the propagation and intracavity (BLIIRA) losses. The pump parameter is large enough for very strong squeezing. The squeezing can be improved by the use of better optics, but for the spin squeezing experiment this is hardly worth the effort. The efficiency of map-

ping the quantum correlations of light onto atoms is very low as we will see in chapter 4. Consequently, this low mapping efficiency and not the degree of polarization squeezing will be the main limiting factor in the spin squeezing experiment.

At 917nm we measure -3.1dB squeezing and +7.8dB antisqueezing in the polarization interferometer setup. Also these numbers are somewhat smaller than expected theoretically. In a balanced homodyne detection using a 50/50 beamsplitter, we measure close to 5dB of squeezing at 917nm with the improvement due to very low propagation losses ($\xi_{pe}^{917} = 0.99$). The 852nm setup is clearly limited in performance by the BLIIRA. Increasing σ further by stronger pumping just increases the BLIIRA, and hence the escape efficiency suffers. At 852nm we measure a decrease in the squeezing when the effective pump power is increased above the typical 70mW. The advantage of the 917nm setup with respect to low BLIIRA is more or less cancelled by the reduced nonlinearity. With the optics optimized specifically for 852nm and for a good crystal and very low propagation losses, it should be possible to reach -6.0dB of squeezing as demonstrated in Ref. [45].

3.5 Sub-shot noise polarization spectroscopy

We now employ our polarization squeezed light at 917nm together with our cold trapped atoms in the MOT in a spectroscopy experiment with sensitivity beyond the standard quantum limit. The first demonstration of improved sensitivity in a polarization interferometer utilizing squeezed light is given in Ref. [73]. Here the authors place a Faraday rotator with an applied oscillating voltage inside the polarization interferometer. The Faraday rotator produces a signal, which is measured with 1.8dB improved sensitivity when the squeezed light is applied. In the present experiment we use a cold atomic gas as the anisotropic medium. The atoms respond only to a resonant probe field, and the tunability of our squeezing source is therefore important.

The squeezing setup is similar to Fig. 3.4 where the polarization squeezed field between PBS1 and PBS2 now passes through the atomic sample. The setup is also equivalent to Fig. 2.4 with the squeezed vacuum field injected into the empty port of PBS1. In this experiment we use the diode laser for atom cooling and trapping. Just as in the previous chapter, we use double-optical resonance with the trapping beams present all the time and probing on the $6P_{3/2}F = 5 \rightarrow 6D_{5/2}F = 6$ transition. We detect the spectral density of the differential photocurrent on the spectrum analyzer as the frequency of the polarization squeezed light is scanned across the 917nm atomic resonance. The squeezed probe is scanned in frequency by scanning the laser driving the squeezing source. The SA works in zero span mode at the fixed frequency $\Omega/2\pi = 3.0\text{MHz}$. In order to observe an atomic signal at 3.0MHz, we modulate the atomic sample. The atoms are modulated by applying intensity modulation to one of the horizontal trapping beams. The squeezed probe field propagates along the z -axis at a small angle with respect to the horizontal trapping beams. The modulation of the trapping light results in a modulated imbalance in the intensity of the two circularly polarized components of the trapping field. An imbalance in circular polarizations results in nonzero orientation ($\langle \hat{F}_z \rangle$) in the $6P_{3/2}F = 5$ state. Consequently $\langle \hat{F}_z \rangle$ is modulated at 3.0MHz, and from Eq. (2.16) we expect to observe a modulation or a signal in the differential photocurrent at 3.0MHz when the probe field approaches the 917nm resonance.

The observed signals are plotted in Fig. 3.6. Curve a is a measurement with the squeezed vacuum path blocked (coherent state probe). Near resonance we observe the atomic signal whereas the noise level off resonance is set by the coherent state shot noise. Curve b is a similar measurement, except that we now employ the polarization squeezed probe. The off resonant noise level is now set by the reduced \hat{S}_y noise with the optical phase between the squeezed vacuum and the coherent field actively stabilized to $\theta = \pi/2$. The home-made spectrum analyzer, used for locking the optical phase, is now analyzing the photocurrent fluctuations a few hundred kHz away from the 3.0MHz modulation frequency. The atoms are modulated only within a narrow bandwidth around 3.0MHz, and the phase locking signal is therefore not influenced when we scan across the atomic resonance. Curve c is the electronic noise when no light reaches the detectors.

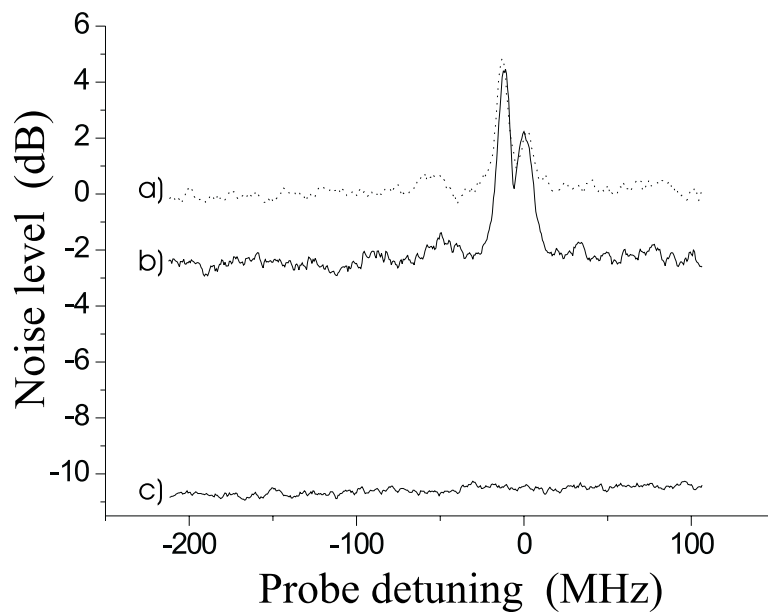


Figure 3.6: Polarization spectroscopy on atoms with sub-shot noise sensitivity. a) Coherent state probe. b) Polarization squeezed probe for increased sensitivity. c) Electronic noise level. The data are taken with a resolution bandwidth of 30kHz. The reference for the dB scale is the sum of the coherent state shot noise plus the small amount of electronic noise.

The peak from the atomic signal plus shot noise is for the coherent state probe measured to be 4.8dB above the shot noise level. The corresponding signal-to-noise ratio (S/N) is given by $S/N = 10^{4.8/10} - 1 = 2.0$. For the polarization squeezed probe we infer a signal-to-noise ratio of $S/N = 3.9$. We see that the use of a polarization squeezed probe increases the S/N by a factor of 2.0. This is close to the S/N increase of 1.8 that we expect from the -2.5 dB of squeezing available in this experiment. We attribute the discrepancy to drifts in the amplitude of the atomic signal.

It is in this experiment, as well as in most experiments demonstrating sub-shot noise sensitivity, important that the probe optical depth is very small. For an appreciable absorption, the propagation efficiency (ξ_{pe}) will suffer, and the probe field will be less squeezed on resonance. The reduced squeezing on resonance is difficult to distinguish from the true atomic signal, and one may arrive at the (false) conclusion that the increase in S/N is larger than predicted by the actual degree of squeezing. In the present experiment we have a resonant optical depth below 3%, and the effect of reduced squeezing at resonance can safely be neglected for the moderate squeezing of -2.5 dB.

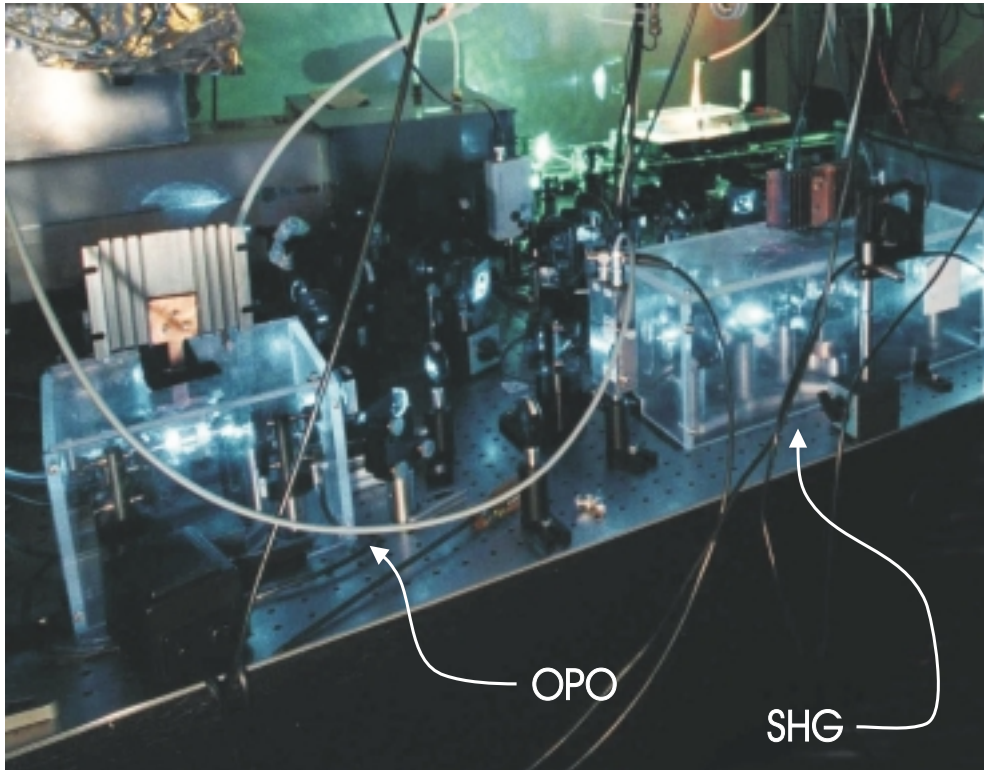


Figure 3.7: A picture of the setup used for generation of squeezed light around 852nm. The doubling cavity (SHG) is placed inside the plastic box to the right. The generated blue light pumps the OPO in the plastic box to the left. The blue reference cavity is located behind the doubling cavity. The Ar-ion laser pumping the Ti:Sapphire laser is seen in the background.

Chapter 4

Mapping the quantum state of light onto atoms

We move on with a theoretical chapter about mapping of the quantum state of light onto an ensemble of multi-level atoms. The idea is that the quantum correlated photons in a nonclassical state of light are absorbed in an optically thick atomic gas and thereby generate quantum correlated or entangled excited state atoms. By entanglement we mean that the quantum state is non-separable, i.e. it cannot be written as a product of single atom states. This quantum state mapping is interesting from, at least, two different viewpoints.

As we know from the squeezed light theory, multiparticle entanglement can be used to reduce quantum fluctuations in certain observables. This is useful in spectroscopy experiments as we have demonstrated with squeezed light in the previous chapter. In some experiments the obtainable signal-to-noise ratio is limited by the quantum noise of uncorrelated atoms. We will give an example of that in chapter 7. A more persuasive example is the state of the art atomic fountain clock, which is limited in stability by the atomic projection noise from uncorrelated atoms [1]. The frequency stability of the atomic clock can be improved by utilizing quantum correlated atoms as discussed in Ref. [74, 75].

The other point of view comes from quantum information. Atoms can be used to store qubits by utilizing long-lived internal states. Photons are the obvious carriers when quantum information is to be transferred from one "quantum memory cell" to another. This approach is discussed theoretically in Ref. [7], where single atoms in cavities act as the quantum memory, and information is transferred by coupling the cavities via an electromagnetic field (photons). The cavities are, in this approach, required for efficient interaction between atoms and photons. Here we follow a different strategy. We do not require strong interaction between the field and a single atom. Instead we use a large number of atoms to ensure complete transfer of the quantum state of a freely propagating continuous wave light beam. Although we in this thesis limit the mapping discussion to the squeezed states of light, other nonclassical states may be mapped in a similar way as shown in Ref. [8]. A very recent proposal involves mapping of the quantum states of travelling light waves onto collective states of atoms in a cavity by utilizing an adiabatic transfer technique [76]. This proposal does not require high-Q cavities, but it relies on strong coupling to the collective atomic variables of a large ensemble of atoms. It is a proposal in the intermediate regime between the "high-Q cavity - one atom" approach of Ref. [7] and our "no cavity - many atoms" approach.

Even if we disregard the two motivating viewpoints above, the manipulation of atoms and photons at the quantum level is basically interesting physics, and our interests in the subject do not even need possible applications in order to be justifiable.

One of the first publications on transferring of the quantum state of squeezed light onto an ensemble of two-level atoms comes from G. S. Agarwal *et al.* in 1990 [77]. Their calculations do predict generation of entangled atoms and squeezing of a collective spin component. However, the premises for their

calculations are difficult to comply with experimentally. It is assumed that all atoms see the same squeezed vacuum mode, and that no unsqueezed (normal) vacuum modes interact with the atoms. This is the "large solid angle"-problem mentioned in the introduction to chapter 3. In the same introduction we note that the "large solid angle"-problem perhaps can be circumvented by using a cavity to enhance the squeezed light interaction. Even more problematic is the assumption that all atoms are contained within a volume much smaller than λ^3 , where λ is the wavelength of the atomic resonance frequency. This requirement comes from the two non-degenerate atomic levels, which constitute the upper and lower levels in the dipole coupling to the electromagnetic field. The multiparticle entanglement involves correlations between the dipole moments of different atoms. An effective dephasing takes place and ruins any correlations when the atoms are distributed over a volume larger than λ^3 , since the phase of the dipole oscillations is set by the spatially dependent phase of the excitation field (e^{ikz}).

An improved proposal in terms of experimental feasibility is presented in Ref. [9]. Here the atomic correlations are related to two degenerate excited atomic states, and this degeneracy removes the λ^3 -volume problem. Furthermore, the squeezed excitation field is propagated through the atomic medium without assumptions about tight focusing and consequently no "large solid angle"-problem. The effect of the unsqueezed vacuum modes is reduced to a decay of correlations, which limits the spin noise reduction to 50% of the standard quantum limit set by the fluctuations of uncorrelated atoms. The results of Ref. [9] are the starting point for our spin squeezing work.

A closely related proposal involves complete absorption of twin-beams in an atomic gas of three-level atoms [78]. The effects are very similar to those in Ref. [9], and the twin-beam theory is much simpler and easier to understand intuitively.

We consider in this thesis the entangling of a large ensemble of atoms through the light-atom mapping, with this chapter presenting the theory behind the experiment in chapter 8. The results presented here are generalizations of the work in Ref. [9]. We allow for an arbitrary polarization squeezed excitation field, and we generalize to Zeeman degenerate atoms with the squeezed light interacting on a $F \rightarrow F' = F + 1$ transition. The results of Ref. [9] are restricted to the three-level system with $F = 0$ and a specific polarization squeezed state of the excitation field. For simplicity, we assume that the atoms in the ground state F are unpolarized. In chapter 6 we will discuss the readout of the atomic quantum correlations; a subject which is only superficially treated in Ref. [9].

This chapter is organized as follows: In the first section we introduce the notation and the equations that drive our system of atoms and fields. In the second section we consider mapping of the Stokes spin component \hat{S}_z onto the collective excited state atomic spin component \hat{F}'_z . The third section includes the calculation of mapping of the Stokes spin components \hat{S}_x and \hat{S}_y onto the atomic variables $\hat{F}'_x - \hat{F}'_y$ and $\hat{F}'_x \hat{F}'_y + \hat{F}'_y \hat{F}'_x$. We end this chapter with a few comments on the applied linearization approach.

4.1 The fundamental equations

The physical system, which we investigate in this theoretical chapter, consists of a Gaussian mode quantum field and a sample of Zeeman degenerate atoms (Fig. 4.1). The quantum field is in a polarization squeezed state. This means that the field description includes both circular polarizations with a monochromatic coherent (classical) component at the carrier frequency ω_0 on top of a broad band, zero mean quantum field. The internal level structure of the atoms is shown in Fig. 4.1b. The total angular momentum of the ground and excited state is respectively F and $F' = F + 1$. The atomic ground and excited state couple to the quantum field through the dipole interaction. The atomic resonance frequency is given by ω_a , and we will assume that the carrier of the excitation field is at exact resonance; $\omega_a = \omega_0$. The coherent component of the excitation field is assumed to be small compared to the atomic saturation intensity, so that the excited state population is much smaller than the ground state population at all positions within the atomic cloud. Furthermore, to simplify the equations for propagation of the quantum field in the atomic medium, we take the atomic ground state to be unpolarized. The calculations are also simplified by the assumption that the characteristic length scales are well separated,

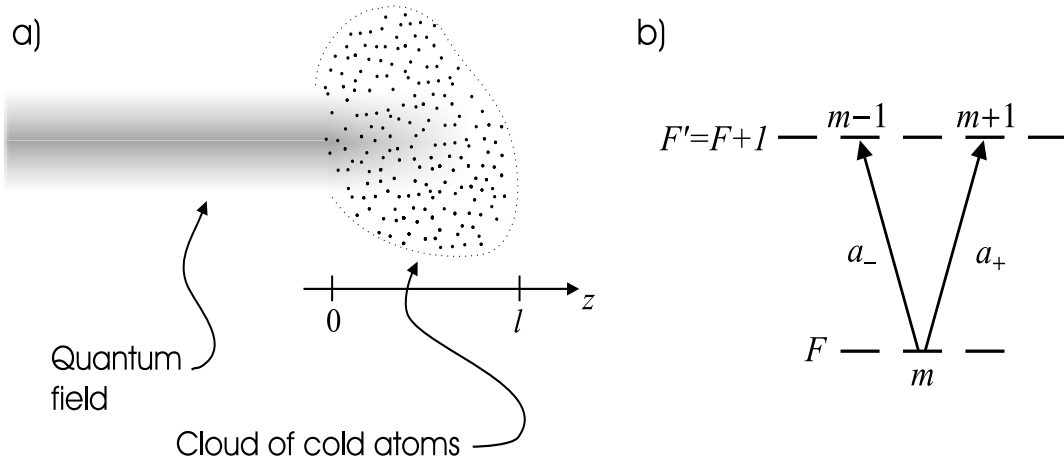


Figure 4.1: a) The freely propagating quantum field with a Gaussian transverse mode is (almost) completely absorbed in a cloud of cold atoms. By this process the quantum properties of the field are transferred to the atomic sample. b) The atomic level scheme with the Zeeman degenerate ground and excited state. F , F' are the total angular momentum quantum numbers and a_{\pm} are the field amplitudes of the two circular polarizations of the quantum field.

i.e. $\lambda \ll L \sim \delta V^{1/3} \ll L' \lesssim l$. λ is the wavelength of the atomic resonance. L is a length, which sets the number of modes included in the expansion of the quantized electromagnetic field. L' is the characteristic length scale for changes in the amplitude of the quantum field due to absorption or dispersion in the atomic medium. δV is a small volume used in the definition of continuous atomic operators. l is the "length" of the atomic cloud (see Fig. 4.1a). Finally, we assume that the transverse size of the atomic cloud is larger than the diameter of the Gaussian mode quantum field. The theory is based on the Heisenberg-Langevin equations [79] for the field and the atomic operators. We will linearize these equations (similar to e.g. Ref. [9, 80, 81, 82]) and arrive at an analytic expression for the fluctuations in the collective (i.e. summed over all atoms) excited state observables \hat{F}'_z , $\hat{F}'_x{}^2 - \hat{F}'_y{}^2$ and $\hat{F}'_x \hat{F}'_y + \hat{F}'_y \hat{F}'_x$. These fluctuations will be expressed through the fluctuations in the Stokes parameters of the quantum excitation field. The starting point for the calculations is the Hamiltonian for the system of atoms and fields, which we derive in the following subsection.

4.1.1 The Hamiltonian

The excitation field is propagating along the z -axis (quantization axis) with a transverse spatial mode function $u(x, y)$. The expression for the excitation field in the basis of right- and left circular polarizations is given by

$$\begin{aligned} \hat{\mathbf{E}}(\mathbf{r}) &= i\zeta \int_{k_0 - \frac{\pi}{L}}^{k_0 + \frac{\pi}{L}} \left[\mathbf{e}_+ u(x, y) \hat{a}_+(k) e^{ikz} - \mathbf{e}_+^* u^*(x, y) \hat{a}_+^\dagger(k) e^{-ikz} \right] dk \\ &+ i\zeta \int_{k_0 - \frac{\pi}{L}}^{k_0 + \frac{\pi}{L}} \left[\mathbf{e}_- u(x, y) \hat{a}_-(k) e^{ikz} - \mathbf{e}_-^* u^*(x, y) \hat{a}_-^\dagger(k) e^{-ikz} \right] dk \\ \zeta &= \sqrt{\frac{\hbar\omega_0}{4\pi\epsilon_0}} \quad , \quad \omega = kc \quad , \quad [\hat{a}_\pm(k), \hat{a}_\pm^\dagger(k')] = \delta(k - k') \end{aligned} \quad (4.1)$$

$\mathbf{e}_\pm = (\mathbf{e}_x \pm i\mathbf{e}_y) / \sqrt{2}$ are the unit vectors for circular polarizations. The field is time dependent in the Heisenberg picture due to time dependent annihilation and creation operators. The frequency compo-

nents very far from atomic resonance do not contribute in the theory, and the integrals are truncated with the limits $k_0 \pm \pi/L$. L is the "quantization length", and it is assumed to be smaller than the characteristic length, L' , for changes in the excitation field due to absorption and dispersion. In Eq. (4.1) we use the assumption $\lambda \ll L$ to pull the frequency ω out of the integral and include it in ζ as ω_0 . The carrier frequency $\omega_0 = k_0 c$ is the only frequency component of the field that has a nonzero mean value.

The Hamiltonian for the system of atoms and fields is given by

$$\begin{aligned} \hat{H} = & \hbar c \int_{k_0 - \frac{\pi}{L}}^{k_0 + \frac{\pi}{L}} k \left[\hat{a}_+^\dagger(k) \hat{a}_+(k) + \hat{a}_-^\dagger(k) \hat{a}_-(k) \right] dk \\ & - \hbar \omega_a \sum_{m=-F}^F \int_V \rho \hat{\sigma}_{Fm, Fm}(\mathbf{r}) d^3 \mathbf{r} \\ & - \int_V \hat{\mathbf{D}}(\mathbf{r}) \cdot \hat{\mathbf{E}}(\mathbf{r}) d^3 \mathbf{r} \end{aligned} \quad (4.2)$$

The Hamiltonian describes the interaction between the excitation fields and the atoms within a volume $V \sim l^3$. The first term is the free Hamiltonian for the excitation field. The second term is the free Hamiltonian for the atoms with the energy $-\hbar \omega_a$ in the ground state and zero energy in the excited state. Instead of a discrete sum over all atoms in the volume V , we integrate over the continuous atomic operators defined below. The last term is the dipole interaction between the atoms and the field with $\hat{\mathbf{D}}(\mathbf{r})$ as the polarization operator. ρ is the (constant) density of atoms.

The normalized continuous atomic operators are defined as (see also Ref. [83])

$$\begin{aligned} \hat{\sigma}_{F'm, F'n}(\mathbf{r}) &= \frac{1}{\rho \delta V} \sum_i |F'm\rangle_{i,i} \langle F'n| \\ \hat{\sigma}_{Fm, Fn}(\mathbf{r}) &= \frac{1}{\rho \delta V} \sum_i |Fm\rangle_{i,i} \langle Fn| \\ \hat{\sigma}_{F'm, Fn}(\mathbf{r}) &= \frac{1}{\rho \delta V} \sum_i |F'm\rangle_{i,i} \langle Fn| e^{ik_0(z_i - z)} \\ \hat{\sigma}_{Fm, F'n}(\mathbf{r}) &= \frac{1}{\rho \delta V} \sum_i |Fm\rangle_{i,i} \langle F'n| e^{-ik_0(z_i - z)} \end{aligned} \quad (4.3)$$

δV is assumed to be large enough to include many atoms ($\rho \delta V \gg 1$). On the other hand, we assume $\delta V^{1/3}$ to be small compared to the characteristic absorption length L' . The sum extends over all atoms within the volume δV around \mathbf{r} . $|F'm\rangle_{i,i} \langle F'n|$ is the usual single-atom projection operator with $|F'm\rangle_i$ as the excited state, Zeeman level m , atom number i , and $|Fn\rangle_i$ as the ground state, Zeeman level n , atom number i . The optical coherences for different atoms in δV have different phases due to the spatial phase change of the excitation field ($\delta V \gg \lambda^3$). The exponentials $e^{\pm ik_0(z_i - z)}$ in Eq. (4.3) compensate for this effect. These exponentials have the same effect as moving all atoms within δV into the same point \mathbf{r} .

The commutators for the continuous atomic operators are derived from the single atom commutators with the result

$$[\hat{\sigma}_{a,b}(\mathbf{r}), \hat{\sigma}_{c,d}(\mathbf{r}')] = \rho^{-1} [\hat{\sigma}_{a,d}(\mathbf{r}) \delta_{c,b} - \hat{\sigma}_{c,b}(\mathbf{r}) \delta_{a,d}] \delta(\mathbf{r} - \mathbf{r}') \quad (4.4)$$

This commutator with the Dirac delta function is valid in integrals where the integrand is slowly varying on the length scale $\delta V^{1/3}$.

The atomic polarization operator $\hat{\mathbf{D}}(\mathbf{r})$ is given by the density of single atom dipole operators in the volume δV around \mathbf{r} . The single atom dipole operator can be written as

$$\hat{\mathbf{d}} = \sum_{n,m} \langle n | \hat{\mathbf{d}} | m \rangle | n \rangle \langle m | \quad (4.5)$$

where the sum runs over all atomic Zeeman levels in the ground- and excited state. The dipole matrix elements are easily evaluated using the spherical tensor theory and the Wigner-Eckart theorem [31]. The nonzero matrix elements of the $\hat{d}_{\pm 1} = \mp(\hat{d}_x \pm i\hat{d}_y)$ components are found to be (see e.g. Ref. [30] for details)

$$\begin{aligned} \langle Fm | \hat{d}_{\mp 1} | F' m \pm 1 \rangle &= -\langle F' m \pm 1 | \hat{d}_{\pm 1} | Fm \rangle = g \sqrt{(F+2 \pm m)(F+1 \pm m)} \\ g &= \sqrt{\frac{3\varepsilon_0 \hbar \lambda^3 \gamma}{8\pi^2 (2F+1)(2F+2)}} \end{aligned} \quad (4.6)$$

γ is the excited state decay rate. The polarization operator is given by

$$\begin{aligned} \hat{\mathbf{D}}(\mathbf{r}) &= \hat{D}_+(\mathbf{r}) \mathbf{e}_+ + \hat{D}_+^\dagger(\mathbf{r}) \mathbf{e}_+^* + \hat{D}_-(\mathbf{r}) \mathbf{e}_- + \hat{D}_-^\dagger(\mathbf{r}) \mathbf{e}_-^* \\ \hat{D}_\pm(\mathbf{r}) &= \pm \sum_{m=-F}^F \rho g \sqrt{(F+2 \pm m)(F+1 \pm m)} \hat{\sigma}_{Fm, F' m \pm 1}(\mathbf{r}) \end{aligned} \quad (4.7)$$

We can now write the interaction term in the Hamiltonian in Eq. (4.2) as

$$\begin{aligned} - \int_V \hat{\mathbf{D}}(\mathbf{r}) \cdot \hat{\mathbf{E}}(\mathbf{r}) d^3\mathbf{r} &= \\ i\hbar\rho \sum_{m=-F}^F \int_V \left\{ \alpha_m^+ u^*(x, y) \hat{\sigma}_{Fm, F' m+1}(\mathbf{r}) \hat{a}_+^\dagger(z) - \alpha_m^+ u(x, y) \hat{\sigma}_{F' m+1, Fm}(\mathbf{r}) \hat{a}_+(z) \right. \\ &+ \left. \alpha_m^- u^*(x, y) \hat{\sigma}_{Fm, F' m-1}(\mathbf{r}) \hat{a}_-^\dagger(z) - \alpha_m^- u(x, y) \hat{\sigma}_{F' m-1, Fm}(\mathbf{r}) \hat{a}_-(z) \right\} d^3\mathbf{r} \\ \alpha_m^\pm &= \frac{\pm \zeta g}{\hbar} \sqrt{\frac{2\pi}{L}} \sqrt{(F+2 \pm m)(F+1 \pm m)} \end{aligned} \quad (4.8)$$

We used the rotating wave approximation where the fast oscillating terms in the Hamiltonian are neglected [79]. The spatial dependent annihilation operators are given by

$$\hat{a}_\pm(z) = \sqrt{\frac{L}{2\pi}} \int_{k_0 - \frac{\pi}{L}}^{k_0 + \frac{\pi}{L}} \hat{a}_\pm(k) e^{ikz} dk \quad (4.9)$$

$$[\hat{a}_\pm(z), \hat{a}_\pm^\dagger(z)] = 1$$

Note that we go from $\hat{a}_\pm(k)$ to $\hat{a}_\pm(z)$ by a spatial Fourier transform involving only the important k -components. We use the same notation for an operator and its Fourier transform and distinguish the two by the arguments.

4.1.2 The field propagation equation

The equation describing propagation of the field through the atomic sample is obtained from the Heisenberg equation for the field operators. We have

$$\dot{\hat{a}}_\pm(k) = \frac{1}{i\hbar} [\hat{a}_\pm(k), H] = -ick \hat{a}_\pm(k) + \rho \sqrt{\frac{L}{2\pi}} \sum_{m=-F}^F \alpha_m^\pm \int_V u^*(x, y) \hat{\sigma}_{Fm, F' m \pm 1}(\mathbf{r}) e^{-ikz} d^3\mathbf{r} \quad (4.10)$$

Multiplying both sides by $e^{ikz'} \sqrt{L/2\pi}$ and integrating over k from $k_0 - \pi/L$ to $k_0 + \pi/L$ gives

$$\hat{a}_\pm(z') + c \frac{\partial}{\partial z'} \hat{a}_\pm(z') = \rho \frac{L}{2\pi} \sum_{m=-F}^F \alpha_m^\pm \int_V u^*(x, y) \hat{\sigma}_{Fm, F' m \pm 1}(\mathbf{r}) \left\{ \int_{k_0 - \frac{\pi}{L}}^{k_0 + \frac{\pi}{L}} e^{ik(z'-z)} dk \right\} d^3\mathbf{r} \quad (4.11)$$

It is convenient to introduce operators that are slowly varying in time and space. For the field annihilation operators we separate the carrier component by writing

$$\hat{a}_{\pm}(z, t) = \tilde{a}_{\pm}(z) e^{-i(\omega_0 t - k_0 z)} \quad (4.12)$$

The continuous atomic optical coherences in steady state oscillate in time and space due to the excitation field. This is similar to the damped harmonic oscillator with a driving force; the steady state oscillator follows the oscillations of the driving force. The slowly varying atomic operators $\tilde{\sigma}$ are then given by

$$\begin{aligned} \hat{\sigma}_{F'm,Fn}(\mathbf{r}, t) &= \tilde{\sigma}_{F'm,Fn}(\mathbf{r}, t) e^{i(\omega_0 t - k_0 z)} \\ \hat{\sigma}_{Fm,F'n}(\mathbf{r}, t) &= \tilde{\sigma}_{Fm,F'n}(\mathbf{r}, t) e^{-i(\omega_0 t - k_0 z)} \\ \hat{\sigma}_{F'm,F'n}(\mathbf{r}, t) &= \tilde{\sigma}_{F'm,F'n}(\mathbf{r}, t) \\ \hat{\sigma}_{Fm,Fn}(\mathbf{r}, t) &= \tilde{\sigma}_{Fm,Fn}(\mathbf{r}, t) \end{aligned} \quad (4.13)$$

Substituting the slowly varying operators into Eq. (4.11) gives

$$\dot{\tilde{a}}_{\pm}(z') + c \frac{\partial}{\partial z'} \tilde{a}_{\pm}(z') = \rho L \sum_{m=-F}^F \alpha_m^{\pm} \int u^*(x, y) \tilde{\sigma}_{Fm, F'm \pm 1}(\mathbf{r}) \left\{ \frac{\sin(\pi(z' - z)/L)}{\pi(z' - z)} \right\} d^3 \mathbf{r} \quad (4.14)$$

The slowly varying atomic operator $\tilde{\sigma}_{Fm, F'm \pm 1}(\mathbf{r})$ is defined so that it only changes substantially over distances much larger than L , and we can substitute the $\{\cdot\}$ -factor by the Dirac delta function $\delta(z - z')$ with the final result

$$\dot{\tilde{a}}_{\pm}(z) + c \frac{\partial}{\partial z} \tilde{a}_{\pm}(z) = \rho L \sum_{m=-F}^F \alpha_m^{\pm} \int \int u^*(x, y) \tilde{\sigma}_{Fm, F'm \pm 1}(x, y, z) dx dy \quad (4.15)$$

The right hand side of this equation is the source term for the field propagation in the atomic sample. It can be rewritten as $\sqrt{2\pi L} \frac{c}{\hbar c} \int \int u^*(x, y) \hat{D}_{\pm}(\mathbf{r}, \Omega) dx dy$. Equation (4.15) is, with this identification, equivalent to the classical Maxwell equation for slowly varying amplitudes [42]. We use Eq. (4.15) in the same way as the Maxwell equation; that is, for propagation of quantum fields in a medium.

We continue by applying a Fourier transform in time to Eq. (4.15), which results in

$$i\Omega \tilde{a}_{\pm}(z, \Omega) + c \frac{\partial}{\partial z} \tilde{a}_{\pm}(z, \Omega) = \rho L \sum_{m=-F}^F \alpha_m^{\pm} \int \int u^*(x, y) \tilde{\sigma}_{Fm, F'm \pm 1}(x, y, z, \Omega) dx dy \quad (4.16)$$

We identify the operators in frequency domain by the argument Ω . We can compare the two terms on the left hand side, and we find that the second term is typically much larger than the first term. In general, only frequency components of the excitation field within the atomic linewidth are affected by the medium, and we are therefore only interested in frequencies $\Omega \lesssim \gamma$. The second term is on the order of $c\tilde{a}_{\pm}(z, \Omega)/L'$, where L' is the characteristic length over which the field amplitude changes. Later on we will require complete absorption of the excitation field, and therefore $L' \lesssim l$ (l is the diameter of the atomic cloud). Thus, we can neglect the first term in Eq. (4.16) if $\gamma^{-1} \gg l/c$, i.e. if light travels through the sample fast compared to the excited state lifetime. This requirement is easily fulfilled experimentally. Consequently, we have

$$\frac{\partial}{\partial z} \tilde{a}_{\pm}(z, \Omega) = \sum_{m=-F}^F \frac{\rho \alpha_m^{\pm} L}{c} \int \int u^*(x, y) \tilde{\sigma}_{Fm, F'm \pm 1}(x, y, z, \Omega) dx dy \quad (4.17)$$

In order to proceed we have to express the source term $\tilde{\sigma}_{Fm, F'm \pm 1}(x, y, z, \Omega)$ in terms of the excitation

field. We continue with the Heisenberg-Langevin equation for $\tilde{\sigma}_{Fm, F'm\pm 1}$ [79]

$$\begin{aligned} \dot{\tilde{\sigma}}_{Fm, F'm\pm 1}(\mathbf{r}) &= \frac{1}{i\hbar} [\hat{\sigma}_{Fm, F'm\pm 1}(\mathbf{r}), H] + \mathcal{L}_{Langevin} \\ \Rightarrow \dot{\tilde{\sigma}}_{Fm, F'm\pm 1}(\mathbf{r}) &= -u(x, y) (\alpha_m^\pm \tilde{\sigma}_{Fm, Fm}(\mathbf{r}) \tilde{a}_\pm(z) + \alpha_{m\pm 2}^\mp \tilde{\sigma}_{Fm, Fm\pm 2}(\mathbf{r}) \tilde{a}_\mp(z)) \\ &\quad + u(x, y) (\alpha_m^\pm \tilde{\sigma}_{F'm\pm 1, F'm\pm 1}(\mathbf{r}) \tilde{a}_\pm(z) + \alpha_{m\mp 1}^\mp \tilde{\sigma}_{F'm\mp 1, F'm\pm 1}(\mathbf{r}) \tilde{a}_\mp(z)) \\ &\quad - \frac{\gamma}{2} \tilde{\sigma}_{Fm, F'm\pm 1}(\mathbf{r}) + \mathcal{F}_{Fm, F'm\pm 1}(\mathbf{r}) \end{aligned} \quad (4.18)$$

Here we use that the carrier frequency of the field matches the atomic resonance frequency ($\omega_0 = \omega_a$). The Langevin terms, in the last line, describe the effect of spontaneous decay caused by the coupling to all the vacuum modes. The atomic coherence decays with the rate $\gamma/2$, where γ^{-1} is the excited state lifetime. The random decay process adds noise to the atomic operators represented by the Langevin force $\mathcal{F}_{Fm, F'm\pm 1}(\mathbf{r})$. The mean value of the Langevin forces is always zero, whereas the higher order moments contribute to the variance of the atomic operators. We calculate the second order moments (or correlation functions) of the Langevin forces in Appendix B. An alternative approach is to include the coupling to the vacuum modes explicitly in the Hamiltonian as in Ref. [9]. However, we find the Langevin approach to be simpler in the present calculation, which allows for a Zeeman degenerate ground state.

We now write the operators as $\tilde{a}(t) = \bar{a} + \delta\tilde{a}(t)$ and $\tilde{\sigma}_{Fm, F'n}(t) = \bar{\sigma}_{Fm, F'n} + \delta\tilde{\sigma}_{Fm, F'n}(t)$. We define \bar{a} and $\bar{\sigma}_{Fm, F'n}$ as the quantum mechanical mean values; $\bar{a} = \langle \tilde{a}(t) \rangle$, $\bar{\sigma}_{Fm, F'n} = \langle \tilde{\sigma}_{Fm, F'n}(t) \rangle$. We assume that the system is in steady state so that the mean values are constant in time. The excitation field has a nonzero mean amplitude only at the carrier frequency, and the rotating frame mean value \bar{a} is time independent and equal to this mean amplitude. We can simplify Eq. (4.18) if we linearize the operator products. Our linearization uses the following assumptions. The excitation field is assumed to be weak, whereby the excited state mean populations and coherences are much smaller than the mean ground state populations, i.e. $|\bar{\sigma}_{F'm, F'n}(\mathbf{r})| \ll \bar{\sigma}_{Fm, Fm}(\mathbf{r})$. In this chapter we calculate the fluctuations in the excited state in a perturbative approach assuming weak excitation. Fluctuations in the excited state are only present when the excitation field is on. The $\delta\tilde{\sigma}_{F'm, F'n}$ terms in Eq. (4.18) are therefore of higher order in the excitation field, and they can be neglected in this equation. We assume that the atomic ground state is unpolarized¹, which, together with the weak excitation, gives: $\bar{\sigma}_{Fm, F'n} = \delta_{m,n} (2F+1)^{-1}$. We also assume that the fields (or at least one of the polarizations) have a coherent amplitude much larger than the quantum fluctuations², i.e. $|\delta\tilde{a}_\pm(z)| \ll |\bar{a}_\pm(z)|$. Finally, we assume that atomic fluctuations in the ground state populations/coherences are much smaller than the mean populations in the following sense $|\delta\tilde{\sigma}_{Fm, F'n}(\mathbf{r})| \ll \frac{|\delta\tilde{a}_\pm|}{\bar{a}_\pm} (2F+1)^{-1}$; the validity of this assumption is based on the weak excitation and the large bandwidth of the field fluctuations as compared to the bandwidth of atomic ground state fluctuations. This is discussed further in Appendix C. These assumptions allow us to rewrite Eq. (4.18) as

$$\begin{aligned} \delta\tilde{\sigma}_{Fm, F'm\pm 1}(\mathbf{r}, \Omega) &= \frac{-u(x, y) \alpha_m^\pm (2F+1)^{-1} \delta\tilde{a}_\pm(z, \Omega) + \mathcal{F}_{Fm, F'm\pm 1}(\mathbf{r}, \Omega)}{(i\Omega + \gamma/2)} \\ \bar{\sigma}_{Fm, F'm\pm 1}(\mathbf{r}) &= \frac{-u(x, y) \alpha_m^\pm (2F+1)^{-1} \bar{a}_\pm(z)}{\gamma/2} \end{aligned} \quad (4.19)$$

We arrive at the first equation after a Fourier transform in time, and the second equation is the steady-state solution to Eq. (4.18) for the mean values. Substituting Eq. (4.19) into Eq. (4.17) gives the

¹This assumption is important in the following derivation. In chapter 8 we discuss to what extent the assumption is fulfilled in the experiment.

²The comparison of fluctuating operators on the left and mean values (c-numbers) on the right should not be taken too literally. It is merely a somewhat sloppy notation for the comparison of terms that enter in a subsequent calculations of spectral densities.

following equation for the quantum field as it propagates through the atomic medium

$$\begin{aligned}\delta\tilde{a}_{\pm}(z, \Omega) &= e^{-\Lambda(\Omega)z}\delta\tilde{a}_{\pm}(0, \Omega) + \int_0^z \Lambda(\Omega) e^{-\Lambda(\Omega)(z-z')} \mathcal{F}_1^{\pm}(z', \Omega) dz' \\ \bar{a}_{\pm}(z) &= e^{-\Lambda_0 z} \bar{a}_{\pm}(0) \\ \Lambda(\Omega) &= \frac{\omega_0 g^2 \rho (F+1)(2F+3)}{\varepsilon_0 c \hbar 3(i\Omega + \gamma/2)}, \quad \Lambda_0 = \Lambda(0) \\ \mathcal{F}_1^{\pm}(z, \Omega) &= \sum_{m=-F}^F \frac{2\rho L \alpha_m^{\pm}}{c\gamma\Lambda_0} \int \int u^*(x, y) \mathcal{F}_{Fm, F'm \pm 1}(\mathbf{r}, \Omega) dx dy\end{aligned}\tag{4.20}$$

This expression for the field as a function of position in the atomic sample is an essential part in the theory for mapping the state of light onto atoms. The interpretation of the result is as follows. The amplitude of the field operator is attenuated and phase-shifted according to the usual absorption and dispersion in the atomic medium. The attenuation/dispersion is set by $\Lambda(\Omega)$ and depends on the actual frequency component of the field through the parameter Ω . We know from the ordinary beamsplitter theory that the field transmitted through the beamsplitter is not only attenuated. Vacuum fluctuations are added from the other port of the beamsplitter in order to preserve the commutation relation for the transmitted field. The Langevin force \mathcal{F}_1^{\pm} acts as the vacuum noise that is added to the field as the atoms absorb the incoming field. We calculate correlation functions similar to $\langle \mathcal{F}_1^{\pm\dagger}(z', \Omega') \mathcal{F}_1^{\pm}(z, \Omega) \rangle$ in Appendix B, and with these results it is easy to verify that the mean value of the commutator $[\delta\tilde{a}_{\pm}(z, \Omega), \delta\tilde{a}_{\pm}^{\dagger}(z, \Omega')]$ is preserved for all z . The decoupling of the equations for \tilde{a}_+ and \tilde{a}_- is a result of the assumption about the unpolarized ground state.

4.2 Fluctuations in the collective spin \hat{F}'_z

We continue with the calculation of the noise properties of the z -component of the collective excited state atomic spin \hat{F}'_z . The observable \hat{F}'_z is proportional to the collective orientation of the excited state. \hat{F}'_z is a sum over the spin components of the individual atoms and is diagonal in the chosen atomic basis with

$$\hat{F}'_z = \rho \sum_{m=-F'}^{F'} m \int_V \tilde{\sigma}_{F'm, F'm}(\mathbf{r}) d^3\mathbf{r}\tag{4.21}$$

We apply a Fourier transform to the linearized Heisenberg-Langevin equation for $\tilde{\sigma}_{F'm, F'm}$ to get the result

$$\begin{aligned}i\Omega\delta\tilde{\sigma}_{F'm, F'm}(\mathbf{r}, \Omega) &= -u(x, y) \alpha_{m-1}^+ (\bar{\sigma}_{F'm, Fm-1}(\mathbf{r}) \delta\tilde{a}_+(z, \Omega) + \bar{a}_+(z) \delta\tilde{\sigma}_{F'm, Fm-1}(\mathbf{r}, \Omega)) \\ &\quad - u^*(x, y) \alpha_{m-1}^+ \left(\bar{\sigma}_{Fm-1, F'm}(\mathbf{r}) \delta\tilde{a}_+^{\dagger}(z, \Omega) + \bar{a}_+^*(z) \delta\tilde{\sigma}_{Fm-1, F'm}(\mathbf{r}, \Omega) \right) \\ &\quad - u(x, y) \alpha_{m+1}^- (\bar{\sigma}_{F'm, Fm+1}(\mathbf{r}) \delta\tilde{a}_-(z, \Omega) + \bar{a}_-(z) \delta\tilde{\sigma}_{F'm, Fm+1}(\mathbf{r}, \Omega)) \\ &\quad - u^*(x, y) \alpha_{m+1}^- \left(\bar{\sigma}_{Fm+1, F'm}(\mathbf{r}) \delta\tilde{a}_-^{\dagger}(z, \Omega) + \bar{a}_-^*(z) \delta\tilde{\sigma}_{Fm+1, F'm}(\mathbf{r}, \Omega) \right) \\ &\quad - \gamma\delta\tilde{\sigma}_{F'm, F'm}(\mathbf{r}, \Omega) + \mathcal{F}_{F'm, F'm}(\mathbf{r}, \Omega)\end{aligned}\tag{4.22}$$

The steady state result for the mean value is given by

$$\begin{aligned}\bar{\sigma}_{F'm, F'm}(\mathbf{r}) &= -\frac{1}{\gamma} \alpha_{m-1}^+ (u(x, y) \bar{\sigma}_{F'm, Fm-1}(\mathbf{r}) \bar{a}_+(z) + u^*(x, y) \bar{\sigma}_{Fm-1, F'm}(\mathbf{r}) \bar{a}_+^*(z)) \\ &\quad - \frac{1}{\gamma} \alpha_{m+1}^- (u(x, y) \bar{\sigma}_{F'm, Fm+1}(\mathbf{r}) \bar{a}_-(z) + u^*(x, y) \bar{\sigma}_{Fm+1, F'm}(\mathbf{r}) \bar{a}_-^*(z))\end{aligned}\tag{4.23}$$

Similar equations can be derived for $\delta\tilde{\sigma}_{F'm, F'm\pm 1}$, $\bar{\sigma}_{F'm, F'm\pm 1}$, and their Hermitian conjugate. Substituting these results into Eq. (4.22) and (4.23) and applying the same approximations as used in deriving Eq. (4.19) gives

$$\begin{aligned} \delta\tilde{\sigma}_{F'm, F'm}(\mathbf{r}, \Omega) = & \quad (4.24) \\ & \frac{1}{2F+1} \frac{4|u(x, y)|^2}{\gamma^2 + i2\gamma\Omega} \left\{ \alpha_{m-1}^{+2} [\bar{a}_+(z) \delta\tilde{a}_+^\dagger(z, \Omega) + \bar{a}_+^*(z) \delta\tilde{a}_+(z, \Omega)] \right. \\ & \quad \left. + \alpha_{m+1}^{-2} [\bar{a}_-(z) \delta\tilde{a}_-^\dagger(z, \Omega) + \bar{a}_-^*(z) \delta\tilde{a}_-(z, \Omega)] \right\} \\ & - \frac{2}{(\gamma + i\Omega)(\gamma + i2\Omega)} \left\{ \alpha_{m-1}^+ \left(u(x, y) \bar{a}_+(z) \mathcal{F}_{Fm-1, F'm}^\dagger(\mathbf{r}, \Omega) + u^*(x, y) \bar{a}_+^*(z) \mathcal{F}_{Fm-1, F'm}(\mathbf{r}, \Omega) \right) \right. \\ & \quad \left. + \alpha_{m+1}^- \left(u(x, y) \bar{a}_-(z) \mathcal{F}_{Fm+1, F'm}^\dagger(\mathbf{r}, \Omega) + u^*(x, y) \bar{a}_-^*(z) \mathcal{F}_{Fm+1, F'm}(\mathbf{r}, \Omega) \right) \right\} \\ & + \frac{1}{\gamma + i\Omega} \mathcal{F}_{F'm, F'm}(\mathbf{r}, \Omega) \end{aligned}$$

For the mean value we get

$$\bar{\sigma}_{F'm, F'm}(\mathbf{r}) = \frac{1}{2F+1} \frac{4|u(x, y)|^2}{\gamma^2} \left\{ \alpha_{m-1}^{+2} \bar{a}_+(z) \bar{a}_+^*(z) + \alpha_{m+1}^{-2} \bar{a}_-(z) \bar{a}_-^*(z) \right\} \quad (4.25)$$

We continue by summing Eq. (4.24) over m and integrating over the transverse coordinates x and y . We use the definitions of ζ , α_m^\pm , and $\Lambda(\Omega)$ from Eq. (4.1), (4.8), and (4.20) together with the fact that the mode function is normalized, Eq. (3.3), to obtain

$$\begin{aligned} \delta\hat{F}'_z(z, \Omega) = & \rho \int \int dx dy \sum_{m=-F'}^{F'} m \delta\tilde{\sigma}_{F'm, F'm}(\mathbf{r}, \Omega) \quad (4.26) \\ = & \frac{(F+2)c}{\gamma L} \Lambda(\Omega) \left\{ \bar{a}_+(z) \delta\tilde{a}_+^\dagger(z, \Omega) + \bar{a}_+^*(z) \delta\tilde{a}_+(z, \Omega) \right. \\ & \quad \left. - \bar{a}_-(z) \delta\tilde{a}_-^\dagger(z, \Omega) - \bar{a}_-^*(z) \delta\tilde{a}_-(z, \Omega) \right\} \\ - & \frac{2\rho}{(\gamma + i\Omega)(\gamma + i2\Omega)} \left\{ \bar{a}_+(z) \mathcal{F}_2^{+\dagger}(z, \Omega) + \bar{a}_+^*(z) \mathcal{F}_2^+(z, \Omega) \right. \\ & \quad \left. + \bar{a}_-(z) \mathcal{F}_2^{-\dagger}(z, \Omega) + \bar{a}_-^*(z) \mathcal{F}_2^-(z, \Omega) \right\} \\ + & \frac{\rho}{\gamma + i\Omega} \mathcal{F}_3(z, \Omega) \end{aligned}$$

The new Langevin forces are defined as

$$\begin{aligned} \mathcal{F}_2^\pm(z, \Omega) = & \int \int dx dy \sum_{m=-F'}^{F'} m u^*(x, y) \alpha_{m\mp 1}^\pm \mathcal{F}_{Fm\mp 1, F'm}(\mathbf{r}, \Omega) \quad (4.27) \\ \mathcal{F}_3(z, \Omega) = & \int \int dx dy \sum_{m=-F'}^{F'} m \mathcal{F}_{F'm, F'm}(\mathbf{r}, \Omega) \end{aligned}$$

We should now integrate $\delta\hat{F}'_z(z, \Omega)$ over z from 0 to l in order to obtain the z -component of the collective excited state spin. We will assume complete absorption³ of the quantum field, so that the upper limit can

³We can, of course, not have complete absorption of all the frequency components of the quantum pump. We require complete absorption of the frequency components within the frequency, Ω , at which we later on detect the atomic spin noise. In the experiments in chapter 8 we have $\Omega/\gamma = 0.4$.

be taken at ∞ instead of l . After a substantial absorption, the fields consist only of vacuum fluctuations, and they do not give any contribution to the excited state spin. Note that if we do not require complete absorption, then a large fraction of the quantum field will leave the atoms, and the correlations initially present in the quantum field will be distributed over the atoms and the transmitted quantum field. We will have correlations between atoms and photons, but not optimum atomic correlations.

The most difficult part of the integration over z is the terms like $\bar{a}_+(z) \delta \tilde{a}_+^\dagger(z, \Omega)$. We apply the results in Eq. (4.20) to write

$$\begin{aligned} \int_0^\infty \bar{a}_\pm^*(z) \delta \tilde{a}_\pm(z, \Omega) dz &= \int_0^\infty e^{-\Lambda_0 z} \bar{a}_\pm^*(0) \left[e^{-\Lambda(\Omega)z} \delta \tilde{a}_\pm(0, \Omega) \right. \\ &\quad \left. + \int_0^z \Lambda(\Omega) e^{-\Lambda(\Omega)(z-z')} \mathcal{F}_1^\pm(z', \Omega) dz' \right] dz \\ &= \frac{1}{\Lambda_0 + \Lambda(\Omega)} [\bar{a}_\pm^{in*} \delta \tilde{a}_\pm^{in}(\Omega) + \Lambda(\Omega) \bar{a}_\pm^{in*} \mathcal{F}_a^\pm(\Omega)] \\ \mathcal{F}_a^\pm(\Omega) &= \int_0^\infty e^{-\Lambda_0 z} \mathcal{F}_1^\pm(z, \Omega) dz \end{aligned} \quad (4.28)$$

We emphasize that $\tilde{a}(0)$ is the field amplitude right before the atomic cloud by writing it as \tilde{a}^{in} . The trick in solving the double integral is to change the order [9], i.e. $\int_0^\infty dz \int_0^z dz' \rightarrow \int_0^\infty dz' \int_{z'}^\infty dz$. Combining Eq. (4.26) and (4.28) and linearizing the operator products in the definition of the Stokes spin components, Eq. (3.15), gives

$$\begin{aligned} \delta \hat{F}'_z(\Omega) &= \int_0^\infty \delta \hat{F}'_z(z, \Omega) dz \\ &= \frac{(F+2)}{\gamma + i\Omega} \delta \hat{\mathcal{S}}_z^{in}(\Omega) \\ &\quad + \frac{\Lambda^2(\Omega)}{\Lambda_0 + \Lambda(\Omega)} \frac{(F+2)c}{\gamma L} \{ \bar{a}_+^{in} \mathcal{F}_a^{+\dagger}(\Omega) + \bar{a}_+^{in*} \mathcal{F}_a^+(\Omega) - \bar{a}_-^{in} \mathcal{F}_a^{-\dagger}(\Omega) - \bar{a}_-^{in*} \mathcal{F}_a^-(\Omega) \} \\ &\quad - \frac{2}{(\gamma + i\Omega)(\gamma + i2\Omega)} \{ \bar{a}_+^{in} \mathcal{F}_b^{+\dagger}(\Omega) + \bar{a}_+^{in*} \mathcal{F}_b^+(\Omega) + \bar{a}_-^{in} \mathcal{F}_b^{-\dagger}(\Omega) + \bar{a}_-^{in*} \mathcal{F}_b^-(\Omega) \} \\ &\quad + \frac{1}{\gamma + i\Omega} \mathcal{F}_c(\Omega) \end{aligned} \quad (4.29)$$

The new collective Langevin forces are defined as

$$\begin{aligned} \mathcal{F}_b^\pm(\Omega) &= \rho \int_0^\infty e^{-\Lambda_0 z} \mathcal{F}_2^\pm(z, \Omega) dz \\ \mathcal{F}_c(\Omega) &= \rho \int_0^\infty \mathcal{F}_3(z, \Omega) dz \end{aligned} \quad (4.30)$$

We see from Eq. (4.29) that a part of the fluctuations in \hat{F}'_z is set by the quantum fluctuations in the excitation field (the $\hat{\mathcal{S}}_z^{in}$ -term). All the Langevin force terms represent the noise entering through the coupling of the atoms to the vacuum modes. This vacuum noise limits the amount of noise reduction or squeezing in \hat{F}'_z that we can obtain with a perfectly polarization squeezed excitation field.

We need the correlation functions for the Langevin forces in Eq. (4.29) before we can finalize the calculation of the spectral density of \hat{F}'_z fluctuations. The derivation of the correlation functions is pure mathematics, and it is given in Appendix B. With the results from Appendix B, Eq. (B.5), and Eq.

(4.29), we arrive at the final expression for the spectral density of fluctuations

$$\begin{aligned} \left(\hat{F}'_z\right)_\Omega^2 &= \frac{1}{2\pi} \int_{-\infty}^{\infty} \langle \delta\hat{F}'_z(\Omega') \delta\hat{F}'_z(\Omega) \rangle d\Omega' \\ &= \frac{(F+2)^2}{\gamma^2 + \Omega^2} \left(\hat{S}_z^{in}\right)_\Omega^2 + \gamma N' \left(\frac{(F+2)(4F+5)}{10(\gamma^2 + \Omega^2)} + \frac{9F(F+2)\gamma^2}{20(\gamma^2 + \Omega^2)(\gamma^2 + 4\Omega^2)} \right) \end{aligned} \quad (4.31)$$

We see that the fluctuations in \hat{F}'_z have two contributions; the first term comes from the quantum properties of the excitation field, and the last term is the noise from the coupling to the vacuum modes. The last term is proportional to the number of atoms, N' , in the excited state F' . We can write N' in terms of the total photon flux $(\Phi_+ + \Phi_-)$ from the coherent state component as⁴ $N' = (\Phi_+ + \Phi_-)/\gamma = (\bar{a}_+^{in*}\bar{a}_+^{in} + \bar{a}_-^{in*}\bar{a}_-^{in})c/(L\gamma)$.

To quantify the efficiency of the light-atom mapping, we introduce the mapping efficiency of quantum correlations, η_z , by comparing the noise reduction (squeezing) of the excitation light to the resulting atomic noise reduction. η_z is defined through the relation

$$\left(\hat{F}'_z\right)_\Omega^2 = \frac{1}{\eta_z + 1} (1 + \eta_z R_z(\Omega)) \left(\hat{F}'_z\right)_{\Omega,coh}^2 \quad (4.32)$$

where $R_z(\Omega) = 4(\hat{S}_z)_\Omega^2/(\Phi_+ + \Phi_-)$ is the degree of squeezing (or antisqueezing) in the excitation field, see Eq. (3.17), and $(\hat{F}'_z)_{\Omega,coh}^2$ is the spectral density with a coherent state excitation ($R_z(\Omega) = 1$).

We can compare the mapping of light on atoms with the "mapping" of squeezed light from one side of a beamsplitter to the other side. If we define $\eta_{BS} = T/R$ as the ratio between the beamsplitter transmissivity and reflectivity, we find the following relation for the Stokes parameter \hat{S}_z^{ab} after the beamsplitter

$$\left(\hat{S}_z^{ab}\right)_\Omega^2 = \frac{1}{\eta_{BS} + 1} (1 + \eta_{BS} R_z(\Omega)) \left(\hat{S}_z^{ab}\right)_{\Omega,coh}^2 \quad (4.33)$$

Again, $R_z(\Omega)$ is the degree of squeezing before the beamsplitter, and $(\hat{S}_z^{ab})_{\Omega,coh}^2$ is the fluctuations after the beamsplitter for a coherent state. We see that we have no transmission of squeezed light for $\eta_{BS} = 0$, and we are left with the coherent state (vacuum) fluctuations, which come from the empty input port of the beamsplitter. When η_{BS} approaches infinity, we have perfect transmission of the squeezed light, and we do not add any vacuum fluctuations. The mapping efficiency η_z plays the same role in light-atom mapping as the η_{BS} parameter in light-light mapping through a beamsplitter.

η_z can easily be derived from Eq. (4.31). In Fig. 4.2a we plot η_z as a function of F for $\Omega/\gamma = 0.4$, (solid line). The chosen ratio for Ω/γ is close to the ratio we use in the measurements in chapter 8. The maximum value for η_z is at $F = 0$, where $\eta_z = 1$. In the beamsplitter analogy this corresponds to a 50/50 beamsplitter, where half of the noise in the transmitted field comes from the incident squeezed field and the other half is the vacuum fluctuations from the empty port. In Fig. 4.2b we plot the relative noise reduction that can be achieved with a perfectly squeezed excitation field, $\eta_z/(\eta_z + 1)$, as a function of F for $\Omega/\gamma = 0.4$, (solid line). The relative noise reduction is increased at larger Ω/γ , but the absolute amount of noise is small at $\Omega/\gamma \gtrsim 1$.

If we integrate the spectral density over all frequencies, we get the variance

$$\left(\Delta\hat{F}'_z\right)^2 = \int_{-\infty}^{\infty} \left(\hat{F}'_z\right)_\Omega^2 \frac{d\Omega}{2\pi} \quad (4.34)$$

⁴This expression is trivial; the number of atoms in the excited state is, for complete absorption, equal to the photon flux divided by the excited state decay rate. The same result is obtained when Eq. (4.25) is summed over all m , multiplied by ρ and integrated over the atomic volume.

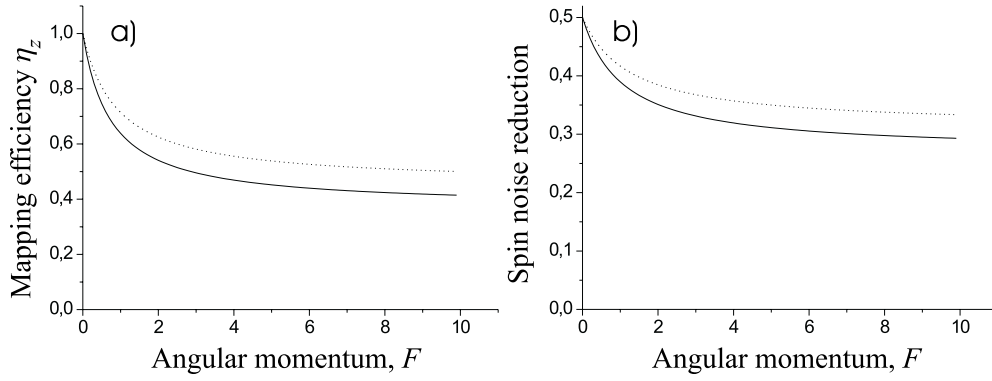


Figure 4.2: a) Theoretical efficiency for mapping quantum correlations from light onto the atomic spin \hat{F}'_z . b) Noise reduction in \hat{F}'_z for perfectly squeezed \hat{S}_z relative to the \hat{F}'_z noise for coherent excitation. a+b) Solid line: spectral density at $\Omega/\gamma = 0.4$. Dotted line: variance $(\Delta\hat{F}'_z)^2$.

We find from Eq. (4.31) and by assuming that the bandwidth of squeezing is much larger than γ ($R_z = R_z(\Omega)$)

$$(\Delta\hat{F}'_z)^2 = \left[\frac{(F+2)^2}{8} R_z + \frac{(F+2)(11F+10)}{40} \right] \frac{\Phi_+ + \Phi_-}{\gamma} \quad (4.35)$$

Using the definition of η_z on the variance gives $\eta_z = 5(F+2)/(11F+10)$. This expressions for η_z as well as the relative noise reduction, $\eta_z/(\eta_z+1)$, are plotted in Fig. 4.2 as dotted lines.

Finally, we give the mean value of collective spin component \hat{F}'_z , which is derived from Eq. (4.25) and (4.21)

$$\langle \hat{F}'_z \rangle = \frac{F+2}{2} \frac{\Phi_+ - \Phi_-}{\gamma} \quad (4.36)$$

4.2.1 Direct calculation of $(\Delta\hat{F}'_z)^2$ for uncorrelated atoms

Equation (4.35) gives the variance of \hat{F}'_z for coherent light excitation when $R_z = 1$. We can test the consistency of the theory by calculating this variance directly without using linearized fluctuations, Langevin correlation functions, complicated spectral densities etc.

We first note that $(\Delta\hat{F}'_z)^2 = \langle (\delta\hat{F}'_z)^2 \rangle$ where $\delta\hat{F}'_z = \hat{F}'_z - \langle \hat{F}'_z \rangle$. The collective fluctuating operator can be written as a sum over all atoms

$$\delta\hat{F}'_z = \sum_i \sum_{m=-F'}^{F'} m \delta\hat{\sigma}_{F'm, F'm}^i \quad (4.37)$$

$\delta\hat{\sigma}_{F'm, F'm}^i = \hat{\sigma}_{F'm, F'm}^i - \langle \hat{\sigma}_{F'm, F'm}^i \rangle$ is the single atom operator for atom number i . We find for the

variance

$$\begin{aligned}
(\Delta \hat{F}'_z)^2 &= \langle (\delta \hat{F}'_z)^2 \rangle = \sum_{i,j} \sum_{m,n} mn \langle \delta \hat{\sigma}'_{F'm,F'm} \delta \hat{\sigma}'_{F'n,F'n} \rangle \\
&= \sum_i \sum_{m,n} mn \langle \delta \hat{\sigma}'_{F'm,F'm} \delta \hat{\sigma}'_{F'n,F'n} \rangle \\
&= \sum_i \sum_{m=-F'}^{F'} m^2 \langle \hat{\sigma}'_{F'm,F'm} \rangle - \sum_i \sum_{m,n} mn \langle \hat{\sigma}'_{F'm,F'm} \rangle \langle \hat{\sigma}'_{F'n,F'n} \rangle
\end{aligned} \tag{4.38}$$

We assumed here that the atoms are uncorrelated, that is, $\langle \delta \hat{\sigma}'_{F'm,F'm} \delta \hat{\sigma}'_{F'n,F'n} \rangle = 0$ for $i \neq j$. The two terms in the last line are most easily calculated by converting the sum over i into an integral over space. We can then use the mean value of the continuous atomic operator $\bar{\sigma}'_{F'm,F'm}(\mathbf{r})$ in Eq. (4.25). Note that Eq. (4.25) is derived without any assumptions about linearized fluctuations or Langevin forces. Equation (4.25) just gives the average population in the excited state from standard perturbation theory with a weak excitation field. We find for the first term in Eq. (4.38)

$$\begin{aligned}
\sum_i \sum_{m=-F'}^{F'} m^2 \langle \hat{\sigma}'_{F'm,F'm} \rangle &= \sum_{m=-F'}^{F'} m^2 \int_V \rho \bar{\sigma}'_{F'm,F'm}(\mathbf{r}) d^3 \mathbf{r} \\
&= \frac{(F+2)(4F+5)}{10} \frac{\Phi_+ + \Phi_-}{\gamma}
\end{aligned} \tag{4.39}$$

In the same way we derive for the second term in Eq. (4.38)

$$\begin{aligned}
\sum_i \sum_{m,n} mn \langle \hat{\sigma}'_{F'm,F'm} \rangle \langle \hat{\sigma}'_{F'n,F'n} \rangle &= \sum_{m,n} mn \int \rho \bar{\sigma}'_{F'm,F'm}(\mathbf{r}) \bar{\sigma}'_{F'n,F'n}(\mathbf{r}) d^3 \mathbf{r} \\
&= \frac{(F+2)^2}{8} (s_{0,+} - s_{0,-}) \frac{\Phi_+ - \Phi_-}{\gamma}
\end{aligned} \tag{4.40}$$

We have introduced the resonant saturation parameters (see chapter 2) for the two polarizations of the pump field, $s_{0,\pm} = \Phi_{\pm} \sigma_0 / (\gamma \pi w^2)$. The resonant absorption cross section σ_0 for the unpolarized ground state is given in Eq. (2.1). $2w$ is the diameter of the excitation field. The general assumption about weak excitation (i.e. $s_{0,\pm} \ll 1$) allows us to discard the second term in Eq. (4.38), and we have

$$(\Delta \hat{F}'_z)^2 = \frac{(F+2)(4F+5)}{10} \frac{\Phi_+ + \Phi_-}{\gamma} \tag{4.41}$$

This is identical to the expression in Eq. (4.35) for excitation with coherent light ($R_z = 1$). The identical expressions for the \hat{F}'_z variance support our general assumption that coherent light excitation produces uncorrelated atoms in the excited state. A reduction in variance below the expression in Eq. (4.41) requires multi-atom correlations. Excitation with polarization squeezed light ($R_z < 1$) results in multi-atom correlations according to Eq. (4.35).

4.3 Fluctuations in $\hat{F}'_x - \hat{F}'_y$ and $\hat{F}'_x \hat{F}'_y + \hat{F}'_y \hat{F}'_x$

We continue with a calculation of the quantum noise in the two collective observables $\hat{F}'_x - \hat{F}'_y$ and $\hat{F}'_x \hat{F}'_y + \hat{F}'_y \hat{F}'_x$. The calculation shows that their quantum noise is set partly by the quantum noise in the Stokes spin components \hat{S}_x and \hat{S}_y of the excitation field. $\hat{F}'_x - \hat{F}'_y$ is proportional to the difference between the excited state collective alignment along the x -axis and along the y -axis. $\hat{F}'_x \hat{F}'_y + \hat{F}'_y \hat{F}'_x$ is

identical to $\hat{F}'_x - \hat{F}'_y$, except that the alignment difference is measured along the x' and y' axes obtained by rotating the x and y axes through 45° around the z -axis. We will go through the calculations for $\hat{F}'_x - \hat{F}'_y$ and apply a geometrical rotation to the final result, whereby we obtain the $\hat{F}'_x \hat{F}'_y + \hat{F}'_y \hat{F}'_x$ result.

The single atom operators $(\hat{F}'_x - \hat{F}'_y)_j$ and $(\hat{F}'_x \hat{F}'_y + \hat{F}'_y \hat{F}'_x)_j$ for atom number j can be expressed through the angular momentum step-up and step-down operators $(\hat{F}'_{\pm,j} = \hat{F}'_{x,j} \pm i\hat{F}'_{y,j})$

$$(\hat{F}'_x - \hat{F}'_y)_j \pm i(\hat{F}'_x \hat{F}'_y + \hat{F}'_y \hat{F}'_x)_j = (\hat{F}'_{\pm,j})^2 \quad (4.42)$$

We use the standard properties of the step-up/step-down operators to arrive at the following expansion on our atomic basis

$$\begin{aligned} (\hat{F}'_x - \hat{F}'_y)_j &= \frac{1}{2} \sum_{m=-F'}^{F'} \sqrt{F'(F'+1) - m(m+1)} \sqrt{F'(F'+1) - (m+1)(m+2)} \\ &\times \left(|F'm+2\rangle_{j,j} \langle F'm| + |F'm\rangle_{j,j} \langle F'm+2| \right) \end{aligned} \quad (4.43)$$

The collective operator $\hat{F}'_x - \hat{F}'_y$ can now be written as

$$\begin{aligned} \hat{F}'_x - \hat{F}'_y &= \frac{1}{2} \sum_{m=-F'}^{F'} \sqrt{F'(F'+1) - m(m+1)} \sqrt{F'(F'+1) - (m+1)(m+2)} \\ &\times \rho \int_V (\hat{\sigma}_{F'm+2,F'm}(\mathbf{r}) + \hat{\sigma}_{F'm,F'm+2}(\mathbf{r})) d^3\mathbf{r} \end{aligned} \quad (4.44)$$

Note that the collective operator $\hat{F}'_x - \hat{F}'_y$ does not involve products of collective operators although the notation might indicate that. As seen in Eq. (4.44), $\hat{F}'_x - \hat{F}'_y$ is just a sum over single atom operators.

The starting point is again the Heisenberg-Langevin equation

$$\dot{\hat{\sigma}}_{F'm+2,F'm}(\mathbf{r}) = \frac{1}{i\hbar} [\hat{\sigma}_{F'm+2,F'm}(\mathbf{r}), H] + \mathcal{L}_{Langevin} \quad (4.45)$$

After the usual linearization procedure and a Fourier transform in time we find

$$\begin{aligned} i\Omega \delta \tilde{\sigma}_{F'm+2,F'm}(\mathbf{r}, \Omega) &= \\ &- \alpha_{m-1}^+ u(x, y) (\bar{\sigma}_{F'm+2,F'm-1}(\mathbf{r}) \delta \tilde{a}_+(z, \Omega) + \bar{a}_+(z) \delta \tilde{\sigma}_{F'm+2,F'm-1}(\mathbf{r}, \Omega)) \\ &- \alpha_{m+1}^+ u^*(x, y) (\bar{\sigma}_{F'm+1,F'm}(\mathbf{r}) \delta \tilde{a}_+^\dagger(z, \Omega) + \bar{a}_+^*(z) \delta \tilde{\sigma}_{F'm+1,F'm}(\mathbf{r}, \Omega)) \\ &- \alpha_{m+1}^- u(x, y) (\bar{\sigma}_{F'm+2,F'm+1}(\mathbf{r}) \delta \tilde{a}_-(z, \Omega) + \bar{a}_-(z) \delta \tilde{\sigma}_{F'm+2,F'm+1}(\mathbf{r}, \Omega)) \\ &- \alpha_{m+3}^- u^*(x, y) (\bar{\sigma}_{F'm+3,F'm}(\mathbf{r}) \delta \tilde{a}_-^\dagger(z, \Omega) + \bar{a}_-^*(z) \delta \tilde{\sigma}_{F'm+3,F'm}(\mathbf{r}, \Omega)) \\ &- \gamma \delta \tilde{\sigma}_{F'm+2,F'm}(\mathbf{r}, \Omega) + \mathcal{F}_{F'm+2,F'm}(\mathbf{r}, \Omega) \end{aligned} \quad (4.46)$$

We derive similar expressions for the mean values and fluctuations of the optical coherences which enters into Eq. (4.46). Substituting these results into Eq. (4.46) and applying the same approximations as used in deriving Eq. (4.19) gives us

$$\begin{aligned} \delta \tilde{\sigma}_{F'm+2,F'm}(\mathbf{r}, \Omega) &= \frac{4}{\gamma^2 + i2\gamma\Omega} \frac{|u(x, y)|^2}{2F+1} \alpha_{m+1}^+ \alpha_{m+1}^- [\bar{a}_-(z) \delta a_+^\dagger(z, \Omega) + \bar{a}_+^*(z) \delta a_-(z, \Omega)] \\ &- \frac{2}{(\gamma + i\Omega)(\gamma + i2\Omega)} [u^*(x, y) (\alpha_{m+1}^+ \bar{a}_+^*(z) \mathcal{F}_{F'm+1,F'm}(\mathbf{r}, \Omega) + \alpha_{m+3}^- \bar{a}_-^*(z) \mathcal{F}_{F'm+3,F'm}(\mathbf{r}, \Omega)) \\ &\quad + u(x, y) (\alpha_{m-1}^+ \bar{a}_+(z) \mathcal{F}_{F'm+2,F'm-1}(\mathbf{r}, \Omega) + \alpha_{m+1}^- \bar{a}_-(z) \mathcal{F}_{F'm+2,F'm+1}(\mathbf{r}, \Omega))] \\ &+ \frac{1}{\gamma + i\Omega} \mathcal{F}_{F'm+2,F'm}(\mathbf{r}, \Omega) \end{aligned} \quad (4.47)$$

Substituting Eq. (4.47) and its Hermitian conjugate into Eq. (4.44) gives, after some algebra which is very similar to the derivation of Eq. (4.29), the following

$$\begin{aligned}
\delta \left(\hat{F}'_x - \hat{F}'_y \right) (\Omega) = & \\
& - \frac{(F+2)(2F+5)}{5(\gamma+i\Omega)} \delta \hat{S}_x^{in} (\Omega) \\
& - \frac{\Lambda^2(\Omega)}{\Lambda_0 + \Lambda(\Omega)} \frac{(F+2)(2F+5)c}{5\gamma L} \left\{ \bar{a}_-^{in} \mathcal{F}_a^{+\dagger}(\Omega) + \bar{a}_-^{in*} \mathcal{F}_a^+(\Omega) + \bar{a}_+^{in} \mathcal{F}_a^{-\dagger}(\Omega) + \bar{a}_+^{in*} \mathcal{F}_a^-(\Omega) \right\} \\
& - \frac{2}{(\gamma+i\Omega)(\gamma+i2\Omega)} \left\{ \bar{a}_+^{in} \mathcal{F}_d^{+\dagger}(\Omega) + \bar{a}_+^{in*} \mathcal{F}_d^+(\Omega) + \bar{a}_-^{in} \mathcal{F}_d^{-\dagger}(\Omega) + \bar{a}_-^{in*} \mathcal{F}_d^-(\Omega) \right\} \\
& + \frac{1}{\gamma+i\Omega} \mathcal{F}_e(\Omega)
\end{aligned} \tag{4.48}$$

The Langevin force \mathcal{F}_a^\pm is defined in Eq. (4.28) and \mathcal{F}_d^\pm and \mathcal{F}_e are given in Appendix B, Eq. (B.8). We calculate the spectral density of quantum fluctuations from Eq. (4.48) and (B.9)

$$\begin{aligned}
\left(\hat{F}'_x - \hat{F}'_y \right)_\Omega^2 = & \frac{(F+2)^2(2F+5)^2}{25(\gamma^2+\Omega^2)} \left(\hat{S}_x^{in} \right)_\Omega^2 + \gamma N' \frac{(F+2)(2F+5)(8F^2+10F+7)}{70(\gamma^2+\Omega^2)} \\
& + \gamma N' \frac{3F(F+2)(2F+5)(66F+37)\gamma^2}{700(\gamma^2+\Omega^2)(\gamma^2+4\Omega^2)}
\end{aligned} \tag{4.49}$$

After a geometrical rotation through 45° around the z -axis, we get

$$\begin{aligned}
\left(\hat{F}'_x \hat{F}'_y + \hat{F}'_y \hat{F}'_x \right)_\Omega^2 = & \frac{(F+2)^2(2F+5)^2}{25(\gamma^2+\Omega^2)} \left(\hat{S}_y^{in} \right)_\Omega^2 + \gamma N' \frac{(F+2)(2F+5)(8F^2+10F+7)}{70(\gamma^2+\Omega^2)} \\
& + \gamma N' \frac{3F(F+2)(2F+5)(66F+37)\gamma^2}{700(\gamma^2+\Omega^2)(\gamma^2+4\Omega^2)}
\end{aligned} \tag{4.50}$$

We observe that the expression for the fluctuations in $\hat{F}'_x \hat{F}'_y + \hat{F}'_y \hat{F}'_x$ has the same structure as the \hat{F}'_z result in Eq. (4.31). The main difference is in the Stokes parameter that contributes to the atomic noise; the $\hat{F}'_x \hat{F}'_y + \hat{F}'_y \hat{F}'_x$ fluctuations are set partly by the quantum noise in \hat{S}_y . We will consider the quantum noise in $\hat{F}'_x \hat{F}'_y + \hat{F}'_y \hat{F}'_x$ to be "spin noise" in the same way as the \hat{F}'_z noise, although $\hat{F}'_x \hat{F}'_y + \hat{F}'_y \hat{F}'_x$ is a more complicated combination of spin components. The efficiency of the quantum state mapping is again quantified by the mapping efficiency η_y defined by the relation

$$\left(\hat{F}'_x \hat{F}'_y + \hat{F}'_y \hat{F}'_x \right)_\Omega^2 = \frac{1}{\eta_y + 1} (1 + \eta_y R_y(\Omega)) \left(\hat{F}'_x \hat{F}'_y + \hat{F}'_y \hat{F}'_x \right)_{\Omega, coh}^2 \tag{4.51}$$

We define $R_y(\Omega) = 4(\hat{S}_y)_\Omega^2 / (\Phi_+ + \Phi_-)$. We derive η_y from Eq. (4.50) and (4.51) and plot it in Fig. 4.3a (solid line) as a function of F for the ratio $\Omega/\gamma = 0.4$. The maximum relative noise reduction in $\hat{F}'_x \hat{F}'_y + \hat{F}'_y \hat{F}'_x$ is given by $\eta_y/(\eta_y + 1)$ for perfect squeezing in \hat{S}_y , and we plot this result versus F for $\Omega/\gamma = 0.4$ in Fig. 4.3b (solid line).

We get the full variance by integrating the spectral density over Ω . The result for constant $R_y(\Omega)$ within the atomic bandwidth γ is

$$\begin{aligned}
\left(\Delta(\hat{F}'_x \hat{F}'_y + \hat{F}'_y \hat{F}'_x) \right)^2 = & \\
& \left[\frac{(F+2)^2(2F+5)^2}{200} R_y + \frac{(F+2)(2F+5)(146F^2+137F+70)}{1400} \right] \frac{\Phi_+ + \Phi_-}{\gamma}
\end{aligned} \tag{4.52}$$

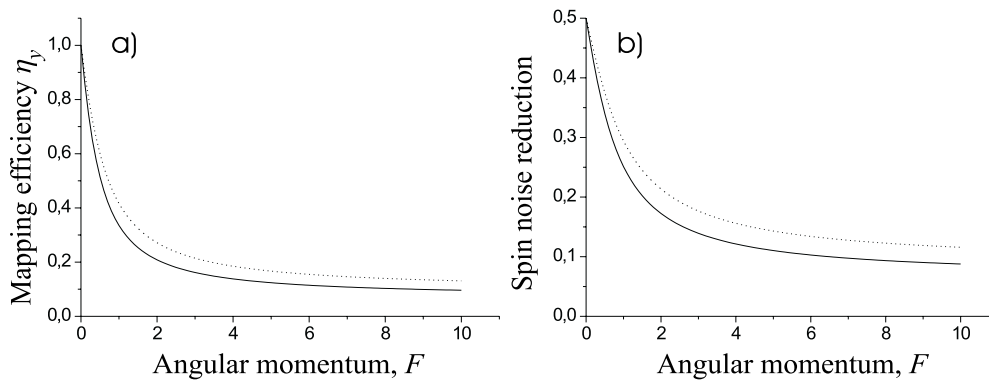


Figure 4.3: a) Theoretical efficiency for mapping quantum correlations from light onto the collective atomic variable $\hat{F}'_x\hat{F}'_y + \hat{F}'_y\hat{F}'_x$. b) Noise reduction in $\hat{F}'_x\hat{F}'_y + \hat{F}'_y\hat{F}'_x$ for perfectly squeezed \hat{S}_y relative to the $\hat{F}'_x\hat{F}'_y + \hat{F}'_y\hat{F}'_x$ noise for coherent excitation. a+b) Solid line: spectral density at $\Omega/\gamma = 0.4$. Dotted line: variance $(\Delta(\hat{F}'_x\hat{F}'_y + \hat{F}'_y\hat{F}'_x))^2$.

The steady state solution to Eq. (4.45) gives the mean values

$$\begin{aligned} \langle \hat{F}'_x{}^2 - \hat{F}'_y{}^2 \rangle &= \frac{(F+2)(2F+5)}{5\gamma} \bar{S}_x^{in} \\ \langle \hat{F}'_x\hat{F}'_y + \hat{F}'_y\hat{F}'_x \rangle &= \frac{(F+2)(2F+5)}{5\gamma} \bar{S}_y^{in} \end{aligned} \quad (4.53)$$

In general we observe a reduction in the mapping efficiency and in the maximum noise reduction when the ground state angular momentum is increased; this holds for both \hat{F}'_z and $\hat{F}'_x\hat{F}'_y + \hat{F}'_y\hat{F}'_x$, (Fig. 4.2 and 4.3). We also see that the best noise reduction is obtained in \hat{F}'_z . In chapter 8 we employ a sample of Cs atoms with $F = 4$ for our spin squeezing experiment. For $F = 4$, $\Omega/\gamma = 0.4$, and perfectly squeezed \hat{S}_z (\hat{S}_y) we expect according to Fig. 4.2b (4.3b) about 32% (12%) noise reduction in \hat{F}'_z ($\hat{F}'_x\hat{F}'_y + \hat{F}'_y\hat{F}'_x$).

The variance of $\hat{F}'_x\hat{F}'_y + \hat{F}'_y\hat{F}'_x$ for uncorrelated atoms can easily be derived from a direct calculation similar to the $(\Delta\hat{F}'_z)^2$ calculation in section 4.2.1. The conclusion for $\hat{F}'_x\hat{F}'_y + \hat{F}'_y\hat{F}'_x$ is similar to the conclusion for \hat{F}'_z ; the variance in Eq. (4.52) for coherent excitation ($R_y = 1$) equals the variance for uncorrelated atoms. This again supports the validity of the linearized operator approach, and it shows that we can use the atomic spin noise observed with coherent light excitation as the standard quantum limit, i.e. the quantum noise limit for uncorrelated particles.

In chapter 5 we investigate the atom-light mapping further in the context of spin squeezed states. In that chapter we also give simple explanations of why the squeezed light excitation results in reduced atomic fluctuations. In addition, the limitations in the mapping efficiencies are explained in qualitative terms in chapter 5.

4.4 Comments on the applied linearization approach

Our solutions to the Heisenberg-Langevin equations are based on a linearization of operator products. Similar linearizations can be found in e.g. Ref. [9, 80, 81, 82] as mentioned earlier. A different and often used approach is to transform the Heisenberg-Langevin equations for operators into c -number equations [83, 84]. For consistency, a certain order of the operators is chosen in this "c-number approach". Together with the transformation into c -numbers, the Langevin correlation functions are modified to make the

operator equations and the c -number equations equivalent for calculations of second order moments within the chosen order. The c -number equations are then solved by linearization and a Fourier transform; this part is similar to our calculations. Finally, the c -number solutions are used to calculate the variance or spectral density of the operators of interest. However, for consistency the variance of these operators (i.e. the square of the operators) must be written in the chosen operator order. Some commutators may enter into the expression for the variance because of this ordering.

We have also carried out our calculations within this "c-number approach" for the $F' = 1$ case. The results obtained with the "c-number approach" are identical to the results presented in the previous sections. We find that the modifications of the Langevin correlation functions cancel out the commutators added in the final normally ordered spectral density expressions.

Chapter 5

Spin squeezed states and entanglement

It is possible to introduce squeezed states in collective quantum systems composed of spin subsystems in a way very similar to the squeezed states of light. In general, the squeezed states are characterized by a redistribution of quantum fluctuations between two conjugate variables. In addition, the squeezed light belongs to the class of nonclassical states of light. This nonclassicality is caused by the presence of quantum correlations in the squeezed light. It is possible to give a definition of spin squeezed states that incorporates both these characteristics; reduced quantum fluctuations in one collective spin component and quantum correlations (entanglement) between the subsystems, which constitute the collective spin state (see Fig. 5.1). In this chapter we discuss some of the properties of the spin squeezed states.

We introduce a spin- s system, which is described by the operator $\hat{\mathbf{s}} = (\hat{s}_x, \hat{s}_y, \hat{s}_z)$ and the commutation relation $[\hat{s}_y, \hat{s}_z] = i\hat{s}_x$ together with similar relations obtained by cyclic permutations. The Heisenberg uncertainty relation, which follows from this commutation relation, is

$$(\Delta\hat{s}_y)^2 (\Delta\hat{s}_z)^2 \geq \frac{1}{4} \langle \hat{s}_x \rangle^2 \quad (5.1)$$

This uncertainty relation differs substantially from the corresponding uncertainty relation for the quadrature phase operators for a single mode electromagnetic field, see Eq. (3.1). The *standard quantum limit* (SQL) for quantum fluctuations in a single mode of the electromagnetic field is basically set by the "1/16"-right hand side in Eq. (3.1). In Eq. (5.1) the right hand side depends on the actual spin state. It is more difficult to identify the SQL for the quantum fluctuations in a spin system because of this spin state dependence. Several proposals for a SQL definition for spin systems can be found in the literature but, as we will see, only one of them can be used to distinguish the nonclassical (entangled or quantum correlated) states from the "classical" states.

In this chapter we will also look at the results from chapter 4. We will present a simple qualitative explanation of the mechanism behind the atomic noise reduction, and we discuss the fundamental limitations in light-atom mapping. In particular, we will see that the atomic states produced by mapping polarization squeezed light onto a large ensemble of atoms can be considered to be generalized spin squeezed states.

5.1 Definition of spin squeezed states

It is convenient to define the x axis to be along the direction of the mean spin; $\langle \hat{\mathbf{s}} \rangle = \langle \hat{s}_x \rangle \mathbf{e}_x$. A natural basis for the spin states is the eigenstates of $\hat{\mathbf{s}}^2$ and \hat{s}_x given by $|s, m_s\rangle$. The only states in this basis that have an equality in the uncertainty relation are $|s, m_s = \pm s\rangle$. These minimum uncertainty states define

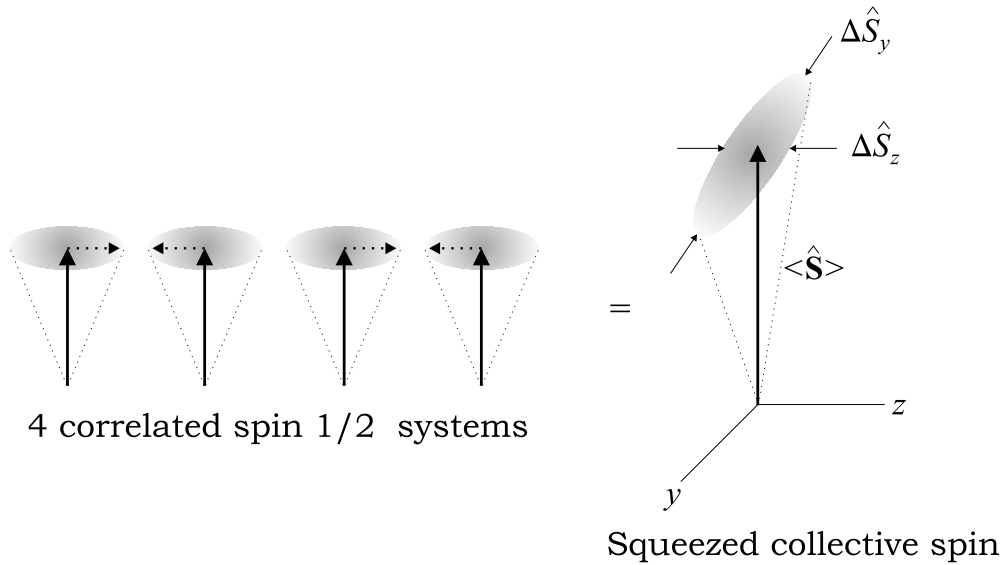


Figure 5.1: Illustration of the idea behind the spin squeezed states. On the left we have four correlated spin 1/2 systems. The thick arrow is the mean spin and the dotted arrow is the transverse spin fluctuation which is confined within the shaded uncertainty disc. The four spins are pair-wise correlated so that the fluctuations along the z -axis cancel and the fluctuations along the y -axis add. This system can also be described by the squeezed collective spin on the right with \hat{S}_z fluctuations below the standard quantum limit and increased \hat{S}_y fluctuations.

the *coherent spin states* (CSS) [85], which have transverse fluctuations given by

$$(\Delta \hat{s}_y)^2 = (\Delta \hat{s}_z)^2 = \langle \hat{s}_x \rangle / 2 = s/2 \quad (5.2)$$

The analogy between the coherent spin state and the coherent state of light is clear; the coherent spin state is a minimum uncertainty state with equal fluctuations in the two conjugate variables.

We can add N spin- s systems to obtain a collective spin $\hat{\mathbf{S}} = \sum_i \hat{\mathbf{s}}^i$ with $S = Ns$. The CSS of the collective spin have transverse fluctuations given by $(\Delta \hat{S}_y)^2 = (\Delta \hat{S}_z)^2 = S/2 = Ns/2$, and we see the linear N -dependence of the fluctuations, which is characteristic for fluctuations of independent systems. The linear N -dependence only holds when the state is composed of independent spins (i.e. a product state; $|s^1 m_s^1\rangle |s^2 m_s^2\rangle \cdots |s^N m_s^N\rangle$) or an incoherent mixture of product states). A state like $|S, M_S = 0\rangle$ can only be written as a coherent superposition of product states, and the transverse noise for this state does indeed have a term quadratic in N .

We first consider the special case of N spin-1/2 systems ($s = 1/2$, $S = N/2$). We will say that the collective spin composed of N spin-1/2 systems is in a *spin squeezed state* if the following inequality is fulfilled

$$\left(\Delta \hat{S}_\perp\right)^2 < \frac{|\langle \hat{\mathbf{S}} \rangle|^2}{2S} = \frac{|\langle \hat{\mathbf{S}} \rangle|^2}{N} \quad (5.3)$$

\hat{S}_\perp is the collective spin component orthogonal to the mean spin $\langle \hat{\mathbf{S}} \rangle$ with the smallest variance.

It is obvious that this definition gives spin squeezed states with the fluctuations in one of the transverse components reduced below the coherent spin state fluctuations. The spin component orthogonal to both \hat{S}_\perp and $\langle \hat{\mathbf{S}} \rangle$ will have fluctuations above the coherent spin state fluctuations so that the uncertainty relation is not violated. We prove in appendix D that entanglement among the N spin-1/2 subsystems is required in order to fulfil the spin squeezing definition.

The definition given above is identical to the definition used in Ref. [74, 75]. Here the spin squeezed states are defined as the states that can improve the signal-to-noise ratio in an frequency standard based on Ramsey's separated oscillatory method. Several explicit examples of spin squeezed states are given in Ref. [75], and a theoretical limit for the degree of spin squeezing is found to be

$$\xi + 1 \equiv \frac{2S \left(\Delta \hat{S}_\perp\right)^2}{|\langle \hat{\mathbf{S}} \rangle|^2} \geq N^{-1} = (2S)^{-1} \quad (5.4)$$

This inequality is easily proven from the uncertainty relation in Eq. (5.1) and the fact that an upper limit on the variance of any collective spin component is given by¹ $S^2 = N^2/4$. ξ is a measure of the amount of spin squeezing with $\xi = 0$ for the coherent spin state and $\xi < 0$ for the nonclassical (entangled) states. It is not proved in Ref. [74, 75] that $\xi < 0$ is possible only for quantum correlated spin states, although this is implicitly assumed.

Mainly three different definitions of spin squeezing have been used in the literature, (see e.g. Ref. [75]). Many authors do not distinguish between these three definitions, although only the definition given above ensures entanglement. For completeness, we discuss the limitations of the other two spin squeezing criteria. A criterion, which is not as strong as Eq. (5.3), is introduced in Ref. [74, 86] by the inequality

$$\left(\Delta \hat{S}_\perp\right)^2 < |\langle \hat{\mathbf{S}} \rangle|/2 \quad (5.5)$$

In one of the original papers on squeezed spin states, Ref. [85], as well as in Ref. [87], the authors introduce a spin squeezing criterion that is even weaker

$$\left(\Delta \hat{S}_\perp\right)^2 < S/2 \quad (5.6)$$

It is claimed in Ref. [85] that the requirement in Eq. (5.6) is enough to ensure entanglement or correlations in the collective system. A similar assertion is found about Eq. (5.5) in Ref. [86]. However, this is clearly not the case as it is seen from the general product state of two spin-1/2 systems. Consider two spin-1/2 systems $\hat{\mathbf{s}}_1$ and $\hat{\mathbf{s}}_2$ in a product state. We can choose the x -axis to be parallel to the collective mean spin $\langle \hat{\mathbf{s}}_1 + \hat{\mathbf{s}}_2 \rangle$, and the z -axis so that the z - x plane is spanned by the two mean spin vectors $\langle \hat{\mathbf{s}}_1 \rangle$ and $\langle \hat{\mathbf{s}}_2 \rangle$ as shown in Fig. 5.2. We define ϕ as the angle between the x -axis and each of the two mean spins $\langle \hat{\mathbf{s}}_1 \rangle$ and $\langle \hat{\mathbf{s}}_2 \rangle$. We find

$$\begin{aligned} \langle \hat{S}_x \rangle &= \langle \hat{s}_{1,x} \rangle + \langle \hat{s}_{2,x} \rangle = \cos \phi & (5.7) \\ \left(\Delta \hat{S}_z\right)^2 &= \langle (\hat{s}_{1,z} + \hat{s}_{2,z})^2 \rangle - \langle (\hat{s}_{1,z} + \hat{s}_{2,z}) \rangle^2 \\ &= \langle \hat{s}_{1,z}^2 \rangle + \langle \hat{s}_{2,z}^2 \rangle + 2\langle \hat{s}_{1,z} \hat{s}_{2,z} \rangle \\ &= \frac{1}{4} + \frac{1}{4} + 2\langle \hat{s}_{1,z} \rangle \langle \hat{s}_{2,z} \rangle = \frac{1}{2} \cos^2 \phi \end{aligned}$$

We have used that the state is a product state to write $\langle \hat{s}_{1,z} \hat{s}_{2,z} \rangle = \langle \hat{s}_{1,z} \rangle \langle \hat{s}_{2,z} \rangle$. We see that the weakest spin squeezing criterion in Eq. (5.6) is reduced to $\cos^2 \phi < 1$ for the general product state of two spin-1/2 systems. Thus, all product states, except for the coherent spin states, will be spin squeezed if we use Eq. (5.6) as the definition. This is clearly not satisfactory, and it is in clear contrast to the assertions in Ref. [85, 86]. The stronger spin squeezing criterion in Eq. (5.5) gives $\cos^2 \phi < \cos \phi$, and it is fulfilled for product states with $\phi \in]-\pi/2, \pi/2[\setminus \{0\}$; i.e. about 50% of all product states composed of two spin-1/2 systems. The strongest criterion (our spin squeezing definition, Eq. (5.3)) requires $\cos^2 \phi < \cos^2 \phi$, which is never fulfilled. This proves that only the strongest requirement may be used as a satisfactory definition

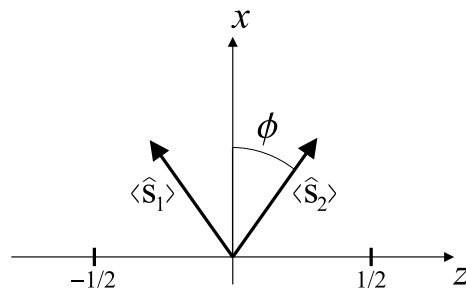


Figure 5.2: A sketch of a general product state composed of two spin-1/2 systems $\hat{\mathbf{s}}_1$ and $\hat{\mathbf{s}}_2$. We have chosen a coordinate system with the x -axis parallel to the collective mean spin $\langle \hat{\mathbf{s}}_1 + \hat{\mathbf{s}}_2 \rangle$ and the z -axis so that the two individual mean spins $\langle \hat{\mathbf{s}}_1 \rangle$ and $\langle \hat{\mathbf{s}}_2 \rangle$ span the z - x plane. ϕ is the angle between the x -axis and each mean spin $\langle \hat{\mathbf{s}}_1 \rangle$, $\langle \hat{\mathbf{s}}_2 \rangle$.

of spin squeezing, if we require spin squeezed systems to be entangled.

When the spin squeezing definition in Eq. (5.3) is applied to higher angular momentum subsystems ($s > 1/2$), we can have spin squeezing without entanglement between the subsystems. This is possible for a spin squeezed state with quantum correlations within each subsystem but without correlations among the subsystems. The maximum spin squeezing without entangled subsystems is set by the maximum squeezing within each subsystem; i.e. Eq. (5.4) with s substituted for S .

Although it is often argued that the spin squeezed states require some kind of quantum correlations, a direct proof of this statement has, to our knowledge, never been published. We present in appendix D such a proof, which is supplied by I. Cirac [88]

5.2 Realization of spin squeezed states

Several proposals for generation of spin squeezed states exist. A general idea is to couple the spin-1/2 subsystems to a common harmonic oscillator through a Jaynes-Cummings type interaction. The harmonic oscillator is prepared in a squeezed state, and the coupling to the spin system transfers the squeezing from the oscillator to the collective spin. This approach is discussed in Ref. [74, 75] for ions trapped in an ion trap. The harmonic oscillator is the collective motion of the ions in a harmonic potential. The coupling between the oscillator and the collective spin can be achieved via e.g. a magnetic interaction $\mu_0 \mathbf{B} \cdot \hat{\mathbf{S}}$ with \mathbf{B} as the magnetic field. The collective motion is now coupled to $\hat{\mathbf{S}}$ through a position dependent \mathbf{B} .

The Jaynes-Cummings interaction can also be realized in the interaction between light and two-level atoms. The two-level atoms constitute the spin system and the squeezed resonant electromagnetic field is the squeezed harmonic oscillator. This approach is used in Ref. [77], but it is hardly experimentally feasible for the reasons of tight focusing and strong atomic confinement, as discussed in the introduction to chapter 4. The idea of squeezing of the collective atomic spin by excitation with squeezed light is discussed further in Ref. [89]. Here the spin squeezing is obtained in an excited state manifold, which removes the strong requirements of squeezing from a large solid angle and confinement of atoms within a cubic wavelength. The excited state spin squeezing idea is refined in Ref. [9] where the spontaneous decay and the quantum field propagation are included.

A completely different suggestion for generation of atomic spin squeezed states is based on QND

¹This is seen by a simple argument. Choose the quantization axis (x') parallel to the spin component of interest. In general we can write the pure states of the collective spin as $|\Psi\rangle = \sum_{i=-S}^S c_i |S, M_S\rangle$ and we have $(\Delta S_{x'})^2 = \sum c_i^2 M^2 - (\sum c_i^2 M)^2 \leq \sum c_i^2 M^2 \leq S^2$. We find $(\Delta S_{x'})^2 = S^2$ for $c_i = \frac{1}{\sqrt{2}} (\delta_{i,S} + \delta_{i,-S})$

measurements of the collective atomic spin [90, 91]. The spin is measured by monitoring the polarization rotation of an off-resonant probe field after interaction with an oriented atomic sample, see Eq. (2.15) and (2.16). A measurement of the rotation angle provides the QND measurement of the atomic spin. After the measurement, the collective spin is projected onto an entangled state with reduced quantum fluctuations. The first experimental results utilizing this idea are presented in Ref. [5, 92].

Finally, we mention a recent idea for generation of spin squeezing in an optical lattice [93]. The authors consider two-level atoms where each level is trapped in its own lattice. Initially the two lattices are on top of each other. Shifting the relative position of the two lattices for a short time results in atomic interactions which depend on the atomic state of neighboring atoms. The theory predicts that the collective atomic spin can be squeezed from this nearest neighbor interaction.

In all the proposals above, the spin squeezing takes place in a collection of atomic spins. However, the general definition of spin squeezing is valid for any spin system. A particular spin, which comes to mind, is the Stokes spin used to characterize the polarization squeezed state of light. The only problem with the polarization squeezed light is that the number of subsystems (i.e. the number of photons) is not a constant. Instead of the number of subsystems $N = 2S$, we now have the photon number operator \hat{n} . If we generalize Eq. (5.3) so that the denominator on the right hand side is $2\langle S \rangle = \langle \hat{n} \rangle$, we see that the polarization squeezed state in Eq. (3.17) fulfils the requirements for being spin squeezed with e.g. $\theta = 0$, $R_-(\Omega) < 1$ and

$$\begin{aligned} (\Delta \hat{S}_z)^2 &= \frac{L^2}{c^2} \int_{-B/2}^{B/2} (\hat{S}_z)_\Omega^2 d\Omega \\ \langle \hat{S}_x \rangle &= \Phi L / 2c \\ 2\langle S \rangle &= \langle \hat{n} \rangle = \Phi L / c \end{aligned} \quad (5.8)$$

The bandwidth B , over which the spectral density is integrated, is the inverse measurement time corresponding to detection of $n = \Phi L / c$ photons; i.e. $B = c / L$. The entangled subsystems in this spin squeezed state are the photons which can be described as spin-1/2 systems due to their polarization. Thus, spin squeezed states have been produced in the laboratory for some time, although this is not always realized in the literature.

5.3 Generation of spin squeezed states by mapping light onto atoms

We now return to the results of section 4.2 and 4.3 and link these results to the notion of spin squeezing. We consider first the particular case of a $F = 0 \rightarrow F' = 1$ transition and rewrite Eq. (4.35), (4.36), (4.52) and (4.53) as

$$\begin{aligned} \langle \hat{J}_z \rangle &= \frac{\langle \hat{S}_z \rangle}{\gamma} & (\Delta \hat{J}_z)^2 &= \frac{1}{8} [R_z + 1] N' \\ \langle \hat{J}_x \rangle &= \frac{\langle \hat{S}_x \rangle}{\gamma} & (\Delta \hat{J}_x)^2 &= \frac{1}{8} [R_x + 1] N' \\ \langle \hat{J}_y \rangle &= \frac{\langle \hat{S}_y \rangle}{\gamma} & (\Delta \hat{J}_y)^2 &= \frac{1}{8} [R_y + 1] N' \end{aligned} \quad (5.9)$$

$N' = \frac{\Phi_+ + \Phi_-}{\gamma}$ is the average number of atoms in the excited state, $R_i = 4(\hat{S}_i)_\Omega^2 / (\Phi_+ + \Phi_-)$ with $i = x, y, z$, and the spectral densities of fluctuations in the excitation field are assumed to be constant over

the atomic linewidth γ . We have defined the collective pseudo-spin $\hat{\mathbf{J}}$ by

$$\begin{aligned} \hat{J}_z &= \frac{1}{2} \hat{F}'_z \\ \hat{J}_x &= \frac{1}{2} (\hat{F}'_x - \hat{F}'_y) \\ \hat{J}_y &= \frac{1}{2} (\hat{F}'_x \hat{F}'_y + \hat{F}'_y \hat{F}'_x) \end{aligned} \quad (5.10)$$

$\hat{\mathbf{J}}$ is easily seen to fulfil the angular momentum commutation relations, but only for $F' = 1$. At the single atom level we see that $\hat{\mathbf{J}}$ describes spin-1/2 systems based on the two excited atomic states $|F', m = \pm 1\rangle$. From Eq. (5.9) we see that in the process of complete absorption of the quantum excitation field, we map the fluctuations in the three Stokes component of the polarization squeezed light onto the three components of the collective pseudo spin. In other words, the quantum correlations in the squeezed light are converted into atomic correlations during the absorption process.

For the polarization squeezed state in Eq. (3.17), we find for $R_-(\Omega) < 1$ within the atomic linewidth γ

$$\begin{aligned} (\Delta \hat{J}_z)^2 &< \frac{\langle \hat{\mathbf{J}} \rangle^2}{N'} \quad , \quad \text{for } \theta = 0 \\ (\Delta \hat{J}_y)^2 &< \frac{\langle \hat{\mathbf{J}} \rangle^2}{N'} \quad , \quad \text{for } \theta = \pi/2 \end{aligned} \quad (5.11)$$

Thus, the produced atomic states seem to have a spin squeezed pseudo-spin according to the definition in Eq. (5.3). However, a closer look shows that this spin squeezing definition is not strictly fulfilled. The single atom subsystems consist of three coupled atomic states; $|F, m = 0\rangle$ and $|F', m = \pm 1\rangle$. The pseudo spin $\hat{\mathbf{J}}$ is only defined on the two excited states. Similar to the polarization squeezed light, the number of subsystems (atoms in the excited state) contributing to the collective spin in a given measurement is not a constant number. The proof in appendix D, which shows that spin squeezing according to Eq. (5.3) requires entanglement, cannot easily be extended to the current system of three-level atoms with the spin defined only on the excited state manifold and with finite probability amplitudes on the ground states. We do, however, strongly believe that multi-atom entanglement is required in order to fulfil Eq. (5.11). A computer search for a disentangled state, which fulfils Eq. (5.11), has been carried out to support our belief. About 10^8 randomly generated states have been tested. Each state is a random statistical mixture over three product states. Each product state is composed of three three-level atoms with arbitrary but normalized amplitudes. In none of the cases did the variance of the collective spin components orthogonal to the mean collective spin fulfil Eq. (5.11).

We can give a somewhat qualitative argument for the requirement of entanglement in order to fulfil Eq. (5.11). When we probe the collective spin, we only see atoms in the excited states. In this way we effectively probe two level atoms (or spin-1/2 systems), and within this interpretation the proof in appendix D is valid with the number of probed spin-1/2 systems (N') instead of total number of atoms (N). In other words, the subset of atoms measured to be in the excited state is in a spin squeezed state. The fact that only atoms in the excited state are probed, i.e. only the small spin squeezed fraction of all the atoms is probed, is one of the great advantages of this idea. The imperfect mapping of light on *all* atoms is not a problem; only the atoms that absorb the squeezed light are spin squeezed, and only these atoms are subsequently probed. The disadvantage of this proposal is that the spin squeezing (noise reduction) cannot be larger than 50%.

The inequalities in Eq. (5.11) become equalities when coherent light excitation is used (i.e. the squeezed vacuum path is blocked). Thus, the *standard quantum limit* (SQL) of atomic fluctuations is measured with coherent light excitation. The coherent state of light can be interpreted as a flux of uncorrelated photons. Therefore, the excitation with coherent light does not cause any atomic correlations. In section 4.2.1 we showed explicitly that the atomic noise level for coherent light excitation is indeed identical to the noise level for uncorrelated atoms.

The 50% noise reduction limit can be explained by the continuous creation and destruction of correlated atoms. In a simple picture, we can think of the squeezed light as a flux of pair-correlated photons. When one photon pair is absorbed, we create one pair of correlated atoms. The rate at which correlated atom pairs are created is then set by half the photon flux ($\Phi/2$) because of the complete absorption. A pair correlation is destroyed whenever a single atom of the pair decays spontaneously. Hence, we lose the correlations at a rate of 2γ . The correlations are lost twice as fast as the excited state population; this is similar to the effect of losses on a squeezed light beam (see page 29). With P_c as the number of correlated pairs in the excited state we have

$$\frac{\partial}{\partial t} P_c = \Phi/2 - 2\gamma P_c \quad (5.12)$$

The steady state number of correlated pairs is $P_c = \Phi/(4\gamma)$. The overall number of atom pairs in the excited state is $N'/2 = \Phi/(2\gamma)$. Thus, on average half of the excited state atoms are part of a correlated pair. This explains the 50% noise reduction when 50% of the excited state atoms are perfectly pair-wise correlated.

A simple argument shows why the fluctuations in \hat{J}_z (or \hat{F}'_z) are reduced when the atoms are excited by polarization squeezed light with sub-shot noise in \hat{S}_z . \hat{S}_z is proportional to the difference between the σ^+ -polarized photon flux and the σ^- -polarized photon flux. Photons with σ^+ -polarization mainly excite atoms into the positive m Zeeman levels, whereas σ^- -polarized photons excite atoms into the negative m Zeeman levels. With the reduced (squeezed) fluctuations in the differential photon flux (\hat{S}_z), we expect reduced fluctuations in the difference between the number of excited atoms in positive m Zeeman levels and the number in negative m Zeeman levels. This difference is quantified by the \hat{J}_z (or generally \hat{F}'_z) operator, and hence the atomic spin squeezing is explained. The three spin operators in Eq. (5.10) are fully equivalent for the simple $F = 0 \rightarrow F' = 1$ transition; a simple unitary transformation (rotation) can change one into another. When such a rotation is accompanied by a unitary transformation of the polarization basis for the excitation field, we find that any pair (\hat{J}_i, \hat{S}_i) , $i \in \{x, y, z\}$ can be rotated into (\hat{J}_z, \hat{S}_z) . We know how to explain the spin squeezing qualitatively for \hat{J}_z , and the same arguments can, with the unitary transformation, be used on any spin component.

Because of technical reasons we are not able to carry out a spin squeezing experiment on a $F = 0 \rightarrow F' = 1$ transition. We can, however, do the experiment on a $F = 4 \rightarrow F' = 5$ transition as shown in chapter 8. The relevant atomic variables can only be described by a pseudo spin in the $F = 0$ case. However, the derivations in section 4.2 and 4.3 are valid for any F , and the physical interpretation of the process in terms of quantum state mapping from light onto atoms is also F -independent. We know from above that the noise reduction in the atomic variables beyond the SQL (measured by coherent light excitation) is caused by multi-atom entanglement in the case of $F = 0$. We therefore argue that a demonstration of fluctuations below the SQL in one of the collective observables \hat{F}'_z , $\hat{F}'_x{}^2 - \hat{F}'_y{}^2$, or $\hat{F}'_x \hat{F}'_y + \hat{F}'_y \hat{F}'_x$ is a demonstration of multi-atom entanglement even for $F > 0$. Moreover, we will refer to this noise reduction as spin squeezing. It is not spin squeezing in the sense of Eq. (5.11) or Eq. (5.3), but it does fulfil the two main requirements: noise reduction in a spin component (especially when \hat{F}'_z fluctuations are reduced) and multi-particle entanglement.

The commutation relation for the pseudo-spin components in the $F = 0$ case is for the larger angular momentum states generalized to

$$[\hat{F}'_z, \hat{F}'_x \hat{F}'_y + \hat{F}'_y \hat{F}'_x] = -2i (\hat{F}'_x{}^2 - \hat{F}'_y{}^2) \quad (5.13)$$

The corresponding uncertainty relation is

$$(\Delta \hat{F}'_z)^2 (\Delta (\hat{F}'_x \hat{F}'_y + \hat{F}'_y \hat{F}'_x))^2 \geq \langle \hat{F}'_x{}^2 - \hat{F}'_y{}^2 \rangle^2 \quad (5.14)$$

For the excitation with polarization squeezed state in Eq. (3.17) we have $\langle \hat{F}'_x{}^2 - \hat{F}'_y{}^2 \rangle \neq 0$ (see (Eq. 4.53)) and quantum noise in \hat{F}'_z and $\hat{F}'_x \hat{F}'_y + \hat{F}'_y \hat{F}'_x$ is therefore expected. The atomic state produced by

coherent or squeezed light excitation is only a minimum uncertainty state when $F = 0$; this is seen from Eq. (4.35) and (4.52).

The optimum noise reduction in the observables \hat{F}'_z , $\hat{F}'_x - \hat{F}'_y$ or $\hat{F}'_x \hat{F}'_y + \hat{F}'_y \hat{F}'_x$ is a decreasing function of F (Fig. 4.2 and 4.3). This is because of the increase in the number of transitions on which a photon of a given polarization can be absorbed. Moreover, the strengths of the different transitions are different although all the excited states decay with the same rate. Two correlated photons of opposite polarization can be absorbed on a multitude of transitions, and not all the possibilities lead to efficient noise cancellation in the collective atomic observables.

Chapter 6

Theory for the atomic state readout

The theory of mapping the quantum state of light onto atoms, which we derived in chapter 4, leaves one question unanswered; how do we verify experimentally that an entangled, or spin squeezed, atomic state is actually produced? We clearly have to somehow probe the atomic state, and this probing is the subject of this chapter. When we consider the probing of spin squeezed atoms, we should keep in mind that the generated spin squeezed state only exists as long as the quantum pump continuously regenerates the atomic correlations, which are lost due to spontaneous decay. Thus, we must probe the atoms in the excited state in the presence of the excitation field.

The authors of the original paper on generation of spin squeezing in the excited state [9] suggest to use a probe of light, which is near-resonant with an excited state transition $F' \rightarrow F''$, to read out information about the quantum properties of the collective atomic state in F' . In this chapter we discuss this idea in more detail, and we derive quantitative expressions for the transfer of atomic properties onto a probe beam of light. The process we investigate in this chapter (transfer of atomic properties onto light) is in a sense opposite to the process explored in the two previous chapters (transfer of the properties of light onto atoms). It is advantageous for the readout process to have a strong atom-light interaction. However, the interaction should not be as strong as in the mapping process, where we find the complete absorption to be the optimum. In the readout process we obtain information about the atoms by analyzing the transmitted probe field, and a too large absorption of the probe will obviously reduce the readout efficiency. A trade off must be made between efficient interaction and probe signal left for analyzing. The optimum probe optical depth is $\alpha' = 1$, but this is hardly realizable in a spin squeezing experiment. The requirement for a completely absorbed weak excitation field results in a small number of atoms in the excited state. Consequently, the probe optical depth cannot be very large. Moreover, it is important that the properties of all excited state atoms are read with the same strength, otherwise the readout of the collective state cannot be ideal. We cannot tolerate a too large probe absorption since the strength in the readout depends on the probe power. In chapter 7 we will see that it is possible to have $\alpha' \simeq 1$ in experiments on spin noise of uncorrelated atoms.

The effects of the atomic properties such as orientation and alignment on a near-resonant probe of light are well known when the discussion is limited to atoms in the ground state and mean values of the atomic and field variables [34]. In this chapter, we extend the discussion to probing of excited state atomic quantum fluctuations in double-optical resonance. The theory and the physical interpretation of double-optical resonance in the weak field limit (weak probe *and* pump) including Zeeman degenerate atomic states have not attracted much attention; most discussions focus on the strong field aspects in double-optical resonance with pure three-level atoms. In the first section of this chapter we discuss the use of double-optical resonance for probing excited state atomic properties. In the second section we finalize the theory for the readout of atomic fluctuations. In the last section we discuss the effect of inhomogeneous broadening on the calculated probe noise spectrum.

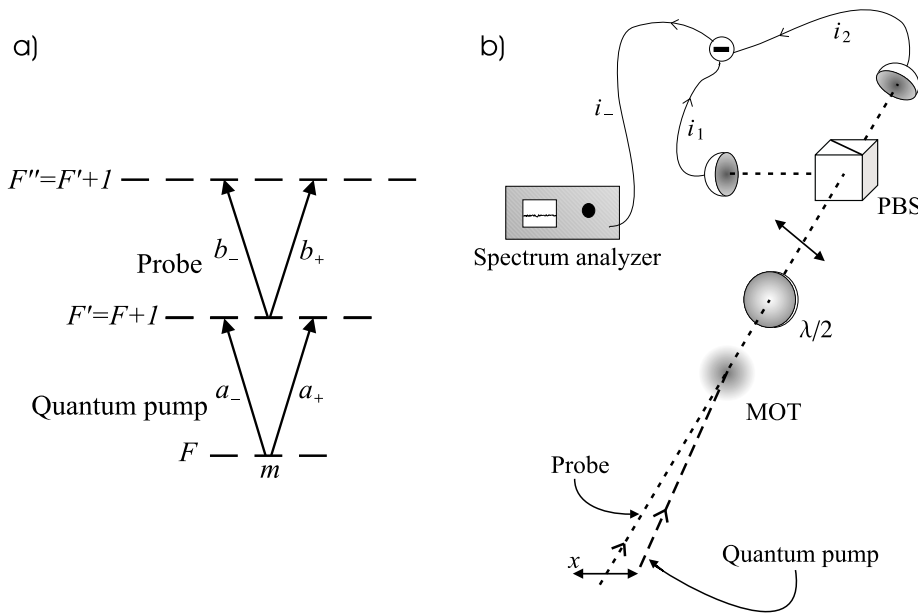


Figure 6.1: a) Atomic level scheme with the ground state (F), the intermediate state (F') and the upper state (F''). The quantum excitation field (pump) and the probe field are decomposed into circular polarizations. b) The configuration used for probing the spin squeezed state of atoms. The quantum pump is completely absorbed by the atoms, whereas the probe is only slightly absorbed. The angle between the pump and the probe beams is assumed to be small. The probe is analyzed by the half-wave retarder, the polarizing beamsplitter and two photodetectors. The spectrum analyzer measures the noise in the differential photocurrent.

6.1 Probing excited state atoms in double-optical resonance

It seems very natural to assume that the properties of the spin squeezed atoms in the intermediate¹ state F' can be read out by utilizing a probe that is near-resonant with an excited state transition $F' \rightarrow F'' = F' + 1$ as shown in Fig. 6.1a. However, this would imply that the dynamics of the pump and probe transitions can be separated, which in general is not possible. By separation of the dynamics we mean that all properties of the probe interaction can be calculated from a Hamiltonian including only the atomic states F' and F'' , the probe field, and the known properties of the atomic variables for the F' state. We show below that the probe interaction can be interpreted as being separated from the pump interaction in experiments on cold atoms with a radiation limited linewidth and weak copropagating fields.

We are interested in the change in the probe polarization caused by the atomic quantum fluctuations. The direction of the probe polarization, or more generally \hat{S}_y^{out} , is measured in a polarization interferometer setup consisting of a half-wave retarder, a polarizing beamsplitter, and two photodetectors; see page 13 for further details. The setup is very similar to Fig. 2.4 with the essential parts redrawn in Fig. 6.1b. We derive an expression for the fluctuations in the probe Stokes parameter \hat{S}_y^{out} measured after interaction with the atomic sample. This derivation is based on the full Hamiltonian for the pump and probe interaction. We assume that the angular momentum quantum numbers for the upper state (F''), the intermediate state (F'), and the ground state (F) fulfil $F'' = F' + 1 = F + 2$. The Hamiltonian for

¹ F' used to be the excited state in chapter 4, but now a higher lying state, F'' , is introduced, and we will then call F' the intermediate state.

the system consisting of the atomic sample, the pump field, and the probe field is given by

$$\hat{H} = \hat{H}_{pump} + \hat{H}_{probe} \quad (6.1)$$

\hat{H}_{pump} is identical to Eq. (4.2) and \hat{H}_{probe} is similar to \hat{H}_{pump} , except that it involves the variables relevant for the probe transition

$$\begin{aligned} \hat{H}_{probe} = & \hbar c \int_{k'_0 - \frac{\pi}{L}}^{k'_0 + \frac{\pi}{L}} k \left[\hat{b}_+^\dagger(k) \hat{b}_+(k) + \hat{b}_-^\dagger(k) \hat{b}_-(k) \right] dk \\ & + \hbar \omega'_a \sum_{m=-F''}^{F''} \int_V \rho \hat{\sigma}_{F''m, F''m}(\mathbf{r}) d^3\mathbf{r} \\ & + i\hbar \rho \sum_{m=-F'}^{F'} \int_V \left\{ \beta_m^+ u'^*(x, y) \hat{\sigma}_{F'm, F''m+1}(\mathbf{r}) \hat{b}_+^\dagger(z) - \beta_m^+ u'(x, y) \hat{\sigma}_{F''m+1, F'm}(\mathbf{r}) \hat{b}_+(z) \right. \\ & \left. + \beta_m^- u'^*(x, y) \hat{\sigma}_{F'm, F''m-1}(\mathbf{r}) \hat{b}_-^\dagger(z) - \beta_m^- u'(x, y) \hat{\sigma}_{F''m-1, F'm}(\mathbf{r}) \hat{b}_-(z) \right\} d^3\mathbf{r} \end{aligned} \quad (6.2)$$

The constants relevant for the probe transition are given by

$$\begin{aligned} \beta_m^\pm &= \frac{\pm \zeta' g'}{\hbar} \sqrt{\frac{2\pi}{L}} \sqrt{(F' + 2 \pm m)(F' + 1 \pm m)} \\ \zeta' &= \sqrt{\frac{\hbar \omega'_0}{4\pi \epsilon_0}} \\ g' &= \sqrt{\frac{3\epsilon_0 \hbar \lambda'^3 \gamma'}{8\pi^2 (2F' + 1)(2F' + 2)}} \end{aligned} \quad (6.3)$$

We use a prime on the parameters related to the probe transition (g' , ζ' , ω'_0 , ω'_a , γ' , $u'(x, y)$ and λ') in order to distinguish them from the corresponding pump parameters. \hat{b}_\pm are the probe field annihilation operators. We assume, for simplicity, identical quantization length L for the probe and the pump and a common direction of propagation.

The propagation equation for the probe field is obtained from the Heisenberg equation for the annihilation operators \hat{b}_\pm with a result similar to Eq. (4.17)

$$\frac{\partial}{\partial z} \tilde{b}_\pm(z, \Omega) = \sum_{m=-F'}^{F'} \frac{\rho \beta_m^\pm L}{c} \int \int u'^*(x, y) \tilde{\sigma}_{F'm, F''m \pm 1}(x, y, z, \Omega) dx dy \quad (6.4)$$

The tilde-notation is again introduced for the slowly varying operators, i.e. $\hat{b}_\pm(z, t) = \tilde{b}_\pm(z, t) e^{-i(\omega'_0 t - k'_0 z)}$, $\hat{\sigma}_{F''m, F'n}(\mathbf{r}, t) = \tilde{\sigma}_{F''m, F'n}(\mathbf{r}, t) e^{i(\omega'_0 t - k'_0 z)}$ and $\hat{\sigma}_{F''m, F'n}(\mathbf{r}, t) = \tilde{\sigma}_{F''m, F'n}(\mathbf{r}, t) e^{i((\omega'_0 + \omega_0)t - (k'_0 + k_0)z)}$. An operator and its Fourier transform are distinguished by the arguments, e.g. t and Ω .

In order to calculate the properties of the transmitted probe field, we look into the source term given by the atomic operators $\tilde{\sigma}_{F'm, F''m \pm 1}$. From the Heisenberg-Langevin equation for $\hat{\sigma}_{F'm, F''m \pm 1}$ we have

$$\begin{aligned} \dot{\tilde{\sigma}}_{F'm, F''m \pm 1}(\mathbf{r}) = & (-i\Delta' - [\gamma' + \gamma]/2) \tilde{\sigma}_{F'm, F''m \pm 1}(\mathbf{r}) + \mathcal{F}_{F'm, F''m \pm 1}(\mathbf{r}) \\ & - u'(x, y) \left\{ \beta_m^\pm \tilde{\sigma}_{F'm, F'm}(\mathbf{r}) \tilde{b}_\pm(z) + \beta_{m \pm 2}^\mp \tilde{\sigma}_{F'm, F'm \pm 2}(\mathbf{r}) \tilde{b}_\mp(z) \right\} \\ & - u^*(x, y) \left\{ \alpha_{m-1}^+ \tilde{\sigma}_{Fm-1, F''m \pm 1}(\mathbf{r}) \tilde{a}_+^\dagger(z) + \alpha_{m+1}^- \tilde{\sigma}_{Fm+1, F''m \pm 1}(\mathbf{r}) \tilde{a}_-^\dagger(z) \right\} \end{aligned} \quad (6.5)$$

We introduce the probe detuning $\Delta' = \omega'_a - \omega'_0$, and we assumed that the upper state populations/coherences are much smaller than the intermediate state populations/coherences, (weak probe approximation). If

we compare Eq. (6.5) to the corresponding expression for the pump transition, Eq. (4.18), we see that the last line in Eq. (6.5) does not have a counterpart in Eq. (4.18). It is because of these $F - F''$ coherence terms in Eq. (6.5) that the pump and probe interaction cannot be separated immediately.

The probe interaction in double-optical resonance is often interpreted as if it is composed of two contributions known as the two-step (or incoherent) and the two-photon (or coherent) processes [28, 94]. The two-step process describes a sequential absorption from the pump and the probe fields, and it is included in the second line of Eq. (6.5). The two-photon process involves the atomic coherence between the ground state F and the upper state F'' , and it is often interpreted as a process that requires two photons simultaneously. The third line in Eq. (6.5) is the contribution from the two-photon process. In general the two processes can have different resonance conditions, different linewidths, and different amplitudes. Such effects have been discussed extensively in the literature, see e.g. the references in Ref. [28]. If the decay rate for the atomic $F - F''$ coherences is large compared to intermediate state decay rate, then the two-photon contribution can be neglected. This can be caused by e.g. collisions or fluctuating laser fields. The remaining two-step contribution is fully described by a separation of the pump and probe interactions, and we can use a two-level Hamiltonian (H_{probe} in Eq. (6.2)) to derive the atom-probe interaction if the intermediate state atomic variables are known. The probe linewidth for the two-step process is set by the *sum* of the intermediate state and the upper state decay rates, just as for a two-level system where the lower state is not the ground state but is populated by incoherent pumping [95]. However, our system is assumed to be an ideal sample of cold atoms with a radiation limited linewidth together with laser fields without excess noise, and we cannot rely on a destruction of coherences for the separation to be valid.

The notion of a two-step and a two-photon process only makes sense in the presence of e.g. a strong and detuned pump field, collisions, large Doppler broadening, or fluctuating laser fields. The two processes cannot be distinguished in the case of weak fields and radiation limited linewidths. We can see that by rewriting the last line in Eq. (6.5) in terms of the intermediate state populations/coherences.

The Heisenberg-Langevin equations for $\tilde{\sigma}_{Fm-1, F''m\pm 1}$ gives

$$\begin{aligned} \dot{\tilde{\sigma}}_{Fm-1, F''m\pm 1}(\mathbf{r}) &= (-i\Delta' - \gamma'/2) \tilde{\sigma}_{Fm-1, F''m\pm 1}(\mathbf{r}) + \mathcal{F}_{Fm-1, F''m\pm 1}(\mathbf{r}) \\ &\quad - u'(x, y) \left\{ \beta_m^\pm \tilde{\sigma}_{Fm-1, F'm}(\mathbf{r}) \tilde{b}_\pm(z) + \beta_{m\pm 2}^\mp \tilde{\sigma}_{Fm-1, F'm\pm 2}(\mathbf{r}) \tilde{b}_\mp(z) \right\} \end{aligned} \quad (6.6)$$

In this expression we utilized that the pump field is weak and at exact resonance. After the usual linearization and a Fourier transform in time, we find

$$\begin{aligned} \bar{\sigma}_{Fm-1, F''m\pm 1}(\mathbf{r}) &= \frac{-u'(x, y)}{i\Delta' + \gamma'/2} \left\{ \beta_m^\pm \bar{\sigma}_{Fm-1, F'm}(\mathbf{r}) \bar{b}_\pm(z) + \beta_{m\pm 2}^\mp \bar{\sigma}_{Fm-1, F'm\pm 2}(\mathbf{r}) \bar{b}_\mp(z) \right\} \\ \delta\tilde{\sigma}_{Fm-1, F''m\pm 1}(\mathbf{r}, \Omega) &= \frac{-u'(x, y)}{i(\Delta' + \Omega) + \gamma'/2} \left\{ \mathcal{F}_{Fm-1, F''m\pm 1}(\mathbf{r}) \right. \\ &\quad + \beta_m^\pm \bar{\sigma}_{Fm-1, F'm}(\mathbf{r}) \delta\tilde{b}_\pm(z, \Omega) + \beta_m^\pm \delta\tilde{\sigma}_{Fm-1, F'm}(\mathbf{r}, \Omega) \bar{b}_\pm(z) \\ &\quad \left. + \beta_{m\pm 2}^\mp \bar{\sigma}_{Fm-1, F'm\pm 2}(\mathbf{r}) \delta\tilde{b}_\mp(z, \Omega) + \beta_{m\pm 2}^\mp \delta\tilde{\sigma}_{Fm-1, F'm\pm 2}(\mathbf{r}, \Omega) \bar{b}_\mp(z) \right\} \end{aligned} \quad (6.7)$$

We now use Eq. (4.19), (4.24), (4.47), (6.5), (6.7), and the similar equation for $\tilde{\sigma}_{Fm+1, F''m\pm 1}$ to obtain

$$\begin{aligned} \delta\tilde{\sigma}_{F'm, F''m\pm 1}(\mathbf{r}, \Omega) &= \frac{-u'(x, y)}{i\Delta' + \gamma'/2} \left\{ \mathcal{F}(\mathbf{r}, \Omega) \right. \\ &\quad + \beta_m^\pm \bar{b}_\pm(z) \delta\tilde{\sigma}_{F'm, F'm}(\mathbf{r}, \Omega) + \beta_{m\pm 2}^\mp \bar{b}_\mp(z) \delta\tilde{\sigma}_{F'm, F'm\pm 2}(\mathbf{r}, \Omega) \\ &\quad \left. + \beta_m^\pm \bar{\sigma}_{F'm, F'm}(\mathbf{r}) \delta\tilde{b}_\pm(z, \Omega) + \beta_{m\pm 2}^\mp \bar{\sigma}_{F'm, F'm\pm 2}(\mathbf{r}) \delta\tilde{b}_\mp(z, \Omega) \right\} \end{aligned} \quad (6.8)$$

We have in this derivation assumed that $\Omega \ll \gamma, \gamma'$. All the Langevin force contributions are lumped into \mathcal{F} , which we do not specify explicitly. We see that Eq. (6.8) does correspond to the two-step process

in Eq. (6.5) except for a modification of the linewidth to γ' instead of $\gamma' + \gamma$. This modification of the linewidth is the sole effect of the two-photon process.

The disappearance of the intermediate state decay rate in Eq. (6.8) is explained physically in Ref. [94]. The excitation field can excite atoms from the ground state F to the intermediate state F' , and in this process an energy of $\hbar\omega_0$ is transferred to the atoms. The probability for excitation of an atom depends on the ratio of the pump detuning to the linewidth of the state F' . The excited atoms are subsequently probed on the $F' \rightarrow F''$ transition. The energy of the atoms in F' is not uncertain as with incoherent pumping; it is set by the pump photon energy $\hbar\omega_0$. Therefore, the linewidth of the probe transition depends only on the linewidth of the upper state F'' , as confirmed experimentally in Ref. [96]. The probe field is resonant when the sum of the probe and pump frequencies corresponds to the atomic transition frequency from F to F'' . We can think of a mechanism that makes the $F - F''$ coherence decay fast, e.g. atomic collisions, as a mechanism which redistributes the energy of the atoms in F' within the intermediate state linewidth and thereby gives a probe linewidth which is the sum of the decay rates for the states F' and F'' .

Following this simple picture and the result in Eq. (6.8), we can treat our atom-probe interaction as if we are probing Zeeman degenerate two-level atoms prepared by the pump, provided that we only include the decay rate of the F'' state (γ') in the linewidth and take the detuning (Δ') to be the sum of the pump- and probe detunings. Since our pump field is at exact resonance, we do not have to distinguish between the probe detuning and the sum of the pump- and probe detunings. We conclude that double-optical resonance can indeed be used to probe the properties of the intermediate atomic state.

In the spin squeezing experiment in chapter 8 we have $\Omega/2\pi = 1.9\text{MHz}$, $\gamma/2\pi = 5.2\text{MHz}$ and $\gamma'/2\pi = 3.1\text{MHz}$. Hence, the requirement $\Omega \ll \gamma, \gamma'$, used in deriving Eq. (6.8), is not really fulfilled in the experiment. A natural way to include (at least partly) the nonzero detection frequency Ω into Eq. (6.8) is to add the detection frequency to the probe detuning in the denominator. This is the exact inclusion when the $F - F''$ coherences can be neglected (incoherent pumping), or when ground state atoms are probed. In addition, this inclusion is found to improve the agreement with the experimental data in chapter 8. We will therefore use the following two expressions in the calculations of the spectrum of probe polarization fluctuations

$$\begin{aligned} \bar{\sigma}_{F'm, F''m\pm 1}(\mathbf{r}) &= \frac{-u'(x, y)}{i\Delta' + \gamma'/2} \{ \beta_m^\pm \bar{b}_\pm(z) \bar{\sigma}_{F'm, F'm}(\mathbf{r}) + \beta_{m\pm 2}^\mp \bar{b}_\mp(z) \bar{\sigma}_{F'm, F'm\pm 2}(\mathbf{r}) \} \\ \delta\tilde{\sigma}_{F'm, F''m\pm 1}(\mathbf{r}, \Omega) &= \frac{-u'(x, y)}{i(\Delta' + \Omega) + \gamma'/2} \{ \mathcal{F}(\mathbf{r}, \Omega) \\ &\quad + \beta_m^\pm \bar{b}_\pm(z) \delta\tilde{\sigma}_{F'm, F'm}(\mathbf{r}, \Omega) + \beta_{m\pm 2}^\mp \bar{b}_\mp(z) \delta\tilde{\sigma}_{F'm, F'm\pm 2}(\mathbf{r}, \Omega) \\ &\quad + \beta_m^\pm \bar{\sigma}_{F'm, F'm}(\mathbf{r}) \delta\tilde{b}_\pm(z, \Omega) + \beta_{m\pm 2}^\mp \bar{\sigma}_{F'm, F'm\pm 2}(\mathbf{r}) \delta\tilde{b}_\mp(z, \Omega) \} \end{aligned} \quad (6.9)$$

After this discussion about atomic probing in double-optical resonance, we continue to calculate the fluctuations in the probe polarization, quantified by the Stokes parameter \hat{S}_y^{out} .

6.2 The readout of atomic fluctuations

We use Eq. (6.9) and (6.4) to derive

$$\begin{aligned} \frac{\partial}{\partial z} \delta\tilde{\mathbf{b}}(z, \Omega) &= -\underline{\mathbf{A}}(z) \delta\tilde{\mathbf{b}}(z, \Omega) + \underline{\tilde{\mathbf{B}}}(z, \Omega) \bar{\mathbf{b}}(z) + \mathcal{F}'(z, \Omega) \\ \frac{\partial}{\partial z} \bar{\mathbf{b}}(z) &= -\underline{\mathbf{A}}(z) \bar{\mathbf{b}}(z) \end{aligned} \quad (6.10)$$

where

$$\begin{aligned}
\delta\tilde{\mathbf{b}}(z, \Omega) &= \left(\delta\tilde{b}_+(z, \Omega), \delta\tilde{b}_-(z, \Omega) \right)^T \tag{6.11} \\
\bar{\mathbf{b}}(z) &= (\bar{b}_+(z), \bar{b}_-(z))^T \\
\mathbf{A}_{n,m}(z) &= \frac{3\lambda'^2}{8\pi(2F'+1)(2F'+2)} \frac{\gamma'}{i\Delta' + \gamma'/2} \int \int dx dy |u'(x, y)|^2 \\
&\times \left\{ \left[(3-2n)(2F'+3) \langle \hat{F}'_z(\mathbf{r}) \rangle + \langle \hat{F}'_z{}^2(\mathbf{r}) + \hat{P}'_z(\mathbf{r}) \right] \delta_{n,m} \right. \\
&\left. + \left[-\langle (\hat{F}'_x - \hat{F}'_y)^2 \rangle(\mathbf{r}) + i(3-2n) \langle (\hat{F}'_x \hat{F}'_y + \hat{F}'_y \hat{F}'_x) \rangle(\mathbf{r}) \right] (1 - \delta_{n,m}) \right\} \\
\tilde{\mathbf{B}}_{n,m}(z, \Omega) &= \frac{-3\lambda'^2}{8\pi(2F'+1)(2F'+2)} \frac{\gamma'}{i(\Delta' + \Omega) + \gamma'/2} \int \int dx dy |u'(x, y)|^2 \\
&\times \left\{ \left[(3-2n)(2F'+3) \delta\hat{F}'_z(\mathbf{r}, \Omega) + \delta\hat{F}'_z{}^2(\mathbf{r}, \Omega) + \delta\hat{P}'_z(\mathbf{r}, \Omega) \right] \delta_{n,m} \right. \\
&\left. + \left[-\delta \left(\hat{F}'_x{}^2 - \hat{F}'_y{}^2 \right) (\mathbf{r}, \Omega) + i(3-2n) \delta \left(\hat{F}'_x \hat{F}'_y + \hat{F}'_y \hat{F}'_x \right) (\mathbf{r}, \Omega) \right] (1 - \delta_{n,m}) \right\}
\end{aligned}$$

$\mathbf{A}_{n,m}$ are the components (row, column) in the 2×2 matrix \mathbf{A} and similar for $\tilde{\mathbf{B}}_{n,m}$. The atomic operators $\hat{P}'(\mathbf{r})$ and $\hat{F}'_z{}^2(\mathbf{r})$ are defined by

$$\begin{aligned}
\hat{P}'(\mathbf{r}) &= \rho \sum_{m=-F'}^{F'} (F'^2 + 3F' + 2) \tilde{\sigma}_{F'm, F'm}(\mathbf{r}) \tag{6.12} \\
\hat{F}'_z{}^2(\mathbf{r}) &= \rho \sum_{m=-F'}^{F'} m^2 \tilde{\sigma}_{F'm, F'm}(\mathbf{r})
\end{aligned}$$

The rest of the atomic variables in Eq. (6.11) are defined in chapter 4. We do not specify the Langevin force in Eq. (6.10). In chapter 4 (Eq. (4.20) and the discussion below), we saw that the effect of the Langevin force is to ensure that a coherent state field remains in a coherent state as it propagates through the atomic sample². This is similar to the attenuation of a coherent state by a beamsplitter; the vacuum fluctuations entering through the empty port ensures that the transmitted field is in a coherent state. We will assume that our atomic sample acts like a simple beam splitter if the atomic noise contribution is ignored (i.e. for $\tilde{\mathbf{B}} = 0$). Instead of keeping track of the Langevin forces, we ensure by addition of a vacuum field that the coherent state probe remains in a coherent state when $\tilde{\mathbf{B}} = 0$, i.e. that the probe field commutator is preserved; $[\delta\tilde{b}_\pm^{out}, \delta\tilde{b}_\pm^{out\dagger}] = [\delta\tilde{b}_\pm^{in}, \delta\tilde{b}_\pm^{in\dagger}]$. We use the indices *in* and *out* for the fields before ($z = 0$) and after ($z = l$) the atomic sample.

6.2.1 Correlated atoms and small optical depth.

In the readout of correlated atoms we would like $\delta\tilde{\mathbf{b}}^{out}(\Omega)$ to carry information about the *collective* intermediate state atomic operators. This requires, as we see by formally integrating Eq. (6.10) over z , that $\bar{\mathbf{b}}(z)$ and $|u'(x, y)|^2$ are constant over the volume with appreciable intermediate state population. In other words, the absorption and phase shift of the probe should be small, and the probe beam diameter should be much larger than the pump beam diameter.

The use of a large diameter probe beam does have a drawback in the experimental implementation as discussed at the end of this section. Nevertheless, we will, for simplicity, assume in the theory derived here that the probe diameter is much larger than the pump diameter.

²This is, of course, only true in the absence of atomic fluctuations. In chapter 4 we neglect the atomic fluctuations due to the arguments in Appendix C.

The maximum absorption (optical depth) of the probe field can be estimated as $\alpha' = N'\sigma'_0/(\pi w'^2)$, see Eq. (6.16) below. N' is the number of atoms in the intermediate state, σ'_0 is the resonant absorption cross section, and $2w'$ is the probe beam diameter. N' is for a completely absorbed pump field given by $N' = \Phi/\gamma = s_0\pi w^2/\sigma_0$. The resonant pump saturation parameter s_0 is defined on page 9, and $2w$ is the pump diameter. For $w \lesssim w'$ we find $\alpha' \lesssim s_0\sigma'_0/\sigma_0$. The ratio between the probe and pump cross sections for the cesium transitions used in chapter 8 is about 1.1, and accordingly $\alpha' \lesssim s_0$. Thus, a weak pump field (small s_0) results in a small probe absorption. The weak absorption can also justify the use of a z -independent spatial mode function.

With these arguments we can pull the $\bar{\mathbf{b}}(z)$ and $\delta\tilde{\mathbf{b}}(z, \Omega)$ factors out of the integral over z of Eq. (6.10). We find

$$\begin{aligned}\delta\tilde{\mathbf{b}}^{out}(\Omega) &= \left(\mathbf{1} - \int_0^l \underline{\mathbf{A}}(z) dz\right) \delta\tilde{\mathbf{b}}^{in}(\Omega) + \int_0^l \tilde{\underline{\mathbf{B}}}(z, \Omega) dz \bar{\mathbf{b}}^{in} + \underline{\mathbf{Q}}\tilde{\mathbf{v}}(\Omega) \\ \bar{\mathbf{b}}^{out} &= \left(\mathbf{1} - \int_0^l \underline{\mathbf{A}}(z) dz\right) \bar{\mathbf{b}}^{in}\end{aligned}\quad (6.13)$$

$\tilde{\mathbf{v}} = (\tilde{v}_+, \tilde{v}_-)^T$ are the vacuum fields, which mimic the effect of the Langevin forces. The vacuum operators commute with all other operators and $[\tilde{v}_\pm(\Omega), \tilde{v}_\pm^\dagger(\Omega')] = 2\pi\delta(\Omega + \Omega')L/c$, see Eq. (3.14). $\underline{\mathbf{Q}}$ is a matrix chosen to preserve the probe field commutators for $\underline{\mathbf{B}} = 0$.

We will, for simplicity, assume that the major contribution to the changes in \bar{b}_\pm is identical for the two circular polarizations. This assumption is not critical for the derivation below, but it is fulfilled in the experimental implementation, and it will simplify the notation. More quantitatively we assume

$$|\langle \hat{P}' + \hat{F}'_z \rangle| \gg (2F' + 3) |\langle \hat{F}'_z \rangle|, \quad |\langle \hat{F}'_x - \hat{F}'_y \rangle|, \quad |\langle \hat{F}'_x \hat{F}'_y + \hat{F}'_y \hat{F}'_x \rangle| \quad (6.14)$$

We can then write $\bar{b}_\pm^{out} = (1 - \alpha'/2 - i\theta)\bar{b}_\pm^{in}$, where α' is the probe optical depth and θ is a common phase shift. The explicit expression for the optical depth is

$$\alpha'/2 + i\theta = \frac{3\lambda'^2}{32\pi(2F' + 1)(F' + 1)} \frac{\gamma'^2 - i2\Delta'}{\Delta'^2 + \gamma'^2/4} \int_V d^3\mathbf{r} |u'(x, y)|^2 \langle \hat{P}'(\mathbf{r}) + \hat{F}'_z(\mathbf{r}) \rangle \quad (6.15)$$

The expression for the optical depth becomes even simpler when the atoms are unpolarized. We then have $\langle \hat{F}'_{x,y,z} \rangle = \rho'(\mathbf{r})F'(F' + 1)/3$ and $\langle \hat{P}'(\mathbf{r}) + \hat{F}'_z(\mathbf{r}) \rangle = \rho'(\mathbf{r})2(F' + 1)(2F' + 3)/3$ with ρ' as the density of atoms in the intermediate state F' . The optical depth for unpolarized atoms is then

$$\begin{aligned}\alpha'_{unpol} &= \frac{\sigma'_0}{1 + 4\Delta'^2/\gamma'^2} \int_V d^3\mathbf{r} |u'(x, y)|^2 \rho'(\mathbf{r}) \\ \sigma'_0 &= \frac{(2F' + 3)\lambda'^2}{(2F' + 1)2\pi}\end{aligned}\quad (6.16)$$

σ'_0 is the resonant absorption cross section for unpolarized atoms. Equation (6.16) is not only valid in double-optical resonance; it can also be used in the probing of unpolarized ground state atoms with F' as the angular momentum of the lower state. The integral over $|u'(x, y)|^2 \rho'(\mathbf{r})$ reduces to just $\rho'l$ for a uniform atomic density and to $2N'/\pi w'^2$ for a large probe diameter.

We can now write Eq. (6.13) as

$$\begin{aligned}\delta\tilde{\mathbf{b}}^{out}(\Omega) &= (1 - \alpha'/2 - i\theta) \delta\tilde{\mathbf{b}}^{in}(\Omega) + \int_0^l \tilde{\underline{\mathbf{B}}}(z, \Omega) dz \bar{\mathbf{b}}^{in} + \sqrt{\alpha'}\tilde{\mathbf{v}} \\ \bar{\mathbf{b}}^{out} &= (1 - \alpha'/2 - i\theta) \bar{\mathbf{b}}^{in}\end{aligned}\quad (6.17)$$

Finally, we assume that the probe diameter is large enough to allow the $|u'(x, y)|^2$ factor in the definition of $\underline{\mathbf{B}}$ to be replaced by its peak value $2/(\pi w'^2)$. We then find

$$\begin{aligned} \delta \tilde{b}_{\pm}^{out}(\Omega) &= (1 - \alpha'/2 - i\theta) \delta \tilde{b}_{\pm}^{in}(\Omega) + \frac{-3\lambda'^2}{4\pi(2F'+1)(2F'+2)\pi w'^2} \frac{\gamma'}{i(\Delta' + \Omega) + \gamma'/2} \\ &\times \left\{ \left[\pm(2F'+3)\delta \hat{F}'_z(\Omega) + \delta \hat{F}'_z{}'^2(\Omega) + \delta \hat{P}'(\Omega) \right] \tilde{b}_{\pm}^{in} \right. \\ &\quad \left. - \delta \left(\hat{F}'_x{}'^2 - \hat{F}'_y{}'^2 \right) (\Omega) \tilde{b}_{\mp}(z) \pm i\delta \left(\hat{F}'_x \hat{F}'_y + \hat{F}'_y \hat{F}'_x \right) (\Omega) \tilde{b}_{\mp}^{in} \right\} + \sqrt{\alpha'} \tilde{v}_{\pm} \end{aligned} \quad (6.18)$$

The atomic operators in this equation are the *collective* operators defined in the chapter 4.

From the Stokes parameter definition in chapter 3, we find to the lowest order in α' and θ

$$\begin{aligned} \delta \hat{S}_y^{t'out}(\Omega) &= \frac{ic}{2L} \left(\bar{b}_-^{out*} \delta \tilde{b}_+^{out}(\Omega) + \bar{b}_+^{out} \delta \tilde{b}_-^{out\dagger}(\Omega) - \bar{b}_+^{out*} \delta \tilde{b}_-^{out}(\Omega) - \bar{b}_-^{out} \delta \tilde{b}_+^{out\dagger}(\Omega) \right) \\ &= (1 - \alpha') \delta \hat{S}_y^{in}(\Omega) + \frac{c\sqrt{\alpha'}}{L} \left\{ \tilde{X}_+^v(\Omega) \bar{Y}_-^{out} + \tilde{Y}_-^v(\Omega) \bar{X}_+^{out} - \tilde{X}_-^v(\Omega) \bar{Y}_+^{out} - \tilde{Y}_+^v(\Omega) \bar{X}_-^{out} \right\} \\ &\quad + \frac{3\lambda'^2}{16\pi^2 w'^2 (2F'+1)(F'+1)} \\ &\quad \times \left\{ \left[-2(2F'+3) \bar{S}_x^{in} \delta \hat{F}'_z(\Omega) - 2\bar{S}_z^{in} \delta \left(\hat{F}'_x{}'^2 - \hat{F}'_y{}'^2 \right) (\Omega) \right] D(\Omega, \Delta') \right. \\ &\quad \left. + \left[-2\bar{S}_y^{in} \left(\delta \hat{F}'_z{}'^2(\Omega) + \delta \hat{P}'(\Omega) \right) + \Phi' \delta \left(\hat{F}'_x \hat{F}'_y + \hat{F}'_y \hat{F}'_x \right) (\Omega) \right] L(\Omega, \Delta') \right\} \end{aligned} \quad (6.19)$$

$\tilde{X}_{\pm}^v, \tilde{Y}_{\pm}^v$ are the quadrature phase operators for the vacuum fields \tilde{v}_{\pm} . $\bar{X}_{\pm}^{out}, \bar{Y}_{\pm}^{out}$ are the average of the quadrature phase operators for the transmitted probe field. Φ' is the incoming probe photon flux, and the functions D and L are defined by

$$\begin{aligned} D(\Omega, \Delta') &= \frac{8\Delta'\gamma'}{4\Delta'^2 + (\gamma' + i2\Omega)^2} \\ L(\Omega, \Delta') &= \frac{4\gamma'(\gamma' + i2\Omega)}{4\Delta'^2 + (\gamma' + i2\Omega)^2} \end{aligned} \quad (6.20)$$

The noise in the differential photocurrent i_- is analyzed on a spectrum analyzer (SA), see Fig. 6.1b. The SA measures the power spectrum, or spectral density, of the differential photocurrent. For unity quantum efficiency, a gain of g , and with e as the electron charge, we have

$$(i_-)_{\Omega}^2 = 4e^2 g^2 \left(\hat{S}_y^{t'out} \right)_{\Omega}^2 = \frac{4e^2 g^2}{2\pi} \int_{-\infty}^{\infty} \left\langle \delta \hat{S}_y^{t'out}(\Omega') \delta \hat{S}_y^{t'out}(\Omega) \right\rangle d\Omega' \quad (6.21)$$

We will assume that the fluctuations in the different atomic operators are uncorrelated. For a coherent state probe polarized along x or y we have $|\bar{S}_x^{in}| = \Phi'/2$, $\bar{S}_y^{in} = \bar{S}_z^{in} = 0$, and $(\hat{S}_y^{in})_{\Omega}^2 = \Phi'/4$, see Eq. (3.17). The power spectrum is then given by

$$\begin{aligned} (i_-)_{\Omega}^2 &= e^2 g^2 \Phi' (1 - \alpha') + e^2 g^2 \Phi' s'_0 \alpha'_{0,unpol} \frac{9\gamma'}{32N' (F'+1)^2 (2F'+3)^2} \\ &\times \left\{ \frac{4\Delta'^2 \gamma'^2}{\left[\gamma'^2/4 + (\Delta' - \Omega)^2 \right] \left[\gamma'^2/4 + (\Delta' + \Omega)^2 \right]} (2F'+3)^2 \left(\hat{F}'_z \right)_{\Omega}^2 \right. \\ &\quad \left. + \frac{4(\gamma'^2/4 + \Omega^2) \gamma'^2}{\left[\gamma'^2/4 + (\Delta' - \Omega)^2 \right] \left[\gamma'^2/4 + (\Delta' + \Omega)^2 \right]} \left(\hat{F}'_x \hat{F}'_y + \hat{F}'_y \hat{F}'_x \right)_{\Omega}^2 \right\} \end{aligned} \quad (6.22)$$

In this derivation we use the expressions for the resonant probe saturation parameter $s'_0 = \sigma'_0 \Phi' / \gamma' \pi w'^2$ and the resonant optical depth $\alpha'_{0,unpol}$ from Eq. (6.16). The first term is simply the shot noise of the coherent state probe, which is attenuated by α' because of the atomic absorption. The second term represents the excess noise transferred from the atomic spin \hat{F}'_z onto the probe. For small Ω the spectrum of this term as a function of the probe detuning Δ' is the square of a dispersion profile. The last term comes from the noise in the atomic alignment difference $\hat{F}'_x \hat{F}'_y + \hat{F}'_y \hat{F}'_x$. The spectrum of this contribution for small Ω is a squared Lorentzian. Note that we will have an extra contribution proportional to the real part of $D(-\Omega, \Delta') L(\Omega, \Delta')$ if cross correlations between $\delta \hat{F}'_z$ and $\delta(\hat{F}'_x \hat{F}'_y + \hat{F}'_y \hat{F}'_x)$ exist. This contribution will be *asymmetric* in the probe detuning and in contrast to the terms in Eq. (6.22), which are *symmetric* in Δ' . We will discuss the asymmetric contribution further in chapter 8.

The signal-to-noise ratio (S/N) in the atomic state readout is set by the ratio of the atomic noise contribution to the probe shot noise. The S/N scales with the probe power, probe diameter, and the number of atoms within the probe as $s'_0 N' / w'^2$. We have assumed here that the spectral densities of the atomic variables are linear in the number of probed atoms; this holds in the case of uncorrelated atoms. The weak probe assumption sets an upper limit on s'_0 . We can gain in S/N by reducing the probe diameter until it becomes comparable to the pump diameter. The physical explanation for this gain is that the probe photons outside the region with atomic excitation do not contribute to the atomic signal, but they are still detected and hence add to the measured probe shot noise. We can only gain in the readout of quantum correlations until the probe diameter approaches the pump diameter. With the probe diameter smaller than the pump diameter, we cannot probe all the entangled atoms, and the noise reduction caused by quantum correlations will suffer. In the spin squeezing experiment in chapter 8 we use a pump and a probe with about the same diameter.

For uncorrelated atoms we have nothing to loose by using a probe beam smaller than the pump beam. But we do not gain either. The number of probed atoms, N' , is for the small probe proportional to the square of the probe diameter. Thus, the S/N is independent of probe diameter for uncorrelated atoms in the small probe limit.

For completeness, we also give the expression for the average Stokes parameter $\bar{S}'_y{}^{out}$. We find for an arbitrarily polarized probe without the assumption about identical changes in \bar{b}_\pm

$$\begin{aligned} \bar{S}'_y{}^{out}(\Omega) &= \frac{ic}{2L} (\bar{b}_-^{out*} \bar{b}_+^{out} - \bar{b}_+^{out*} \bar{b}_-^{out}) \\ &= (1 - \alpha') \bar{S}'_y{}^{in} + \frac{3\lambda'^2 \gamma'}{8\pi^2 w'^2 (2F' + 1)(F' + 1)(\gamma'^2/4 + \Delta'^2)} \\ &\quad \times \left[-2(2F' + 3) \Delta' \bar{S}'_x{}^{in} \bar{F}'_z(\Omega) - 2\Delta' \bar{S}'_z{}^{in} \langle \hat{F}'_x{}^2 - \hat{F}'_y{}^2 \rangle + \frac{\gamma' \Phi'}{2} \langle \hat{F}'_x \hat{F}'_y + \hat{F}'_y \hat{F}'_x \rangle \right] \end{aligned} \quad (6.23)$$

Here we use the definition of α' given in Eq. (6.15).

6.2.2 Uncorrelated atoms and large optical depth

It is, as discussed above, not important to match the pump and the probe beam profiles in the readout of the quantum noise of uncorrelated atoms. In fact, in our first experiment on observation of the atomic quantum noise (chapter 7), we use excitation with large diameter beams from six different directions (the trapping beams of the MOT). It is then possible to have a large probe optical depth. The large probe absorption prevents an ideal readout of the collective atomic state as discussed in the previous section. However, we do not need a perfect readout of the collective state when the atoms are uncorrelated. In this section we derive an expression for the measured spectral density under the conditions of chapter 7. We will allow for a large probe optical depth, but this generalization is not for free. We now have to assume that the average density of atoms in the intermediate state F' is constant over the probe interaction volume ($\rho'(\mathbf{r}) = \rho'$), whereby $\underline{\mathbf{A}}(z)$ becomes independent of z . The isotropic excitation in

chapter 7 makes this a valid assumption. With $\underline{\mathbf{A}}(z) = \underline{\mathbf{A}}$ we find from Eq. (6.10)

$$\delta\tilde{\mathbf{b}}(z, \Omega) = \exp(-\underline{\mathbf{A}}z) \delta\tilde{\mathbf{b}}^{in}(\Omega) + \int_0^z \exp(-\underline{\mathbf{A}}[z-z']) \tilde{\underline{\mathbf{B}}}(z', \Omega) \bar{\mathbf{b}}(z') dz' + \underline{\mathbf{Q}}\tilde{\mathbf{v}}(\Omega) \quad (6.24)$$

$\tilde{\mathbf{v}} = (\tilde{v}_+, \tilde{v}_-)^T$ are again the vacuum fields, which mimic the effect of the Langevin forces. $\underline{\mathbf{Q}}$ is a matrix chosen to preserve the probe field commutators for $\tilde{\underline{\mathbf{B}}} = 0$.

In accordance with the experiment we assume almost identical changes in the two polarization components. Thus, we can define an absorption coefficient κ and a refractive index n so that $\underline{\mathbf{A}} = (\kappa + in)\underline{\mathbf{1}}$, $\kappa l = \alpha'/2$ and $nl = \theta$. From Eq. (6.24) and (6.10) we deduce

$$\delta\tilde{\mathbf{b}}(z, \Omega) = e^{-(\kappa+in)z} \delta\tilde{\mathbf{b}}^{in}(\Omega) + e^{-(\kappa+in)z} \int_0^z \tilde{\underline{\mathbf{B}}}(z', \Omega) dz' \bar{\mathbf{b}}^{in} + \sqrt{1 - e^{-2\kappa z}} \tilde{\mathbf{v}}(\Omega) \quad (6.25)$$

From this expression we derive the fluctuations in the probe Stokes parameter $\hat{S}_y^{'out}$ for a probe field initially polarized along x

$$\begin{aligned} \delta\hat{S}_y^{'out}(\Omega) &= \frac{ic}{2L} \left(\bar{b}_-^{out*} \delta\tilde{b}_+^{out}(\Omega) + \bar{b}_+^{out} \delta\tilde{b}_-^{out\dagger}(\Omega) - \bar{b}_+^{out*} \delta\tilde{b}_-^{out}(\Omega) - \bar{b}_-^{out} \delta\tilde{b}_+^{out\dagger}(\Omega) \right) \\ &= e^{-\alpha'} \delta\hat{S}_y^{'in}(\Omega) + \frac{c\sqrt{1-e^{-\alpha'}}}{L} \left\{ \tilde{X}_+^v(\Omega) \bar{Y}_-^{out} + \tilde{Y}_-^v(\Omega) \bar{X}_+^{out} - \tilde{X}_-^v(\Omega) \bar{Y}_+^{out} - \tilde{Y}_+^v(\Omega) \bar{X}_-^{out} \right\} \\ &+ \frac{3\lambda'^2}{32\pi(2F'+1)(F'+1)} e^{-\alpha'} \int_V d^3\mathbf{r} |u'(x, y)|^2 \left\{ -2(2F'+3) \bar{S}_x^{in} \delta\hat{F}_z'(\mathbf{r}, \Omega) D(\Omega, \Delta') \right. \\ &\quad \left. + \Phi' \delta \left(\hat{F}_x' \hat{F}_y' + \hat{F}_y' \hat{F}_x' \right) (\mathbf{r}, \Omega) L(\Omega, \Delta') \right\} \end{aligned} \quad (6.26)$$

We can write the atomic correlation functions for the uncorrelated atoms as (compare to e.g. Appendix C, section C.1)

$$\begin{aligned} \langle \delta\hat{F}_z'(\mathbf{r}, \Omega) \delta\hat{F}_z'(\mathbf{r}', \Omega') \rangle &= \rho' (\hat{F}_z')_{sa, \Omega}^2 \delta(\mathbf{r} - \mathbf{r}') \delta(\Omega + \Omega') \\ \langle \delta(\hat{F}_x' \hat{F}_y' + \hat{F}_y' \hat{F}_x')(\mathbf{r}, \Omega) \delta(\hat{F}_x' \hat{F}_y' + \hat{F}_y' \hat{F}_x')(\mathbf{r}', \Omega') \rangle &= \rho' (\hat{F}_x' \hat{F}_y' + \hat{F}_y' \hat{F}_x')_{sa, \Omega}^2 \delta(\mathbf{r} - \mathbf{r}') \delta(\Omega + \Omega') \end{aligned} \quad (6.27)$$

We use the subscript sa on the single atom spectral densities. We can now calculate the spectral density of the detected differential photocurrent i_-

$$\begin{aligned} (i_-)_{\Omega}^2 &= e^2 g^2 e^{-\alpha'} \Phi' + e^2 g^2 \Phi' e^{-2\alpha'} \alpha'_{0, unpol} s'_0 \frac{9\gamma'}{64(F'+1)^2(2F'+3)^2} \\ &\times \left\{ (2F'+3)^2 (\hat{F}_z')_{sa, \Omega}^2 D(\Omega, \Delta') D(-\Omega, \Delta') + (\hat{F}_x' \hat{F}_y' + \hat{F}_y' \hat{F}_x')_{sa, \Omega}^2 L(\Omega, \Delta') L(-\Omega, \Delta') \right\} \end{aligned} \quad (6.28)$$

We have again used the expressions for s'_0 and $\alpha'_{0, unpol}$ (for the small probe). The variance of a sum of uncorrelated variables equals the sum of the variances of each variable. Therefore we expect that for uncorrelated atoms $(\hat{F}_z')_{\Omega}^2 = N' (\hat{F}_z')_{sa, \Omega}^2$. This is indeed what makes Eq. (6.22) and (6.28) equal, except for a factor of two and the validity of Eq. (6.28) for large α' . This factor of two is the effect of the Gaussian probe profile; in Eq. (6.22) we use the peak intensity to probe all atoms, whereas in Eq. (6.28) we use the whole probe with a smaller average intensity. A result very similar to Eq. (6.28) is used in Ref. [5] for the readout of atomic ground state fluctuations in a pulsed experiment.

It is possible to give a simple interpretation of the noise formulas (6.22) and (6.28) based on the classical description of the polarization interferometer in section 2.3. The incoming probe with a flux Φ' is polarized along x , and the half-wave retarder and the polarizing beamsplitter (PBS) is oriented to measure the field components along x' and y' . As a result, the photon flux difference between the two output arms of the PBS is proportional to the rotation angle θ of the probe polarization caused

by the atomic interaction. We can write the difference in the fluxes as $\Phi'_- = \Phi'_1 - \Phi'_2 = 2\theta\Phi'_+$ with $\Phi'_+ = \Phi'_1 + \Phi'_2 = e^{-\alpha'}\Phi'$, see Eq. (2.15). If the mean value of θ is small, we can write the fluctuations in the differential flux as $\delta\Phi'_- = 2\bar{\Phi}'_+\delta\theta$. Three possible contributions to θ exist. The first contribution is the optical activity, where the two circular polarization components of the probe experience different phase shifts. The rotation angle is proportional to the difference between the phase shifts, and the spectrum of θ versus probe detuning Δ' is a dispersion-like profile. Optical activity occur when the atomic sample is oriented along the z axis, that is, for non-zero \hat{F}'_z . The second contribution is related to linear dichroism with different absorption of the linearly polarized components along the x' - and y' axis. This effect has a Lorentzian spectrum and depends on the difference in atomic alignment along the x' - and y' axis quantified by $\hat{F}'_x\hat{F}'_y + \hat{F}'_y\hat{F}'_x$. The calculations above show that if the atomic parameters are noisy, then this noise is converted into noise in the probe polarization angle θ , which is directly observed in the noise of the differential flux. Finally, the quantum fluctuations in the coherent state polarization give a shot noise contribution to $\delta\theta$ as discussed in chapter 3. The shot noise contribution to the variance of the angle θ is given by $(\Delta\theta)_{SN}^2 = 1/(4\Phi'_+)$; the stronger the coherent state is the more well-defined is the polarization direction. The atomic contribution to the variance of θ is for uncorrelated atoms given by a sum over the contributions from each atom. Since each atom is assumed to add the same amount of noise, we find that $(\Delta\theta)_{atom}^2 = kN'$. For a weak probe the atomic response is linear, and the proportionality constant k is independent of the photon flux. Thus, for the total variance in the differential photon flux we have

$$(\Delta\Phi'_-)^2 = 4\bar{\Phi}'_+{}^2(\Delta\theta)^2 = e^{-2\alpha'}\bar{\Phi}'^2 + 4kN'e^{-2\alpha'}\bar{\Phi}'^2 \quad (6.29)$$

The dependence on the probe flux and the number of atoms (optical depth) is identical to the result of the more thorough calculation in Eq. (6.28). The signal-to-noise ratio in the readout of atomic fluctuations is given by the ratio of the atomic noise to the shot noise in Eq. (6.29). Since $N' \propto \alpha'$ we find that the signal-to-noise ratio has a maximum at $\alpha' = 1$.

6.3 Inhomogeneous broadening of the atomic noise spectrum

It turns out that we have some excess line broadening in the experimental realization of the spin squeezing proposal in chapter 8. One reason is that the weak unidirectional excitation field accelerates and heats the atoms, even though the atoms are first cooled to the mK level. In this section we look at an atomic sample with a distribution of atomic resonance frequencies. We consider in particular a velocity distribution with a Doppler width comparable to the linewidths γ and γ' , but the final results will be valid for any kind of inhomogeneous broadening. The excitation field is still assumed to be completely absorbed, and we will not look at the effect of the Doppler broadening on the generation of spin squeezed atoms. We limit the discussion to a simple model for the effect of the velocity distribution on the readout process.

Consider the term proportional to $\delta\hat{F}'_z(\Omega)D(\Omega, \Delta')$ in the $\delta\hat{S}'_{y^{out}}(\Omega)$ expression in Eq. (6.19). $\delta\hat{F}'_z$ is a collective atomic operator that represents a sum over all single atom operators, $\sum_j \delta\hat{F}'_{z,j}$. We can also express the collective operator as a spatial integral over the continuous atomic operators introduced in chapter 4. Here we introduce, in the same way, continuous operators in velocity space together with a density function ρ_v . We define

$$\delta\hat{F}'_z(v, \Omega) = \frac{1}{\rho_v(v)\Delta v} \sum_{m=-F'}^{F'} m \sum_i \delta\tilde{\sigma}_{F'm, F'm}^i(\Omega) \quad (6.30)$$

$N\rho_v(v)\Delta v$ is the number of atoms with a velocity in the z -direction in the interval Δv around v . ρ_v is normalized so that³ $\int \rho_v(v)dv = 1$. The sum over i is a sum over all atoms with the z -component of the

³Note that we use a different normalization for the density in velocity space $\rho_v(v)$ as compared to the spatial density $\rho(\mathbf{r})$, which integrates up to N .

velocity in the small interval Δv around v . Δv is chosen to be large enough to include many atoms, but small compared to the width of the velocity distribution. We then have

$$\delta \hat{F}'_z(\Omega) = \int \rho_v(v) \delta \hat{F}'_z(v, \Omega) dv \quad (6.31)$$

The different atomic velocity groups have different detunings because of the Doppler shift. We write the velocity dependent detuning as $\Delta'(v) = \Delta' - 2\pi v/\lambda_t$. The detuning in the probe interaction is in fact the sum of the probe and the pump detuning (see page 69), and hence λ_t is the wavelength corresponding to the two-photon excitation from the ground state F to the upper state F'' . We can now substitute the $\delta \hat{F}'_z(\Omega) D(\Omega, \Delta')$ factor by a corresponding factor which includes the atomic velocity distribution

$$\int \rho_v(v) \delta \hat{F}'_z(v, \Omega) D(\Omega, \Delta'(v)) dv \quad (6.32)$$

The \hat{F}'_z -contribution to the detected spectral density is then proportional to

$$\int d\Omega' \int \int dv dv' \rho_v(v') \rho_v(v) \langle \delta \hat{F}'_z(v, \Omega) \delta \hat{F}'_z(v', \Omega') \rangle D(\Omega, \Delta'(v)) D(\Omega', \Delta'(v')) \quad (6.33)$$

Some general statements about the correlation function for $\delta \hat{F}'_z(v, \Omega)$ can be given. We first consider a sample of uncorrelated atoms. From the definition in Eq. (6.30) we find that $\langle \delta \hat{F}'_z(v, \Omega) \delta \hat{F}'_z(v', \Omega') \rangle \Delta v = 0$ for $v' \neq v$. For $v' = v$ we have

$$\begin{aligned} \langle \delta \hat{F}'_z(v, \Omega) \delta \hat{F}'_z(v, \Omega') \rangle \Delta v &= \frac{1}{\rho_v(v)^2 \Delta v} \sum_i \sum_{m,n} mn \langle \delta \tilde{\sigma}_{F'm, F'm}^i(\Omega) \delta \tilde{\sigma}_{F'n, F'n}^i(\Omega') \rangle \\ &= \frac{1}{\rho_v(v)} f(v, \Omega) \delta(\Omega + \Omega') \end{aligned} \quad (6.34)$$

$f(v, \Omega) \delta(\Omega + \Omega')$ is the average single atom correlation function for atoms with a velocity in the z -direction around v .

In general we can have correlations between the atoms, which we describe by a function $g(v, v')$. In the continuous limit we can then write the correlation function as

$$\langle \delta \hat{F}'_z(v, \Omega) \delta \hat{F}'_z(v', \Omega') \rangle = \delta(\Omega + \Omega') \{ \rho_v^{-1}(v) f(v, \Omega) \delta(v - v') + g(v, v', \Omega) \} \quad (6.35)$$

We now assume that the functions f and g are independent of v, v' and insert this correlation function into Eq. (6.33) with the result

$$f(\Omega) \widetilde{D}^2(\Omega, \Delta') + g(\Omega) \tilde{D}^2(\Omega, \Delta') \quad (6.36)$$

The new functions \widetilde{D}^2 and \tilde{D}^2 are defined by

$$\begin{aligned} \widetilde{D}^2(\Omega, \Delta') &= \int dv \rho_v(v) D(-\Omega, \Delta'(v)) D(\Omega, \Delta'(v)) \\ \tilde{D}^2(\Omega, \Delta') &= \left(\int dv \rho_v(v) D(-\Omega, \Delta'(v)) \right) \left(\int dv \rho_v(v) D(\Omega, \Delta'(v)) \right) \end{aligned} \quad (6.37)$$

In the limit of small Ω the first function, \widetilde{D}^2 , is a Doppler broadening of a squared dispersion profile. This function is for a nonzero Doppler width strictly positive for all Δ' . The function $\tilde{D}^2(0, \Delta')$ is the square of a Doppler broadened dispersion profile. This function always goes to zero at resonance. We

introduce Doppler broadened versions of $L(\Omega, \Delta')$ in a similar way. With these simple modifications we can rewrite Eq. (6.22) as

$$\begin{aligned}
(i_-)_{\Omega}^2 &= e^2 g^2 \Phi' e^{-\alpha'} + e^2 g^2 \Phi' e^{-2\alpha'} s'_0 \alpha'_{0,unpol} \frac{9\gamma'}{32N'(F'+1)^2(2F'+3)^2} \\
&\times \left\{ (2F'+3)^2 \left(\hat{F}'_z \right)_{uc,\Omega}^2 \widetilde{D}^2(\Omega, \Delta') + (2F'+3)^2 \left(\hat{F}'_z \right)_{c,\Omega}^2 \check{D}^2(\Omega, \Delta') \right. \\
&\left. + \left(\hat{F}'_x \hat{F}'_y + \hat{F}'_y \hat{F}'_x \right)_{uc,\Omega}^2 \widetilde{L}^2(\Omega, \Delta') + \left(\hat{F}'_x \hat{F}'_y + \hat{F}'_y \hat{F}'_x \right)_{c,\Omega}^2 \check{L}^2(\Omega, \Delta') \right\}
\end{aligned} \tag{6.38}$$

Here the spectral densities of the atomic fluctuations have been separated into two contributions. We use the index uc for the spectral densities for uncorrelated atoms and the index c for the corrections due to multi-atom correlations. Thus, the c -terms like $(\hat{F}'_z)_{c,\Omega}^2$ are not true spectral densities in themselves, and they may even be negative. We only see the uc terms when coherent light is used for excitation. The c terms are added when e.g. polarization squeezed light is used for excitation. The spectral densities for atomic fluctuations of uncorrelated atoms are, per definition, always nonnegative. However, the corrections in the presence of atomic correlations may be negative and thereby reduce the spectral density of the collective spin below the standard quantum limit set by uncorrelated atoms.

We have in Eq. (6.38) included the "large optical depth" exponentials from the previous section. This joins Eq. (6.22) and (6.28) in one equation, which furthermore allows for an inhomogeneously broadened medium. Note that the atomic noise contributions in Eq. (6.38) should be reduced by a factor of two in the small probe diameter limit.

In the experiment it is quite easy to measure the sum of the photocurrents i_1 and i_2 instead of the difference. The corresponding spectral density for i_+ is derived in a way similar to Eq. (6.38). The result for uncorrelated atoms is

$$\begin{aligned}
(i_+)_{\Omega}^2 &= e^2 g^2 \Phi' e^{-\alpha'} + e^2 g^2 \Phi' e^{-2\alpha'} s'_0 \alpha'_{0,unpol} \frac{9\gamma'}{32N'(F'+1)^2(2F'+3)^2} \\
&\times \left(\hat{F}'_x{}^2 - \hat{F}'_y{}^2 + \hat{F}'_z{}^2 + \hat{P} \right)_{uc,\Omega}^2 \widetilde{L}^2(\Omega, \Delta')
\end{aligned} \tag{6.39}$$

We find in chapter 8 that the experimental data for $(i_+)_{\Omega}^2$ fit the $\widetilde{L}^2(\Omega, \Delta')$ profile better than the $\check{L}^2(\Omega, \Delta')$ profile when uncorrelated atoms are probed. We find that the contribution to $(i_-)_{\Omega}^2$ from multi-atom correlations matches the $\check{D}^2(\Omega, \Delta')$ profile when non-coherent light is used to induce atomic correlations in \hat{F}'_z . In conclusion we find that this simple theory for the inhomogeneous broadening is sufficient to explain the experimental data.

Chapter 7

Quantum noise of uncorrelated atoms

In the previous three chapters we discussed the theory behind excited state atomic fluctuations and the readout of these fluctuations. We now return to the experiments, and in this chapter we describe our measurements on the quantum noise of uncorrelated atoms. The experiments presented in this chapter can be considered as the first step towards generation of a macroscopic entangled spin squeezed state of atoms. Before we suppress the atomic spin fluctuations by means of quantum correlations, we have to demonstrate that we, in fact, can measure these fluctuations; this is the subject in this chapter.

Atomic fluctuations are important in a number of physical systems or processes. The efficiency of squeezed light generation by four-wave mixing in an atomic gas can be limited by the atomic noise due to spontaneous decay [2]. The momentum diffusion for the atomic motion within an optical field can be limited by atomic dipole fluctuations [97]. The signal-to-noise ratio in spectroscopy experiments can be limited by the atomic noise [1, 3, 4, 98, 99]. Atomic noise in the resonance fluorescence spectrum is investigated in Ref. [100, 101].

The quantum noise of uncorrelated atoms (i.e. the variance of a collective atomic operator) has a characteristic linear dependence on the number of atoms which contribute to the noise. This is for example seen in Eq. (6.29) in the limit of small optical depth. The physical argument for this dependence is simple; the variance of a sum of uncorrelated atomic variables, e.g. $\sum_i \hat{F}_{z,i}$, is the sum of the single atom variances. We find the overall contribution to be proportional to the number of atoms (N) if all atoms have identical variances. If, on the other hand, all the atoms fluctuate in phase (i.e. correlated), then we can substitute the sum by $N\hat{F}_{z,i}$, and the variance of the collective atomic variable is proportional to N^2 . The N^2 dependence is, for example, seen when all the atoms are exposed to the same laser field, which is modulated in intensity or frequency. Thus, the N^2 dependence is typical for atoms that are exposed to some kind of classical modulation or noise. This is very similar to the fluctuations in light; a shot noise limited light field (a coherent state) will have intensity fluctuations that scale linearly with the mean intensity. If the field is exposed to any classical or technical noise, the intensity fluctuations will scale quadratically with the mean intensity.

The linear dependence on N does not necessarily ensure that the observed noise is of quantum origin. If the number of atoms under investigation fluctuates in time in a random but classical way, then the same linear N -dependence can be found. This is the case for the thermal fluctuations of unpolarized atoms in a gas cell probed by a small diameter laser beam [98]. If the number of atoms is fixed, or if the number fluctuations happen with a frequency much smaller than the frequency at which we detect the noise spectral density, then we expect that noise observed with a linear N -dependence is of quantum origin.

Only a few experiments have aimed at probing the quantum noise of atoms with a demonstration of the characteristic N -dependence. The first experiment is based on a few trapped ions, which are

prepared in a superposition of two eigenstates [3]. A subsequent measurement of the number of ions in a given eigenstate results in a projection of the wave function with a random outcome. The observed noise is termed projection noise, and the variance is found experimentally to scale linearly in N , although not with overwhelming statistics.

In this chapter we present our experiments where the quantum noise of excited state atoms is measured and found to be in agreement with the expected linear N -dependence. These results are also published in Ref. [4]. In contrast to the ion experiment, we do not observe the quantum noise induced by our measurements of an atomic variable (the projection noise). Our quantum noise is caused mainly by the coupling of the atoms to the electromagnetic vacuum modes, which leads to the spontaneous decay. In a qualitative picture we can think of this quantum noise as the projection noise induced by the "measurements" carried out by the vacuum fields. We use a weak probe of light to readout the quantum noise, and this probing is assumed not to contribute to the atomic noise. Besides the noise from spontaneous decay, we also have a contribution from the quantum noise of the field used to excite the atoms back into the excited state. The fast spontaneous decay results in a broad band atomic noise spectrum. This is advantageous when the noise is read out by a probe of light. The typical low frequency technical noise of the probe laser requires a detection frequency above a few MHz, and we measure the spectral density of atomic fluctuations at 3MHz. The atoms are trapped in a magneto-optical trap (MOT) where they live for about one second before they escape due to collisions. The probe diameter is somewhat smaller than the size of the atomic sample, but the atomic velocity in the MOT is very small, and trapped atoms enter/leave the probe region quite slowly. Thus, the detection frequency is much higher than the frequency at which atoms enter/leave the probe region, and we do not have to worry about classical number fluctuations.

Subsequently, the linear N -dependence have been observed in the frequency fluctuations of an atomic fountain frequency standard [1]. The frequency fluctuations are caused by the quantum projection noise as in Ref. [3]. Finally, the linear N -dependence is found in the variance of a collective spin measurement on cesium atoms in the ground state [5].

We continue this chapter with a description of the setup used in the experiment. In the second section we present the experimental results.

7.1 The setup for detection of atomic quantum noise

The setup for this experiment is very similar to the setup in Fig. 2.4. A sketch of the setup with the elements relevant for the present experiment is shown in Fig. 7.1. The cesium atoms are trapped in a MOT as described in chapter 2. The noise of the excited state atoms in the MOT is probed on the 917nm $6P_{3/2} \rightarrow 6D_{5/2}$ transition utilizing a Ti:Sapphire laser (Microlase MBR-110). We use the polarization interferometer setup to analyze the transmitted probe field as described in chapter 2 and 6. The polarization interferometer and the two photodetectors in the output arms of PBS2 are the same as in section 2.4.1. The 3MHz detectors are set at the broad 640kHz bandwidth with a noise equivalent power (for both detectors) of about $80\mu\text{W}$. The differential photocurrent i_- holds information about the polarization of the probe field after the atomic interaction. i_- is proportional to the Stokes parameter \hat{S}_y^{out} for the probe field. Fluctuations in \hat{S}_y^{out} induced by the atoms are measured on the spectrum analyzer (SA) as fluctuations in i_- . The SA measures the spectral density $(i_-)_{\Omega}^2$ at the frequency $\Omega/2\pi = 3.0\text{MHz}$. The SA runs in the following at zero span with a resolution bandwidth of 300kHz, unless other parameters are given explicitly.

In the first attempt at observing the atomic quantum noise, we use the diode laser for trapping in the MOT. The intrinsic broad band phase noise of the diode laser output results in a classical modulation of the trapped atoms (Ref. [20, 35] and section 2.4.4). It seems like a bad idea to use a noisy trapping laser when the goal is to observe the quantum noise of atoms. However, if the atomic sample is perfectly isotropic, then the classical noise of the diode laser will have the same influence on both circular polarization components of the linearly polarized probe, and the polarization of the probe is not modulated.

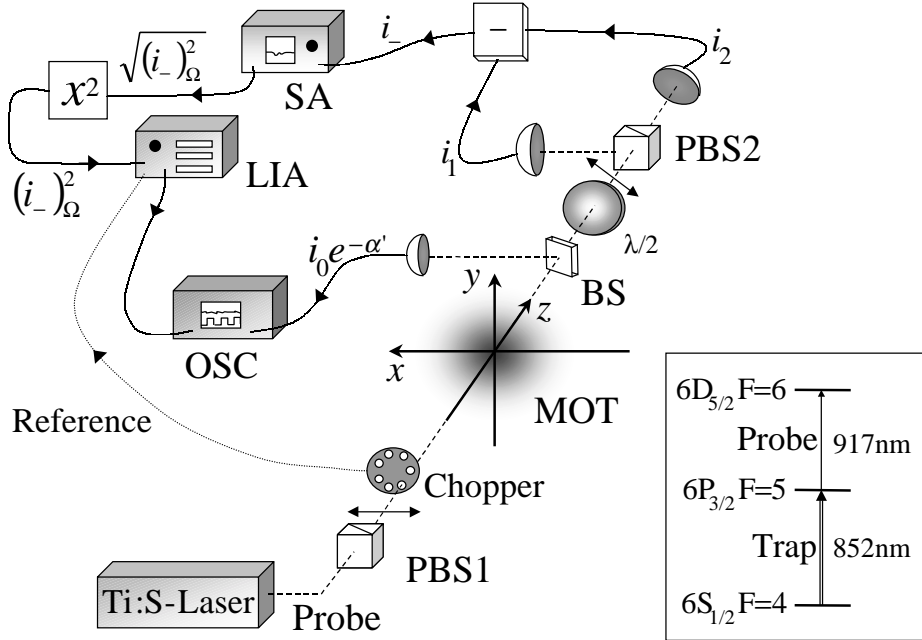


Figure 7.1: The setup used to observe the quantum noise of uncorrelated atoms. A MOT is sustained by six laser beams at 852nm (not shown). A probe field at 917nm probes the atomic fluctuations in the $6P_{3/2} F = 5$ state. The abbreviations OSC, LIA, SA, BS and PBS stand for digital oscilloscope, lock-in amplifier, spectrum analyzer, beamsplitter and polarizing beamsplitter. Further details about the setup are given in the text.

This is similar to what we see in section 2.4.3 with balanced trapping beams. The induced modulation of the probe amplitude is balanced out in the polarization interferometer. Accordingly, it is in principle possible to see the quantum spin noise with a noisy pump laser. Even if some of the classical noise is transferred into polarization noise owing to a slightly non-isotropic trap, one might still hope to see the quantum noise prevailing at small¹ N . However, we did not succeed in observing the quantum noise with a diode trapping laser; the classical noise was persistently prevailing at lowest possible N [20].

To circumvent the classical noise problem, a second Ti:Sapphire laser was constructed [23]. This home-made laser, as well as the Ti:Sapphire probe laser, provides light that is shot noise limited in both amplitude and phase above 2MHz for an optical power at the mW level. The available trapping power increases to 200mW with the Ti:Sapphire laser. Furthermore, the MOT is changed from a five beam configuration to a six beam configuration with retro-reflected beams. That gives improved trapping conditions with a 6mm trap diameter (FWHM of 852nm fluorescence) and an optical depth of more than one for the 917nm probe. For comparison the measured optical depth at 917nm with a diode trapping laser is only about 0.05. The locking of the laser frequency to the atomic transition is done by standard FM saturation spectroscopy techniques, where an electro-optical modulator running at 20MHz is used for frequency modulation. Only the part of the laser output that is used for locking is modulated in order to keep the trapping light as quiet as possible.

¹The quantum noise is linear in N , whereas the classical noise is quadratic in N in the limit of small optical depth. Thus the quantum noise may be predominant at small N .

The probe laser can be locked to the atomic resonance at 917nm by an error-signal from a (almost) Doppler-free two-photon FM spectroscopy setup. Cs atoms in a gas cell are excited by a fraction of the 852nm light with 20MHz frequency modulation. A counterpropagating 917nm beam completes the Doppler-free two-photon transition [28]. The frequency modulation at 852nm is converted into amplitude modulation of the 917nm beam, just as in the experiments in section 2.4. An error signal is finally derived by phase sensitive demodulation of the detected 20MHz signal in the 917nm field. Two acousto-optic modulators (AOM's) in the locking setup allow us to tune the locked laser around the closely spaced atomic resonances $6P_{3/2}F = 5 \rightarrow 6D_{5/2}F = 4, 5, 6$.

The output of the probe Ti:Sapphire laser has slow intensity fluctuations (up to about $\pm 5\%$), which limits the accuracy when long integration time is required. We therefore actively stabilize the probe power with a feedback loop. An AOM is placed in the probe beam, and the unshifted zeroth order is used for the probe. The intensity in the probe is set by the RF power supplying the AOM. A part of the probe beam is split off onto a photodiode before the polarization interferometer, and by comparing the resulting photocurrent with a reference, we obtain an error signal for the intensity stabilizing feedback loop. The probe is initially polarized along the x -axis and it has a diameter of about 1.5mm. We use probe powers between 0.10mW and 1.0mW.

A 2% beamsplitter is placed in the setup right after the MOT. The beamsplitter reflects a small fraction of the probe light onto a DC detector. The detector signal goes to a digital oscilloscope (OSC, HP 54601B), and it is used to measure the transmission of the probe through the atomic sample. The transmission ($e^{-\alpha'}$) is used later on to extract the probe optical depth α' .

The chopper wheel, the lock-in amplifier (LIA), and the square box (x^2), shown in Fig. 7.1, are not used in the first part of the experiment. The purpose of these devices will be described later on.

7.2 Measurements and results

The purpose of the experiments in this chapter is to demonstrate the observation of atomic quantum noise of uncorrelated atoms. In chapter 6 we derived an expression, Eq. (6.28), for the spectral density of the differential photocurrent with contributions from the probe shot noise and the atomic spin noise added by the probe-atom interaction. In the present experiments we use the rather strong trapping beams for excitation. In the derivation of Eq. (6.28) we assumed that the atoms are excited by a weak, resonant pump field. However, the general dependencies in Eq. (6.28) are found not to depend critically on this assumption. We will take Eq. (6.28) as our starting point and then discuss the limitations or the required modifications due to the strong excitation field. We first rewrite the spectral density of the differential photocurrent

$$\begin{aligned}
 (\bar{i}_-)_\Omega^2 &= (\bar{i}_-)^2_{E,\Omega} + e^{-\alpha'} + \alpha'_{0,unpol} e^{-2\alpha'} s'_0 \frac{9\gamma'}{64(2F'+3)^2(F'+1)^2} \\
 &\times \left\{ (2F'+3)^2 \left(\hat{F}'_z \right)_{sa,\Omega}^2 D(\Omega, \Delta') D(-\Omega, \Delta') + \left(\hat{F}'_x \hat{F}'_y + \hat{F}'_y \hat{F}'_x \right)_{sa,\Omega}^2 L(\Omega, \Delta') L(-\Omega, \Delta') \right\}
 \end{aligned} \tag{7.1}$$

We have normalized the spectral density to the shot noise of the unabsorbed probe; $e^2 g^2 \Phi'$. We use a bar on i_- to indicate this shot noise normalization. In addition, we have added the electronic noise of the detectors as $(\bar{i}_-)^2_{E,\Omega}$. The electronic noise represents the noise seen on the spectrum analyzer when no light hits the detectors. The electronic noise is not correlated to the light or atom noise and just adds to the i_- spectral density. The main double-optical resonance transition is $6S_{1/2}F = 4 \rightarrow 6P_{3/2}F = 5 \rightarrow 6D_{5/2}F = 6$. The quantum numbers F and F' for the lower and intermediate state are $F' = F + 1 = 5$.

We can from simple arguments derive an estimate of the atomic noise contribution to $(\bar{i}_-)_\Omega^2$. We start with the single atom spectral density $(\hat{F}'_z)_{sa,\Omega}^2$. It follows from the definition in section 6.2.2 that the integral of $(\hat{F}'_z)_{sa,\Omega}^2$ over Ω is equal to the variance of the single atom operator $\hat{F}'_{z,i}$ divided by the

probability P' for the atom to be in the intermediate state. That is,

$$\langle \hat{F}'_{z,i}{}^2 \rangle - \langle \hat{F}'_{z,i} \rangle^2 = P' \int (\hat{F}'_{z,sa,\Omega})^2 \frac{d\Omega}{2\pi} \quad (7.2)$$

The atoms are excited with laser beams from six directions with different polarizations, so we expect the atomic state to be almost unpolarized. Thus, we have for the single atom operator $\langle \hat{F}'_{z,i}{}^2 \rangle = P'F'(F'+1)/3$ and $\langle \hat{F}'_{z,i} \rangle = 0$. We assume for simplicity that $(\hat{F}'_{z,sa,\Omega})^2$ is constant within the bandwidth of spin fluctuations γ_{spin} and zero outside. This gives $(\hat{F}'_{z,sa,\Omega})^2 = \pi F'(F'+1)/(3\gamma_{spin})$. A similar approximation gives $(\hat{F}'_x \hat{F}'_y + \hat{F}'_y \hat{F}'_x)_{sa,\Omega}^2 = \pi F'(F'+1)(2F'-1)(2F'+3)/(15\gamma_{spin})$. Inserting these results into Eq. (7.1) shows that the \hat{F}'_z noise predominates. We evaluate $D(\Omega, \Delta')$ and $L(\Omega, \Delta')$ at the detuning for maximum $D(\Omega, \Delta')$ and assume $\Omega \ll \gamma'$. This gives us for small detection frequencies Ω

$$\kappa = (\bar{i}_-)_\Omega^2 - (\bar{i}_-)^2_{E,\Omega} - e^{-\alpha'} = 0.54 \frac{\gamma'}{\gamma_{spin}} \alpha' e^{-2\alpha'} s'_0 \quad (7.3)$$

Here we introduce κ as the atomic noise contribution normalized to the shot noise of the unabsorbed probe. Furthermore, we do the measurements close to resonance, and for the estimate of κ we do not distinguish between α'_0 and α' . We note that the atomic noise is increased when the bandwidth of the spin fluctuations is reduced. Hence, it is advantageous to use atomic states with long-lived spins. However, we use a probe of light to read out the fluctuations, and we have to detect at frequencies above a couple of MHz to avoid the low frequency technical laser noise. In our case the bandwidth of spin fluctuations cannot be smaller than the spontaneous decay rate and we take $\gamma_{spin} = \gamma$. It is possible that the magnetic field gradient and the strong fields effectively increase the bandwidth of spin fluctuations. With $\gamma_{spin}/2\pi = \gamma/2\pi = 5.3\text{MHz}$ and $\gamma'/2\pi = 3.0\text{MHz}$ we find

$$\kappa = (\bar{i}_-)_\Omega^2 - (\bar{i}_-)^2_{E,\Omega} - e^{-\alpha'} = \kappa_0 \alpha' e^{-2\alpha'} s'_0 \quad (7.4)$$

where $\kappa_0 = 0.16$ is the theoretical estimate. This is a crude estimate of the atomic noise contribution, but this is all we can hope for in the current experiment. The trap environment modifies the line shape with AC Stark splitting, polarization gradient effects and the magnetic field broadening (see section 2.2). Equation (7.4) also includes crude estimates of the bandwidths, and it assumes a small detection frequency. Nevertheless, we can compare the measured dependencies on the optical depth and probe power with the predictions of Eq. (7.4), and we will also see that the measured ratio of atomic noise to shot noise (κ_0) is not far from the estimated value.

The atomic noise term in Eq. (7.4) is clearly linear in α' for small α' . This is just as it should be for the atomic noise from uncorrelated atoms since the optical depth is proportional to the number of atoms. The nonlinearity at larger α' is not a deviation from the linear N -dependence for uncorrelated atoms. The exponential $e^{-2\alpha'}$ merely represents the attenuation of the probe power and the subsequent reduction in the readout efficiency. If classical atomic noise is present, we should add a term like $\kappa_{0,cl} \alpha'^2 e^{-2\alpha'}$ to Eq. (7.4). The α'^2 factor is the quadratic dependence on the number of atoms and the exponential $e^{-2\alpha'}$ is again just the probe attenuation.

7.2.1 The spectrum of atomic spin noise

We first scan the 917nm probe across the atomic resonance while monitoring the transmission from the DC detector on the oscilloscope and the spectral density $(i_-)_\Omega^2$ on the spectrum analyzer. The result of the measurement is shown in Fig. 7.2 with curve 2 as the DC measurement of the probe transmission and curve 1 as the spectral density of the differential photocurrent i_- . The electronic noise $(i_-)^2_{E,\Omega}$ is measured with blocked detectors and subtracted in curve 1. The remaining noise is normalized to the shot noise of the off-resonant probe. In the same way we normalize the DC measurement to the

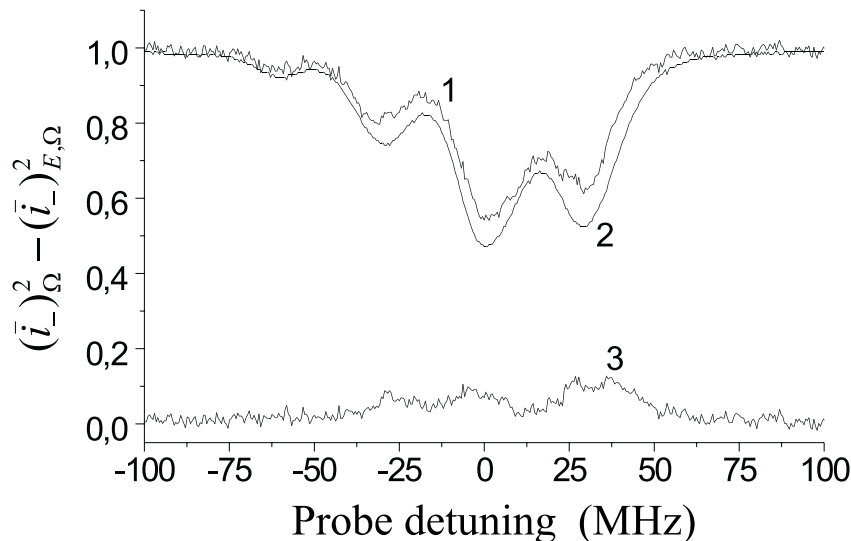


Figure 7.2: Atomic spin noise as a function of probe detuning. 1) Spectral density noise at 3.0MHz with a 300kHz resolution bandwidth. 2) DC transmission; corresponds to the probe shot noise. 3) Atomic spin noise (difference between 1 and 2).

off-resonant DC level. The absorption spectrum is identical to the spectrum that we analyzed in section 2.2, and it includes different hyperfine components as well as AC Stark splitting.

If the atoms are passive absorbers², then curve 1 and 2 would be indistinguishable; the probe would remain shot noise limited and shot noise is proportional to the optical power. The discrepancy between curve 1 and 2 clearly shows that atoms are not passive absorbers. The atoms do not just attenuate the coherent state probe; extra noise is added to the probe field by the atom-probe interaction. The extra atomic noise is given by the difference between curve 1 and 2 and is shown as curve 3 in Fig. 7.2.

We can see from curve 3 that the atomic noise contribution is largest (when normalized to the optical depth) at the resonance close to 30MHz. This resonance is one of the AC Stark components of the $6P_{3/2}F = 5 \rightarrow 6D_{5/2}F = 6$ transition. In the following we consider the dependence of the atomic noise on the optical depth and the probe power at fixed probe detuning.

7.2.2 Atomic noise versus optical depth

The probe laser is now locked and tuned to the atomic resonance at 30MHz (Fig. 7.2). We can derive the atomic spin noise as a function of optical depth from the measured spectral density $(i_-)_\Omega^2$ and the DC absorption. We implement a lock-in technique to improve the quality of our measurements [102]. The idea, which is sketched in Fig. 7.1, is to chop the probe beam with an optical chopper at a frequency around 1KHz. The spectral density measured by the SA then alternates between the background noise and the full spectral density, which includes the noise of the probe light. The background noise is mainly the electronic noise $(i_-)_{E,\Omega}^2$, but it also includes any contribution from stray light that may hit the detectors. The SA has a video output, which gives a voltage proportional to $\sqrt{(i_-)_\Omega^2}$ when the SA runs on the linear scale. The SA output is subsequently squared electronically to get a voltage proportional to $(i_-)_\Omega^2$, and this voltage is fed into a digital lock-in amplifier (LIA, Stanford Research Systems, model SR810). The reference for the LIA is the frequency of the chopper wheel. The output of the LIA

²We define a passive absorber as an absorber which gives an attenuated coherent state output for a coherent state input. The ideal beamsplitter is a passive absorber.

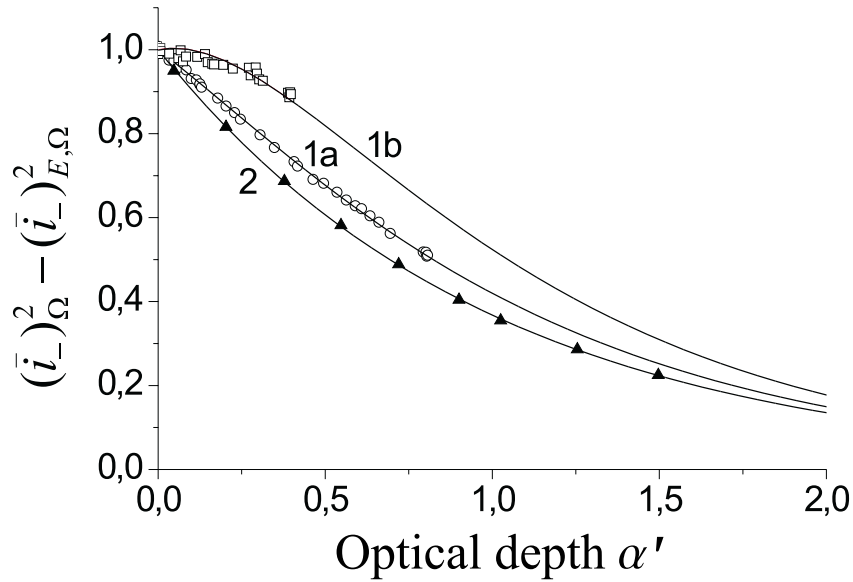


Figure 7.3: Normalized spin noise plus shot noise versus the probe optical depth. 1a) The noise for 0.34mW probe power. 1b) The noise for 0.95mW probe power. 2) Shot noise from passive absorption (for comparison).

is a voltage, which is proportional to amplitude of the alternating input signal; i.e. proportional to $(i_-)_\Omega^2 - (i_-)_{E,\Omega}^2$, where we now use $(i_-)_\Omega^2$ for the spectral density with the probe on. In this way we subtract the background noise very efficiently, and we are left with a signal that is proportional to the probe and atom contribution to the spectral density. The LIA output is finally averaged on the digital oscilloscope together with the signal from the DC detector. The signal from the DC detector is of course now modulated due to the chopped probe, but the peak-to-peak voltage is still proportional to the probe transmission.

We can vary the number of atoms in the trap by changing the power in the repumping beam for the MOT. The importance of the repumping beam is discussed in chapter 2. The atoms interact only with the repumping beam in a small fraction of their time in the trap. For this reason, we do not expect that the changes in the repumping power will change any important trapping parameters except for the number of trapped atoms. The important parameters, like the power on the trapping transition, the detuning of the trapping field, the magnetic field gradient, and the Cs pressure in the vacuum chamber, are kept constant.

We now measure corresponding values for the optical depth α' (derived from the DC transmission measurement) and the spectral density of the probe fluctuations. We normalize the spectral density to a measurement without atoms in the trap (no repumping beam). In this way we arrive at experimental measurements of $(\bar{i}_\Omega)^2 - (\bar{i}_{E,\Omega})^2$ versus α' . The results are shown in Fig. 7.3 for two different probe powers (circles: 0.34mW, squares: 0.95mW). Each data point is a result of about 30 seconds of averaging on the digital oscilloscope. The data are fitted to Eq. (7.4) with $\kappa_0 s'_0$ as a free parameter, and the fits are shown in the figure as solid lines. The fit in curve 1a gives $\kappa_0 s'_0 = 0.38$ and for curve 1b we get $\kappa_0 s'_0 = 1.15$. We see that the agreement between the measurements and the fits is excellent. With the larger probe power we approach the atomic saturation. Moreover, the data in curve 1a and 1b are from different days with possibly different trap conditions. This explains the smaller maximum optical depth in curve 1b.

For comparison, we have carried out similar measurements with a passive absorber instead of the

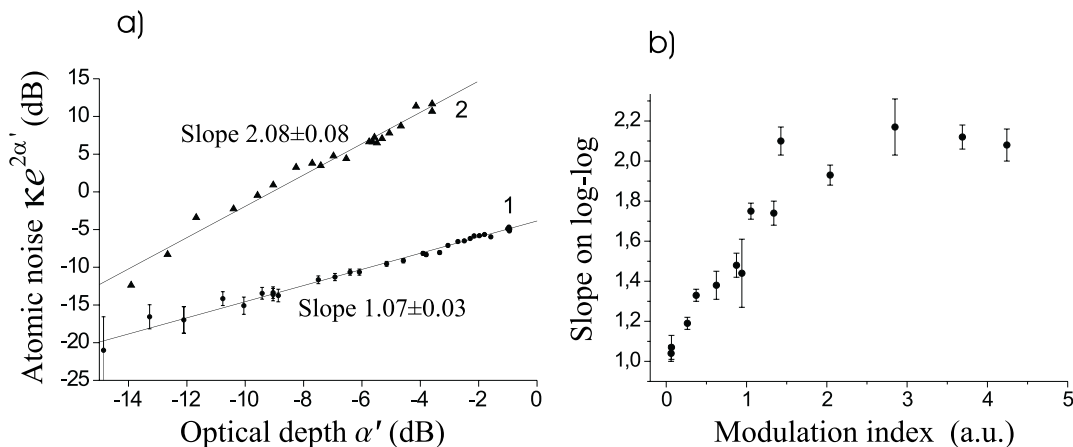


Figure 7.4: a) The spin noise κ normalized to $\exp(-2\alpha')$ versus α' . 1) Quantum noise for 0.34mW probe power. 2) Classical noise for 0.30mW probe power. b) "Slope of spin noise versus optical depth" as a function of the classical modulation index.

trapped atomic sample. We use a half-wave plate followed by a polarizer as our passive absorber. The absorption is changed simply by a rotation of the wave plate. We derive the (effective) optical depth of the passive absorber in the same way as for the atomic absorber. The data are shown in Fig. 7.3 (triangles), and they fit the $e^{-\alpha'}$ curve very well (solid line). The $e^{-\alpha'}$ dependence is expected for a shot noise limited probe and passive absorption according to Eq. (7.4) with $\kappa_0 = 0$.

We expect from Eq. (7.3) that the atomic spin noise will increase if the bandwidth of the atomic spin fluctuations γ_{spin} is reduced. This is in fact observed in a recent publication [5], where a graph very similar to Fig. 7.3 shows the atomic spin noise of ground state atoms.

We now subtract the fitted shot noise graph in Fig. 7.3 (trace 2) from the measured noise data (trace 1a) and obtain the pure spin noise, that is, κ in Eq. (7.4). The spin noise κ is then multiplied by $e^{2\alpha'}$ and plotted as function of the optical depth α' on a log-log scale in Fig. 7.4a (graph 1). The data are plotted on dB scales, although the optical depth is not a "power measurement". The dB is merely a short-hand notation for a plot of $10 \log[\kappa e^{2\alpha'}]$ versus $10 \log(\alpha')$. According to the theory, Eq. (7.4), the data should fall on a straight line with a slope of one. This slope of one is the characteristic linear dependence of the quantum noise of uncorrelated atoms on the number of atoms; the number of atoms is proportional to the optical depth. The $e^{-2\alpha'}$ normalization of the data compensates the readout reduction due to the probe absorption. The slope from a least square fit to the data in Fig. 7.4a (including error bars) is 1.07 ± 0.03 . This shows that the observed noise is indeed predominated by the noise of uncorrelated atoms, and from the previous bandwidth considerations regarding the classical number fluctuations, we conclude that the atomic quantum noise is observed.

We have previously in this chapter argued that classical atomic noise is quadratic in the number of atoms. The quadratic dependence can also be seen directly from Eq. (2.4) and Eq. (2.20). Equation (2.4) shows that the probe susceptibility is proportional to the density of atoms in the intermediate state. Equation (2.20) shows that the classical probe signal is quadratic in the susceptibility. A log-log plot of the classical atomic noise versus optical depth should therefore give a slope of two. We apply a 3MHz frequency modulation to the trapping laser to check that we actually do get a slope of two when classical noise is the predominant noise contribution. The modulation is achieved by applying a 3MHz voltage to a KNbO_3 crystal placed in the path of the trapping beams. The frequency modulation, obtained from the electrooptic properties of KNbO_3 , turns out to be very sensitive to temperature fluctuations. Hence, the measured data show more scatter than the data without modulation, even though the temperature of the crystal is actively stabilized.

Note that this situation with a frequency modulated trapping/pump field is identical to the experimental conditions in section 2.4. Here we concentrate on the signal strength as a function of modulation index and the number of atoms, whereas in section 2.4 we investigated the spectrum with a scanned probe frequency and a very strong modulation.

Graph 2 in Fig. 7.4a shows the observed noise versus optical depth when a substantial frequency modulation is applied to the trapping laser. The data points in graph 2 are obtained in the same way as the quantum noise data in graph 1. The linear fit gives a slope of 2.08 ± 0.08 . This is in fine agreement with the expected quadratic dependence for the classical noise. The fit does not include any error bars on the log scale. This is because the scatter in the data at large modulation depth increases with increasing optical depth (signal size) on a linear scale. Hence, on the log scale all the data points have the same uncertainty, independent of the optical depth.

Figure 7.4b shows what happens to the spin noise when the amount of classical FM applied to the trapping laser is varied. In the figure the slope calculated from graphs like Fig. 7.4a is plotted as a function of the modulation index. As a measure of the modulation index we could have used the rms voltage applied to the KNbO_3 crystal. However, because of the temperature and laser frequency drifts we use, instead, the square root of the recorded noise level at large optical depth as our modulation index measure.

The transition from (almost) quantum spin noise with a slope of one to (almost) classical noise with a slope of two is obvious in Fig. 7.4b. The data in Fig. 7.4b are taken over two days, and this can explain some of the scatter.

7.2.3 Atomic noise versus probe power

The resonant two-level saturation parameter can be expressed through a saturation power P_{sat} and the actual power P as $s'_0 = \Phi' \sigma'_0 / \pi \gamma' w'^2 = P / P_{sat}$. The saturation power for our 1.5mm probe diameter is $P_{sat} = 46 \mu\text{W}$. It is this saturation parameter (s'_0) that enters into Eq. (7.4). It is interesting to compare this saturation parameter to the actual degree of saturation in the experimental situation with a probe and a detuned strong pump in double-optical resonance

The resonant optical depth for two-level atoms scales with increasing probe power as $(1 + 2s'_0)^{-1}$ in the limit of small absorption. For arbitrary absorption we have

$$\frac{\partial}{\partial z} P(z) = \frac{-k}{1 + 2P(z)/P_{sat}} P(z) \quad (7.5)$$

$$\alpha' = -\ln \left(\frac{P(l)}{P(0)} \right)$$

l is the length of the atomic sample and k is a constant.

Figure 7.5a shows an actual measurement of the probe optical depth at the resonance at 30MHz as a function of probe power. The measurements (dots) are fitted to the solution of Eq. (7.5) with k and P_{sat} as free parameters. The fit gives an effective saturation power of³ $P_{sat}^{eff} = 0.95\text{mW}$. The excited state transition is clearly not saturated as fast as the theoretical saturation power P_{sat} predicts. This is related to the AC Stark splitting of the intermediate state, which reduces the excitation probability on the upper transition even when the probe is resonant with one of the AC Stark components.

The fit to the 0.34mW data in Fig. 7.3 gave $\kappa_0 s'_0 = 0.38$. With $P_{sat} = 46 \mu\text{W}$ we find $s'_0 = 7.4$, and the experimental κ_0 parameter is $\kappa_{0,exp} = 0.05$. Note that the large resonant saturation parameter is not necessarily in contradiction to the theoretical assumptions. The theory assumes weak probe excitation, and that can still be fulfilled with e.g. a detuned probe or an AC Stark splitted intermediate state. The result for $\kappa_{0,exp}$ is not that far from the theoretical value given below Eq. (7.4); $\kappa_{0,theo} = 0.16$. We cannot expect a better agreement with all the crude estimates and assumptions together with the

³We use P_{sat}^{eff} for the saturation power obtained from the fit in order to distinguish it from the theoretical value for the resonant saturation power $P_{sat} = 46 \mu\text{W}$.

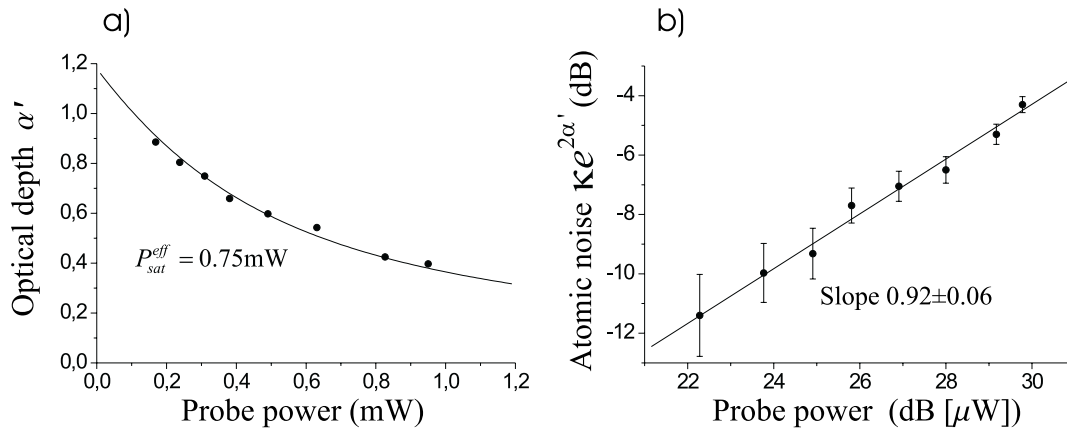


Figure 7.5: a) Probe optical depth versus probe power. A fit to the saturation formula (solution to Eq. (7.5)) gives an effective saturation power of $P_{sat}^{eff} = 0.75\text{mW}$. b) The normalized quantum spin noise $\kappa e^{2\alpha'}$ measured at $\alpha' = 0.32$ (-5dB) as a function of probe power. The scales are logarithmic with $1\mu\text{W}$ as the reference for the probe power.

nonideal experimental situation with a strong pump field, magnetic field gradients, polarization gradients etc.

The last test for the quantum spin noise is the dependence on probe power. This is not a test of the quantum nature, but it is still a test of the expected dependence in Eq. (7.4). The spin noise level at an optical depth of $\alpha' = 0.32$ (-5dB on the log-scale) is measured as a function of probe power. The measurements are shown in figure 7.5b on a log-log scale; i.e. $10\log[\kappa e^{2\alpha'}]$ at $\alpha' = 0.32$ versus $10\log[P/1\mu\text{W}]$. The theory for the measurements in Fig. 7.5b predicts a linear dependence with a slope of one on the log-log plot. The slope from a least square linear fit gives 0.92 ± 0.06 - an acceptable agreement.

7.2.4 A quantum spin noise limited experiment

We have performed a simple experiment, which shows a reduction in the signal-to-noise ratio (S/N) due to the atomic spin noise. The experiment is invented just to demonstrate that fundamental atomic quantum noise can limit the S/N in spectroscopy. A much more sophisticated demonstration is the atomic quantum noise limited stability of the atomic fountain frequency standard [1].

The probe laser is still locked at the resonance at 30MHz , but we remove the chopper and look at the signal directly on the spectrum analyzer. The SA frequency span is increased from zero to about 70kHz , and we apply frequency modulation to the trapping beams at 3.0MHz . We want in this experiment to measure the size of the modulation transferred from the pump laser via the atoms to the probe laser polarization. The signal from the SA is shown in Fig. 7.6. At 3.0MHz we see the peak from the classical modulation of the atoms (trace 1). The width of this peak is set by the 30kHz resolution bandwidth of the SA. The noise level outside the classical noise peak is given by the shot noise and the atomic quantum spin noise. This noise level sets the noise floor for our experiment, and it is also shown in trace 2 with the classical modulation turned off. For the same detected intensity but without the atoms present (in fact, slightly higher detected intensity just to be on the safe side), we get the shot noise level shown in trace 3. The shot noise is 0.3dB below the shot noise plus quantum spin noise level. We deduce that the spin noise contribution in curve 2 is about 8% of the shot noise level in curve 3. If perfectly spin squeezed atoms are used for this experiment (i.e. no contribution from the atomic quantum noise), we will gain 8% in the signal-to-noise ratio for the classical modulation measurement. This demonstrates

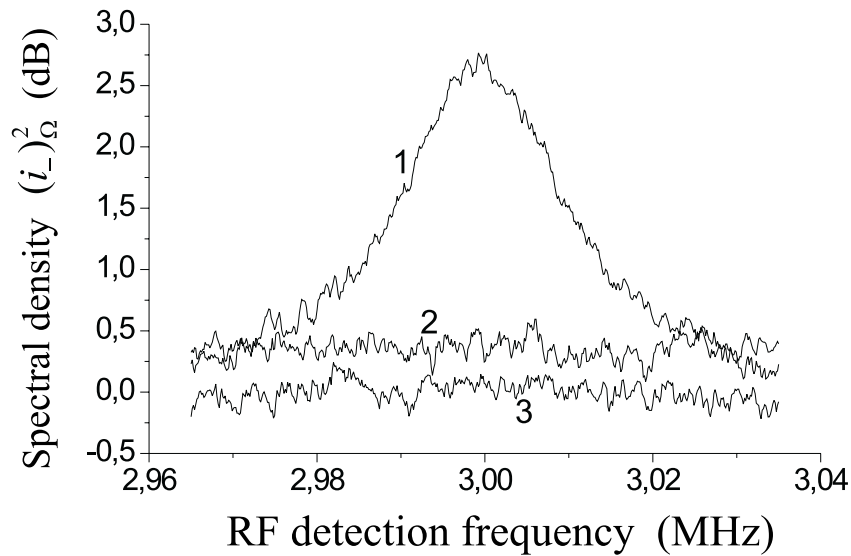


Figure 7.6: Spectroscopy signal with fixed laser frequencies and nonzero SA-span. 1) The "signal" consisting of shot noise + spin noise + classical signal. 2) The noise floor of shot noise + spin noise. 3) The shot noise level measured with a "passive" absorption equal to the atomic absorption in curve 1 and 2. SA settings: 70kHz full span and 30kHz resolution bandwidth. The reference for the vertical dB scale is the shot noise in curve 3.

that atomic quantum noise can be a limiting factor, and that spin squeezed atoms may be advantageous in spectroscopy experiments. A squeezed probe of light may be useful too, as we saw in chapter 3. However, the squeezed light probe only makes sense for small optical depth; just a moderate absorption, which corresponds to losses, deteriorates the squeezing substantially.

The 8% contribution from the atomic quantum noise is a small effect, but it can in principle be much larger if e.g. long-lived atoms are probed, see Eq. (7.3). The atomic quantum noise can indeed be the predominating noise source, as shown in the atomic fountain clock[1].

Chapter 8

Spin squeezing in a cold atomic ensemble

In the previous chapter we demonstrated that we indeed can observe the quantum noise of uncorrelated atoms. In chapter 4 we presented the theory for mapping the statistics of nonclassical light onto atoms. Thus, we are now ready to demonstrate a macroscopic entangled ensemble of atoms in a spin squeezed state. This demonstration is the topic of this chapter.

To the best of our knowledge, there are only two other experiments demonstrating atomic entanglement. Both of these experiments deal with only one pair of atoms at a time. The first experiment is by the group of S. Haroche [103], where highly excited Rydberg atoms exchange single photons with high finesse RF-cavities. One excited state atom can leave "half" a photon while traversing a cavity; i.e. the atom and the cavity mode are subsequently entangled as $(|1, g\rangle + |0, e\rangle) / \sqrt{2}$, where the first number is the cavity photon number and the second letter is the internal atomic state. When a second atom is injected into the cavity, it can pick up the "half" photon, and it becomes entangled with the first atom. This method for producing entanglement utilizes a strong coupling between a single cavity mode of the electromagnetic field and a single atom. This interaction allows an exchange between the atomic excitation and the excitation of the electromagnetic field.

Two ions in an ion trap have been prepared in an entangled state in the group of D. J. Wineland [104]. The ions are cooled to the vibrational ground state and subsequently entangled by utilizing laser pulses and a coupling of the ions through the collective vibrational motion.

We presented the first demonstration of multi-atom entanglement in a large ensemble of atoms in Ref. [6]. We also rely on an exchange between atomic excitation and excitation of the electromagnetic field. However, we do not require strong coupling between the field and individual atoms. Instead, we use a free propagating quantum field and a large ensemble of atoms. In this way we can have a strong coupling to the collective atomic properties although the single atom coupling is weak. In contrast to the previous experiments, we generate entanglement between a large number of atoms. In the present experiment we do not have a spatial separation of the entangled components as in the other two experiments. However, this may be achieved by the use of two Einstein-Podolsky-Rosen-correlated light beams for the quantum excitation instead of a single squeezed light beam [8].

A very recent experiment demonstrates spin squeezing in an ensemble of atoms after a quantum non-demolition (QND) measurement of a single component of the collective atomic spin with an off-resonant probe of light [92]. The QND experiment uses the idea that the polarization of an off-resonant probe field is rotated after interaction with an oriented atomic sample, see Eq. (2.15), (2.16) or (6.23). A measurement of the rotation angle provides the QND measurement of the atomic spin. After the measurement, the collective spin is projected onto a spin squeezed state with reduced quantum fluctuations [90, 91].

We continue this chapter with a section about the setup used in the spin squeezing experiment. This is followed by a section where we give a characterization of the physical system based on simple DC

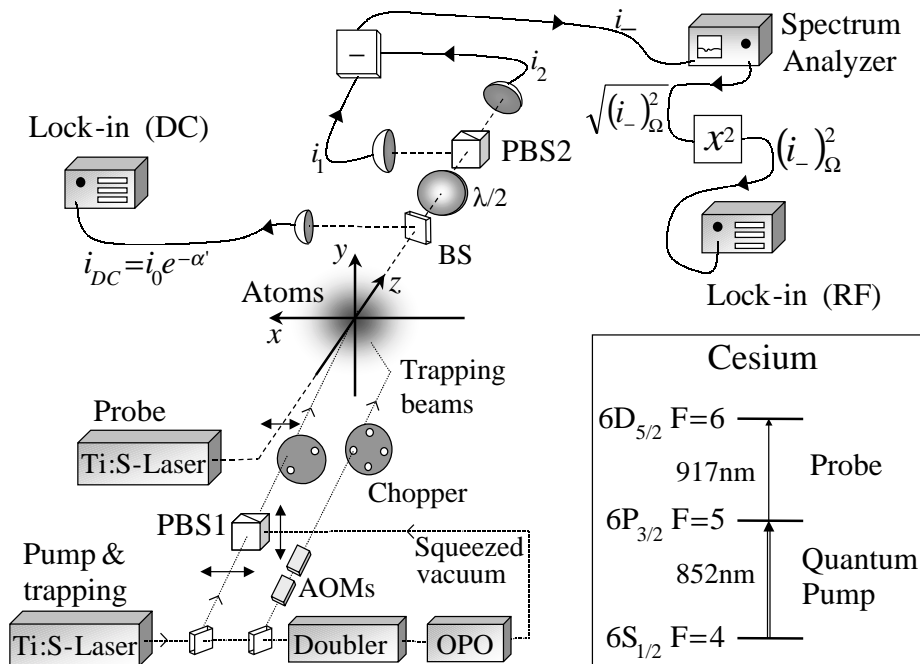


Figure 8.1: The experimental setup used for atomic spin squeezing measurements. Note that the two choppers in the figure are in the experiment one rotating disc with two sets of holes. The abbreviations BS and PBS stand for beamsplitter and polarizing beamsplitter. Further details about the setup are given in the text.

measurements. In the third section, we continue with the atomic noise measurements on uncorrelated atoms in a weak excitation field. Section four describes noise measurements on classically correlated atoms. In section five we finally demonstrate the spin squeezed state of atoms, and in the last two sections we analyze the spin squeezing data in more detail.

8.1 The spin squeezing setup

The setup for the spin squeezing experiment basically combines the squeezed light source setup in chapter 3 and the setup for the readout of atomic fluctuations in chapter 7. This means that we use the sub-threshold OPO for generation of polarization squeezed light. We use the magneto-optical trap (MOT) to collect a cold sample of cesium atoms, and we use a near-resonant probe field and a polarization interferometer to read out the atomic fluctuations. These devices or techniques have been described previously, but the implementation for the current experiment is somewhat different. The quantum pump acts on the $6S_{1/2} F=4 \rightarrow 6P_{3/2} F=5$ transition, and the intermediate state atoms are probed on the $6P_{3/2} F=5 \rightarrow 6D_{5/2} F=6$ transition. As usual we use F , F' and F'' for the angular momentum quantum numbers for the ground, intermediate, and excited state, that is $F'' = F' + 1 = F + 2 = 6$. The basic components of the setup are shown in Fig. 8.1 and will be described below.

8.1.1 The atomic sample and laser sources

The atomic sample used for observation of spin squeezing is a collection of cesium atoms trapped and cooled in a vapor-cell MOT (chapter 2). The diameter of the six trapping beams is about 25mm, and the typical power in each beam is 60mW. The laser generating the trapping light is the Microlase MBR-110 Ti:Sapphire laser pumped by an Ar-ion laser. The Ti:Sapphire laser is locked exactly at the $6S_{1/2}F = 4 \rightarrow 6P_{3/2}F = 5$ resonance, and the light used for trapping is subsequently detuned around 13MHz to the red by two acousto-optic modulators (AOMs) running at 124MHz and 111MHz respectively. We have about 300-350mW of resonant light before the two AOMs. The trapping beams go through an optical chopper running at about 500Hz. That gives "dark" periods of about 1ms to do measurements on the atoms without the presence of the strong trapping field. The atoms are recaptured and cooled again in the "bright" periods. The magnetic field gradient for the MOT is turned off at the time when the chopper turns off the trapping beams. The current in the coils generating the magnetic field gradient decays in about 200 μ s. We do not attempt to cancel out the residual field (ion pump, earth field etc.) in the dark periods. In fact, the residual field may be advantageous since the theory in chapter 4 is derived for an unpolarized ground state, and the residual magnetic field will help to prevent optical pumping due to the quantum excitation field. The repumping field (chapter 2) is not chopped; it is on all the time. The repumping field cannot do any harm; the atoms rarely end up in the $F = 3$ ground state and hence rarely see the repumping field.

The squeezed light source is driven by the same Ti:Sapphire laser as we use for trapping. This explains why the trapping/squeezing laser is locked at exact resonance. The center frequency of the squeezed vacuum field is needed exactly at the $6S_{1/2}F = 4 \rightarrow 6P_{3/2}F = 5$ resonance, whereas the trapping light must be red-detuned by a few atomic linewidths. Our squeezed light source takes about 700mW of laser power at 852nm, whereas the MOT can do with only 200mW. The cheapest solution in terms of laser power is to lock the laser at resonance and downshift the frequency of the trapping light. We require a total power of about 1.1W from the Ti:Sapphire laser, but because of losses in an optical isolator and an electro-optic modulator (EOM), the actual laser output is about 1.6W.

The demands on laser power also explain why the trapping/pump laser at 852nm and the probe laser at 917nm have been swapped since the experiments in the previous chapter. The commercial Ti:Sapphire laser (MBR-110) is designed to give a large and frequency stable output. With only 20W of green light from a single Ar-ion laser for pumping both Ti:Sapphire lasers, we choose to use the MBR-110 for trapping and squeezing at 852nm and the home-made Ti:Sapphire laser for the 917nm probe. In the experiments we only need about 15mW of power at 917nm (including locking and intensity stabilization), so the threshold of the home-made laser is minimized by the use of a very small output coupler.

8.1.2 The quantum pump

We generate the squeezed vacuum field in the same way as we described in detail in chapter 3. The basic parts of the setup are shown in Fig. 3.4, except that we now split off about 350mW of the laser output for the MOT trapping beams. The coherent component of the quantum excitation field, which is resonant with the $6S_{1/2}F = 4 \rightarrow 6P_{3/2}F = 5$ transition, is provided by a part of the MBR-110 laser output. The pump field has typically a power of 50 μ W and a beam diameter of $2w = 4.0$ mm at the trap site. The coherent part of the pump is mode cleaned and stabilized in power by the mode cleaning cavity in Fig. 3.4. This field is linearly polarized along the x -axis and mixed with the orthogonally polarized squeezed vacuum field on PBS1 (Fig. 8.1).

The polarization squeezed light must be (almost) completely absorbed by the atoms in order to produce the spin squeezed state. The typical resonant optical depth α_0 for the pump field is in the range of three to five. It is important that the relative phase between the squeezed vacuum field and the coherent field is actively stabilized at e.g. $\theta = 0$ for squeezed \hat{S}_z or $\theta = \pm\pi/2$ for squeezed \hat{S}_y , see Eq. (3.17). We cannot absorb the squeezed light in the atoms and at the same time measure the degree of squeezing on a pair of photodetectors as required for the phase stabilization loop (see page 35). The solution to this dilemma comes from the fact that the quantum pump is only used for atomic

excitation in about 25% of the time; this is discussed in more detail in section 8.1.3. In the remaining 75% of the time, the quantum pump is reflected off a gold coated chopper disc and onto a detection setup used for \hat{S}_y measurements and for the phase locking loop. The phase locking detection system is identical to the detection system in Fig. 3.4, and it is composed of the half-wave plate, PBS2, and a pair of photodetectors with a peaked response at 3.0MHz, (the phase locking setup is not included in Fig. 8.1). We use the same 3MHz detectors as described in section 2.4.1 except for a reduced bandwidth. Here we use a bandwidth of about 180kHz, which lowers the noise equivalent power to nearly $25\mu\text{W}$. The phase locking method is described in detail on page 35. In each measurement cycle we use about 3ms for phase stabilization and 1ms for quantum excitation of the atoms. The lock-in amplifier in the phase locking feedback loop has a time constant of 33ms. The chopping of the phase locking signal reduces the quality of the phase lock, and that reduces the average amount of squeezing. Moreover, each spin squeezing experiment is carried out over several hours (up to 12h). It is difficult to keep the crystal temperatures and all the alignment at the optimum over this extended period, and the typical squeezing measured on the phase locking detectors is around -2.3dB relative to the shot noise level. The fact that the squeezing path is different for the phase locking and for excitation of atoms is found to deteriorate the squeezing even more. This can be caused by different phase shifts or absorptions for the two polarizations in each of the two paths. The squeezing at the trap site is estimated to be $-1.8 \pm 0.2\text{dB}$. This estimate is based on a squeezing measurement with a pair of detectors right after the MOT vacuum chamber and with the phase locking system running as in the spin squeezing experiments, but without atoms in the trap. The amount of anti-squeezing available at the trap site is estimated to be $4.5 \pm 0.6\text{dB}$ for the data presented in this chapter. This squeezing/antisqueezing is unfortunately not at the level of the best observed squeezing/antisqueezing at 852nm in Fig. 3.5; -3.0dB and +7.9dB. However, we do not expect an efficient mapping of correlations from the squeezed light onto the atoms. The theoretical (ideal) mapping efficiencies are shown in Fig. 4.2 and 4.3. Therefore, it will be the mapping efficiency and not the available squeezing in light that ultimately limits the observed amount of spin squeezing.

We note that the bandwidth of the produced squeezing and antisqueezing is given by $\Gamma_{cav}(1 \pm \sigma)$. Γ_{cav} is the OPO bandwidth of $\Gamma_{cav}/2\pi = 15\text{MHz}$ (page 33), σ is the pump parameter, which in our case is around 0.5 (section 3.4), and $+/-$ is for squeezing/antisqueezing. We see that the squeezing/antisqueezing bandwidths are much larger than the frequency at which the phase locking system measures squeezing (3.0MHz) and the detection frequency for the atomic spin squeezing (1.9MHz, see the following section).

8.1.3 The probe and the lock-in detection scheme

The home-made Ti:Sapphire laser generates the probe light at 917nm. The probe frequency is close to the $6P_{3/2} F = 5 \rightarrow 6D_{5/2} F = 6$ resonance in Cs. We lock the probe frequency in the same way as described in section 7.1. We actively stabilize the probe power by using the transmission of an optical resonator locked on the side of a fringe. This is similar to the locking of the mode cleaning cavity described on page 34. This stabilizes the probe power over hours to better than 1%, and in addition we get a nice Gaussian beam profile. The probe is linearly polarized along x , and it is propagating at an angle of about 1.5° relative to the quantum pump beam. The two fields are overlapped at the trap site. The typical probe power for the experiments is $190\text{-}250\mu\text{W}$ with a beam diameter at the trap site of $2w' = 3.7\text{mm}$. Before the probe polarization is analyzed, we reflect 4% of the light onto a DC photodetector. This detector is used to measure the probe transmission $e^{-\alpha'}$, from which we can derive the optical depth α' . We use a $\lambda/2$ plate to rotate the probe polarization by 45° followed by a polarizing beamsplitter (PBS2, Fig. 8.1) to analyze the probe polarization. The difference in the photon fluxes in the two output arms of PBS2 is proportional to the probe Stokes parameter \hat{S}'_y . The two photon fluxes are measured by two fast photodetectors producing photocurrents i_1 and i_2 . Two interference filters, with a transmission of 82% at 917nm and less than 10^{-5} at 852nm, are placed right in front of the two photodetectors in order to prevent any stray light at 852nm from hitting the detectors.

The two detector photodiodes have a quantum efficiency better than 98%, and the detectors are tuned

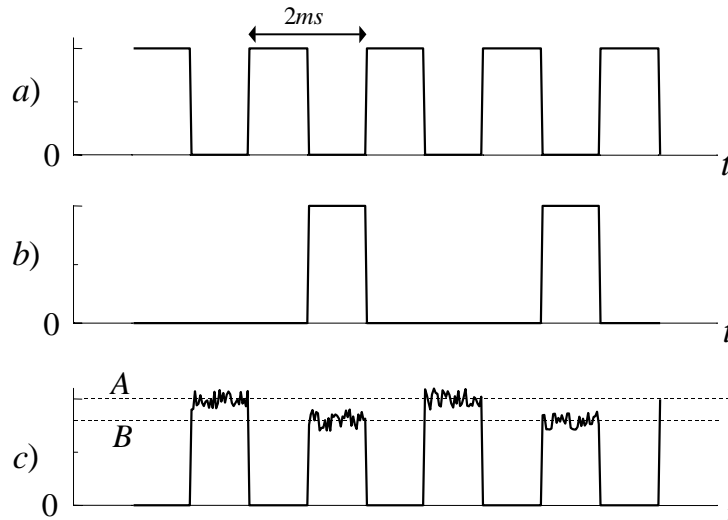


Figure 8.2: Schematic picture of the lock-in technique. a) The trapping beam power versus time. b) The power in the weak excitation field; out of phase and at half the frequency of the trapping beam modulation. c) The signal from the spectrum analyzer after the electronic gate. A is the noise level for the probe shot noise when no atoms are in the F' state. B is the noise level with (reduced) shot noise plus atomic noise. The RF lock-in amplifier measures $\Delta V_{RF} \propto A - B$.

to 1.9MHz with a 100kHz bandwidth. The two currents i_1 and i_2 are subtracted in a hybrid junction, and the differential photocurrent i_- , which is proportional to \hat{S}'_y , is sent to a spectrum analyzer (SA) used for noise measurements. The SA is set at the frequency $\Omega/2\pi = 1.9\text{MHz}$ with zero frequency span. The resolution bandwidth is set at 300kHz, and the video bandwidth is set at 10kHz. The resolution bandwidth is larger than the detector bandwidth, and the latter sets the effective bandwidth in the experiment. When the SA runs on a linear scale, it provides a video output which is proportional to $\sqrt{(i_-)_{\Omega}^2}$. The video output of the SA is squared electronically to obtain a signal proportional to $(i_-)_{\Omega}^2$ with a small contribution from the electronic noise. The noise equivalent power for this detection system is approximately $10\mu\text{W}$, and it is set mainly by the electronic noise of the photodetectors.

The hybrid junction has an output junction, which gives the sum of the two photocurrents. We will use the sum junction and the resulting spectral density $(i_+)_{\Omega}^2$ for comparison measurements in one of the subsequent experiments.

The quantum pump is only turned on in half of the dark periods, as shown in Fig. 8.2. This is done by using a second set of holes in the chopper used for chopping the trapping beams. In Fig. 8.1 we represent the chopper with two sets of holes by two choppers running out of phase and with twice as many holes in the trapping beam chopper. In this way we have weak excitation of the atoms in every second dark period. The probe, which is on all the time, interacts with the excited atoms in F' in every second dark period, and that results in a 250Hz modulation of the transmitted probe power. We use two digital lock-in amplifiers (Stanford Research Systems, model SR810) with a 250Hz reference signal to measure the difference in the probe signals when the weak pump is on and when the weak pump is off; this is illustrated in Fig. 8.2. One lock-in amplifier (DC) is used for the signal from the DC photodetector, and it gives a voltage proportional to $1 - e^{-\alpha'}$. We define ΔV_{DC} as the DC lock-in voltage; $\Delta V_{DC} = k_{DC}(1 - e^{-\alpha'})$. k_{DC} is a proportionality constant, which depends on the probe power, the detector gain, and the lock-in amplifier gain. We can measure k_{DC} by comparing

ΔV_{DC} to a direct measurement of the probe absorption. Another lock-in amplifier (RF) is used after the squared video output of the spectrum analyzer to measure the change in the probe polarization noise. We define ΔV_{RF} as the RF lock-in voltage; $\Delta V_{RF} = k_{RF}(1 - e^{-\alpha'} - \kappa)$. The first two terms are similar to the terms in ΔV_{DC} , and they represent the reduction in shot noise due to probe absorption. κ represents any excess probe noise caused by interaction with the atoms. The parameter k_{RF} depends on probe power, detector gain, resolution bandwidth, and the lock-in amplifier gain. The theory predicts $\Delta V_{RF}/k_{RF} = 1 - (e^2 g^2 \Phi')^{-1} (i_-)_{\Omega}^2$ with $(i_-)_{\Omega}^2$ given by Eq. (6.38)¹. We can measure k_{RF} by applying a passive absorption modulated at 250Hz to the probe field. The pump field is not present when this calibration is made, which means that $\kappa = 0$. Instead we reduce the probe power in every second dark period by an amount that corresponds to the typical atomic probe absorption. This modulation of the probe power is achieved by adding a small modulated voltage to the feedback loop that stabilizes the probe power. Knowing α' from ΔV_{DC} and measuring ΔV_{RF} makes it possible to determine k_{RF} . We tested that ΔV_{RF} and ΔV_{DC} are proportional for the passive modulation, and this shows that the probe is indeed shot noise limited. Note that the measured lock-in voltage ΔV_{RF} is insensitive to the background noise (electronic noise).

The probe absorption and the probe polarization noise from the bright periods will not show up in the average lock-in signals because the frequency for this modulation is 500Hz; this is twice the lock-in reference frequency. However, the signals from the bright periods will, for a finite averaging time, contribute to the fluctuations in the measured lock-in voltages. We use an electronic gate just before the two lock-in amplifiers to reduce especially the fluctuations in ΔV_{RF} . The gate is only open in the dark periods, and hence any signals or fluctuations from the bright periods are eliminated. Furthermore, the gate is kept closed in approximately the first 250 μ s of the dark periods, while the magnetic field gradient decays.

In the atomic noise measurements we generally average the lock-in voltages for about six minutes with all parameters fixed. We use a time constant of three seconds with a 24dB/oct roll off on both lock-in amplifiers. The lock-in voltages are monitored on a digital oscilloscope (HP 54601B), which averages over the last eight measurements. A computer reads the oscilloscope signals once a second and stores the data on a disk. The data are stored for about six minutes for adequate statistics.

8.2 DC absorption measurements

We can obtain useful information about the properties of the atomic sample from DC measurements. We measure the absorption spectrum (optical depth) obtained from the DC lock-in voltage as a function of probe detuning. We do not apply the squeezed vacuum to the pump; we merely excite the atoms with a coherent field. The pump frequency is fixed at the $6S_{1/2} F = 4 \rightarrow 6P_{3/2} F = 5$ resonance, while the probe frequency is scanned across the $6P_{3/2} F = 5 \rightarrow 6D_{5/2} F = 6$ resonance. The probe laser frequency is locked during the measurement, but an AOM in the locking setup makes it possible to change the locking point and hence scan the probe frequency. We derive the probe detuning from the frequency of the RF signal driving the AOM.

We first consider the case of a weak probe and a weak pump field. Fig. 8.3a shows the measured probe optical depth as the probe detuning is scanned across resonance (dots). We take zero detuning to be at the frequency of maximum optical depth. The probe and pump powers are 2 μ W and 11 μ W respectively. This corresponds to a resonant saturation parameter $s'_0 = 7 \cdot 10^{-3}$ for the probe and $s_0 = 1.7 \cdot 10^{-2}$ for the pump. The measured resonant optical depth is $\alpha'_0 = 0.083$. We can calculate the theoretical optical depth from the formula $\alpha'_0 = \sigma'_0 N' / \pi w'^2$. We assume that the atomic sample is almost unpolarized and use Eq. (6.16) for the resonant absorption cross section. $N' = \Phi / \gamma$ is the number of atoms in the excited state, and Φ is the photon flux in the (almost) completely absorbed pump field. We find the theoretical resonant optical depth to be 0.021, and it is reduced to 0.019 when the Gaussian profiles of the pump

¹This expression for ΔV_{RF} assumes that we actually look at the differential photocurrent. If we choose to look at the sum $i_+ = i_1 + i_2$, we should use $(i_+)_{\Omega}^2$ and Eq. (6.39) instead.

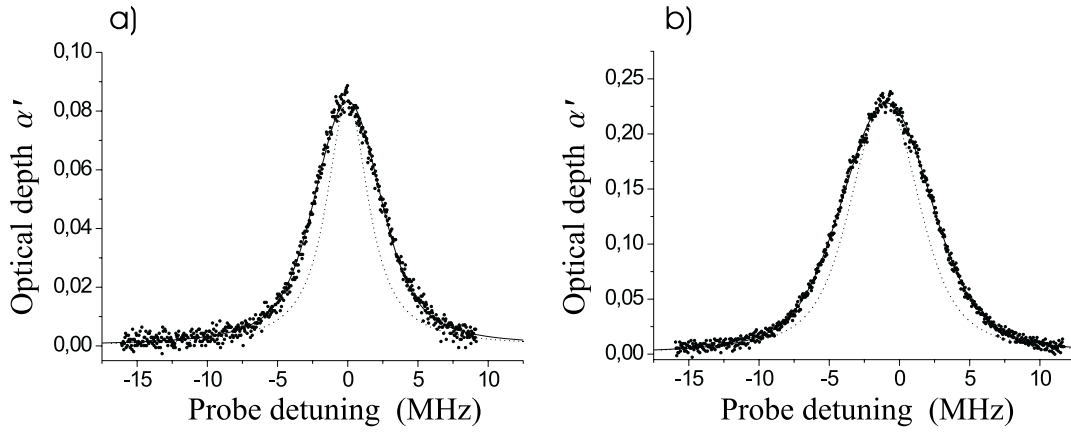


Figure 8.3: a) Dots: Probe optical depth as a function of probe detuning. Probe power: $2\mu\text{W}$, pump power: $11\mu\text{W}$. The sweep time for the scan is 14sec., the time constant on the DC lock-in amplifier is 3ms and the signal is averaged over 8 sweeps. Solid line: Voigt fit. Dotted line: theoretical curve. b) The same as a), except for a pump power of $54\mu\text{W}$.

and the probe beams are taken into account. We find that the theoretical optical depth is about four times smaller than the measured value. We believe that this discrepancy is a result of radiation trapping in the optically dense atomic sample. The fluorescence photons are reabsorbed before they escape the atomic cloud if the optical depth is large. Radiation trapping can be avoided if one uses a pencil shaped atomic sample with a length much larger than the diameter. This gives a small transverse optical depth, and the fluorescence photons can escape in the transverse directions. However, our MOT produces an almost spherical cloud of atoms. The effect of radiation trapping can be estimated by a simple Monte Carlo simulation of the diffusion of photons in the optically dense gas. We use a Gaussian density profile for the MOT and a Gaussian spatial mode for the pump field in such a simulation. The simulation neglects saturation effects, and it assumes that all photons are at exact resonance. We find for the typical resonant optical depths (α_0) for our MOT that each pump photon will scatter about $0.9\alpha_0$ times before it escapes the atomic cloud. This corresponds roughly to an effective increase in the pump power by a factor of $(1 + 0.9\alpha_0)$. The typical pump optical depth for the experiments in this chapter is in the range of three to five. Thus, the effectively increased pump power, due to radiation trapping, explains the measured probe optical depth in Fig. 8.3a.

The reemitted photons are not correlated because of the random atomic decay process. Hence, the radiation trapping results in a substantial atomic excitation caused by uncorrelated photons even for a perfectly squeezed pump field. We will later in this chapter look into this undesirable effect of radiation trapping in relation to spin squeezing.

The theoretical absorption lineshape for the weak probe in Double-optical resonance with a weak pump is a Lorentzian profile with a linewidth set by the upper state decay rate γ' , see Eq. (6.15) and (2.4). The decay rate γ' is measured to $\gamma'/2\pi = 3.1 \pm 0.1\text{MHz}$ in Ref. [29], although the authors note that the true decay rate may be a little smaller. The solid line in Fig. 8.3a is the result of a fit to a Voigt² profile with a Gaussian width of $3.8 \pm 0.1\text{MHz}$ and a Lorentzian width of $3.1 \pm 0.1\text{MHz}$. If we fit the data in Fig. 8.3a with a pure Lorentzian (Gaussian) profile, we get a χ^2 value for the fit that is 2.3 (2.9) times larger than for the Voigt fit. We conclude from the Gaussian contribution to the lineshape that some excess broadening is present in Fig. 8.3a.

We can learn more about the excess broadening by looking at the probe absorption with a stronger

²We choose a Voigt fit because it has the expected Lorentzian shape in the wings, but allows for some non-Lorentzian broadening closer to resonance. The true profile is probably not an exact Voigt profile.

pump field. In Fig. 8.3b we show the absorption measurements for a $54\mu\text{W}$ pump field ($s_0 = 0.080$) and with the rest of the parameters as in Fig. 8.3a. We observe that the increased pump power results, as expected, in an increased resonant optical depth. Furthermore, the linewidth is increased, and the detuning for maximum absorption is shifted to -0.9MHz . The displacement of the absorption profile is explained by the Doppler shift induced by acceleration of the atoms. This acceleration is caused by photon absorption from the unidirectional pump field. The atoms are accelerated during each measurement cycle of 1ms (Fig. 8.2). The acceleration, and hence the average Doppler shift, depends on the photon flux in the pump field. The observed displacement is consistent with a simple estimate of the total number of photons (or photon momenta) absorbed by a single atom during 1ms .

A Voigt fit to the data in Fig. 8.3b gives a Lorentzian width of $2.9 \pm 0.1\text{MHz}$ and a Gaussian width of $6.0 \pm 0.1\text{MHz}$ (solid line). The linewidth increase, as compared to Fig. 8.3b, has several contributions. The acceleration during the 1ms measurement cycle results in some broadening of the line. The atomic velocity changes in time, and in the measurement we effectively add the contributions corresponding to the velocities (or Doppler shifts) at different times within the 1ms measurement cycle. In addition, the effective intensity in the pump field approaches the saturation intensity when the effect of radiation trapping is included. We see from Eq. (2.4) that the profile becomes non-Lorentzian at small probe detunings when s_0 approaches unity.

We can write the theoretical optical depth spectrum including saturation and the average over atomic velocities as

$$\alpha'(\Delta') = \frac{2\pi l}{\lambda a s_0} \int_0^{a s_0} \chi_i \left(\Delta + \frac{917}{852} x, \Delta' + x, s_0 \right) dx \quad (8.1)$$

$\chi_i(\Delta, \Delta', s_0)$ is the imaginary part of the probe susceptibility in double-optical resonance for the pump detuning Δ , probe detuning Δ' , and a resonant pump saturation parameter s_0 . The explicit expression for χ_i is given in Eq. (2.4). The ratio $917/852$ is the ratio between the Doppler shifts on the pump and probe transition. The integral over x includes the changing velocity (Doppler shift) during the measurement. We assume that the maximum Doppler shift is linear in the pump power. This allows us to write the upper limit as $a s_0$, with a as a constant. We take s_0 to be the same for all atoms, whereby we neglect the attenuation of the pump beam and the transverse beam profile. We use the pump detuning Δ that gives the maximum probe absorption for the $11\mu\text{W}$ pump in accordance with the measurements. We use s_0 values that are six times larger than for the pump field alone to include the effect of radiation trapping. We find $a \simeq 2$ if we require a displacement of the absorption profile by 0.9MHz when we go from $s_0 = 6 \times 0.017$ to $s_0 = 6 \times 0.08$. The calculated optical depth spectra $\alpha'(\Delta')$ for $a = 2$ and $s_0 = 0.10$ ($s_0 = 0.48$) are shown in Fig. 8.3a (8.3b) as dotted lines, and they are scaled in amplitude to match the measurements.

A comparison of the measurements and the theoretical spectra in Fig. 8.3 shows that the measured linewidths cannot be fully explained by pump saturation, radiation trapping, and acceleration. If the theoretical spectra in Fig. 8.3a and 8.3b are further averaged over a Gaussian distribution with a width of 3.8MHz , they do coincide with the actual measurements. The broadening effects discussed so far have all been homogeneous, i.e. all atoms have the same resonance frequency at a given time. It is not unlikely that inhomogeneous contributions, like the thermal Doppler broadening, will have a significant contribution to the linewidth. The temperature of the usual "large" MOT gives relatively small Doppler broadening (chapter 2). However, the present situation is somewhat different with the chopped trapping beams and the unidirectional pump field in the dark periods. In addition, the non-uniform pump intensity results in different accelerations of atoms at different positions, and this also adds to the inhomogeneous line broadening.

In most of the spin noise experiments presented in the following sections, we use a probe power of about $190\mu\text{W}$. This corresponds to a resonant saturation parameter of $s'_0 = 0.69$. The stronger probe is required for an adequate signal-to-noise ratio in the atomic noise experiments (see page 73). The drawback of the stronger probe is additional modifications of the lineshape. In Fig. 8.4 we plot optical depth measurements for $190\mu\text{W}$ probe power and $46\mu\text{W}$ pump power. The data are taken together with

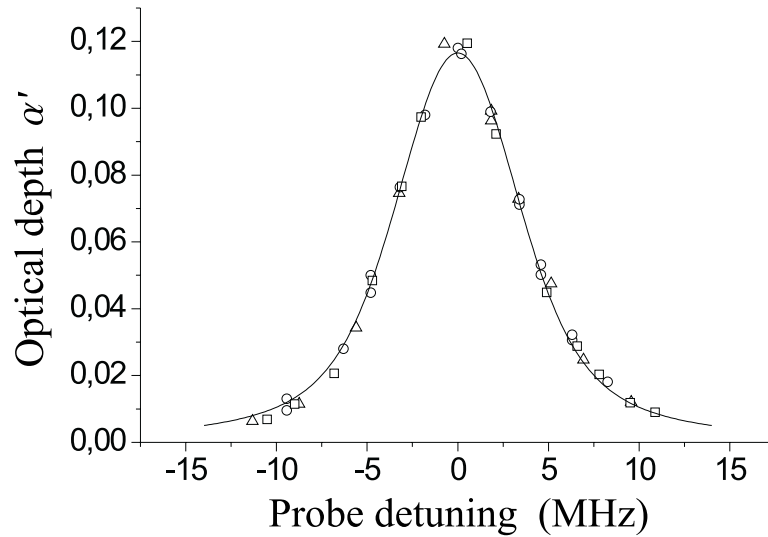


Figure 8.4: Probe optical depth versus detuning. The three different symbols represent data from three different days. The solid line is a Voigt fit with a Lorentzian linewidth of 4.6MHz and a Gaussian linewidth of 5.4MHz.

the coherent excitation spin noise data presented in the following section. The three different symbols in Fig. 8.4 correspond to data from three different days. The data are averaged measurements at different fixed detunings, i.e. we do not scan the probe frequency in these measurements. The absorption data for each day is scaled to the average of the three days. The relative change in amplitudes by this scaling is less than 12%. The data fit a Voigt profile (solid line) with a Gaussian width of 5.4MHz and a Lorentzian width of 4.6MHz. The increase in the Lorentzian component is expected for the larger probe power. The power broadened absorption linewidth for a two-level atom is given by $\gamma' \sqrt{1 + 2s'_0}$, with γ' as the upper state decay rate. Although the two-level result is not exact in the double-optical resonance situation, it still explains the origin for the increase in the Lorentzian component in Fig. 8.4.

The theory for the spin noise spectra in chapter 4 and 6 is developed in the limit of weak pump and probe fields and with a possible inhomogeneous broadening. It is difficult to incorporate all the effects that modify the DC absorption spectrum in Fig. 8.4 into the spin noise theory. We will instead use the lineshapes determined by the functions \tilde{D}^2 , \tilde{D}^2 , L^2 , and \tilde{L}^2 from chapter 6, but with the Lorentzian width adjusted to the value for the Lorentzian width in the fit in Fig. 8.4. For the inhomogeneous broadening we use a simple Gaussian distribution with the Gaussian width from the fit in Fig. 8.4. Although this is a somewhat heuristic inclusion of the experimental imperfections, it does give a adequate description of the spin noise measurements in the following sections.

8.3 Atomic spin noise - coherent excitation

We now return to the atomic spin noise in the case of coherent light excitation. This subject was investigated in the previous chapter, but only for a strongly saturating pump field. In this section we consider a non-saturating pump field, and we look into the details of the spectrum of atomic noise versus probe detuning.

The relevant quantity in the measurements of atomic spin noise is κ , which is defined as the atomic noise transferred from the atoms onto the probe and normalized to the shot noise of the probe in the absence of atoms. The theoretical expression for κ is for i_- measurements derived from Eq. (6.38)

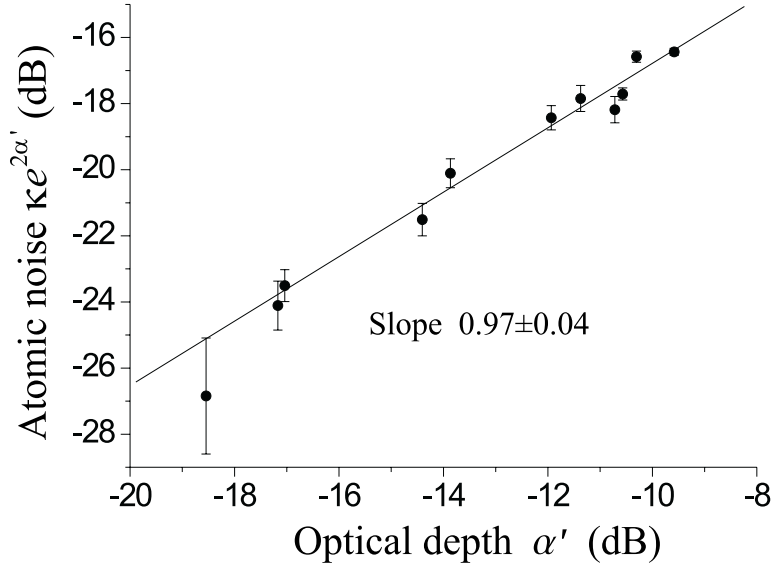


Figure 8.5: Normalized atomic noise $\kappa e^{2\alpha'}$ versus probe optical depth for resonant probe and pump fields. Probe saturation parameter $s'_0 = 0.40$. The solid line is a linear fit to with a slope of 0.97 ± 0.04 . The theoretical slope for the quantum noise of uncorrelated atoms is one. By the units "dB" we mean a plot of $10 \log \kappa e^{2\alpha'}$ versus $10 \log \alpha'$.

$$\kappa = \frac{(i_-)_{\Omega}^2}{e^2 g^2 \Phi'} - e^{-\alpha'} = \alpha'_{0,unpol} e^{-2\alpha'} s'_0 \frac{9\gamma'}{32N'(F'+1)^2(2F'+3)^2} \times \left\{ (2F'+3)^2 \left(\hat{F}'_z \right)_{uc,\Omega}^2 \widetilde{D}^2(\Omega, \Delta') + \left(\hat{F}'_x \hat{F}'_y + \hat{F}'_y \hat{F}'_x \right)_{uc,\Omega}^2 \widetilde{L}^2(\Omega, \Delta') \right\} \quad (8.2)$$

The terms proportional to $(\hat{F}'_z)_{c,\Omega}^2$ and $(\hat{F}'_x \hat{F}'_y + \hat{F}'_y \hat{F}'_x)_{c,\Omega}^2$ in Eq. (6.38) do not contribute for coherent excitation. The spectral densities $(\hat{F}'_z)_{uc,\Omega}^2$ and $(\hat{F}'_x \hat{F}'_y + \hat{F}'_y \hat{F}'_x)_{uc,\Omega}^2$ are calculated from Eq. (4.31) and (4.50) with $R_{z,y}(\Omega) = 1$ for the coherent pump field. With these results inserted into Eq. (8.2) together with $\Omega/2\pi = 1.9\text{MHz}$ and $\gamma/2\pi = 5.2\text{MHz}$, we find

$$\kappa = \alpha'_{0,unpol} e^{-2\alpha'} s'_0 \frac{\gamma'}{\gamma} \left(0.20 \widetilde{D}^2(\Omega, \Delta') + 0.021 \widetilde{L}^2(\Omega, \Delta') \right) \quad (8.3)$$

The current setup is different and the pump power is much smaller than in chapter 7. The first thing to check with the new setup is whether it is possible to see the atomic quantum noise. The atomic quantum noise for uncorrelated atoms is for small α' linear in the number of probed atoms and hence linear in α' . On the other hand, classical or technical noise is found to produce noise quadratic in the number of probed atoms. In the same way as in chapter 7, we identify the quantum noise of uncorrelated atoms by a linear dependence on α' . The optical depth is adjusted by varying the power in the repumping beam and thereby the number of trapped atoms. The optical depth of the pump field can of course not be sustained at a high level in this experiment, but this is not a problem for the coherent excitation. In Fig. 8.5 we plot the measurements of $\kappa e^{2\alpha'} = (1 - e^{-\alpha'} - \Delta V_{RF}/k_{RF}) e^{2\alpha'}$ as a function of $\alpha' = -\ln(1 - \Delta V_{DC}/k_{DC})$. We use the same logarithmic scales (dB) as in Fig. 7.4a. The measurements are carried out close to resonance, and each data point is averaged for about six minutes

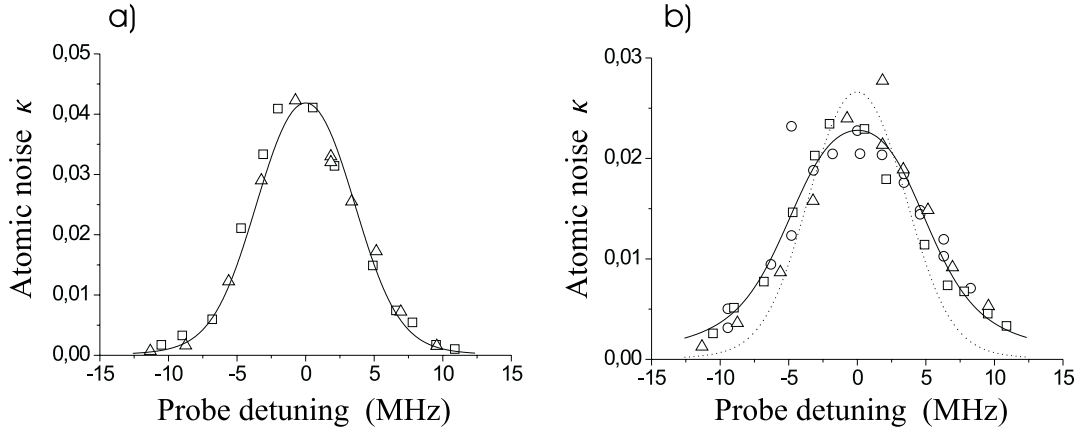


Figure 8.6: Measured atomic noise κ as a function of probe detuning. Measurements from different days have different symbols. a) Atomic noise when the photocurrents are added (i_+). The solid line is a fit to $a\widetilde{L}^2(\Omega, \Delta')e^{-2\alpha'}$ with a as a free parameter. b) Atomic noise when the photocurrents are subtracted (i_-). The dotted line is a fit to $a\widetilde{L}^2(\Omega, \Delta')e^{-2\alpha'}$ with a as a free parameter. The solid line is a fit to $[b\widetilde{D}^2(\Omega, \Delta) + c\widetilde{L}^2(\Omega, \Delta)]e^{-2\alpha'}$ with b and c as free parameters.

as described in section 8.1.3. The probe power for this experiment is $110\mu\text{W}$ and the pump power is $50\mu\text{W}$. In this particular measurement we use a somewhat larger pump diameter ($2w = 4.7\text{mm}$) than in the other experiments in this chapter. The solid line in Fig. 8.5 is linear fit with a slope of 0.97 ± 0.04 . The fit confirms that the atomic noise is linear in the number of probed atoms, and we conclude that the quantum spin noise of uncorrelated atoms can be observed in the dark periods with a weak unidirectional pump beam.

In the next experiment we maximize the number of trapped atoms and look at the atomic noise as a function of probe detuning. We first look at the measured noise when the two photocurrents i_1 and i_2 are added. We use the subscript $+$ on κ for the atomic noise measured in i_+ . We find the theoretical expression for κ_+ from Eq. (6.39)

$$\kappa_+ = \frac{(i_+)^2}{e^2 g^2 \Phi'} - e^{-\alpha'} = \alpha'_{0,unpol} e^{-2\alpha'} s'_0 \frac{9\gamma'}{32N'(F'+1)^2(2F'+3)^2} \times \left(\hat{F}'_x - \hat{F}'_y + \hat{F}'_z + \hat{P} \right)_{uc,\Omega}^2 \widetilde{L}^2(\Omega, \Delta') \quad (8.4)$$

We plot the measured atomic noise κ_+ as a function of probe detuning Δ' in Fig. 8.6a. Each data point is obtained by averaging the two lock-in voltages ΔV_{DC} and ΔV_{RF} for about six minutes while keeping all parameters constant. This long averaging time is important because the atomic noise contribution is quite small compared to the shot noise of the probe. The different symbols in Fig. 8.6a correspond to measurements from different days (same symbols/days as in Fig. 8.4). We choose to make the same scaling of the data sets in Fig. 8.6a as in Fig. 8.4 to compensate for the different resonant optical depths on the different days. This scaling is valid because the atomic noise is (almost) linear in α' at small α' . The probe and pump parameters for the data in Fig. 8.4 and in Fig. 8.6 are identical. We have tested that the noise observed in the sum photocurrent i_+ is linear in the number of atoms; i.e. we do observe the atomic quantum noise in i_+ .

The solid line in Fig. 8.6a is a fit to the theoretical expression $a\widetilde{L}^2(\Omega, \Delta')e^{-2\alpha'}$ from Eq. (8.4) with the amplitude a as only the free parameter and $e^{-2\alpha'}$ from the Voigt fit in Fig. 8.4. The function $\widetilde{L}^2(\Omega, \Delta')$ depends on three parameters besides the probe detuning Δ' , see Eq. (6.20) and (6.37).

These parameters are the detection frequency Ω , the "Lorentzian" linewidth γ' and the inhomogeneous linewidth γ_{Dop} . We use the detection frequency $\Omega/2\pi = 1.9\text{MHz}$. We include the saturation effects and the possible inhomogeneous broadening by using the Lorentzian and Gaussian widths from the fit in Fig. 8.4 for the parameters γ' and γ_{Dop} . Hence, we use a Gaussian inhomogeneous broadening with $\gamma_{Dop}/2\pi = 5.4\text{MHz}$ and a "Lorentzian" width of $\gamma'/2\pi = 4.6\text{MHz}$ in $\widetilde{L}^2(\Omega, \Delta')$.

We see in Fig. 8.6a that the measured noise spectrum is well described by the function $\widetilde{L}^2(\Omega, \Delta')$. The χ^2 value for the fit is $1.4 \cdot 10^{-4}$. If we instead use a model with $\Omega = 0$, then the χ^2 value increases by a factor of 2.5. If the "correlated noise" expression $a\widetilde{L}^2(\Omega, \Delta')e^{-2a'}$ is used, we get an increase in χ^2 by a factor of 2.3.

We now return to the noise that we observe when the two photocurrents i_1 and i_2 are subtracted. In Fig. 8.6b we plot the atomic noise κ for the differential photocurrent (i_-) measurements. The three different symbols correspond to the symbols in Fig. 8.4, and we have made the same scaling of the atomic noise data as in Fig. 8.4 and 8.6a. The dotted line in Fig. 8.6b is a fit to the same expression, $a\widetilde{L}^2(\Omega, \Delta')e^{-2a'}$, as we used in Fig. 8.6a. The fit is clearly not very good. We do, of course, not expect a good fit according to the theoretical expression in Eq. (8.3). The width of the noise spectrum measured in i_- is clearly larger than for the spectrum measured in i_+ . The solid line in Fig. 8.6b is a fit to the theoretical lineshape $[b\widetilde{D}^2(\Omega, \Delta') + c\widetilde{L}^2(\Omega, \Delta')]e^{-2a'}$ with two free parameters, b and c . This fit gives a χ^2 value of $2.0 \cdot 10^{-4}$ with $b = 3.4 \cdot 10^{-3}$ and $c = 3.2 \cdot 10^{-3}$. The dotted curve gives a 3.4 times larger χ^2 value. These data show, in agreement with the theory, that a resonant (Lorentzian like) as well as an off-resonant (dispersive like) noise contribution is present when we look at the i_- noise.

Two of the measurements in Fig. 8.6b (a triangle at 1.8MHz and a circle at -4.8MHz) seem to deviate substantially more from the solid line than the typical scatter. These deviations may be caused by a change in the experimental conditions due to some external perturbation; e.g. someone is slamming the door next to the lab with in an unhappy laser as the result. With the very long integration time, we become rather sensitive to such perturbations.

We can compare the parameters b and c from the fit to a theoretical estimate from Eq. (8.3). In this estimate we have to include the propagation losses in the probe path after the probe-atom interaction. The overall losses are measured to be around 25% (4% on the beamsplitter after the MOT, 2% on the detector quantum efficiency, 18% on the 917nm interference filters and 3% on imperfect mirror and window coatings). These losses reduce the measured atomic noise κ by 25% since the measured atomic noise is quadratic in probe power whereas the shot noise is linear in probe power. After inserting $\alpha'_{0,unpol} \simeq \alpha'_0 = 0.12$, $s'_0 = 0.69$, and $\gamma'/\gamma = 3.1/5.2$ into Eq. (8.3) and including the 25% probe losses, we obtain the theoretical values $b_{theory} = 7.4 \cdot 10^{-3}$ and $c_{theory} = 7.7 \cdot 10^{-4}$. An individual comparison of b_{theory} and c_{theory} to the experimental b and c values shows an acceptable agreement with $b/b_{theory} \simeq 0.5$ and $c/c_{theory} \simeq 4$. The discrepancy can be caused by experimental imperfections such as pump and probe saturation effects, the influence on α_0 from excess broadening, comparable probe and pump beam diameters, possible homogeneous broadening, and maybe the theoretical assumption about an unpolarized ground state is not truly fulfilled. If we instead look at the ratios b/c and b_{theory}/c_{theory} , we see a larger difference between theory and experiment. We do not know the origin for this discrepancy, but it is possible that the experimental imperfections have a different effect on the resonant (\widetilde{L}^2) and the off-resonant (\widetilde{D}^2) contributions. It is also possible that other noise sources, besides the fluctuations in the spin of the intermediate state, contribute at resonance. This could for example be the effect of spontaneous decay from the $6D_{5/2}F = 6$ state, which may become important at resonance for the actual probe power. The noise induced by spontaneous emission into the spatial mode of the probe beam is investigated in Ref. [101].

8.4 Atomic spin noise - excitation with classical noise

Before we carry out the experiments with squeezed or antisqueezed quantum pump, we look at the change in the atomic spin noise spectrum when a pump field with huge classical noise is used for excitation. These classical noise measurements can be used to estimate the effect of antisqueezed/squeezed light excitation. We can model the noise properties of antisqueezed light (noisy \hat{S}_y or \hat{S}_z) by using a very weak classical field with strong amplitude modulation in place of the squeezed vacuum field. The weak noisy field is mixed with the strong coherent field on PBS1 (Fig. 8.1) in the same way as the usual mixing of the squeezed vacuum and the coherent component. We can write the classical field after PBS1 as

$$\mathbf{e}_x E_{coh} \cos(\omega_0 t) + \mathbf{e}_y E_{cl} \cos(\omega_0 t + \theta) f(t) \quad (8.5)$$

E_{coh} and E_{cl} are the amplitudes of the strong coherent field and the weak modulated field. The two fields are mixed in orthogonal linear polarizations. We use the subscript cl for classical modulation. $f(t)$ is a function, which describes the amplitude modulation of the weak field. We can easily calculate the classical contribution to the spectral density of the Stokes parameters \hat{S}_y and \hat{S}_z . After adding the coherent state shot noise, we find

$$\begin{aligned} \left(\hat{S}_y\right)_\Omega^2 &= \frac{\Phi}{4} R_{cl}(\Omega) \cos^2 \theta + \frac{\Phi}{4} \\ \left(\hat{S}_z\right)_\Omega^2 &= \frac{\Phi}{4} R_{cl}(\Omega) \sin^2 \theta + \frac{\Phi}{4} \\ R_{cl}(\Omega) &= \Phi_{cl} (f)_\Omega^2 \end{aligned} \quad (8.6)$$

Φ and Φ_{cl} are the photon fluxes in the coherent field and in the weak modulated field ($\Phi_{cl} \ll \Phi$). Equation (8.6) includes the coherent state shot noise given by $\Phi/4$. We note that the classical excess noise is very similar to the antisqueezed excess noise in Eq. (3.17). The main difference between the classically induced noise and polarization squeezing is that the classical noise contribution is always positive. We cannot get below the shot noise level without quantum correlations, but we can still use the classical noise to model the effect of antisqueezing.

In this section we are interested in the excess atomic spin noise induced by the excess noise in the excitation field Stokes parameters. We define κ_{cl} as the atomic spin noise with the classically modulated weak beam present, and κ_{coh} as the atomic spin noise for coherent excitation, i.e. with the weak noisy field blocked. The theoretical expression for the difference $\kappa_{cl} - \kappa_{coh}$ is derived from Eq. (4.31), (4.50) and (6.38)

$$\begin{aligned} \kappa_{cl} - \kappa_{coh} &= e^{-2\alpha'} s_0' \alpha_{0,unpol}' \frac{9}{128} \frac{\gamma' \gamma}{\gamma^2 + \Omega^2} \\ &\times \left\{ [R_z(\Omega) - 1] \tilde{D}^2(\Omega, \Delta') + \frac{1}{25} [R_y(\Omega) - 1] \tilde{L}^2(\Omega, \Delta') \right\} \end{aligned} \quad (8.7)$$

As usual, we define $R_{z,y}(\Omega)$ as the ratio of the spectral density $(\hat{S}_{z,y})_\Omega^2$ to the spectral density for a coherent state pump field ($\Phi/4$).

In practice, we generate the noisy excitation field in the following way. An AOM is inserted in the path of a weak 852nm coherent field. We can modulate the intensity in the zeroth order from the AOM by amplitude modulation of the RF signal that drives the AOM. For this purpose we use a function generator (HAMEG 1831-2) that has a "white noise" output with a 10MHz bandwidth. The RF signal, which drives the AOM, is amplitude modulated by the white noise signal from the function generator by means of an electronic attenuator. We block the blue beam pumping the OPO and instead we inject the weak zeroth order from the AOM into the OPO. This weak field is transmitted through the OPO output coupler, and it emerges in the same spatial mode as the squeezed vacuum output. The average power in the weak noisy beam after the OPO is around 5nW.

With a strong modulation it is possible to achieve up to 20dB of excess noise relative to the shot noise level. Ideally, when the noise in one Stokes component (e.g. \hat{S}_y) is maximized ($\theta = 0$), we have only shot noise in the other Stokes component (\hat{S}_z). However, this is not possible to achieve in the experiment since the phase lock is not ideal. We use the same phase locking setup as described in section 8.1.2 for the polarization squeezed light. The detectors in the phase locking setup are arranged to measure the noise in \hat{S}_y . In the experiment we typically have 19-20dB excess noise in \hat{S}_y when we lock to the maximum noise ($\theta = 0$) and 3-4dB excess noise in \hat{S}_y when we lock to the minimum noise ($\theta = \pi/2$). This is when the phase θ is stabilized without chopping the optical fields. When the fields (and the phase locking signal) are chopped, we find that the noise in \hat{S}_y drops about 1dB when we lock at $\theta = 0$. This is a relatively small change in the \hat{S}_y noise, but it results in a huge change in the "quiet" \hat{S}_z component. A change in the \hat{S}_y noise from 19.5dB to 18.5dB above the shot noise level results in about 13dB of excess noise in the quiet \hat{S}_z because the sum $(\hat{S}_y)_\Omega^2 + (\hat{S}_z)_\Omega^2$ is a constant according to Eq. (8.6).

In the experiment, we have $46\mu\text{W}$ in the resonant 852nm pump and $190\mu\text{W}$ in the 917nm probe. We measure the two lock-in voltages ΔV_{DC} and ΔV_{RF} while the probe frequency is scanned slowly across the resonance. The measured voltage versus frequency spectra are typically averaged over 50 individual frequency scans on the digital oscilloscope. The scan rate for each scan is 4.5MHz/s, and we use a time constant of 30ms on the lock-in amplifiers. From the measured voltages we calculate the atomic spin noise κ as a function of probe detuning. A noise measurement with classical noise is followed by a measurement with the weak noisy beam blocked. The difference between the two measured spectra gives the excess noise $\kappa_{cl} - \kappa_{coh}$ as a function of probe detuning. In Fig. 8.7 we plot the measured excess atomic noise $\kappa_{cl} - \kappa_{coh}$ for the two phases $\theta = \pi/2$ (solid line) and $\theta = 0$ (dotted line).

We observe for $\theta = \pi/2$ that the excess noise is peaked off-resonance at around $\pm 5.0\text{MHz}$. This is exactly what we expect from Eq. (8.7). Excess noise in \hat{S}_z leads to excess noise in \hat{F}'_z , which we measure with an off-resonant probe. The $\theta = 0$ spectrum has in general a smaller amplitude than the $\theta = \pi/2$ spectrum. However, the figure indicates that the noise on resonance is comparable for $\theta = 0$ and for $\theta = \pi/2$. This is again consistent with the theory; noisy \hat{S}_y gives noisy $\hat{F}'_x\hat{F}'_y + \hat{F}'_y\hat{F}'_x$, which is seen with a resonant probe. The amount of off-resonant noise in the $\theta = 0$ measurement is clearly too large for the profile expected from Eq. (8.7), $\tilde{L}^2(\Omega, \Delta') e^{-2\alpha'}$. This can be explained by the imperfect phase lock. We estimated above that the imperfect phase lock at $\theta = 0$ results in about 13dB of excess noise in \hat{S}_z . This corresponds to about 28% of the \hat{S}_z noise at $\theta = \pi/2$. This is in agreement with Fig. 8.7, where the off-resonant excess noise is reduced to about 25-30% when we go from $\theta = \pi/2$ to $\theta = 0$.

The smooth solid line in Fig. 8.7 is a fit to the $\theta = \pi/2$ data with the expression $d[R_z(\Omega) - 1]\tilde{D}^2(\Omega, \Delta') e^{-2\alpha'}$. We use the same parameters in $\tilde{D}^2(\Omega, \Delta')$ as we used for $\tilde{L}^2(\Omega, \Delta')$ in the previous section. d is the only free parameter, and we find $d = (4.6 \pm 0.7) \cdot 10^{-4}$ for $R_z(\Omega) = 71 \pm 9$, (18.5dB \pm 0.5dB). We note that the measured spectrum for $\theta = \pi/2$ and the fitted curve agree quite well. The fact that the data in Fig. 8.7 do not go all the way to zero at zero detuning can be explained by frequency drifts during the averaging of the many scans, $\hat{F}'_x\hat{F}'_y + \hat{F}'_y\hat{F}'_x$ noise from the imperfect phase lock, and broadening effects that are not included in $\tilde{D}^2(\Omega, \Delta')$. The small asymmetry in the measured data can also be a result of the imperfect phase lock. The fluctuations in \hat{S}_z and \hat{S}_y are correlated at phases between $\theta = 0$ and $\theta = \pi/2$. This results in correlated fluctuations in the atomic variables \hat{F}'_z and $\hat{F}'_x\hat{F}'_y + \hat{F}'_y\hat{F}'_x$, and according to page 73 that can explain an asymmetric lineshape. The excitation field either goes to the phase locking setup or to the atomic sample. If birefringence is present in one of the two paths, we may have $\theta = 0$ at the phase locking setup and $\theta \neq 0$ at the atomic sample and hence correlations between the fluctuations in \hat{F}'_z and $\hat{F}'_x\hat{F}'_y + \hat{F}'_y\hat{F}'_x$.

If we subtract the estimated contribution from \hat{F}'_z noise due to the imperfect phase lock from the $\theta = 0$ data in Fig. 8.7, we get a noise spectrum that is peaked at resonance. The theoretical profile for this spectrum is, according to Eq. (8.7), given by the function $e[R_y(\Omega) - 1]\tilde{L}^2(\Omega, \Delta') e^{-2\alpha'}$. If we adjust the parameter e to fit the experimental data, we find $e = (4.0 \pm 1.1) \cdot 10^{-5}$ for $R_y(\Omega) = 71 \pm 9$.

We can compare the experimental values for d and e with the theoretical values obtained from Eq. (8.7). With the experimental parameters $s'_0 = 0.69$, $\alpha'_{0,unpol} \simeq \alpha'_0 = 0.11$, $\gamma'/2\pi = 3.1\text{MHz}$,

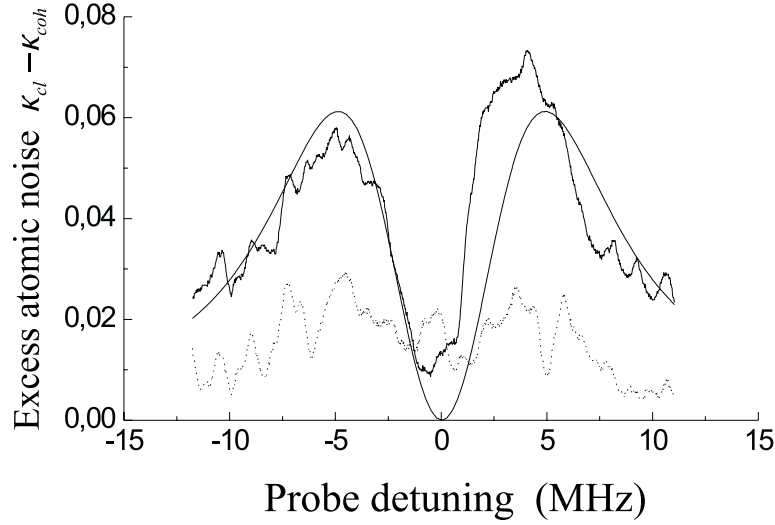


Figure 8.7: Measured atomic excess noise $\kappa_{cl} - \kappa_{coh}$ as a function of probe detuning. The solid line is measured with $\theta = \pi/2$ (noisy \hat{S}_z). The smooth solid line is a fit to the expression $d\tilde{D}^2(\Omega, \Delta') e^{-2\alpha'}$ with d as the free parameter. The dotted line is measured with $\theta = 0$ (noisy \hat{S}_y).

$\gamma/2\pi = 5.2\text{MHz}$, $\Omega/2\pi = 1.9\text{MHz}$, and inclusion of the 25% losses in the probe path after the atomic sample, we find $d_{theory} = 2.1 \cdot 10^{-3}$ and $e_{theory} = 8.4 \cdot 10^{-5}$. In general we find that the observed amount of excess noise is smaller than the theoretically predicted excess noise with $d/d_{theory} = 0.22$ and $e/e_{theory} = 0.5$. This indicates that our mapping of the classical correlations in the pump field onto the atomic sample is less efficient than predicted. The reason for that can be the previously mentioned experimental imperfections, but it is likely that the essential cause is radiation trapping of the pump photons. We will discuss this effect in more detail in section 8.7. The experimental data as well as the theoretical estimates show that we are much more sensitive to off-resonant excess noise due to \hat{F}'_z fluctuations than to the resonant excess noise caused by fluctuations in $\hat{F}'_x\hat{F}'_y + \hat{F}'_y\hat{F}'_x$.

It is convenient to introduce the experimental mapping-readout efficiencies similar to the theoretical mapping efficiencies in chapter 4, Eq. (4.32) and (4.51). We define $\tilde{\eta}_z$ and $\tilde{\eta}_y$ through

$$\begin{aligned}\kappa_{cl} &= \frac{1}{\tilde{\eta}_z + 1} (1 + \tilde{\eta}_z R_z(\Omega)) \kappa_{coh} \\ \kappa_{cl} &= \frac{1}{\tilde{\eta}_y + 1} (1 + \tilde{\eta}_y R_y(\Omega)) \kappa_{coh}\end{aligned}\tag{8.8}$$

We use a tilde on the experimental mapping-readout efficiencies to distinguish them from the theoretical mapping efficiencies. The experimental efficiencies include the efficiency of mapping the correlations onto the atoms as well as the efficiency for the readout of the atomic correlations. For a given efficiency ($\tilde{\eta}_z$ or $\tilde{\eta}_y$), we measure the atomic noise at the probe detuning that maximizes $|\kappa_{cl} - \kappa_{coh}|$. Thus, for $\tilde{\eta}_z$ we measure the atomic noise around $\Delta'/2\pi \simeq 5.0\text{MHz}$ and for $\tilde{\eta}_y$ we measure at $\Delta' = 0$. From the graphs in Fig. 8.7 together with the measurements of κ_{coh} (similar to Fig. 8.6b), we derive $\tilde{\eta}_z = 6\% \pm 2\%$ and $\tilde{\eta}_y = 0.7\% \pm 0.5\%$. These mapping-readout efficiencies are much smaller than the theoretical mapping efficiencies from chapter 4. This can be explained by the readout method and the effect of radiation trapping, which we discuss in section 8.7. For now we will just use the efficiencies to estimate the degree of atomic spin squeezing and spin antisqueezing for a polarization squeezed excitation field.

8.5 Atomic spin noise - excitation with nonclassical light

We are now ready to shine polarization squeezed light onto our atoms and see how they react. The theory for mapping quantum correlations in light onto atoms together with the theory for the readout of the produced atomic correlations show that the best mapping-readout efficiency is obtained for off-resonant \hat{F}'_z measurements. This is confirmed by the experimental results with classical modulation in the previous section. In this section we will therefore concentrate on squeezing/antisqueezing of the fluctuations in the collective atomic spin component \hat{F}'_z and a subsequent readout with an off-resonant probe. The estimated degree of antisqueezing/squeezing available at the trap site is $+4.5 \pm 0.6\text{dB}$ and $-1.8 \pm 0.2\text{dB}$ relative to the shot noise level. On a linear scale that converts into $R_z(\Omega) = 2.8 \pm 0.4$ for $\theta = \pi/2$ and $R_z(\Omega) = 0.66 \pm 0.03$ for $\theta = 0$. We use the notation κ_{sq} for the atomic noise measured with squeezed light excitation. We define the observed degree of spin squeezing as $\xi = (\kappa_{sq} - \kappa_{coh})/\kappa_{coh}$. If ξ is negative, we have spin squeezing. For positive ξ we have spin antisqueezing. In the case of spin squeezing, ξ is equivalent to the relative spin noise reduction (see Fig. 4.2b and Fig. 4.3b) except for a change in sign³. We can estimate the degree of observed \hat{F}'_z spin squeezing if we use the mapping-readout efficiency from the last section, $\tilde{\eta}_z = 6\% \pm 2\%$, and Eq. (8.8) with κ_{sq} instead of κ_{cl} . We find

$$\xi = \frac{[R_z(\Omega) - 1]}{\tilde{\eta}_z^{-1} + 1} \quad (8.9)$$

Inserting the values for $\tilde{\eta}_z$ and $R_z(\Omega)$ gives $\xi = 10\% \pm 4\%$ for $\theta = \pi/2$ and $\xi = -1.9\% \pm 0.6\%$ for $\theta = 0$. The typical amount of spin noise for coherent excitation is from Fig. 8.6b found to be $\kappa_{coh} \simeq 0.014$ at $\Delta'/2\pi = \pm 5.0\text{MHz}$. We find for $\theta = 0$ that the expected atomic noise reduction is $\kappa_{sq} - \kappa_{coh} \simeq -3 \cdot 10^{-4}$ in units of the probe shot noise. This is an extremely small signal compared to the overall noise level, which is predominated by the probe shot noise. Instead of going directly for the demonstration of atomic spin squeezing, we start with the spin antisqueezing measured off resonance with $\theta = \pi/2$. The signal-to-noise ratio (S/N) in the spin squeezing/antisqueezing measurement is proportional to $|\xi|$. We estimate that the S/N should be about 5 times larger for antisqueezing in \hat{F}'_z than for \hat{F}'_z squeezing. However, in the actual experiment it turns out to be more like a 10 times difference. Thus, we can do the spin antisqueezing measurement with about two orders of magnitude shorter integration time than the spin squeezing measurement for the same S/N.

8.5.1 Spin antisqueezing - $\theta = \pi/2$

We apply the polarization squeezed excitation field by mixing the coherent component and the squeezed vacuum field in orthogonal polarizations on PBS1 (Fig. 8.1). The relative phase between the two fields is actively stabilized at $\theta = \pi/2$, and the Stokes component \hat{S}_z for the excitation field has a noise level about 4.5dB above the standard quantum limit (shot noise). The quantum correlations between the atomic spins induced by absorption of the nonclassical light are expected to give excess noise in the excited state collective atomic spin variable \hat{F}'_z . This is accompanied by a small reduction below the standard quantum limit in the noise of the spin variable $\hat{F}'_x\hat{F}'_y + \hat{F}'_y\hat{F}'_x$. Consequently, we expect to measure excess atomic noise ($\kappa_{sq} - \kappa_{coh} > 0$) with the off-resonant probe

We use a $46\mu\text{W}$ nonclassical pump field and a $190\mu\text{W}$ probe field. The measurements for $\theta = \pi/2$ are all from the same day as the data with circle symbols in Fig. 8.4 and Fig. 8.6b. To obtain a single (individual) spin noise measurement we first average the two lock-in voltages ΔV_{RF} and ΔV_{DC} for six minutes with all parameters fixed and with the squeezed vacuum present. This measurement is followed by six minutes of averaging with the squeezed vacuum path blocked and hence coherent excitation. From the lock-in voltages we calculate the atomic noise with nonclassical excitation (κ_{sq}) and the atomic noise with coherent excitation (κ_{coh}). The circles in Fig. 8.6b are the κ_{coh} measurements scaled by the factor 0.89, and the circles in Fig. 8.4 are the corresponding optical depths scaled by the same factor 0.89.

³This definition of ξ is analogous to the ξ definition in chapter 5.

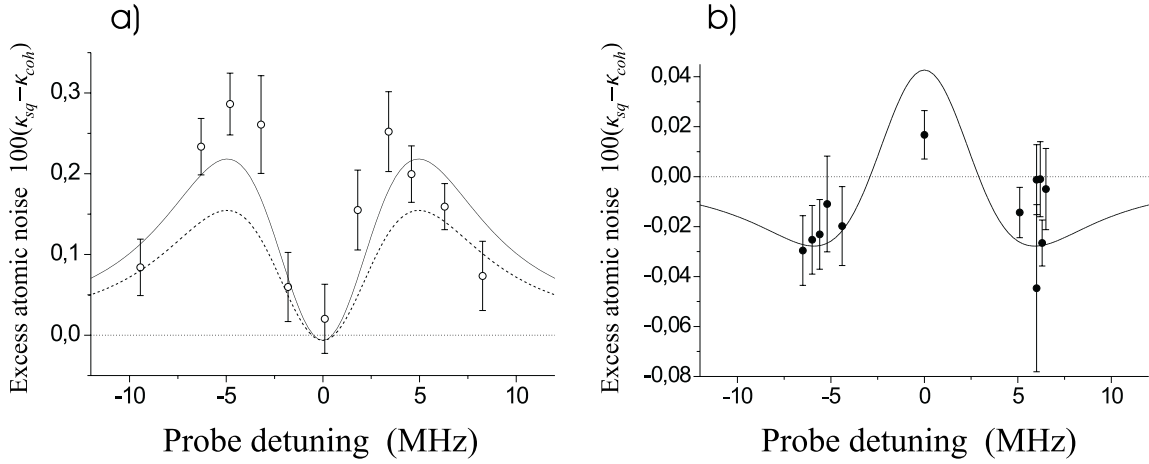


Figure 8.8: Atomic excess noise for nonclassical excitation. a) $\theta = \pi/2$ which results in antisqueezed \hat{F}'_z fluctuations measured off resonance. Circles: the measurements. Dashed and solid lines: predicted line shape, see the text for the details. Dotted line at zero: the standard quantum limit. Note that the vertical scale is expanded by a factor of 100. b) $\theta = 0$ with squeezed \hat{F}'_z fluctuations measured off resonance. The "excess noise" is now negative off resonance. Dots: measurements. Solid line: predicted spectrum. Dotted line: the standard quantum limit. Note that the antisqueezed $\hat{F}'_x \hat{F}'_y + \hat{F}'_y \hat{F}'_x$ fluctuations at resonance become significant at $\theta = 0$.

The reason for this scaling is explained in section 8.2. The results for $\kappa_{sq} - \kappa_{coh}$ averaged over 1 to 4 individual measurements are shown in Fig. 8.8a for different probe detunings. The error bars in the figure are based on the statistical uncertainty in the measurements of κ_{sq} and κ_{coh} , and they do not include any uncertainty or drift in the degree of antisqueezing in the excitation field.

Equation (8.7) is also valid for the nonclassical pump field if we substitute κ_{sq} for κ_{cl} . We have

$$\kappa_{sq} - \kappa_{coh} = \left\{ d[R_z(\Omega) - 1]\tilde{D}^2(\Omega, \Delta') + e[R_y(\Omega) - 1]\tilde{L}^2(\Omega, \Delta') \right\} e^{-2\alpha'} \quad (8.10)$$

The parameters d and e can be derived from the theoretical expression in Eq. (8.7), but we found in section 8.4 that the experimental mapping-readout efficiencies are significantly smaller than the theoretical values. We will therefore use the experimental parameters from the data in Fig. 8.7 for d and e . The dashed line in Fig. 8.8a is the expected atomic noise level from Eq. (8.10) with $d = 4.6 \cdot 10^{-4}$, $e = 4 \cdot 10^{-5}$, $R_y(\Omega) = 0.66$, and $R_z(\Omega) = 2.8$. The functions $\tilde{D}^2(\Omega, \Delta')$ and $\tilde{L}^2(\Omega, \Delta')$ are the same as we used in section 8.4. The dashed line in Fig. 8.1a has the same double peaked structure as the actual measurements, but the amplitude of the graph seems to be too small. This can be explained by the relatively large uncertainty in d and $R_z(\Omega)$. The solid line in Fig. 8.8a is also from Eq. (8.10), but now with $d = 5.3 \cdot 10^{-4}$ and $R_z(\Omega) = 3.2$. We note that the predicted noise reduction (spin squeezing) at zero detuning is indeed very small, and it is limited to a small frequency interval. The small line broadening from the atomic acceleration during the 1ms measurement cycle will be enough to "wash out" the resonant noise reduction⁴.

We can derive the mapping-readout efficiency $\tilde{\eta}_{z,nc}$ for nonclassical excitation in the same way as we derived $\tilde{\eta}_z$ in the previous section. We find $\tilde{\eta}_{z,nc} = 8\% \pm 2\%$. This efficiency is in agreement with the measured mapping-readout efficiency for classical noise in the excitation field, $\tilde{\eta}_z = 6\% \pm 2\%$.

⁴The acceleration broadening is an homogeneous effect, where all atoms have same resonance frequency. However, this resonance frequency is changing during the 1ms measurement cycle, and this leads to line broadening. This homogeneous broadening is not included in the spectra described by \tilde{D}^2 and \tilde{L}^2 .

8.5.2 Spin squeezing - $\theta = 0$

With the phase fixed at $\theta = 0$, we now expect the off-resonant atomic noise κ_{sq} to go below the standard quantum limit set by κ_{coh} . The experimental data for $\kappa_{sq} - \kappa_{coh}$ is plotted in Fig. 8.8b. Each off-resonant data point in Fig. 8.8b corresponds to one run. Each run lasts between 4 and 12 hours and includes between 13 and 45 individual measurements. The total number of off-resonant individual measurements is 263. An individual measurement consists again of six minutes averaging of the lock-in voltages while nonclassical excitation is applied followed by six minutes of averaging with the squeezed vacuum path blocked (coherent excitation). The error bars in Fig. 8.8b are given by the statistical uncertainty in $\kappa_{sq} - \kappa_{coh}$ for each run. The dotted line at $\kappa_{sq} - \kappa_{coh} = 0$ represents the standard quantum limit. Measurements below the standard quantum limit require spin squeezed atoms. The probe power is in this experiment increased to $235\mu\text{W}$, except for the run at 6.2MHz, which is taken with $190\mu\text{W}$. The pump power is at the usual $46\mu\text{W}$. In about 1/3 of the measurements we use a probe polarized along the y -axis instead of polarized along x . We do not see any dependence on the probe polarization. This is in agreement with the theory; we are not sensitive to the sign of the probe Stokes parameter \hat{S}_x^{in} , only the amplitude is important. Three runs are taken at zero detuning including one run with only 9 individual measurements and consequently an uncertain average. We are not that interested in the resonant excess noise, and we average all the individual resonant measurements into just one data point in Fig. 8.8b.

The solid line in Fig. 8.8b is the expected atomic noise level from Eq. (8.10) with $d = 5.7 \cdot 10^{-4}$, $e = 5 \cdot 10^{-5}$, $R_z(\Omega) = 0.66$, and $R_y(\Omega) = 2.8$. We have taken into account that most of the data in Fig. 8.8b are taken with 24% more probe power than the corresponding measurements with classical noise in Fig. 8.7. The atomic noise κ is linear in s'_0 , and we include the larger probe power by increasing the d and e parameters by 24%.

The experimental data in Fig. 8.8b show on average a noise reduction (spin squeezing) off resonance and a noise increase on resonance, just as we expected. The resonant noise increase is smaller than predicted, but that can be explained by the uncertainty in the e parameter and in the degree of antisqueezing, $R_y(\Omega)$. Nevertheless, the resonant excess noise is comparable to the off-resonant noise reduction because the degree of antisqueezing in \hat{S}_y is "larger" than the degree of squeezing in \hat{S}_z . If we neglect the positive resonant contribution in the predicted spectrum (the solid line in Fig. 8.8b), we get a 33% increase in the predicted off-resonant noise reduction. Thus, the resonant excess noise does have some influence on the observed spin squeezing, although the actual measurement at resonance indicates more like a 15% effect.

In the following section we discuss the statistics of the off-resonant spin squeezing data in more detail.

8.6 Analysis of the spin squeezing data

The spin squeezing measurements presented in Fig. 8.8b do indicate that the atomic noise have been reduced beyond the standard quantum limit. However, a more quantitative analysis of the data is required before we conclude that a macroscopic spin squeezed state of entangled atoms have been generated and observed. Each data point in Fig. 8.8b is not far below the standard quantum limit. It is therefore relevant to ask the question: "What is the probability for observing a data set as in Fig. 8.8b if the true mean value is at the standard quantum limit or above?". In this section we will try to answer this question.

It is convenient to use the observed degree of spin squeezing $\xi = (\kappa_{sq} - \kappa_{coh}) / \kappa_{coh}$, which normalizes the observed spin noise reduction to the spin noise for coherent excitation. This normalization has the advantage that measurements at slightly different probe optical depth, probe frequency, or probe power can be compared since both the numerator and the denominator in the ξ definition have (almost) the same dependencies on these parameters. Thus, we expect the distributions of the individual ξ measurements from the 11 off-resonant runs to be described by normal distributions with almost identical mean values. The variances of the distributions for the different runs do not have to be identical; in fact, a Bartlett test [105] shows that the variances are most likely not identical. In section 8.7 we show that the statistical

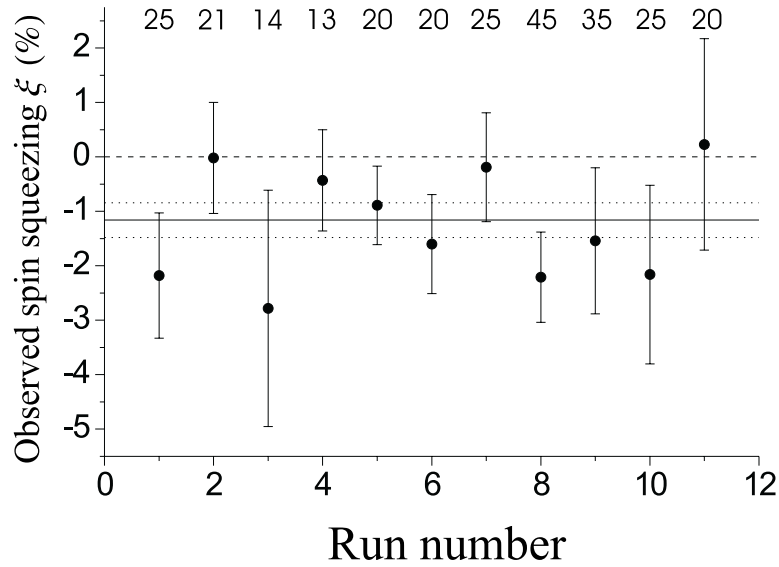


Figure 8.9: The average observed degree of spin squeezing ξ from each run. The error bars represent the statistical errors within each run. The numbers above the measurements show the number of individual ξ measurement within the actual run. The solid line is the average $\bar{\xi}$ with the 1σ confidence interval represented by the dotted lines. The dashed line at $\xi = 0$ sets the standard quantum limit.

error on the ξ measurements can be explained by the fundamental quantum noise (shot noise) of the probe that is used to read out the atomic fluctuations. In section 8.7 we also explain why different runs have different variances. Figure 8.9 shows the average degree of spin squeezing ξ together with its statistical error for each off-resonant run.

We can combine the 11 measurements in Fig. 8.9 into a single number by taking a weighted average with the square of the inverse errors as the weights [106].

$$\bar{\xi} = S^2 \sum_{i=1}^{11} s_i^{-2} \xi_i \quad (8.11)$$

$$S^{-2} = \sum_{i=1}^{11} s_i^{-2}$$

ξ_i is the estimated mean value for ξ from run number i , and s_i is the corresponding estimate of the standard error. $\bar{\xi}$ is the estimated mean value of the combined 11 runs, and S is the estimated standard error for $\bar{\xi}$. We find for the data in Fig. 8.9 that $\bar{\xi} = -1.16\% \pm 0.32\%$. Hence, the 263 spin squeezing measurements give an average observed degree of spin squeezing which is about 3.6 standard errors below the standard quantum limit. We note that $\bar{\xi}$ represents the *observed* degree of spin squeezing. The actual squeezing of \hat{F}'_z is probably greater than what we observe due to an imperfect readout. The quality of the readout is discussed in section 8.7.

The overall probability distribution for all the individual spin squeezing data can be described by a weighted sum of normal distributions. The mean and the variance for each normal distribution is given by the estimates from the corresponding run, and the weight is the relative number of measurements in the run. The accumulated probability distribution for this sum of normal distributions is plotted in Fig. 8.10 (solid line) together with the measured probability distribution (dots). The measured probability distribution is given by points (x_i, y_i) , where y_i is the fraction of all the individual measurements with

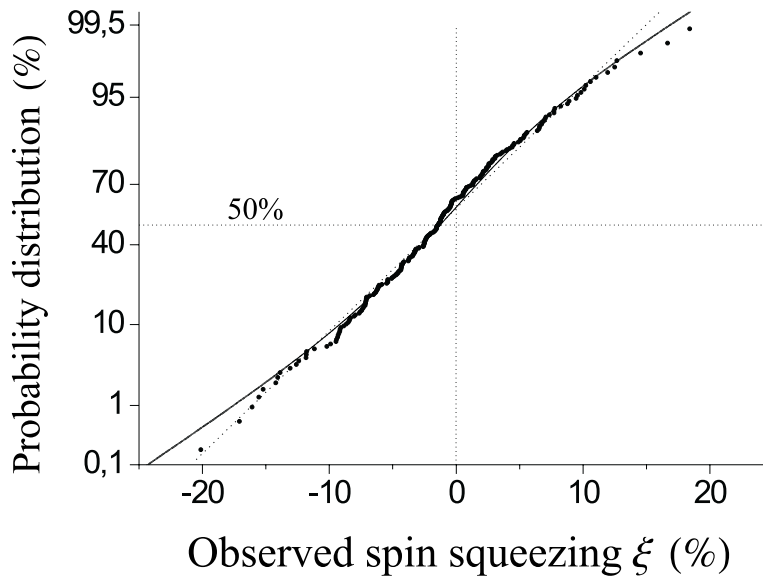


Figure 8.10: Probability distribution which includes all 263 individual spin squeezing measurements. Dots: the measured distribution. Solid line: a weighted sum of normal distributions; see the text for details. Dotted line: approximation to a (single) normal distribution. The vertical "probability scale" makes normal distributions linear.

$\xi \leq x_i$. We find good agreement between the measurements and the probability distribution based on the assumption about normally distributed data within each run.

We can make a simple test of our data by dividing them into two groups; one with $\xi \geq 0$ and the other with $\xi < 0$. We will assume that the atomic spin noise measured with squeezed \hat{S}_z is the same as with coherent excitation, i.e. that the squeezed vacuum field does not make a difference. Hence, the true value of ξ is zero, and we have the probability of 1/2 for obtaining a positive as well as a negative ξ measurement. The distribution of data in the two groups is a simple binomial distribution. A total of 167 measurements are negative. The probability for getting 167 or more negative measurements out of a total of 263 measurements is for a binomial distribution given by

$$P = \sum_{i=167}^{263} \binom{263}{i} \left(\frac{1}{2}\right)^{263} = 7 \cdot 10^{-6} \quad (8.12)$$

We see that it is highly unlikely that we obtain such an asymmetric distribution of data around zero. We conclude that the assumption must be wrong, and that the squeezed vacuum in the excitation field really does make a difference.

A more thorough analysis includes the continuous distribution of the observed data. An interesting hypothesis to test is whether it is possible to obtain the measured data from a distribution whose true mean value is nonnegative. We can test this hypothesis if we approximate the actual distribution (estimated by the solid line in Fig. 8.10) with a normal distribution having the same mean and variance (dotted line in Fig. 8.10). The mean and standard deviation for the two distributions are $(\mu, \sigma) = (-1.36, 6.33)$. We use the Student's t -test [105] to test the hypothesis. The t -test gives a test probability of $\varepsilon = 0.03\%$. ε is the probability for getting a set of data, under the hypothesis about a nonnegative mean value, which is "worse" than the actual data set. We reject the hypothesis about the nonnegative mean value because of the small ε .

We can now conclude that spin squeezing in a macroscopic entangled atomic sample has been gener-

ated and observed.

8.7 The limiting factors - radiation trapping and probe shot noise

In the previous section we measured the observed degree of spin squeezing to be $\bar{\xi} = -1.16\% \pm 0.32\%$. The signal-to-noise ratio (S/N) for the spin squeezing measurements is the absolute ratio of the mean value to the estimated error, i.e. $S/N = 1.16/0.32 = 3.6$. The S/N is limited by the degree of spin squeezing and the fluctuations in the individual spin squeezing measurements. The degree of spin squeezing is set by the mapping-readout efficiency and the available squeezing in the quantum pump. In the following subsection we will discuss effects that limit the mapping-readout efficiency. In particular, we will see that radiation trapping plays an important role in the efficiency at which quantum correlations are mapped from the light onto the atoms. In the second subsection we show that the probe shot noise can explain the fluctuations in the individual spin squeezing measurements.

8.7.1 The degree of spin squeezing and radiation trapping

We found in section 8.4 that the mapping-readout efficiency for classical correlations in \hat{F}'_z is $\tilde{\eta}_z = 6\% \pm 2\%$. The corresponding efficiency for quantum excitation with excess noise in \hat{S}_z is about the same with $\tilde{\eta}_{z,nc} = 8\% \pm 2\%$, see section 8.5. Thus, the experimental mapping-readout efficiency is substantially smaller than the theoretical mapping efficiency $\eta_z = 47\%$ from chapter 4, Fig. 4.2a. The small efficiency $\tilde{\eta}_z$ results in a small degree of spin squeezing. In this subsection we discuss the most important reasons for the low mapping efficiency and the small degree of spin squeezing.

Reabsorption of spontaneously emitted photons at the pump wavelength can put severe limits on the produced spin squeezing. The quantum correlations between pairs of photons in the squeezed excitation field are lost when the photons are absorbed by the atoms. We expect no correlations between the subsequently emitted photons from different atoms, since the atoms decay at random. As a result, the fluorescence field consists of uncorrelated photons, which do not produce any spin squeezing. Nevertheless, the fluorescence photons can excite atoms and thereby generate uncorrelated atomic noise as for a coherent state excitation field.

The total noise in the Stokes parameter \hat{S}_z of the excitation field can be written as a sum of the noise from the incoming pump field, $(\hat{S}_z)_{\Omega,i}^2$, and the noise from the fluorescence field, $(\hat{S}_z)_{\Omega,f}^2$, i.e. $(\hat{S}_z)_{\Omega}^2 = (\hat{S}_z)_{\Omega,i}^2 + (\hat{S}_z)_{\Omega,f}^2$. The \hat{S}_z noise, normalized to the shot noise level, defines the degree of squeezing $R_z(\Omega)$. We use the notation $R_{z,i}(\Omega)$ for the degree of squeezing in the incoming pump field. We assume that the fluorescence field is shot noise limited. The total noise normalized to the total shot noise level can then be written as

$$R_z(\Omega) = R_{z,i}(\Omega) \frac{\Phi_i}{\Phi_i + \Phi_f} + \frac{\Phi_f}{\Phi_i + \Phi_f} \quad (8.13)$$

Φ_f and Φ_i are the photon flux in the incoming field and the fluorescence field. We will use the assumption that $\Phi_f = 0.9\alpha_0\Phi_i$, see page 97. α_0 is the resonant optical depth for the pump field.

We do not have an ideal transfer of correlations if the incoming field is not completely absorbed. In a simple picture we can imagine the partial absorption as a beamsplitter with a reflectivity of $e^{-\alpha_0}$ followed by an atomic cloud, which completely absorbs the rest of the pump⁵. The beamsplitter effect reduces the effective degree of squeezing in the absorbed pump field. The overall degree of squeezing in the pump field is

$$R_z(\Omega) = 1 - \frac{1 - e^{-\alpha_0}}{1 + 0.9\alpha_0} [1 - R_{z,i}(\Omega)] \quad (8.14)$$

⁵This is a simple picture, which neglects the frequency response of the atoms. We measure the probe fluctuations at 1.9MHz, and it is sufficient to assume that the atomic response is frequency independent within a 2MHz bandwidth.

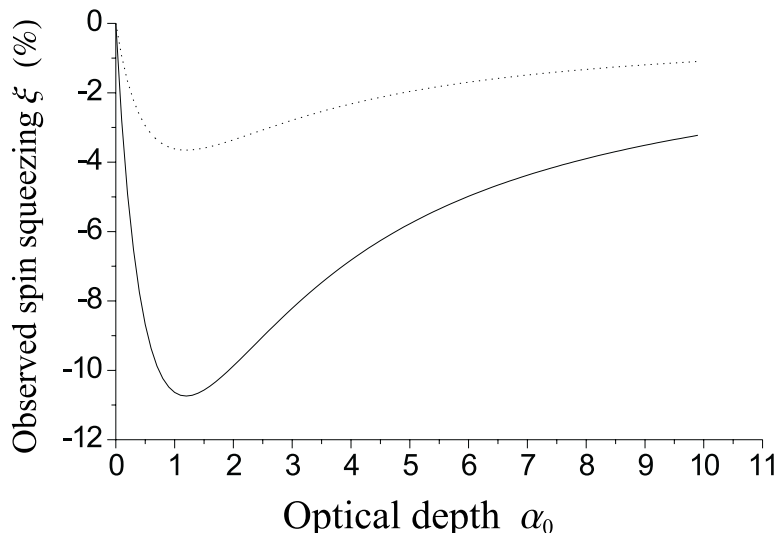


Figure 8.11: The predicted degree of spin squeezing versus the pump optical depth when incomplete absorption and radiation trapping are included. Solid line: perfect squeezing in the quantum pump and a mapping efficiency of $\eta_z = 0.47$. Dotted line: as the solid line, but for -1.8dB of squeezing in the pump.

The denominator, $1 + 0.9\alpha_0$, represents the effective reduction in squeezing due to the fluorescence field. The numerator, $1 - e^{-\alpha_0}$, is the squeezing reduction due to incomplete absorption.

From Eq. (8.9) we have

$$\xi = \frac{\kappa_{sq} - \kappa_{coh}}{\kappa_{coh}} = \frac{R_z(\Omega) - 1}{\eta_z^{-1} + 1} \quad (8.15)$$

In Fig. 8.11 we plot ξ versus α_0 using Eq. (8.14) and (8.15). The solid line is the best we can hope for in the actual light-atom configuration with perfect squeezing of the excitation field ($R_{z,i}(\Omega) = 0$) and the theoretical mapping efficiency $\eta_z = 0.47$. We see that the reabsorbed fluorescence reduces the maximum spin squeezing from -32% (Fig. 4.2b) to only -11%, with the best spin squeezing at $\alpha_0 \simeq 1.3$. With the actual polarization squeezing of -1.8dB, we see from the dotted line in Fig. 8.11 that we should not expect more than about -2.5% spin squeezing for the typical pump optical depth of $\alpha_0 \simeq 3 - 4$. The typical pump optical depth is somewhat larger than the optimum α_0 according to Fig. 8.11. However, the model used in the figure and in Eq. (8.14) is quite crude, and it is better to have α_0 a little too large rather than too small. The effect of radiation trapping can be reduced if the atomic sample is shaped like a pencil with a length much larger than the diameter, but this is not possible with our MOT.

The observed degree of spin squeezing is also influenced by the fact that the readout method is not perfect. We cannot read out the off-resonant \hat{F}'_z fluctuations around ± 5 MHz without seeing the resonant contribution. We see from the fit in Fig. 8.6b that the resonant part contributes with about 45% of the atomic noise measured at ± 5 MHz for coherent excitation. We found in section 8.5.2 that the resonant contribution from antisqueezed $\hat{F}'_x \hat{F}'_y + \hat{F}'_y \hat{F}'_x$ can reduce the measured off-resonant noise reduction $\kappa_{sq} - \kappa_{coh}$ by up to 30%. Hence, these noise contributions, which are not related to \hat{F}'_z fluctuations, can reduce the observed degree of spin squeezing by another factor of two.

In conclusion, we find that the small observed degree of spin squeezing can be explained by the theoretical efficiency of mapping light onto atoms, the effect of radiation trapping, and the fact that the readout of \hat{F}'_z fluctuations is not perfectly separated from the fluctuations that predominate at resonance. Other experimental imperfections like the matching of the spatial modes of the pump and

probe field, optical pumping, residual magnetic field effects, saturation effects, and excess broadening can also influence the mapping-readout efficiency, but these effects are difficult to quantify.

8.7.2 Fluctuations in the spin squeezing data

In appendix E we derive an expression for the S/N in the spectral density measurement of the probe shot noise. If Y is the stochastic variable that represents the output of the spectrum analyzer (SA), we have according to Eq. (E.7)

$$\frac{\langle Y \rangle}{\sqrt{\text{Var}(Y)}} = k_{sc} \sqrt{\frac{\nu_{RB}}{\nu_{VB}}} \quad (8.16)$$

ν_{RB} is the resolution bandwidth, and ν_{VB} is the video bandwidth. The parameter k_{sc} is expected to be close to one. If we implement the lock-in method described in section 8.1.3, then the combined system of spectrum analyzer, electronic squaring device, and the lock-in amplifier measures the difference between two stochastic variables, A and B . These two variables correspond to the shot noise levels A and B in Fig. 8.2c. We assume here that the difference between A and B is due a 250Hz intensity modulation of the probe; the same modulation as used for the shot noise calibration and determination of k_{RF} in section 8.1.3. A and B are independent variables, but the distribution for B is identical to the distribution for $(1 - a)A$, where a is the small modulation depth. If we define $Z = A - B$, we have

$$\begin{aligned} Z &= A - B & (8.17) \\ \langle Z \rangle &= \langle A \rangle - \langle B \rangle = a\langle A \rangle \\ \text{Var}(Z) &= \text{Var}(A) + \text{Var}(B) \simeq 2\text{Var}(A) \end{aligned}$$

The SA is in the spin squeezing experiment set to a resolution bandwidth of 300kHz, but the effective bandwidth for the measurements is set by the narrower detector bandwidth so that $\nu_{RB} = 100\text{kHz}$. The video bandwidth of the SA is set to 30kHz. This gives a sufficiently short averaging time so that the signals in each of the dark periods in Fig. 8.2 (i.e. A and B) are completely independent. The lock-in amplifier and the following data acquisition set the effective video bandwidth of the measurements, which last about six minutes. Half of these six minutes consist of bright periods, which are not used; an electronic gate is used to switch off the signal from these periods. The remaining time is divided between B measurements and A measurements. The fact that the electronic gate is closed in the first part of the dark periods leaves us with about 74 seconds for A measurements. This corresponds to an effective video bandwidth of $\nu_{VB} = 13.6\text{mHz}$. With these numbers, we have from Eq. (8.16) and (8.17)

$$\frac{\langle Z \rangle}{\sqrt{\text{Var}(Z)}} = \frac{a}{\sqrt{2}} \frac{\langle A \rangle}{\sqrt{\text{Var}(A)}} = \frac{a}{\sqrt{2}} k_{sc} \sqrt{\frac{\nu_{RB}}{\nu_{VB}}} = 1920 k_{sc} a \quad (8.18)$$

We have carried out 14 independent measurements of Z with 4.1% modulation of the shot noise level, six minutes of averaging, 235 μW probe power, and the bandwidths given above. The conditions for these measurements are the same as for the spin squeezing measurements, except for the passive shot noise modulation. From the statistics of these 14 measurements we deduce a S/N of 82, and we conclude that the experimental value for the scaling constant is $k_{sc} = 1.0$. This is in perfect agreement with the estimate in appendix E.

We can use Eq. (8.18) to derive the uncertainty in ξ due to the shot noise fluctuations of the probe. From the definition $\xi = (\kappa_{sq} - \kappa_{coh}) / \kappa_{coh}$, we find for the error $s(\xi)$

$$\begin{aligned} s(\xi) &= \frac{1}{\kappa_{coh}} \sqrt{\left(\frac{\kappa_{sq}}{\kappa_{coh}}\right)^2 s(\kappa_{coh})^2 + s(\kappa_{sq})^2} & (8.19) \\ &= \sqrt{2} \frac{s(\kappa_{coh})}{\kappa_{coh}} = \sqrt{2} \frac{\alpha' - \kappa_{coh}}{\kappa_{coh}} \frac{s(\alpha' - \kappa_{coh})}{\alpha' - \kappa_{coh}} \end{aligned}$$

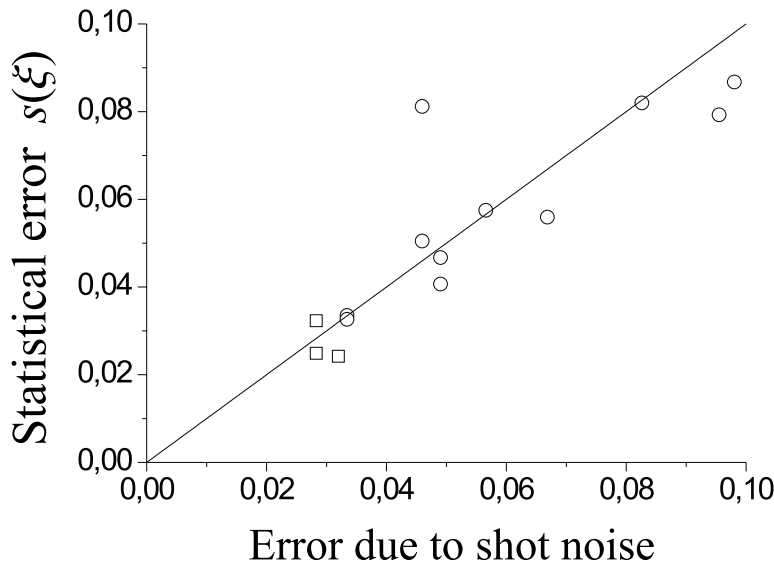


Figure 8.12: The statistical error on the individual spin squeezing measurements for each run as a function of the estimated error due to the probe shot noise fluctuations. Circles: off-resonant runs. Squares: runs at resonance. Solid line: a straight line with a slope of one.

We use the fact that the effect of the squeezed pump is small so that $\kappa_{sq}/\kappa_{coh} \simeq 1$ and $s(\kappa_{coh})^2 + s(\kappa_{sq})^2 \simeq 2s(\kappa_{coh})^2$. We furthermore assume that we can measure the probe optical depth α' with high precision from the DC lock-in voltage so that $s(\kappa_{coh} - \alpha') = s(\kappa_{coh})$. The RF lock-in voltage for coherent light excitation is given by $\Delta V_{RF} = k_{RF}(1 - e^{-\alpha'} - \kappa_{coh}) \simeq k_{RF}(\alpha' - \kappa_{coh})$. The modulation depth $a = \alpha' - \kappa_{coh}$ has a contribution from the reduction in shot noise (α' term) and a contribution from the atomic spin noise (κ_{coh}). Although the atomic noise κ_{coh} has a significant influence on the modulation depth, κ_{coh} is still very small compared to the overall probe shot noise. The last factor in Eq. (8.19) represents the relative error (or inverse S/N) in the measurement of the spectral density modulation depth, and we can substitute it with Eq. (8.18) to get the estimated error due to shot noise fluctuations

$$\begin{aligned} s'(\xi) &= \sqrt{2} \frac{\kappa_{coh} - \alpha'}{\kappa_{coh}} \frac{1}{1920(\kappa_{coh} - \alpha')} \\ &= \frac{1}{1360\kappa_{coh}} \end{aligned} \quad (8.20)$$

In Fig. 8.12 we plot the statistical error $s(\xi)$ on an individual spin squeezing measurement for all the spin squeezing runs as a function of the error calculated from Eq. (8.20), with κ_{coh} averaged over all the measurements within each run. The statistical errors $s(\xi)$ are just the length of the error bars in Fig. 8.9 multiplied by the square root of the number of measurements within the actual run. The κ_{coh} values for the different runs are different because of different probe detunings and different trapping conditions (e.g. optical depth). The solid line in Fig. 8.12 is a straight line with a slope of one. We conclude from this figure that the fundamental quantum noise of the coherent state probe indeed limits the S/N in the spin squeezing measurements. We know from Eq. (8.16) that there is only two ways of reducing the effect of the shot noise; either average for a longer time (smaller ν_{VB}) or measure the fluctuations in a larger bandwidth (larger ν_{RB}). Alternatively, we could use a squeezed probe, but that would require a second squeezing setup. It is now clear that we could have improved the statistics of our spin squeezing data if we had used detectors with a bandwidth equal to the spectrum analyzer resolution bandwidth of 300kHz. The next resolution bandwidth on the Anritsu MS710A spectrum analyzer is 1MHz, and this is

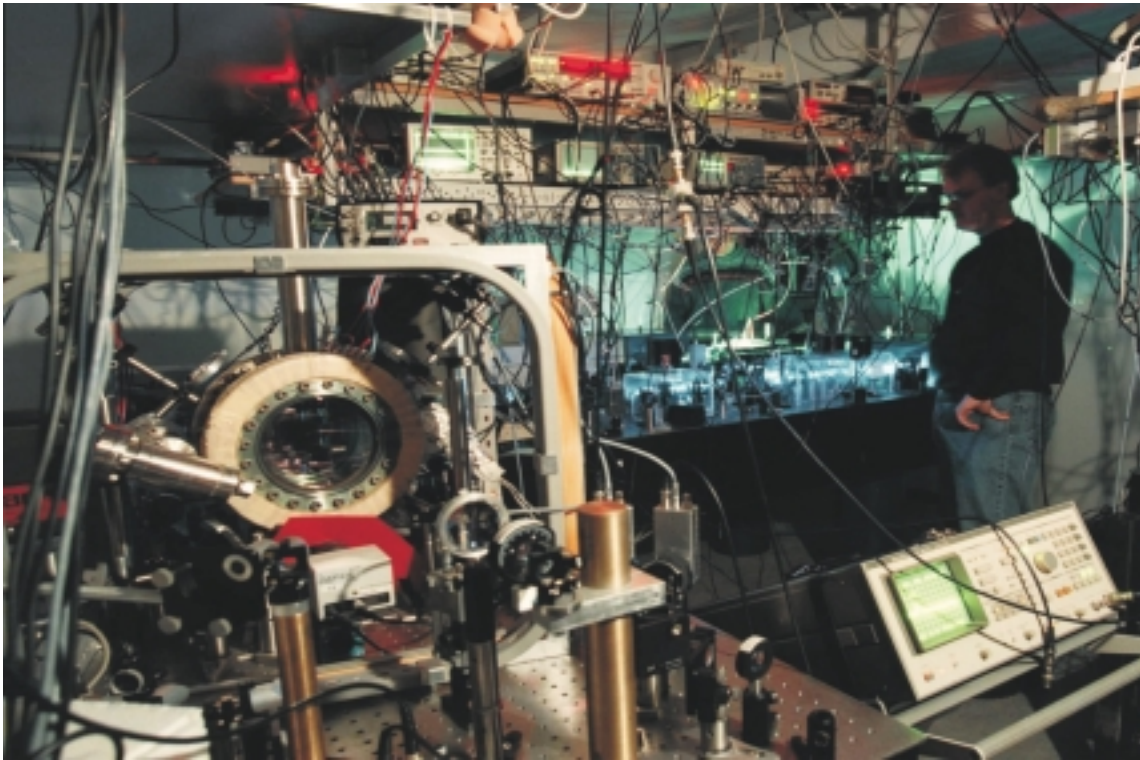


Figure 8.13: Atomic spins are being squeezed in the lab. On the left we have the vacuum chamber which holds the MOT. On the right we find Jens who is generating a squeezed quantum pump. The blue light at the squeezing setup is the pump field for the OPO produced by second harmonic generation.

too large since we measure the atomic noise close to the low frequencies, where the pump and the probe lasers have excess classical/technical amplitude noise.

In conclusion, we have in this chapter observed the spin squeezed state of atoms. We believe that we can explain the relatively small degree of spin squeezing from the theoretical limitations and the experimental imperfections such as the effect of radiation trapping. The accuracy of the observed degree of spin squeezing is limited by the fundamental quantum fluctuations in the probe used to read out the atomic state.

Chapter 9

Future prospects for spin squeezed atoms

We have in this thesis investigated the concept of spin squeezing in a large ensemble of atoms. The discussion has focused on generation of spin squeezing in a short-lived excited state by continuous absorption of squeezed light. We found a theoretical maximum noise reduction of 50% due to the spontaneous decay of the atoms. In chapter 4 we deduced that the degree of spin squeezing is further reduced when the atomic Zeeman degeneracy is increased. For our Cesium atoms in $6P_{3/2}F = 5$, the theory predicts a maximum noise reduction in \hat{F}'_z of about 32%. Because of the short lifetime of the spin squeezed state, we cannot store the quantum correlations for an extended period. Hence, we cannot demonstrate quantum memory.

In chapter 8 we verified experimentally that spin squeezing in the excited state can be generated by squeezed light absorption. The observed noise reduction in \hat{F}'_z is just $1.16\% \pm 0.32\%$, although the theory predicts about 11% for the actual degree of squeezing in the excitation field. We find that experimental imperfections, like the effect of radiation trapping and imperfect readout of the relevant atomic spin variable, can explain the small observed degree of spin squeezing. Furthermore, the readout with an off-resonant probe gives a very small signal as compared to the shot noise of the coherent state probe. An extremely long averaging time is therefore required in order to see the small effect of spin squeezing. Hence, we cannot claim that our spin squeezing results are directly useful in terms of improved spectroscopy or as a quantum information tool. But our results are important as a proof-of-principle experiment, and it is very well possible that spin squeezed atoms will play a significant role in future applications.

The theoretical limits and the experimental imperfections discussed above are not fundamental limitations in atomic spin squeezing. Theoretical calculations [82] show that 100% spin squeezing can be generated in the ground state by squeezed light interaction. The atomic fountain frequency standard [1] uses a method to read out the final atomic state that is much more efficient than the method we have used in chapter 7 and 8¹. This frequency standard is today limited in stability by the atomic quantum noise, and it can therefore take advantage of quantum correlated atoms with reduced spin noise.

An experiment on spin squeezed atoms in an atomic fountain setup is currently prepared in our group in collaboration with the group of Christophe Salomon at École Normale Supérieure in Paris. The goal for this project is to demonstrate that quantum correlated atoms in principle can be used to improve the stability of a frequency standard. Furthermore, this project will be aimed at a demonstration of storage of the atomic correlations for some time in an interaction free region, i.e. a quantum memory demonstration. In the following we present the basic ideas behind this experiment as a demonstration

¹The method used in Ref. [1] for the readout cannot be used for spin squeezing in the excited state. It can only be applied to correlations between long-lived states.

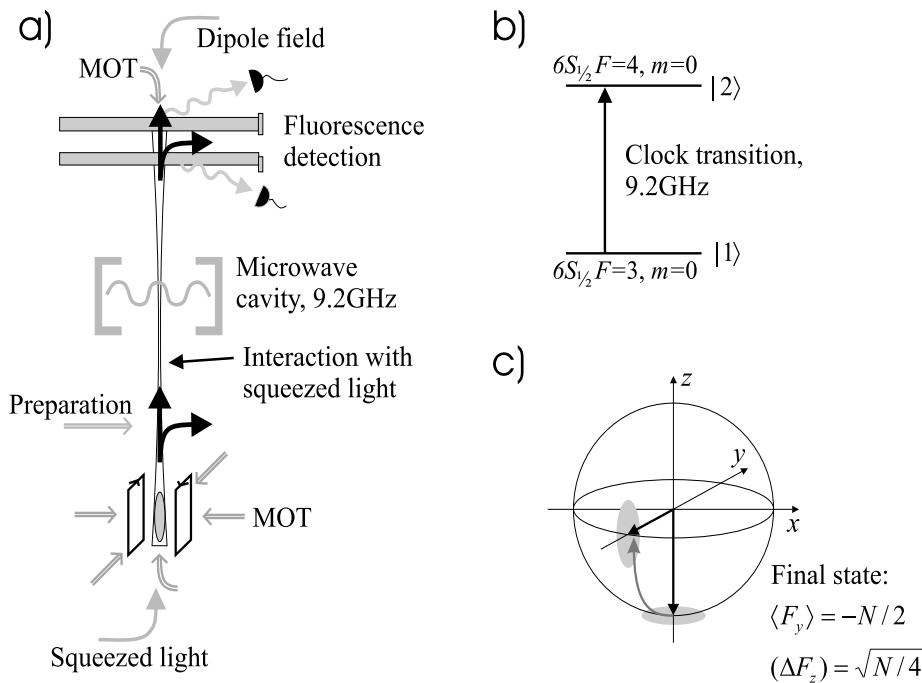


Figure 9.1: a) Schematic overview of the atomic fountain setup. Atoms are first trapped and cooled in a MOT. The atoms are then launched by detuning of the vertical trapping beams. After preparation of the atoms in the $F = 3, m = 0$ state, they interact with the 9.2GHz microwave field. This interaction results in a $\pi/2$ rotation of the atomic pseudo spin. Finally, the populations in the two $m = 0$ states are measured by fluorescence detection. b) The effective two-level atom. A pseudo spin-1/2 system is defined from these two levels. c) Representation of the $\pi/2$ rotation of the collective pseudo spin. The "noise circles" represent the quantum fluctuations in the directions orthogonal to the mean spin (arrows).

of the potential of spin squeezed states of atoms.

9.1 The atomic fountain

The basic parts of the projected fountain setup are shown in Fig. 9.1a. Cesium atoms are collected and trapped in a magneto-optical trap. With rectangular current coils for the magnetic field gradient, we get larger gradients in the radial directions than in the longitudinal direction. This produces a cigar shaped cloud of atoms elongated in the vertical direction as demonstrated in Ref. [107]. After collection of a large number of atoms in the MOT, we will launch the cloud in the vertical direction by detuning of the vertical trapping beams. In a normal fountain the atomic cloud expands in the transverse directions after the launch. However, when the squeezed light is shined onto the atoms, we must have a large optical depth to get an efficient transfer of correlations. It is therefore important that we somehow prevent this transverse spread so that a large optical depth is preserved. This can be accomplished by using a strong far-detuned laser beam, which guides the atoms in a dipole potential. The guiding laser field will be traveling vertically through the fountain setup. We plan to use a standard Nd:YAG laser at 1064nm with about 10W of optical power for the guiding. The guiding is most efficient when the initial atomic cloud in the MOT is shaped like a cigar. A similar guiding of rubidium atoms launched from a MOT is demonstrated in Ref. [107].

To obtain a simple, clean two-level system, we have to prepare all our atoms in the same quantum

state. By a combination of microwave pulses and laser pulses, we can clean up the atomic sample so that about 10% of the atoms are put into the $6S_{1/2}F = 3, m = 0$ state and all other atoms are removed [108]. After the atoms are prepared in a single quantum state, we can apply our squeezed light and produce the correlated atomic sample. The squeezed light will be applied in a pulse of a few ms duration. We discuss the squeezed light interaction in more detail in the following section; here we continue under the assumption that no squeezed light is applied as for an ordinary fountain clock.

The atoms continue their journey into a resonator, which holds a microwave field near-resonant with the well-known 9.2GHz clock transition, $|1\rangle = 6S_{1/2}F = 3, m = 0 \rightarrow |2\rangle = 6S_{1/2}F = 4, m = 0$, see Fig. 9.1b. When the fountain is used as an atomic clock, the amplitude of the microwave field is adjusted so that the atoms experience a π pulse when the field is at exact resonance. The field is then slightly detuned so that the pulse area is close to $\pi/2$ and each atom ends up in a superposition; $c_1|1\rangle + c_2|2\rangle$ with $|c_1|^2 \simeq |c_2|^2 \simeq 1/2$. The population in each of the two states (i.e. $|c_1|^2$ and $|c_2|^2$) depends on the exact pulse area, which again depends on the microwave frequency. A population measurement can therefore produce a feedback signal to the frequency of the microwave field, which is then locked to the atomic transition.

The populations in the two atomic states are measured by fluorescence detection. After the atoms have left the microwave cavity, they go into a standing wave laser beam, which is resonant with the optical transition $6S_{1/2}F = 4 \rightarrow 6P_{3/2}F = 5$. A fraction of the fluorescence from the atoms is detected with a signal which is proportional to the number of atoms in $|2\rangle$. A traveling wave laser beam resonant with the same transition is subsequently used to push away all atoms in the $|2\rangle$ state. A second standing wave with light on the $6S_{1/2}F = 4 \rightarrow 6P_{3/2}F = 5$ and $6S_{1/2}F = 3 \rightarrow 6P_{3/2}F = 4$ transitions provides a fluorescence signal proportional to the number of atoms in $|1\rangle$. Usually hundreds of fluorescence photons from each atom are detected [1]. This detection technique is very efficient and without the huge noise we found for the readout with a near-resonant probe.

The atoms are in a superposition state before the population measurement, and hence the measurement results in a projection with a random outcome. This randomness in the measurement is the fundamental quantum projection noise [1, 3]. The projection noise can also be seen as spin noise if we introduce a pseudo spin $\hat{\mathbf{J}}^n$ for atom number n by

$$\begin{aligned}\hat{J}_x^n &= \frac{1}{2} \left(|2\rangle_{n,n} \langle 1| + |1\rangle_{n,n} \langle 2| \right) \\ \hat{J}_y^n &= \frac{1}{2i} \left(|2\rangle_{n,n} \langle 1| - |1\rangle_{n,n} \langle 2| \right) \\ \hat{J}_z^n &= \frac{1}{2} \left(|2\rangle_{n,n} \langle 2| - |1\rangle_{n,n} \langle 1| \right)\end{aligned}\tag{9.1}$$

The collective spin is given by the sum $\hat{\mathbf{J}} = \sum_n \hat{\mathbf{J}}^n$. Before the microwave interaction, we have all N atoms in the state $|1\rangle$, i.e. $\langle \hat{J}_z \rangle = -N/2$, and the spin is in a coherent spin state as shown in Fig. 9.1c, (the coherent spin state is defined on page 57). The $\pi/2$ pulse rotates the mean spin into the $x - y$ plane while the spin remains in a coherent spin state. The difference between the population in $|2\rangle$ and $|1\rangle$ is given by $2\hat{J}_z$, and the projection noise is basically the variance of \hat{J}_z , $(\Delta \hat{J}_z)^2 = N/4$. In Fig. 9.1c we represent the noise in the spin components orthogonal to the mean spin by a "noise circle".

The description above is, apart from the squeezed light interaction and the dipole guiding, very similar to the working principles of *PHARAO* - an atomic clock designed for microgravity conditions [109]. Earth based atomic fountain clocks usually use the separated oscillatory method of Ramsey [75], where the atoms pass through the microwave resonator twice before detection. The long interrogation time between the microwave interactions, which is set basically by the gravity, gives narrow fringes (steep population versus frequency slope) and hence high stability of the clock.

In our initial experiment we will probably not work in this "clock mode". We are interested in the projection noise and squeezing hereof, and we will be less sensitive to frequency fluctuations if we use broad fringes and a resonant $\pi/2$ pulse. When the projection noise for uncorrelated atoms, which

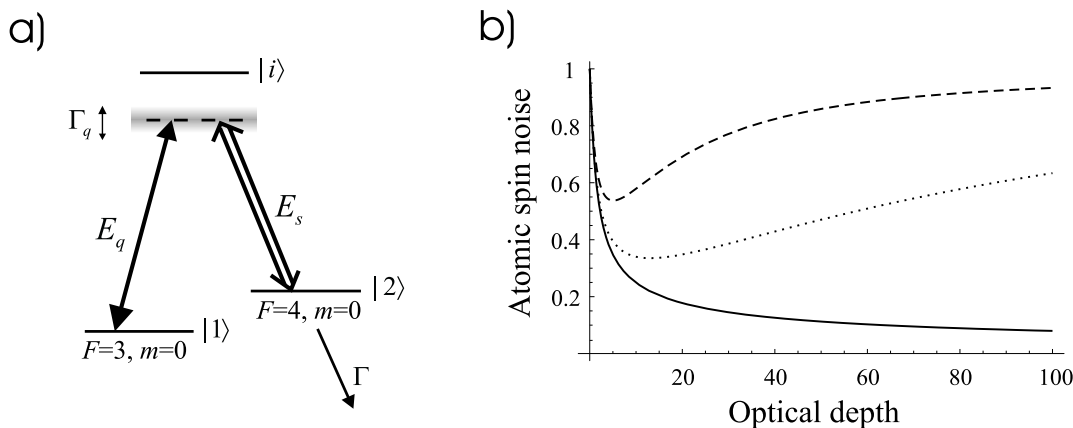


Figure 9.2: a) The scheme for generation of spin squeezing in the ground state. E_q and E_s are the squeezed vacuum field and the strong coherent field which interact with the states $|1\rangle$ and $|2\rangle$ in a Raman process. Both fields are far from resonance with the intermediate state $|i\rangle$. Γ_q is the bandwidth of squeezing and Γ is the dephasing rate for the $|1\rangle \leftrightarrow |2\rangle$ coherence. b) Theoretical spin noise versus optical depth for the quantum field. The spin noise is normalized to the noise of the coherent spin state. Solid line: infinite bandwidth Γ_q . Dotted line: $\Gamma_q/\Gamma = 50$. Dashed line: $\Gamma_q/\Gamma = 10$. The figure is borrowed from Ref. [82].

establishes the standard quantum limit of spin noise, is measured in this setup, we can apply the squeezed light interaction to produce spin squeezing and demonstrate quantum memory.

9.2 Spin squeezing in a fountain

It is shown in Ref. [74, 75] that spin squeezing can improve the sensitivity in a system which is completely equivalent to the fountain setup described in the previous section. A method for generation of spin squeezed atoms in the fountain setup is proposed in Ref. [82]. This proposal is based on the scheme shown in Fig. 9.2a. After the atoms are prepared in the state $|1\rangle$, we apply a pulse of squeezed vacuum (E_q) together with a strong coherent field (E_s). The two fields constitute the two arms of a Raman process, and they are far detuned from the intermediate state $|i\rangle$. Multi-atom correlations are induced by absorption of the squeezed vacuum field. These correlations reduce the fluctuations in the transverse pseudo spin components \hat{J}_y at the expense of excess noise in the other spin component \hat{J}_x . The typical photon number in a squeezed vacuum field is very small. Thus, the absorption does not transfer any significant population from $|1\rangle$ to $|2\rangle$ and $\langle \hat{J}_z \rangle$ remains (almost) unchanged. The fields E_s and E_q are on for a time longer than the inverse dephasing time Γ^{-1} for the $|1\rangle \leftrightarrow |2\rangle$ coherence. Γ includes the power broadening from the strong field E_s caused by spontaneous Raman scattering. Thus, Γ is large in the presence of E_s and small in the absence of E_s . We will therefore reach the steady state spin squeezing relatively fast when the fields are on. The induced correlations will be preserved after the fields are turned off, because Γ then becomes small. After the squeezed light interaction, the pseudo spin is rotated by the microwave interaction so that $\hat{J}_y \rightarrow \hat{J}_z$, and consequently the measured spin component \hat{J}_z will have the projection noise reduced. The calculated variance of the final \hat{J}_z variable, normalized to the coherent spin state variance, is plotted in Fig. 9.2b as a function of the optical depth for the quantum field E_q . The solid line is for infinite bandwidth Γ_q of the perfectly squeezed vacuum field. The dotted line is for $\Gamma_q/\Gamma = 50$, and the dashed line is for $\Gamma_q/\Gamma = 10$. We see that a significant noise reduction is possible with this scheme.

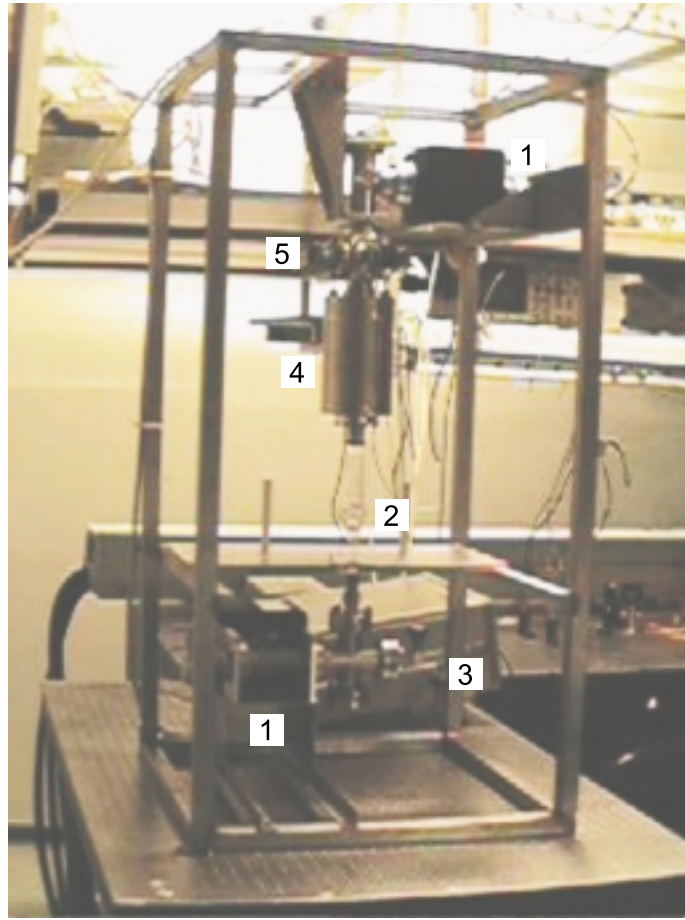


Figure 9.3: A picture of the atomic fountain vacuum chamber. 1: ion pumps. 2: small glass vacuum chamber for the MOT. 3: Cs reservoir. 4: the chamber for the microwave resonator. 5: detection zone.

The theory used to derive the graphs in Fig. 9.2b is based on an elimination of the intermediate state $|i\rangle$, which is valid for a large intermediate state detuning. The atoms can after the elimination be treated as effective two-level systems. The equations for this two-level system are fully equivalent with the Heisenberg-Langevin equations for the fields and the optical coherences in chapter 4. The equations can be solved with the same techniques as we used in chapter 4, with the result shown in Fig. 9.2b.

The proposal for generation of spin squeezing via a Raman interaction has some advantages over spin squeezing in the excited state. The fact that the atoms remain in the ground states removes the fundamental limit on the degree of spin squeezing due to spontaneous decay. Furthermore, the long-lived states make it possible to store the quantum information for some time after the fields E_q and E_s have been turned off. The quantum information will be stored for the time it takes atoms to travel from the squeezed light interaction zone to the detection zone. In contrast, the excited state spin squeezing requires continuous regeneration of atomic correlations. The Raman interaction idea also has a drawback which is not present in the excited state spin squeezing. In the Raman process it is important that all atoms see the squeezed light, otherwise only some of the atoms will participate in the collective correlated state. On the other hand, we must absorb all the squeezed light in the atomic sample so that no correlations are lost. This requires a careful matching of the quantum field intensity profile and the density profile of the atomic sample. This problem does not exist in the excited state spin squeezing. In this case only

the atoms that interact with the squeezed light are excited, and only the excited atoms are detected in the readout process.

Our project on spin squeezing in a fountain is in progress, but there is still a long way to go before we can demonstrate storage of quantum correlations and improved performance of the atomic clock. So far we have finished the construction of the fountain vacuum chamber. A picture of the vacuum chamber is shown in Fig. 9.3.

Chapter 10

Résumé

In the last chapter of this thesis, we give a short résumé of the main results and conclusions from the previous chapters.

10.1 Introduction

In the first chapter of this thesis we motivate the work on interaction between nonclassical (squeezed) light and atoms. Squeezed light can be used for improved sensitivity in spectroscopy, where the limiting factor often is the shot noise of the coherent state probe. We can get below the shot noise level when a probe of squeezed light is utilized. However, more interesting experiments involve quantum control and manipulation, which are essential elements in the context of quantum information. Squeezed light can also be used for experiments within this area. One example is generation of spin squeezed atoms, where the quantum correlations between photons in the squeezed light beam are converted into quantum correlations between atoms in a gas. This idea about mapping the statistics of light onto atoms can also be seen as storage of the quantum information in light on a medium of atoms. The spin squeezed atoms, which have reduced quantum fluctuations in one collective spin component, can subsequently be used in experiments that are limited in sensitivity by the atomic quantum noise. The demonstration of atomic spin squeezing is the prime experiment in this thesis.

10.2 Spectroscopy on classically modulated atoms

In chapter 2 we introduce our magneto-optical trap for neutral cesium atoms. The trap is characterized by means of absorption spectroscopy, and we find an average density of about $\rho = 3 \cdot 10^{10} \text{cm}^{-3}$ with nearly $3 \cdot 10^9$ atoms in the trap. These numbers are typical for a large MOT. The large MOT is important for our experiments because the interaction strength between a nonclassical excitation field and the atomic sample is set by the resonant optical depth α_0 . We have measured $\alpha_0 \simeq 23$ with a weak resonant probe beam in the absence of the MOT trapping beams.

We introduce the double-optical resonance technique as a tool to read out the properties of an intermediate atomic state with a probe of light. The readout is refined by using a polarization interferometer, which gives access to the anisotropic effects such as circular birefringence and linear dichroism. The measured anisotropy is related to the intermediate state atomic variables.

A new method for efficient spectroscopy on a MOT is demonstrated. We apply frequency modulation to our MOT trapping beams, which are near the $6S_{1/2}F = 4 \rightarrow 6P_{3/2}F = 5$ transition at 852nm. The atoms in the $6P$ state are probed on the $6P_{3/2}F = 5 \rightarrow 6D_{5/2}F = 4, 5, 6$ transitions at 917nm. The frequency modulation of the trapping beams is converted in the amplitude and polarization modulation of the resonant probe. This provides a large spectroscopy signal measured at the frequency of modulation.

The pump modulation technique is an easy way to achieve shot noise limited spectroscopy in contrast to ordinary FM spectroscopy, where the (imperfect) frequency modulation is applied to the probe. The measured FM absorption and polarization rotation spectra are compared to simple theoretical models. The modulated pump spectroscopy is not only interesting from a spectroscopists viewpoint, it is also a natural starting point for our subsequent study of the effects of quantum fluctuations in the pump field. Finally, we demonstrate how the intrinsic phase noise of the diode trapping laser provides enough "modulation" to give a clear signal on the probe transition. This shows that diode lasers cannot be used to study the fundamental quantum noise of excited state atoms.

10.3 Squeezed states of light

The squeezed states of light are introduced in chapter 3. We show how the sub-threshold optical parametric oscillator (OPO) provides a squeezed vacuum output. When the squeezed vacuum is mixed with a strong coherent field in the same polarization, we get the usual quadrature squeezed states. In this thesis we are more interested in the polarization squeezed states, which we obtain when the squeezed vacuum beam and the coherent state beam are overlapped in orthogonal polarizations. The polarization squeezed state is described by an angular momentum operator which is closely related to the usual Stokes parameters.

Our source of polarization squeezed light, which is build around the OPO, can run at wavelengths between 850nm and 920nm. We have used 917nm for the excited state transition $6P_{3/2}F = 5 \rightarrow 6D_{5/2}F = 6$ in cesium and 852nm for the $6S_{1/2}F = 4 \rightarrow 6P_{3/2}F = 5$ transition. We find almost identical squeezing at the two wavelengths with a spectral density about 3.0dB below the shot noise level. The factors that limit the squeezing are somewhat different for the two wavelengths. At 917nm we have low passive losses and small blue-light-induced infrared absorption (BLIIRA), but we also have a small nonlinearity of our KNbO_3 crystal. At 852nm we find larger passive losses and BLIIRA, but this is compensated by a larger nonlinearity. We finally demonstrate that the squeezed light can be used for polarization spectroscopy on cold atoms trapped in a MOT with the sensitivity beyond the standard quantum limit.

10.4 Mapping the quantum state of light onto atoms

The theory for mapping the statistics of polarization squeezed light onto an ensemble of atoms is derived in chapter 4. The theory assumes complete absorption of a weak quantum field on a $F \rightarrow F' = F + 1$ transition, where F is the total atomic angular momentum. In addition, the theory assumes that the atomic ground state F is unpolarized. We use the method of linearized Heisenberg-Langevin equations to derive explicit expressions for the fluctuations in the excited state variables \hat{F}'_z , $\hat{F}'_x\hat{F}'_y + \hat{F}'_y\hat{F}'_x$, and $\hat{F}'_x{}^2 - \hat{F}'_y{}^2$. We show that excitation with a coherent state of light gives the same atomic quantum noise as if we assume that the atoms are uncorrelated. This is not a surprise since the coherent state can be described as a stream of uncorrelated photons. The noise level measured with coherent light excitation can thus be used to establish the standard quantum limit (SQL) of atomic fluctuations. If a polarization squeezed state of light is used for excitation, we have fluctuations below the SQL in one of the atomic variables. The noise reduction takes place in a continuous scheme, where we constantly absorb correlated photons in order to regenerate the atomic correlations lost by spontaneous decay. The atomic variable with suppressed noise is determined by the Stokes parameter which is squeezed. A maximum of 50% noise reduction is found for $F = 0$; this limit is due to the random spontaneous decay. We find the noise reduction to be even smaller when the Zeeman degeneracy is increased; about 32% for \hat{F}'_z noise and 12% for $\hat{F}'_x\hat{F}'_y + \hat{F}'_y\hat{F}'_x$ noise, when a perfectly polarization squeezed field is applied on the $6S_{1/2}F = 4 \rightarrow 6P_{3/2}F = 5$ transition of cesium.

10.5 Spin squeezed states and entanglement

The concept of spin squeezed states is introduced in chapter 5. The commutation relations for the spin components result in Heisenberg uncertainty relations given by $(\Delta\hat{s}_y)^2(\Delta\hat{s}_z)^2 \geq \langle\hat{s}_x\rangle^2/4$, together with cyclic permutations of this expression. It seems natural to define spin squeezing in analogy with the squeezed states of light by taking $\langle\hat{s}_x\rangle/2$ as the SQL and just require that either $(\Delta\hat{s}_y)^2$ or $(\Delta\hat{s}_z)^2$ is below the SQL. However, this definition does not guarantee that a spin squeezed collection of spin-1/2 systems has any nonclassical correlations or entanglement between the individual spins. In order to make spin squeezed states something special, we require from our definition that spin squeezing implies entanglement. Several different definitions of spin squeezing have been given in the literature, and although they have been said to imply correlations, we show that only one of the definitions fulfils our requirements.

We end this chapter by relating the concept of spin squeezing to the results derived in chapter 4. We find the $F = 0$ case of chapter 4 to be spin squeezed when a polarization squeezed excitation field is applied. We choose to use the term "spin squeezing" for the situations with $F > 0$ since they also show noise reduction in a spin component because of multi-atom entanglement.

10.6 Theory for the atomic state readout

In chapter 4 we derived the theory for generation of spin squeezing in the excited state, but we still need a method to read out the excited state properties to prove that the spin noise is below the SQL. In chapter 6 we show that a near resonant probe in double-optical resonance with the quantum pump will do the job. The excited state spin fluctuations result in fluctuations in the linear dichroism and circular birefringence on the probe transition. Hence, the atomic fluctuations are mapped onto the polarization state of the probe, which can then be analyzed in a polarization interferometer. We discuss the requirements for an efficient readout of the collective atomic spin state, and we derive explicit expressions for the spectral density of the differential photocurrent from the polarization interferometer. We find that the resonant probe is sensitive to noise in $\hat{F}'_x\hat{F}'_y + \hat{F}'_y\hat{F}'_x$, whereas \hat{F}'_z noise is prevailing for the off-resonant probe. We complete this chapter by a discussion of the effect of inhomogeneous broadening (e.g. Doppler broadening).

10.7 Quantum noise of uncorrelated atoms

The noise (i.e. the variance) for a sum of identically distributed but independent (uncorrelated) stochastic variables scales linearly with the number of variables. On the other hand, if the variables are perfectly correlated (e.g. all identical), we find the variance to scale with the square of the number of variables. The same is true for atomic noise. The cesium cloud in the MOT is believed to be an undisturbed sample with a fixed number of atoms. Hence, only the quantum noise of uncorrelated atoms should be seen when we probe the sample.

In chapter 7 we report observations of the atomic noise when the atoms are excited by the rather strong trapping beams. A probe on the $6P_{3/2}F = 5 \rightarrow 6D_{5/2}F = 6$ transition, which completes the double-optical resonance, is used to read out the atomic noise in the $F = 5$ state. The atomic noise is found to be linear in the number of probed atoms, which shows that the noise of the atomic sample is limited by the quantum noise of uncorrelated atoms. Only in one previous experiment has this linear dependence been observed, and that with rather poor statistics [3]. We observe that the atomic noise is predominated by a term quadratic in the number of atoms when frequency modulation is applied to the trapping beams. The gradual change from predominantly quantum noise (linear dependence) to predominantly classical noise (quadratic dependence) is observed when the FM index is varied. We end the chapter by an experiment which shows that the quantum spin noise of an atomic sample can indeed limit the signal-to-noise ratio in spectroscopy.

These experiments are the first step towards the observation of spin squeezed atoms. They show that it is possible to observe the atomic quantum noise with the readout method that we investigated theoretically in chapter 6.

10.8 Spin squeezing in a cold atomic ensemble

In chapter 8 we continue our experimental investigation of the spin noise of atoms in the excited state. The experiment is refined so that the excitation is obtained with a weak unidirectional pump beam on exact resonance with the $6S_{1/2}F = 4 \rightarrow 6P_{3/2}F = 5$ transition. The spin noise in $F = 5$ is read out with a copropagating probe field on the $6P_{3/2}F = 5 \rightarrow 6D_{5/2}F = 6$ transition. We use the coherent light excitation to establish the standard quantum limit of atomic spin fluctuations. We can induce classical excess noise in the Stokes parameter \hat{S}_z or \hat{S}_y by adding a vertically polarized, weak, amplitude modulated field to the horizontally polarized coherent excitation field. We observe off-resonant excess noise in our probe signal when the noise in the Stokes parameter \hat{S}_z is above the SQL. This is in agreement with the theory from chapter 4 and 6, which predicts that a noisy \hat{S}_z results in a noisy \hat{F}'_z , which is seen by an off-resonant probe. When the classical noise gives excess noise in \hat{S}_y , we find a resonant excess noise contribution in the probe signal. The noisy \hat{S}_y results in a noisy $\hat{F}'_x\hat{F}'_y + \hat{F}'_y\hat{F}'_x$, which is seen by a resonant probe. We find that we are much more sensitive to the \hat{F}'_z noise than to the $\hat{F}'_x\hat{F}'_y + \hat{F}'_y\hat{F}'_x$ noise, and we therefore choose to look for spin squeezing in \hat{F}'_z .

Only a nonclassical pump field can have the \hat{S}_z noise below the SQL as required for generation of spin squeezing. After 53 hours of effective data acquisition, we find that the observed \hat{F}'_z noise is changed by $-1.16\% \pm 0.32\%$ due to the nonclassical correlations in the excitation field. This is in agreement with the estimates from the classical noise measurements and the -1.8dB of squeezing in the pump field. The very long measurement time is required because the noise reduction is only about 0.02% of the probe shot noise level. The theory of chapter 4 predicts a spin squeezing of about -11% for -1.8dB of squeezing in the pump field. We find that the fluorescence field caused by radiation trapping and an imperfect readout of \hat{F}'_z can explain the major part of the discrepancy between theory and experiment.

We conclude that spin squeezing due to multi-atom entanglement is observed, although the noise reduction is too small for a direct application in spectroscopy or quantum information. Our experiment, which is a proof-of-principle experiment, is the first demonstration of spin squeezed atoms. It is the first experiment that demonstrates mapping of the quantum properties of a nonclassical beam of light onto a large ensemble of atoms.

10.9 Future prospects for spin squeezed atoms

The excited state spin squeezing, which we demonstrate in chapter 8, has some practical disadvantages. First of all, the degree of spin squeezing is theoretically limited to 50% because of the spontaneous decay whereby atomic correlations are lost. Furthermore, the atomic correlations are lost almost immediately after the quantum pump is turned off. Thus, we cannot use the excited state spin squeezing idea to store quantum information for an extended period. We have also seen that our experimental implementation has imperfections, which severely reduce the degree of spin squeezing. However, these drawbacks are not fundamental to spin squeezed states of atoms generated by squeezed light interaction.

In chapter 9 we outline the ideas behind a new project, which is designed for demonstration of spin squeezing in the atomic ground state. The squeezed light together with a strong coherent field couples two ground states in a Raman process. Ideally the ground states do not decay, and we can have 100% spin squeezing. The spin squeezing will stay after the nonclassical field is turned off, and this allows for a demonstration of quantum memory. We will use a setup similar to the atomic fountain clock setup for detection of the spin squeezed atoms in the ground state. The state of the art atomic fountain clock is today limited in stability by the fundamental atomic quantum noise, and it will gain in stability if a spin

squeezed sample of atoms is utilized. This project is in progress, but a lot of hard work is still needed before the demonstration of quantum memory and an atomic clock based on entangled atoms.

Appendix A

Circular birefringence for two different transitions

We show in this Appendix that the circular birefringence on the $6P_{3/2}F = 5 \rightarrow 6D_{5/2}F = 6$ transition is substantially larger than on the $6P_{3/2}F = 5 \rightarrow 6D_{5/2}F = 5$ transition for a given orientation in the $6P_{3/2}F = 5$ state. The derivation in this appendix is based on the results of chapter 6.

The absorption and birefringence is calculated from the Maxwell equation in Eq. (6.4) and the equation for the source term in Eq. (6.9). Combining these two equations gives

$$\begin{aligned} \frac{\partial}{\partial z} \bar{b}_{\pm}(z) &= \frac{-u'(x, y)}{i\Delta' + \gamma'/2} \frac{\rho L}{c} \int \int u'^*(x, y) \\ &\times \sum_{m=-F'}^{F'} \beta_m^{\pm} \{ \beta_m^{\pm} \bar{b}_{\pm}(z) \bar{\sigma}_{F'm, F'm}(\mathbf{r}) + \beta_{m\pm 2}^{\mp} \bar{b}_{\mp}(z) \bar{\sigma}_{F'm, F'm\pm 2}(\mathbf{r}) \} dx dy \end{aligned} \quad (\text{A.1})$$

The circular birefringence does not mix the two circular polarizations, they just experience different phase shifts. Hence, the last term in the sum over m can be ignored in the present calculations. We can now write the refractive indices (n_{\pm}) and the absorption coefficients (κ_{\pm}) as

$$\kappa_{\pm} + in_{\pm} = \frac{C}{i\Delta' + \gamma'/2} \sum_{m=-F'}^{F'} \beta_m^{\pm 2} \bar{\sigma}_{F'm, F'm} \quad (\text{A.2})$$

C is a proportionality constant, and we have ignored the spatial dependence. The coupling strengths β_m^{\pm} are given in Eq. (6.3) for the $F = 5 \rightarrow F = 6$ transition

$$\beta_m^{\pm 2} = \frac{c\lambda^2\gamma}{352\pi L} (7 \pm m) (6 \pm m) \quad (\text{A.3})$$

The $\kappa_{\pm} + in_{\pm}$ expression in Eq. (A.2) for the $F = 5 \rightarrow F = 6$ transition can then be written as

$$\kappa_{\pm} + in_{\pm} = \frac{C}{i\Delta' + \gamma'/2} \frac{c\lambda^2\gamma}{352\pi L} \left(42\rho' \pm 13\bar{F}'_z + \bar{F}'_z{}^2 \right) \quad (\text{A.4})$$

ρ' is the density of atoms in the $6P_{3/2}F = 5$ state. \bar{F}'_z is the average z -component of the spin of the atoms in $6P_{3/2}F = 5$, and $\bar{F}'_z{}^2$ is the average of the squared z -component of the spin. It is the term proportional to $\pm 13\bar{F}'_z$ that is responsible for the circular birefringence.

The coupling strength $\tilde{\beta}_m^{\pm}$ for the $F = 5 \rightarrow F = 5$ transition can be derived from the results in Ref. [30]

$$\tilde{\beta}_m^{\pm 2} = \frac{7c\lambda^2\gamma}{4000\pi L} (6 \pm m) (5 \mp m) \quad (\text{A.5})$$

The refractive indices and the absorption coefficients for the $F = 5 \rightarrow F = 5$ transition are

$$\tilde{\kappa}_{\pm} + i\tilde{n}_{\pm} = \frac{C}{i\Delta' + \gamma'/2} \frac{7c\lambda^2\gamma}{4000\pi L} \left(30\rho' \pm \bar{F}'_z - \overline{F'^2_z} \right) \quad (\text{A.6})$$

A comparison between Eq. (A.3) and (A.6) shows that the circular birefringence on the $F = 5 \rightarrow F = 5$ transition (i.e. $\tilde{n}_+ - \tilde{n}_-$) is only 4.8% of the birefringence on the $F = 5 \rightarrow F = 6$ transition for the same orientation (\bar{F}'_z) in the $6P_{3/2}F = 5$ state. The FM polarization rotation spectra in section 2.4.3 are proportional to the square of the susceptibility. Hence, we expect the size of the FM polarization rotation signal from the $F = 5 \rightarrow F = 5$ transition to be only about 0.2% of the signal from the $F = 5 \rightarrow F = 6$ transition.

For unpolarized atoms in the $6P_{3/2}F = 5$ state, we have $\langle F'_{x,y,z} \rangle = \rho' F(F+1)/3 = 10\rho'$ and $\bar{F}'_z = 0$. In this situation the ratio of the absorption on $F = 5 \rightarrow F = 5$ and on $F = 5 \rightarrow F = 6$ is found to be $\frac{77}{325}$; the same result as we obtain from Eq. (2.10).

Appendix B

Correlation functions of Langevin forces

We will use the generalized Einstein relation to derive the correlation functions of Langevin forces. The generalized Einstein relation for the single atom operators (e.g. $\sigma_{a,b} = |a\rangle\langle b|$) and the corresponding Langevin forces ($f_{a,b}$) can be written as [79]

$$\langle f_{a,b}(t) f_{c,d}(t') \rangle = \langle \mathcal{D}(\sigma_{a,b}\sigma_{c,d}) - \mathcal{D}(\sigma_{a,b})\sigma_{c,d} - \sigma_{a,b}\mathcal{D}(\sigma_{c,d}) \rangle \delta(t-t') \quad (\text{B.1})$$

Here $\mathcal{D}(\sigma_{a,b})$ is the expression for $\dot{\sigma}_{a,b}$ obtained from the Heisenberg-Langevin equation for $\sigma_{a,b}$ but without the Langevin force term. Note that the operator product $\sigma_{a,b}\sigma_{c,d}$ can be reduced to either one single atom operator ($\sigma_{a,d}$) if $b=c$ or the product equals zero. The Dirac delta function in Eq. (B.1) represents the short memory of the reservoir of vacuum modes responsible for the Langevin forces.

The single atom correlation functions can be calculated in the absence of the excitation field \hat{a}_\pm because the coupling to the vacuum modes is independent of the coupling to the excitation field \hat{a}_\pm . This can also be seen explicitly; we can write $\mathcal{D}(\sigma_{a,b}) = [\sigma_{a,b}, H]/(i\hbar) + \Gamma_{a,b}$, where the first term is the Heisenberg term and $\Gamma_{a,b}$ represents the damping term. The interaction with the excitation field is included in the Heisenberg terms in Eq. (B.1), but these terms cancel because of the equality $[\sigma_{a,b}\sigma_{c,d}, H] = \sigma_{a,b}[\sigma_{c,d}, H] + [\sigma_{a,b}, H]\sigma_{c,d}$.

From Eq. (B.1) we derive the following single atom correlation functions

$$\begin{aligned} \langle f_{Fm, F'n}(t) f_{F'k, Fl}(t') \rangle &= \gamma \langle \sigma_{Fm, Fl} \rangle \delta_{n,k} \delta(t-t') \\ \langle f_{F'm, F'n}(t) f_{F'k, Fl}(t') \rangle &= \gamma \langle \sigma_{F'm, Fl} \rangle \delta_{n,k} \delta(t-t') \\ \langle f_{Fm, F'n}(t) f_{F'k, F'l}(t') \rangle &= \gamma \langle \sigma_{Fm, F'l} \rangle \delta_{n,k} \delta(t-t') \\ \langle f_{F'm, F'n}(t) f_{F'k, F'l}(t') \rangle &= \gamma \langle \sigma_{F'm, F'l} \rangle \delta_{n,k} \delta(t-t') \end{aligned} \quad (\text{B.2})$$

These are the only nonzero correlation functions of single atom Langevin forces, except for $\langle f_{Fm, F'n}(t) f_{Fk, Fl}(t') \rangle$, which we do not need. In the first of the listed correlation functions in Eq. (B.2), we assume that the excited state population is much smaller than the ground state population. We can use the equality $f_{a,b}^\dagger = f_{b,a}$ in the correlation functions that involve the hermitian conjugate of a Langevin force.

The Langevin forces in the equations for the continuous atomic operators are defined from the single atom Langevin forces, in the same way as the continuous atomic operators are defined from the single atom operators, that is

$$\mathcal{F}_{a,b}(\mathbf{r}, t) = \frac{1}{\rho\delta V} \sum_i f_{a,b}^i(t) \quad (\text{B.3})$$

The sum is over all atoms within the small volume δV around \mathbf{r} . We will assume that different atoms couple to independent vacuum modes, which means that Langevin forces for different atoms are uncorrelated. With this assumption we arrive at the following relations for the nonzero correlation functions of the continuous Langevin forces

$$\begin{aligned}
\langle \mathcal{F}_{Fm,F'n}(\mathbf{r},t) \mathcal{F}_{F'k,F'l}(\mathbf{r}',t') \rangle &= \rho^{-1} \gamma \bar{\sigma}_{Fm,F'l}(\mathbf{r}) \delta_{n,k} \delta(t-t') \delta(\mathbf{r}-\mathbf{r}') & (B.4) \\
\langle \mathcal{F}_{F'm,F'n}(\mathbf{r},t) \mathcal{F}_{F'k,F'l}(\mathbf{r}',t') \rangle &= \rho^{-1} \gamma \bar{\sigma}_{F'm,F'l}(\mathbf{r}) \delta_{n,k} \delta(t-t') \delta(\mathbf{r}-\mathbf{r}') \\
\langle \mathcal{F}_{Fm,F'n}(\mathbf{r},t) \mathcal{F}_{F'k,F'l}(\mathbf{r}',t') \rangle &= \rho^{-1} \gamma \bar{\sigma}_{Fm,F'l}(\mathbf{r}) \delta_{n,k} \delta(t-t') \delta(\mathbf{r}-\mathbf{r}') \\
\langle \mathcal{F}_{F'm,F'n}(\mathbf{r},t) \mathcal{F}_{F'k,F'l}(\mathbf{r}',t') \rangle &= \rho^{-1} \gamma \bar{\sigma}_{F'm,F'l}(\mathbf{r}) \delta_{n,k} \delta(t-t') \delta(\mathbf{r}-\mathbf{r}')
\end{aligned}$$

The continuous Langevin forces also fulfil $\mathcal{F}_{a,b}^\dagger = \mathcal{F}_{b,a}$. We can express the average continuous atomic operators in terms of the mean amplitude of the excitation field if we apply the Heisenberg-Langevin equations in steady state, and use the assumptions about weak excitation and an unpolarized ground state. The calculations are similar to those leading to Eq. (4.19) and (4.25). After a Fourier transform in time, we have the following expressions for the correlation functions

$$\begin{aligned}
\langle \mathcal{F}_{Fm,F'n}(\mathbf{r},\Omega) \mathcal{F}_{F'k,F'l}(\mathbf{r}',\Omega') \rangle &= 2\pi \rho^{-1} \gamma \delta_{n,k} \delta(\Omega + \Omega') \delta(\mathbf{r}-\mathbf{r}') \delta_{m,l} (2F+1)^{-1} & (B.5) \\
\langle \mathcal{F}_{F'm,F'n}(\mathbf{r},\Omega) \mathcal{F}_{F'k,F'l}(\mathbf{r}',\Omega') \rangle &= -4\pi \rho^{-1} \delta_{n,k} \delta(\Omega + \Omega') \delta(\mathbf{r}-\mathbf{r}') u^*(x,y) \times \\
&\quad (2F+1)^{-1} \{ \delta_{m,l+1} \alpha_{m-1}^+ \bar{a}_+^*(z) + \delta_{m,l-1} \alpha_{m+1}^- \bar{a}_-^*(z) \} \\
\langle \mathcal{F}_{Fm,F'n}(\mathbf{r},\Omega) \mathcal{F}_{F'k,F'l}(\mathbf{r}',\Omega') \rangle &= \langle \mathcal{F}_{F'l,F'k}(\mathbf{r},\Omega) \mathcal{F}_{F'n,Fm}(\mathbf{r}',\Omega') \rangle^* \\
\langle \mathcal{F}_{F'm,F'n}(\mathbf{r},\Omega) \mathcal{F}_{F'k,F'l}(\mathbf{r}',\Omega') \rangle &= 2\pi \rho^{-1} \delta_{n,k} \delta(\Omega + \Omega') \delta(\mathbf{r}-\mathbf{r}') \times \\
&\quad \left\{ \delta_{ml} \frac{4|u(x,y)|^2}{\gamma(2F+1)} \{ \alpha_{m-1}^{+2} \bar{a}_+(z) \bar{a}_+^*(z) + \alpha_{m+1}^{-2} \bar{a}_-(z) \bar{a}_-^*(z) \} \right. \\
&\quad + \delta_{m+2,l} \frac{4|u(x,y)|^2}{\gamma(2F+1)} \alpha_{m+1}^+ \alpha_{m+1}^- \bar{a}_+(z) \bar{a}_-^*(z) \\
&\quad \left. + \delta_{m-2,l} \frac{4|u(x,y)|^2}{\gamma(2F+1)} \alpha_{m-1}^+ \alpha_{m-1}^- \bar{a}_+^*(z) \bar{a}_-(z) \right\}
\end{aligned}$$

B.1 Langevin forces used in the F'_z calculations

The Langevin forces that enters into the final expression for $\delta \hat{F}'_z$ in Eq. (4.29) are defined in Eq. (4.20), (4.27), (4.28), and (4.30), and they are summarized here

$$\begin{aligned}
\mathcal{F}_a^\pm(\Omega) &= \frac{2\rho L}{c\gamma\Lambda_0} \sum_{m=-F}^F \alpha_m^\pm \int_0^\infty dz e^{-\Lambda_0 z} \int \int dxdy u^*(x,y) \mathcal{F}_{Fm,F'm\pm 1}(\mathbf{r},\Omega) & (B.6) \\
\mathcal{F}_b^\pm(\Omega) &= \rho \sum_{m=-F'}^{F'} m \alpha_{m\mp 1}^\pm \int_0^\infty dz e^{-\Lambda_0 z} \int \int dxdy u^*(x,y) \mathcal{F}_{Fm\mp 1,F'm}(\mathbf{r},\Omega) \\
\mathcal{F}_c(\Omega) &= \rho \sum_{m=-F'}^{F'} m \int_0^\infty dz \int \int dxdy \mathcal{F}_{F'm,F'm}(\mathbf{r},\Omega)
\end{aligned}$$

It is now a straight forward calculation to derive the correlation functions of the Langevin forces \mathcal{F}_a^\pm , \mathcal{F}_b^\pm and \mathcal{F}_c . In the derivation we use the definitions in Eq. (4.1), (4.8), and (4.20) together with the expressions in this Appendix. The nonzero correlation functions are listed here

$$\begin{aligned}
 \langle \mathcal{F}_a^+ (\Omega), \mathcal{F}_a^{+\dagger} (\Omega') \rangle &= \langle \mathcal{F}_a^- (\Omega), \mathcal{F}_a^{-\dagger} (\Omega') \rangle = \frac{2\pi L}{c\Lambda_0^2} \delta (\Omega + \Omega') \\
 \langle \mathcal{F}_b^+ (\Omega), \mathcal{F}_b^{+\dagger} (\Omega') \rangle &= \langle \mathcal{F}_b^- (\Omega), \mathcal{F}_b^{-\dagger} (\Omega') \rangle = \frac{\pi\gamma^2 c (F+2) (4F+5)}{20L} \delta (\Omega + \Omega') \\
 \langle \mathcal{F}_c (\Omega), \mathcal{F}_c (\Omega') \rangle &= \frac{\pi c (F+2) (4F+5)}{5L} (\bar{a}_+^{in*} \bar{a}_+^{in} + \bar{a}_-^{in*} \bar{a}_-^{in}) \delta (\Omega + \Omega') \\
 \langle \mathcal{F}_b^\pm (\Omega), \mathcal{F}_a^{\pm\dagger} (\Omega') \rangle &= \langle \mathcal{F}_a^\pm (\Omega), \mathcal{F}_b^{\pm\dagger} (\Omega') \rangle^* = \pm \frac{\pi\gamma (F+2)}{2\Lambda_0} \delta (\Omega + \Omega') \\
 \langle \mathcal{F}_c (\Omega), \mathcal{F}_a^{\pm\dagger} (\Omega') \rangle &= \langle \mathcal{F}_a^\pm (\Omega), \mathcal{F}_c (\Omega') \rangle^* = \mp \frac{\pi (F+2) \bar{a}_\pm^{in*}}{\Lambda_0} \delta (\Omega + \Omega') \\
 \langle \mathcal{F}_c (\Omega), \mathcal{F}_b^{\pm\dagger} (\Omega') \rangle &= \langle \mathcal{F}_b^\pm (\Omega), \mathcal{F}_c (\Omega') \rangle^* = -\frac{\pi c\gamma (F+2) (4F+5) \bar{a}_\pm^{in*}}{10L} \delta (\Omega + \Omega')
 \end{aligned} \tag{B.7}$$

B.2 Langevin forces used in the $\hat{F}_x'^2 - \hat{F}_y'^2$ calculations

The Langevin forces that enters into the expression for $\delta(\hat{F}_x'^2 - \hat{F}_y'^2)$ are, besides \mathcal{F}_a^\pm in Eq. (B.6), defined by

$$\begin{aligned}
 \mathcal{F}_d^\pm &= \frac{\rho}{2} \sum_{m=-F'}^{F'} \sqrt{F'(F'+1) - m(m+1)} \sqrt{F'(F'+1) - (m+1)(m+2)} \\
 &\times \int_0^\infty dz e^{-\Lambda_0 z} \iint dxdy u^*(x, y) \{ \alpha_{m+2\mp 1}^\pm \mathcal{F}_{Fm+2\mp 1, F'm}(\mathbf{r}, \Omega) + \alpha_{m\mp 1}^\pm \mathcal{F}_{Fm\mp 1, F'm+2}(\mathbf{r}, \Omega) \} \\
 \mathcal{F}_e &= \frac{\rho}{2} \sum_{m=-F'}^{F'} \sqrt{F'(F'+1) - m(m+1)} \sqrt{F'(F'+1) - (m+1)(m+2)} \\
 &\times \int_0^\infty dz \iint dxdy (\mathcal{F}_{F'm+2, F'm}(\mathbf{r}, \Omega) + \mathcal{F}_{F'm, F'm+2}(\mathbf{r}, \Omega))
 \end{aligned} \tag{B.8}$$

The nonzero correlation functions involving \mathcal{F}_a^\pm , \mathcal{F}_d^\pm , and \mathcal{F}_e are

$$\begin{aligned}
 \langle \mathcal{F}_a^+ (\Omega), \mathcal{F}_a^{+\dagger} (\Omega') \rangle &= \langle \mathcal{F}_a^- (\Omega), \mathcal{F}_a^{-\dagger} (\Omega') \rangle = \frac{2\pi L}{c\Lambda_0^2} \delta (\Omega + \Omega') \\
 \langle \mathcal{F}_d^+ (\Omega), \mathcal{F}_d^{+\dagger} (\Omega') \rangle &= \langle \mathcal{F}_d^- (\Omega), \mathcal{F}_d^{-\dagger} (\Omega') \rangle = \frac{\pi\gamma^2 c (F+2) (2F+5) (8F^2 + 10F + 7)}{140L} \delta (\Omega + \Omega') \\
 \langle \mathcal{F}_e (\Omega), \mathcal{F}_e (\Omega') \rangle &= \frac{\pi c (F+2) (2F+5) (8F^2 + 10F + 7)}{35L} (\bar{a}_+^{in*} \bar{a}_+^{in} + \bar{a}_-^{in*} \bar{a}_-^{in}) \delta (\Omega + \Omega') \\
 \langle \mathcal{F}_d^\pm (\Omega), \mathcal{F}_a^{\mp\dagger} (\Omega') \rangle &= \langle \mathcal{F}_a^\mp (\Omega), \mathcal{F}_d^{\pm\dagger} (\Omega') \rangle^* = -\frac{\gamma\pi (F+2) (2F+5)}{10\Lambda_0} \delta (\Omega + \Omega') \\
 \langle \mathcal{F}_e (\Omega), \mathcal{F}_a^{\pm\dagger} (\Omega') \rangle &= \langle \mathcal{F}_a^\pm (\Omega), \mathcal{F}_e (\Omega') \rangle^* = \frac{\pi (F+2) (2F+5)}{5\Lambda_0} \bar{a}_\mp^{in*} \delta (\Omega + \Omega') \\
 \langle \mathcal{F}_e (\Omega), \mathcal{F}_d^{\pm\dagger} (\Omega') \rangle &= \langle \mathcal{F}_d^\pm (\Omega), \mathcal{F}_e (\Omega') \rangle^* = -\frac{\pi\gamma c (F+2) (2F+5) (8F^2 + 10F + 7)}{70L} \bar{a}_\pm^{in*} \delta (\Omega + \Omega')
 \end{aligned} \tag{B.9}$$

Appendix C

The ground state fluctuations in light-atom mapping

We show in this appendix that the ground state fluctuations can be neglected in the calculations on mapping of light onto atoms in chapter 4. We consider here only the ground state fluctuations present in the absence of the excitation field. This is in accordance with the applied perturbative approach, where the excitation field is assumed to be weak. The existence of ground state fluctuations for $F > 0$ can easily be seen from the ground state angular momentum commutator, e.g. $[\hat{F}_x, \hat{F}_y] = i\hat{F}_z$, and the corresponding uncertainty relation. Only a $F = 0$ ground state does not have fluctuations in the absence of an excitation field.

The ground state fluctuations are, in the perturbative limit, not correlated with the fluctuations in the excitation field or the fluctuations caused by the coupling to the electromagnetic vacuum (represented by Langevin forces). We can therefore calculate the effect of the ground state fluctuations by repeating the derivation in chapter 4, except that we now keep terms proportional to e.g. $\delta\tilde{\sigma}_{Fm,Fn}(\mathbf{r})$ and neglect the Langevin force contribution. We can always add the Langevin contribution from chapter 4 to the final result. Here we consider only the contribution to $(\hat{F}'_z)_\Omega^2$ from the ground state fluctuations. We assume that the contribution to $(\hat{F}'_x - \hat{F}'_y)_\Omega^2$ is of a similar negligible magnitude.

We first rewrite Eq. (4.19) to include the fluctuating ground state populations and coherences

$$\begin{aligned} \delta\tilde{\sigma}_{Fm,F'm\pm 1}(\mathbf{r}, \Omega) &= \frac{-u(x, y)}{(i\Omega + \gamma/2)} \\ &\times \left[\alpha_m^\pm \bar{a}_\pm(z) \delta\tilde{\sigma}_{Fm, Fm}(\mathbf{r}, \Omega) + \alpha_{m\pm 2}^\mp \bar{a}_\mp(z) \delta\tilde{\sigma}_{Fm, Fm\pm 2}(\mathbf{r}, \Omega) + \alpha_m^\pm (2F + 1)^{-1} \delta\tilde{a}_\pm(z, \Omega) \right] \end{aligned} \quad (\text{C.1})$$

Substituting this result into Eq. (4.17) gives for the field fluctuations at position z

$$\begin{aligned} \delta\tilde{a}_\pm(z, \Omega) &= e^{-\Lambda(\Omega)z} \delta\tilde{a}_\pm(0, \Omega) + \frac{3\Lambda(\Omega)}{2(F+1)(2F+3)} \int_0^z dz' e^{-\Lambda(\Omega)(z-z')} \\ &\times \int \int dx' dy' |u(x', y')|^2 [\bar{a}_\pm(z') \delta\Sigma_1^\pm(\mathbf{r}', \Omega) + \bar{a}_\mp(z') \delta\Sigma_2^\pm(\mathbf{r}', \Omega)] \end{aligned} \quad (\text{C.2})$$

Here we have introduced the fluctuating atomic variables $\delta\Sigma_{1,2}^\pm$, which are defined by

$$\begin{aligned} \delta\Sigma_1^\pm(\mathbf{r}, \Omega) &= \sum_{m=-F}^F (F+2 \pm m)(F+1 \pm m) \delta\tilde{\sigma}_{Fm, Fm}(\mathbf{r}, \Omega) dx dy \\ \delta\Sigma_2^\pm(\mathbf{r}, \Omega) &= - \sum_{m=-F}^F \sqrt{(F+2 \pm m)(F+1 \pm m)(F \mp m)(F-1 \mp m)} \delta\tilde{\sigma}_{Fm, Fm\pm 2}(\mathbf{r}, \Omega) dx dy \end{aligned} \quad (\text{C.3})$$

We take Eq. (4.22) as our starting point for the calculation of \hat{F}'_z -noise. In contrast to the derivation in chapter 4, we now keep the lowest order contribution to $\delta\tilde{\sigma}_{F'm, F'm}(\mathbf{r}, \Omega)$ from the ground state fluctuations and neglect the Langevin forces. After substitution of Eq. (C.1) and the mean value in Eq. (4.19) into Eq. (4.22) we obtain

$$\begin{aligned} \delta\tilde{\sigma}_{F'm, F'm}(\mathbf{r}, \Omega) = & \tag{C.4} \\ & \frac{4|u(x, y)|^2}{(2F+1)(\gamma^2 + i2\gamma\Omega)} \left(\alpha_{m-1}^{+2} \left[\bar{a}_+^*(z) \delta\tilde{a}_+(z, \Omega) + \bar{a}_+(z) \delta\tilde{a}_+^\dagger(z, \Omega) \right] \right. \\ & \left. + \alpha_{m+1}^{-2} \left[\bar{a}_-^*(z) \delta\tilde{a}_-(z, \Omega) + \bar{a}_-(z) \delta\tilde{a}_-^\dagger(z, \Omega) \right] \right) \\ & + \frac{4|u(x, y)|^2}{(\gamma + i\Omega)(\gamma + i2\Omega)} \left(\alpha_{m-1}^{+2} \bar{a}_+(z) \bar{a}_+^*(z) \delta\tilde{\sigma}_{Fm-1, Fm-1}(\mathbf{r}, \Omega) + \alpha_{m+1}^{-2} \bar{a}_-(z) \bar{a}_-^*(z) \delta\tilde{\sigma}_{Fm+1, Fm+1}(\mathbf{r}, \Omega) \right. \\ & \left. + \alpha_{m-1}^+ \alpha_{m+1}^- \left[\bar{a}_+(z) \bar{a}_-^*(z) \delta\tilde{\sigma}_{Fm+1, Fm-1}(\mathbf{r}, \Omega) + \bar{a}_+^*(z) \bar{a}_-(z) \delta\tilde{\sigma}_{Fm-1, Fm+1}(\mathbf{r}, \Omega) \right] \right) \end{aligned}$$

We use Eq. (C.4) in the definition of $\delta\hat{F}'_z(\Omega)$ in Eq. (4.21). Before the final integration over z we have

$$\begin{aligned} \delta\hat{F}'_z(z, \Omega) = & \rho \int \int dx dy \sum_{m=-F'}^{F'} m \delta\tilde{\sigma}_{F'm, F'm}(\mathbf{r}, \Omega) \tag{C.5} \\ & = \frac{(F+2)c}{\gamma L} \Lambda(\Omega) \left\{ \bar{a}_+^*(z) \delta\tilde{a}_+(z, \Omega) + \bar{a}_+(z) \delta\tilde{a}_+^\dagger(z, \Omega) \right. \\ & \quad \left. + \bar{a}_-^*(z) \delta\tilde{a}_-(z, \Omega) + \bar{a}_-(z) \delta\tilde{a}_-^\dagger(z, \Omega) \right\} \\ & + \frac{3c\Lambda(\Omega)(F+2)}{(\gamma + i\Omega)2L(F+1)(2F+3)} \int \int dx dy |u(x, y)|^2 \left\{ \bar{a}_+(z) \bar{a}_+^*(z) \delta\Sigma_3^+(\mathbf{r}, \Omega) \right. \\ & \quad \left. + \bar{a}_-(z) \bar{a}_-^*(z) \delta\Sigma_3^-(\mathbf{r}, \Omega) - \bar{a}_+(z) \bar{a}_-^*(z) \delta\Sigma_4(\mathbf{r}, \Omega) - \bar{a}_+^*(z) \bar{a}_-(z) \delta\Sigma_4^\dagger(\mathbf{r}, \Omega) \right\} \end{aligned}$$

The fluctuating atomic variables $\delta\Sigma_3^\pm$ and $\delta\Sigma_4$ are defined by

$$\begin{aligned} \delta\Sigma_3^\pm(\mathbf{r}, \Omega) = & \frac{2}{F+2} \sum_{m=-F-1}^{F+1} m(F+1 \pm m)(F \pm m) \delta\tilde{\sigma}_{Fm \mp 1, Fm \mp 1}(\mathbf{r}, \Omega) \tag{C.6} \\ \delta\Sigma_4(\mathbf{r}, \Omega) = & \frac{2}{F+2} \sum_{m=-F-1}^{F+1} m \sqrt{(F+1+m)(F+m)(F+1-m)(F-m)} \delta\tilde{\sigma}_{Fm+1, Fm-1}(\mathbf{r}, \Omega) \end{aligned}$$

We now integrate Eq. (C.5) over z and use the complete absorption to set the upper integration limit at infinity. The integration is carried out by a change in the integration order, similar to Eq. (4.28). The result is

$$\begin{aligned} \delta\hat{F}'_z(\Omega) = & \rho \int_0^\infty dz \int \int dx dy \sum_{m=-F'}^{F'} m \delta\tilde{\sigma}_{F'm, F'm}(\mathbf{r}, \Omega) = \frac{(F+2)}{\gamma + i\Omega} \delta\hat{S}_z^{in}(\Omega) \tag{C.7} \\ & + \frac{3c\Lambda(\Omega)(F+2)}{2L(\gamma + i\Omega)(F+1)(2F+3)} \int_0^\infty dz e^{-2\Lambda_0 z} \int \int dx dy |u(x, y)|^2 \\ & \quad \times \left\{ \bar{a}_+^{in*} \bar{a}_+^{in} [\delta\Sigma_3^+(\mathbf{r}, \Omega) + \delta\Sigma_1^+(\mathbf{r}, \Omega)] + \bar{a}_-^{in*} \bar{a}_-^{in} [\delta\Sigma_3^-(\mathbf{r}, \Omega) + \delta\Sigma_1^-(\mathbf{r}, \Omega)] \right. \\ & \quad \left. + \bar{a}_+^{in*} \bar{a}_-^{in} [\delta\Sigma_2^+(\mathbf{r}, \Omega) - \delta\Sigma_4^\dagger(\mathbf{r}, \Omega)] + \bar{a}_+^{in} \bar{a}_-^{in*} [\delta\Sigma_2^-(\mathbf{r}, \Omega) - \delta\Sigma_4(\mathbf{r}, \Omega)] \right\} \end{aligned}$$

The correlation functions for the $\delta\Sigma$ -operators are calculated in the subsequent section. We use the results of Eq. (C.15) to calculate the spectral density of fluctuations $(\hat{F}'_z)^2_\Omega$. We assume for simplicity

equal photon flux in the two circularly polarized components; $\Phi_+ = \Phi_- = \Phi/2$. The derivation is lengthy but trivial, with the result

$$\begin{aligned} \left(\hat{F}'_z\right)_\Omega^2 &= \frac{(F+2)^2}{\gamma^2 + \Omega^2} \left(\hat{S}_z^{in}\right)_\Omega^2 \\ &+ \frac{(F+2)^2 \Phi}{4(\gamma^2 + \Omega^2)} \frac{s\gamma\gamma_0}{(1 + 4\Omega^2/\gamma^2) \Omega^2} \frac{F(158F^2 + 477F + 394)}{35(F+1)(F+2)(2F+3)} \end{aligned} \quad (\text{C.8})$$

The first term is the fluctuations in the excited state spin component induced by the fluctuations in the excitation field; the same term as in Eq. (4.31). The second term is the contribution from the ground state fluctuations. We have introduced the saturation parameter (see page 9) $s = \Phi\sigma_0/(\pi w^2\gamma)$ with $2w$ as the diameter of the Gaussian mode excitation field (Eq. (3.3)) and $\sigma_0 = (2F+3)\lambda^2/2\pi(2F+1)$ as the resonant absorption cross section, see Eq. (6.16). γ_0 is defined in the following section as the bandwidth of ground state fluctuations. The first factor in the second term is equal to the first term for a coherent state excitation field. The last factor in the second term is zero at $F=0$, and it approaches $79/35 \simeq 2.3$ asymptotically for large F . Thus, we conclude that the contribution from the ground state fluctuations can be neglected if the second factor in the second term is much smaller than one, i.e.

$$\frac{s\gamma\gamma_0}{(1 + 4\Omega^2/\gamma^2) \Omega^2} \ll 1 \quad (\text{C.9})$$

The typical parameters are $s \lesssim 0.1$ (weak excitation), and $\Omega/\gamma \simeq 0.5$. Hence, we can safely neglect the ground state fluctuations if $\gamma_0 \ll \gamma$, i.e. if the bandwidth of ground state fluctuations is much smaller than the bandwidth of excited state fluctuations; a requirement which is easily fulfilled. If $s \ll 1$, we can neglect the ground state fluctuations when the variance $(\Delta\hat{F}'_z)^2$ is derived by integrating $(\hat{F}'_z)_\Omega^2$ over Ω . This is easily seen when the full expression for $W(\Omega, \Omega')$ in Eq. (C.14) is used in the correlation functions.

Note that the contribution from the ground state fluctuations in Eq. (C.8) is quadratic in the photon flux of the excitation field. In the experiments we find $(\hat{F}'_z)_\Omega^2$ to be linear in the number of excited state atoms, $N' = \Phi/\gamma$. This also shows that the ground state fluctuations play no role in the excited state fluctuations.

C.1 Correlation functions of ground state variables

We first calculate the equal time correlation functions for the fluctuating part of the ground state populations and coherences. We have from the definition in Eq. (4.3)

$$\int_V d^3\mathbf{r}' \langle \delta\tilde{\sigma}_{Fi,Fj}(\mathbf{r}) \delta\tilde{\sigma}_{Fm,Fn}(\mathbf{r}') \rangle = \frac{1}{\delta V \rho^2} \sum_{l,k} \langle (\tilde{\sigma}_{Fi,Fj}^l - \bar{\sigma}_{Fi,Fj}^l) (\tilde{\sigma}_{Fm,Fn}^k - \bar{\sigma}_{Fm,Fn}^k) \rangle \quad (\text{C.10})$$

The sum over l is a sum over all single atom operators for the atoms within the small volume δV around \mathbf{r} . The sum over k is a sum over all the atoms in the volume $V \gg \delta V$. We assume that the ground state fluctuations for different atoms are uncorrelated, which for $l \neq k$ gives

$$\langle (\tilde{\sigma}_{Fi,Fj}^l - \bar{\sigma}_{Fi,Fj}^l) (\tilde{\sigma}_{Fm,Fn}^k - \bar{\sigma}_{Fm,Fn}^k) \rangle = \langle (\tilde{\sigma}_{Fi,Fj}^l - \bar{\sigma}_{Fi,Fj}^l) \rangle \langle (\tilde{\sigma}_{Fm,Fn}^k - \bar{\sigma}_{Fm,Fn}^k) \rangle = 0 \quad (\text{C.11})$$

For the remaining terms with $l = k$ we have

$$\begin{aligned} \int_V d^3\mathbf{r}' \langle \delta\tilde{\sigma}_{Fi,Fj}(\mathbf{r}) \delta\tilde{\sigma}_{Fm,Fn}(\mathbf{r}') \rangle &= \frac{1}{\delta V \rho^2} \sum_l \langle (\tilde{\sigma}_{Fi,Fj}^l - \bar{\sigma}_{Fi,Fj}^l) (\tilde{\sigma}_{Fm,Fn}^l - \bar{\sigma}_{Fm,Fn}^l) \rangle \\ &= \frac{1}{\rho} \left((2F+1)^{-1} \delta_{j,m} \delta_{i,n} - (2F+1)^{-2} \delta_{i,j} \delta_{m,n} \right) \end{aligned} \quad (\text{C.12})$$

In the last equality we used the "unpolarized ground state"-assumption; $\bar{\sigma}_{Fm,Fn} = (2F+1)^{-1} \delta_{m,n}$. We now assume that the correlations decay exponentially in time, i.e.

$$\begin{aligned} \langle \delta \tilde{\sigma}_{Fi,Fj}(\mathbf{r}, t) \delta \tilde{\sigma}_{Fm,Fn}(\mathbf{r}', t') \rangle &= \langle \delta \tilde{\sigma}_{Fi,Fj}(\mathbf{r}) \delta \tilde{\sigma}_{Fm,Fn}(\mathbf{r}') \rangle e^{-\gamma_0 |t-t'|} \\ &= \frac{1}{\rho} \left((2F+1)^{-1} \delta_{j,m} \delta_{i,n} - (2F+1)^{-2} \delta_{i,j} \delta_{m,n} \right) \delta(\mathbf{r}-\mathbf{r}') e^{-\gamma_0 |t-t'|} \end{aligned} \quad (\text{C.13})$$

In the frequency domain we find after a Fourier transform

$$\langle \delta \tilde{\sigma}_{Fi,Fj}(\mathbf{r}, \Omega) \delta \tilde{\sigma}_{Fm,Fn}(\mathbf{r}', \Omega') \rangle = \frac{1}{\rho} \left((2F+1)^{-1} \delta_{j,m} \delta_{i,n} - (2F+1)^{-2} \delta_{i,j} \delta_{m,n} \right) \delta(\mathbf{r}-\mathbf{r}') W(\Omega, \Omega') \quad (\text{C.14})$$

$$W(\Omega, \Omega') = \frac{2\gamma_0^{-1}}{1 + \Omega^2/\gamma_0^2} 2\pi \delta(\Omega + \Omega') \simeq \frac{4\pi\gamma_0}{\Omega^2} \delta(\Omega + \Omega')$$

The last approximation is valid for $\gamma_0 \ll \Omega$. In the limit of unperturbed or isolated atoms in the ground state we expect γ_0 to approach zero, i.e. infinite "lifetime". We can therefore assume $\gamma_0 \ll \Omega$ to be fulfilled at typical detection frequencies Ω . With Eq. (C.14) we can calculate the correlation functions involving the $\delta\Sigma$ -operators defined in the previous section. The calculation is trivial but lengthy with the following final result for the nonzero correlation functions

$$\langle \delta\Sigma_1^\pm(\mathbf{r}, \Omega) \delta\Sigma_1^\pm(\mathbf{r}', \Omega') \rangle = \frac{4F(F+1)(2F+3)(8F+11)}{45} \frac{\delta(\mathbf{r}-\mathbf{r}')}{\rho} W(\Omega, \Omega') \quad (\text{C.15})$$

$$\langle \delta\Sigma_1^\pm(\mathbf{r}, \Omega) \delta\Sigma_1^\mp(\mathbf{r}', \Omega') \rangle = \frac{-2F(F+1)(2F+3)(14F+23)}{45} \frac{\delta(\mathbf{r}-\mathbf{r}')}{\rho} W(\Omega, \Omega')$$

$$\langle \delta\Sigma_2^\pm(\mathbf{r}, \Omega) \delta\Sigma_2^\mp(\mathbf{r}', \Omega') \rangle = \frac{2F(F+1)(2F-1)(2F+3)}{15} \frac{\delta(\mathbf{r}-\mathbf{r}')}{\rho} W(\Omega, \Omega')$$

$$\langle \delta\Sigma_3^\pm(\mathbf{r}, \Omega) \delta\Sigma_3^\pm(\mathbf{r}', \Omega') \rangle = \frac{4F(F+1)(2F+3)(194F^2+549F+349)}{315(F+2)} \frac{\delta(\mathbf{r}-\mathbf{r}')}{\rho} W(\Omega, \Omega')$$

$$\langle \delta\Sigma_3^\pm(\mathbf{r}, \Omega) \delta\Sigma_3^\mp(\mathbf{r}', \Omega') \rangle = \frac{4F(F+1)(2F+3)(82F^2+381F+461)}{315(F+2)} \frac{\delta(\mathbf{r}-\mathbf{r}')}{\rho} W(\Omega, \Omega')$$

$$\begin{aligned} \langle \delta\Sigma_4(\mathbf{r}, \Omega) \delta\Sigma_4^\dagger(\mathbf{r}', \Omega') \rangle &= \langle \delta\Sigma_4^\dagger(\mathbf{r}, \Omega) \delta\Sigma_4(\mathbf{r}', \Omega') \rangle \\ &= \frac{8F(F-1)(F+1)(2F-1)(2F+3)}{105(F+2)} \frac{\delta(\mathbf{r}-\mathbf{r}')}{\rho} W(\Omega, \Omega') \end{aligned}$$

$$\langle \delta\Sigma_3^\pm(\mathbf{r}, \Omega) \delta\Sigma_1^\pm(\mathbf{r}', \Omega') \rangle = \langle \delta\Sigma_1^\pm(\mathbf{r}, \Omega) \delta\Sigma_3^\pm(\mathbf{r}', \Omega') \rangle = \frac{\pm 4F(F+1)(2F+3)(14F+17)}{45} \frac{\delta(\mathbf{r}-\mathbf{r}')}{\rho} W(\Omega, \Omega')$$

$$\langle \delta\Sigma_3^\pm(\mathbf{r}, \Omega) \delta\Sigma_1^\mp(\mathbf{r}', \Omega') \rangle = \langle \delta\Sigma_1^\mp(\mathbf{r}, \Omega) \delta\Sigma_3^\pm(\mathbf{r}', \Omega') \rangle = \frac{\mp 4F(F+1)(2F+3)(10F+19)}{45} \frac{\delta(\mathbf{r}-\mathbf{r}')}{\rho} W(\Omega, \Omega')$$

Appendix D

Proof of entanglement in spin squeezed states

We prove in this appendix that the spin squeezing definition in Eq. (5.3) can only be fulfilled for an entangled ensemble of spin-1/2 subsystems. The proof, which is unpublished, is supplied by I. Cirac [88].

We first assume that we have an ensemble of N spin-1/2 systems that are disentangled (i.e. without entanglement). We show that the collective spin *cannot* fulfil Eq. (5.3) under this assumption. We therefore conclude that Eq. (5.3) can only be fulfilled for an entangled ensemble of spin-1/2 systems.

We define a disentangled or separable state as a state with a density matrix that can be written as a direct product of density matrices for each of the N spin-1/2 systems [110]

$$\rho = \sum_i p_i \rho^i, \quad \rho^i = \rho_1^i \otimes \rho_2^i \otimes \cdots \otimes \rho_N^i \quad (\text{D.1})$$

The sum over i includes an average over a statistical ensemble with $\sum_i p_i = 1$ and $p_i \geq 0$ for all i . Each of the density matrices ρ^i is a direct product of the reduced density matrices for each spin-1/2 subsystem. The mean value of an operator \hat{O} is given by $\langle \hat{O} \rangle = \text{Tr}(\rho \hat{O}) = \sum_i p_i \langle \hat{O} \rangle_i = \sum_i p_i \text{Tr}(\rho^i \hat{O})$.

We define the x -axis to be parallel to the mean collective spin $\langle \hat{\mathbf{S}} \rangle$, and we take the z -component of the collective spin to be the orthogonal component with the smallest variance, i.e. $\hat{S}_\perp = \hat{S}_z$. We introduce a new set of operators for the individual spins with zero mean values; $\delta \hat{s}_z^n = \hat{s}_z^n - \langle \hat{s}_z^n \rangle$. The linearity in the definition of the collective spin gives $\delta \hat{S}_z = \sum_{n=1}^N \delta \hat{s}_z^n$. We can now find a lower limit for the \hat{S}_z variance

$$\begin{aligned} (\Delta \hat{S}_z)^2 &= \langle \hat{S}_z^2 \rangle - \langle \hat{S}_z \rangle^2 = \langle \delta \hat{S}_z^2 \rangle = \sum_{n,m=1}^N \langle \delta \hat{s}_z^n \delta \hat{s}_z^m \rangle = \sum_{n=1}^N \langle \delta \hat{s}_z^{n2} \rangle + \sum_{n \neq m} \langle \delta \hat{s}_z^n \delta \hat{s}_z^m \rangle \\ &\stackrel{1}{=} \sum_{n=1}^N \langle \delta \hat{s}_z^{n2} \rangle + \sum_i p_i \left(\sum_{n,m} \langle \delta \hat{s}_z^n \rangle_i \langle \delta \hat{s}_z^m \rangle_i - \sum_{n=1}^N \langle \delta \hat{s}_z^n \rangle_i^2 \right) \\ &= \sum_{i,n} p_i \langle \delta \hat{s}_z^{n2} \rangle_i + \sum_i p_i \langle \delta \hat{S}_z \rangle_i^2 - \sum_{i,n} p_i \langle \delta \hat{s}_z^n \rangle_i^2 \stackrel{2}{\geq} \sum_{i,n} p_i (\langle \delta \hat{s}_z^{n2} \rangle_i - \langle \delta \hat{s}_z^n \rangle_i^2) \end{aligned} \quad (\text{D.2})$$

$$\begin{aligned}
&= \sum_{i,n} p_i (\langle \hat{s}_z^{n2} \rangle_i - \langle \hat{s}_z^n \rangle_i^2) \stackrel{3}{=} \sum_{i,n} p_i \left(\frac{1}{4} - \langle \hat{s}_z^n \rangle_i^2 \right) \stackrel{4}{=} \sum_{i,n} p_i (\langle \hat{s}_x^n \rangle_i^2 + \langle \hat{s}_y^n \rangle_i^2) \\
&= \frac{1}{N} \left(\sum_{i,n} p_i \right) \left(\sum_{i,n} p_i \langle \hat{s}_x^n \rangle_i^2 \right) + \frac{1}{N} \left(\sum_{i,n} p_i \right) \left(\sum_{i,n} p_i \langle \hat{s}_y^n \rangle_i^2 \right) \\
&\stackrel{5}{\geq} \frac{1}{N} \left(\sum_{i,n} p_i \langle \hat{s}_x^n \rangle_i \right)^2 + \frac{1}{N} \left(\sum_{i,n} p_i \langle \hat{s}_y^n \rangle_i \right)^2 = \frac{\langle \hat{S}_x \rangle^2 + \langle \hat{S}_y \rangle^2}{N} = \frac{\langle \hat{S}_x \rangle^2}{2S}
\end{aligned}$$

The less trivial steps in the derivation above are now explained in detail.

- 1. It follows from the direct product expression for ρ^i that the mean value of the product of operators belonging to different subsystems can be written as the product of the mean values; i.e. $\langle \delta \hat{s}_z^n \delta \hat{s}_z^m \rangle_i = \langle \delta \hat{s}_z^n \rangle_i \langle \delta \hat{s}_z^m \rangle_i$ for all $m \neq n$. This factorization is identical to the definition of uncorrelated random variables in classical probability theory. We cannot use this factorization as a definition of quantum correlations since for a statistical mixture we can have $\langle \delta \hat{s}_z^n \delta \hat{s}_z^m \rangle \neq \langle \delta \hat{s}_z^n \rangle \langle \delta \hat{s}_z^m \rangle$ because of classical correlations. An example of classical correlations without entanglement is found in the statistical mixture of the two product states $|\uparrow\rangle|\downarrow\rangle$ and $|\downarrow\rangle|\uparrow\rangle$.
- 2. We simply drop the nonnegative sum in the middle. The inequality is an equality in the absence of the statistical average.
- 3. For any spin-1/2 system we have $\langle \hat{s}_z^{n2} \rangle_i = 1/4$.
- 4. Consider the scalar product of the average (with respect to ρ^i) of spin number n with itself; $\langle \hat{\mathbf{s}}^n \rangle_i \cdot \langle \hat{\mathbf{s}}^n \rangle_i = \langle \hat{s}_x^n \rangle_i^2 + \langle \hat{s}_y^n \rangle_i^2 + \langle \hat{s}_z^n \rangle_i^2$. The scalar product is independent of the coordinate system, and in the system with the x' axis parallel to the mean spin we have $\langle \hat{\mathbf{s}}^n \rangle_i \cdot \langle \hat{\mathbf{s}}^n \rangle_i = \langle \hat{s}_{x'}^n \rangle_i^2 = 1/4$. Consequently, $1/4 - \langle \hat{s}_z^n \rangle_i^2 = \langle \hat{s}_x^n \rangle_i^2 + \langle \hat{s}_y^n \rangle_i^2$.
- 5. We apply the Cauchy/Schwarz' inequality; $\mathbf{x}^2 \mathbf{y}^2 \geq (\mathbf{x} \cdot \mathbf{y})^2$ for any vectors $\mathbf{x}, \mathbf{y} \in R^N$. We use the inequality with $x_{i,n} = \sqrt{p_i}$ and $y_{i,n} = \sqrt{p_i} \langle \hat{s}_x^n \rangle_i$.

This ends our proof, and we conclude that a squeezed spin state fulfilling the definition in Eq. (5.3) is composed of entangled spin-1/2 systems.

Appendix E

The uncertainty in a spectral density measurement

In many of the experiments presented in this thesis we use a spectrum analyzer (SA) to measure the noise or the fluctuations in a photocurrent i_{in} at a given frequency Ω . The noise at the frequency Ω is quantified by the spectral density $(i_{in})_{\Omega}^2$, see Eq. (6.21). The main contributions to $(i_{in})_{\Omega}^2$ in the spin noise experiments are the fundamental quantum noise of the light probe and the atomic noise, which is transferred to the probe by the atom-light interaction. We usually do not care about how the SA measures the spectral density. However, this is important in the final spin squeezing experiment in chapter 8. In this experiment our signal is a change in the atomic noise contribution, which we derive from spectral density measurements. The uncertainty in the spin squeezing measurement depends on the uncertainty in the $(i_{in})_{\Omega}^2$ measurement. In other words, the signal-to-noise ratio (S/N) in our spin squeezing experiment depends on the noise of the "noise measurement". The purpose of this appendix is to derive an expression for this "noise of noise" which we can compare with the estimated standard error in the spin squeezing measurement.

In Fig. E.1 we show a schematic diagram of a spectrum analyzer [48, 111, 62]. The input signal i_{in} from the photodetectors is divided into two paths. In one path we multiply the signal i_{in} by a signal that oscillates as $\cos(\Omega t)$. After the multiplication, we filter the product in the band pass filter (BPF). We consider a BPF which is centered at zero frequency. In most commercial spectrum analyzers the BPF is centered at a large frequency [111], but this is due to technical reasons, and it is of no importance in the present discussion. Thus, the BPF is here a low-pass filter with a resolution bandwidth ν_{RB} . The filtered signal is subsequently squared and added to the other component, which was multiplied by a $\sin(\Omega t)$ signal. Finally, the video filter (VF) averages the signal for a time set by the inverse video bandwidth ν_{VB}^{-1} . For a long averaging time ($\nu_{VB} \ll \nu_{RB}$), the output signal i_{out} is proportional to the spectral density $(i_{in})_{\Omega}^2$ integrated over the resolution bandwidth ν_{RB} . This is quite easy to verify for any input signal that can be written as a Fourier transform

$$i_{in}(t) = \int_0^{\infty} [i_s(\Omega') \cos(\Omega' t) + i_c(\Omega') \sin(\Omega' t)] d\Omega' \quad (\text{E.1})$$

In the diagram in Fig. E.1, the BPF and the VF are both low-pass filters. The different effects of the two filters are due to the different positions in the circuit relative to the squaring device.

The home-made SA, which we use in chapter 3 and 8 to actively stabilize the relative phase between the squeezed vacuum field and the overlapped coherent state, is based on the same principles as in Fig. E.1. We do not explicitly have a BPF in the home-made SA. The resolution bandwidth of the measurement is set by the 50kHz bandwidth of the electronic squaring device. Furthermore, the home-made SA includes only one quadrature (or one path in Fig. E.1). This is sufficient when the input signal is random noise without any phase information.

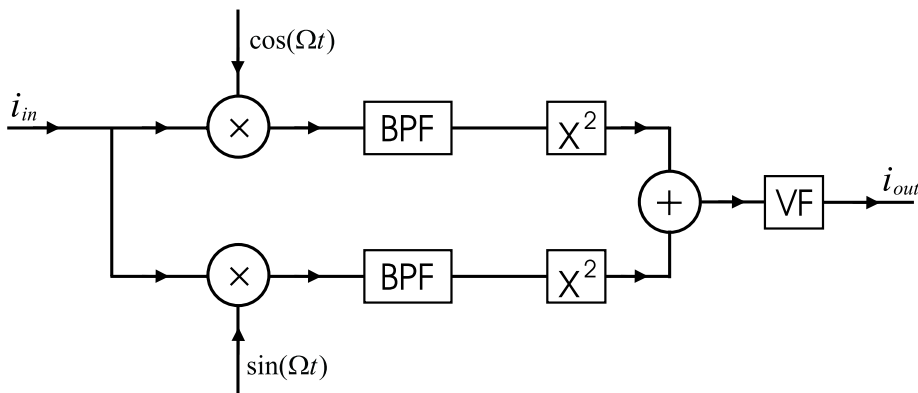


Figure E.1: Schematic diagram of a spectrum analyzer. The input signal i_{in} is divided into two paths. The upper path is multiplied by a signal oscillating as $\cos(\Omega t)$. The signal is subsequently filtered by the band pass filter (BPF), which is centered at zero frequency and has a resolution bandwidth of ν_{RB} . The filtered signal is squared and added to the other component which was multiplied by a $\sin(\Omega t)$ signal. The video filter finally averages the signal for a time given by the inverse video bandwidth ν_{VB}^{-1} . The output signal i_{out} is proportional to the spectral density $(i_{in})_{\Omega}^2$ integrated over the resolution bandwidth ν_{RB} .

We now consider the situation where the input i_{in} consists of random Gaussian noise which is delta-correlated in time. This is the situation when i_{in} is the photocurrent produced by detection of a shot noise limited (coherent) state of light. We limit the discussion to include only one quadrature; the two quadratures of the noisy input are uncorrelated and contribute with the same amount of signal. The mixer converts the noise at frequency Ω into low frequency noise around zero frequency. In this way we limit the detection to the fluctuations around Ω , and we avoid the low frequency fluctuations in i_{in} , which may be predominated by classical/technical noise. The BPF is a low-pass filter with a bandwidth $\nu_{RB} < \Omega$. Hence, the BPF averages the fluctuations at frequency Ω for a time ν_{RB}^{-1} . The probability for observing a signal after the BPF in an interval dx around x is now given by the Gaussian distribution

$$f_{BPF}(x) dx = \frac{1}{\sqrt{2\pi}\sigma} \exp(-x^2/2\sigma^2) dx \quad (\text{E.2})$$

The average signal for the random Gaussian noise is zero, but the variance of the signal is nonzero. We expect the variance to be linear in the inverse averaging time of the BPF, i.e. $\sigma^2 = \sigma_0^2 \nu_{RB}$, because the signal before the BPF is delta-correlated in time. The interesting parameter is σ_0^2 , which represents the noise in the input signal per unit bandwidth. We can extract σ_0^2 by squaring the signal. That converts the distribution in Eq. (E.2) into

$$f_{x^2}(x) dx = \begin{cases} f_{BPF}(\sqrt{x}) \frac{1}{\sqrt{x}} dx & \text{for } x > 0 \\ 0 & \text{for } x \leq 0 \end{cases} \quad (\text{E.3})$$

The average and the variance for a stochastic variable X_{x^2} with a f_{x^2} distribution are given by

$$\begin{aligned} \langle X_{x^2} \rangle &= \sigma^2 = \sigma_0^2 \nu_{RB} \\ \text{Var}(X_{x^2}) &= 2\sigma_0^4 \nu_{RB}^2 \end{aligned} \quad (\text{E.4})$$

Thus, the average of the signal after the squaring device holds information about σ_0 . However, this signal is quite noisy with a standard deviation that is larger than the mean value. The VF averages the output of the squaring device for a time ν_{VB}^{-1} . The signal after the squaring device changes on a

time scale set by the inverse bandwidth of the first filter, ν_{RB}^{-1} . Hence, the VF effectively averages over ν_{RB}/ν_{VB} independent measurements of the signal after the squaring device. The output of the VF can therefore be described by the stochastic variable Y

$$Y = \frac{\nu_{VB}}{\nu_{RB}} \sum_{i=1}^{\nu_{RB}/\nu_{VB}} X_{x^2,i} \quad (\text{E.5})$$

$X_{x^2,i}$ are independent stochastic variables with the same distribution as X_{x^2} . The average and the variance of the SA output are then given by

$$\begin{aligned} \langle Y \rangle &= \sigma_0^2 \nu_{RB} \\ \text{Var}(Y) &= 2\sigma_0^4 \nu_{RB} \nu_{VB} \end{aligned} \quad (\text{E.6})$$

The S/N for a noise or spectral density measurement on the SA is now given by¹

$$\frac{\langle Y \rangle}{\sqrt{\text{Var}(Y)}} = k_{sc} \sqrt{\frac{\nu_{RB}}{\nu_{VB}}} \quad (\text{E.7})$$

We see that the S/N is increased when ν_{RB} is increased. In other words, the S/N is increased when we measure the fluctuations in a larger frequency interval. The S/N is also increased when ν_{VB} is reduced, that is, when the signal is averaged for a longer time. This scaling becomes invalid when ν_{VB} approaches ν_{RB} ; a video bandwidth comparable to or larger than the resolution bandwidth does not make much sense according to the derivation above. The scaling factor k_{sc} in Eq. (E.7) depends on the precise definitions of the bandwidths. The derivation above gives $k_{sc} = 1$ when the contributions from both quadratures are added, but a careful measurement should be used to establish the scaling factor for the spectrum analyzer applied in the experiment. Such a measurement for the lock-in detection scheme used in chapter 8 (Fig. 8.2) gives $k_{sc} = 1.0$. Furthermore, the predicted scaling with ν_{RB} and ν_{VB} is confirmed experimentally.

¹Note that the "signal" in S/N is actually the noise of the SA input, whereas the "noise" in S/N is the noise of the noise of the input.

Bibliography

- [1] G. Santarelli, P. Laurent, P. Lemonde, A. Clairon, A. G. Mann, S. Chang, A. N. Luiten, and C. Salomon, *Phys. Rev. Lett.* **82**, 4619 (1999).
- [2] R. E. Slusher, L. Hollberg, B. Yurke, J. Mertz, and J. F. Valley, *Phys. Rev. Lett.* **55**, 2409 (1985).
- [3] W. M. Itano, J. C. Bergquist, J. J. Bollinger, J. M. Gilligan, D. J. Heinzen, F. L. Moore, M. G. Raizen, and D. J. Wineland, *Phys. Rev. A* **47**, 3554 (1993).
- [4] J. L. Sørensen, J. Hald, and E. S. Polzik, *Phys. Rev. Lett.* **80**, 3487 (1998).
- [5] A. Kuzmich, L. Mandel, J. Janis, Y. E. Young, R. Eijnisman, and N. P. Bigelow, *Phys. Rev. A* **60**, 2346 (1999).
- [6] J. Hald, J. L. Sørensen, C. Schori, and E. S. Polzik, *Phys. Rev. Lett.* **83**, 1319 (1999).
- [7] J. I. Cirac, P. Zoller, H. J. Kimble, and H. Mabuchi, *Phys. Rev. Lett.* **78**, 3221 (1997).
- [8] E. S. Polzik, *Phys. Rev. A* **59**, 4202 (1999).
- [9] A. Kuzmich, K. Mølmer, and E. S. Polzik, *Phys. Rev. Lett.* **79**, 4782 (1997).
- [10] E. L. Raab, M. Prentiss, A. Cable, S. Chu, and D. E. Pritchard, *Phys. Rev. Lett.* **59**, 2631 (1987).
- [11] M. Drewsen, P. Laurent, A. Nadir, G. Santarelli, A. Clairon, Y. Castin, D. Grison, and C. Salomon, *Appl. Phys. B* **59**, 283 (1994).
- [12] M. H. Anderson, J. R. Ensher, M. R. Matthews, C. E. Wieman, and E. A. Cornell, *Science* **269**, 198 (1995).
- [13] K. E. Gibble, S. Kasapi, and S. Chu, *Opt. Lett.* **17**, 526 (1992).
- [14] D. W. Sesko, T. G. Walker, and C. E. Wieman, *J. Opt. Soc. Am. B* **8**, 946 (1991).
- [15] S. Grego, M. Colla, A. Fioretti, J. H. Müller, P. Verkerk, and E. Arimondo, *Opt. Commun.* **132**, 519 (1996).
- [16] J. Dalibard and C. Cohen-Tannoudji, *J. Opt. Soc. Am. B* **6**, 2023 (1989).
- [17] N. Jørgensen, Master's thesis, Institute of Physics and Astronomy, Aarhus University, 1996.
- [18] R. C. Neelen, D. M. Boersma, M. P. V. Exter, G. Nienhuis, and J. P. Woerdman, *Phys. Rev. Lett.* **69**, 593 (1992).
- [19] P. Lodahl, Master's thesis, Institute of Physics and Astronomy, Aarhus University, 1997.
- [20] J. L. Sørensen, J. Hald, and E. S. Polzik, *J. Mod. Opt.* **44**, 1917 (1997).

- [21] J. L. Hall, L. Hollberg, T. Baer, and H. G. Robinson, *Appl. Phys. Lett.* **39**, 680 (1981).
- [22] G. C. Bjorklund, M. D. Levenson, W. Lenth, and C. Ortiz, *Appl. Phys. B* **32**, 145 (1983).
- [23] L. Leick, Master's thesis, Institute of Physics and Astronomy, Aarhus University, 1998.
- [24] L. Young, W. T. Hill, S. J. Sibener, S. D. Price, C. E. Tanner, C. E. Wieman, and S. R. Leone, *Phys. Rev. A* **50**, 2174 (1994).
- [25] R. W. Fox, S. L. Gilbert, L. Hollberg, J. H. Marquardt, and H. G. Robinson, *Opt. Lett.* **18**, 1456 (1993).
- [26] J. H. Marquardt, H. G. Robinson, and L. Hollberg, *J. Opt. Soc. Am. B* **13**, 1384 (1996).
- [27] R. M. Whitley and C. R. Stroud, Jr., *Phys. Rev. A* **14**, 1498 (1976).
- [28] S. Stenholm, *Foundations of Laser Spectroscopy* (Wiley, New York, 1983).
- [29] N. P. Georgiades, E. S. Polzik, and H. J. Kimble, *Opt. Lett.* **19**, 1474 (1994).
- [30] E. de Clercq, M. de Labachellerie, G. Avila, P. Cerez, and M. Tetu, *J. Physique* **45**, 239 (1984).
- [31] I. I. Sobelman, *Atomic Spectra and Radiative Transitions* (Springer, Berlin, 1992).
- [32] R. Guenther, *Modern Optics* (Wiley, New York, 1990).
- [33] C. Wieman and T. W. Hänsch, *Phys. Rev. Lett.* **36**, 1170 (1976).
- [34] F. Laloë, M. Leduc, and P. Minguzzi, *J. Physique* **30**, 277 (1969).
- [35] J. L. Sørensen, J. Hald, and E. S. Polzik, *Opt. Lett.* **23**, 25 (1998).
- [36] M. Gehrtz, G. C. Bjorklund, and E. A. Whittaker, *J. Opt. Soc. Am. B* **2**, 1510 (1985).
- [37] E. A. Whittaker, M. Gehrtz, and G. C. Bjorklund, *J. Opt. Soc. Am. B* **2**, 1320 (1985).
- [38] N. C. Wong and J. L. Hall, *J. Opt. Soc. Am. B* **2**, 1527 (1985).
- [39] S. Machida, Y. Yamamoto, and Y. Itaya, *Phys. Rev. Lett.* **58**, 1000 (1987).
- [40] D. J. McIntyre, C. E. Fairchild, J. Cooper, and R. Walser, *Opt. Lett.* **18**, 1816 (1993).
- [41] S. Lathi, S. Kasapi, and Y. Yamamoto, *Opt. Lett.* **21**, 1600 (1996).
- [42] L. Mandel and E. Wolf, *Optical Coherence and Quantum Optics* (Cambridge University Press, Cambridge, 1995).
- [43] P. K. Lam, T. C. Ralph, B. C. Buchler, D. E. McClelland, H.-A. Bachor, and J. Gao, *J. Opt. B: Quantum Semiclass. Opt.* **1**, 469 (1999).
- [44] K. Schneider, M. Lang, J. Mlynek, and S. Schiller, *Optics Express* **2**, 59 (1998).
- [45] E. S. Polzik, J. Carri, and H. J. Kimble, *Appl. Phys. B* **55**, 279 (1992).
- [46] D. C. Kilper, D. G. Steel, R. Craig, and D. R. Scifres, *Opt. Lett.* **21**, 1283 (1996).
- [47] E. S. Polzik, J. Carri, and H. J. Kimble, *Phys. Rev. Lett.* **68**, 3020 (1992).
- [48] F. Marin, A. Bramati, V. Jost, and E. Giacobino, *Opt. Comm.* **140**, 146 (1997).
- [49] S. Kasapi, S. Lathi, and Y. Yamamoto, *Opt. Lett.* **22**, 478 (1997).

- [50] E. S. Polzik, J. L. Sørensen, and J. Hald, *Appl. Phys. B.* **66**, 759 (1998).
- [51] N. P. Georgiades, E. S. Polzik, K. Edamatsu, H. J. Kimble, and A. S. Parkins, *Phys. Rev. Lett.* **75**, 3426 (1995).
- [52] N. P. Georgiades, E. S. Polzik, and H. J. Kimble, *Phys. Rev. A* **55**, R1605 (1997).
- [53] Q. A. Turchette, N. P. Georgiades, C. J. Hood, H. J. Kimble, and A. S. Parkins, *Phys. Rev. A* **58**, 4056 (1998).
- [54] A. Furusawa, J. L. Sørensen, S. L. Braunstein, C. A. Fuchs, H. J. Kimble, and E. S. Polzik, *Science* **282**, 706 (1998).
- [55] R. Bruckmeier, K. Schneider, S. Schiller, and J. Mlynek, *Phys. Rev. Lett.* **78**, 1243 (1997).
- [56] D. T. Smithey, M. Beck, M. G. Raymer, and A. Faridani, *Phys. Rev. Lett.* **70**, 1244 (1993).
- [57] S. Schiller, G. Breitenbach, S. F. Pereira, T. Müller, and J. Mlynek, *Phys. Rev. Lett.* **77**, 2933 (1996).
- [58] D. M. Meekhof, C. Monroe, B. E. King, W. M. Itano, and D. J. Wineland, *Phys. Rev. Lett.* **76**, 1796 (1996).
- [59] M. Morinaga, I. Bouchoule, J.-C. Karam, and C. Salomon, *Phys. Rev. Lett.* **83**, 4037 (1999).
- [60] P. Meystre and M. Sargent, *Elements of Quantum Optics* (Springer, Berlin, 1991).
- [61] D. F. Walls and G. J. Milburn, *Quantum Optics* (Springer-Verlag, Berlin, 1994).
- [62] H.-A. Bachor, *A Guide to Experiments in Quantum Optics* (Wiley-VCH, Weinheim, 1998).
- [63] H. J. Kimble, in *Fundamental Systems in Quantum Optics*, edited by J. Dalibard, J. M. Raimond, and J. Zinn-Justin (North-Holland, Amsterdam, 1992), pp. 545–674.
- [64] C. Fabre and S. Reynaud, in *Fundamental Systems in Quantum Optics*, edited by J. Dalibard, J. M. Raimond, and J. Zinn-Justin (North-Holland, Amsterdam, 1992), pp. 675–712.
- [65] A. Heidmann, R. J. Horowicz, S. Reynaud, E. Giacobino, C. Fabre, and G. Camy, *Phys. Rev. Lett.* **59**, 2555 (1987).
- [66] V. N. Beskrovnyi and A. S. Chirkin, *Quantum Semiclass. Opt.* **10**, 263 (1998).
- [67] J. L. Sørensen, Ph.D. thesis, Institute of Physics and Astronomy, Aarhus University, 1998.
- [68] G. D. Boyd and D. A. Kleinman, *J. Appl. Phys.* **39**, 3597 (1968).
- [69] H. Mabuchi, E. S. Polzik, and H. J. Kimble, *J. Opt. Soc. Am. B* **11**, 2023 (1994).
- [70] L. Shiv, J. L. Sørensen, E. S. Polzik, and G. Mizell, *Opt. Lett.* **20**, 2270 (1995).
- [71] L. A. Wu, M. Xiao, and H. J. Kimble, *J. Opt. Soc. Am. B* **4**, 1465 (1987).
- [72] R. W. P. Drever, J. L. Hall, F. V. Kowalski, J. Hough, G. M. Ford, A. J. Munley, and H. Ward, *Appl. Phys. B* **31**, 97 (1983).
- [73] P. Grangier, R. E. Slusher, B. Yurke, and A. LaPorta, *Phys. Rev. Lett.* **59**, 2153 (1987).
- [74] D. J. Wineland, J. J. Bollinger, W. M. Itano, F. L. Moore, and D. J. Heinzen, *Phys. Rev. A* **46**, R6797 (1992).

- [75] D. J. Wineland, J. J. Bollinger, W. M. Itano, and D. J. Heinzen, *Phys. Rev. A* **50**, 67 (1994).
- [76] M. Fleischhauer, S. F. Yelin, and M. D. Lukin, To appear in *Optics Communications* (quant-ph/9912022) (1999).
- [77] G. S. Agarwal and R. R. Puri, *Phys. Rev. A* **41**, 3782 (1990).
- [78] K. Mølmer, *Eur. Phys. J. D.* **5**, 301 (1999).
- [79] C. Cohen-Tannoudji, J. Dupont-Roc, and G. Grynberg, *Atom-Photon Interactions* (John Wiley, New York, 1992).
- [80] Y. Yamamoto, S. Machida, and O. Nilsson, *Phys. Rev. A* **34**, 4025 (1986).
- [81] Y. Yamamoto and S. Machida, *Phys. Rev. A* **35**, 5114 (1987).
- [82] A. E. Kozhokin, K. Mølmer, and E. S. Polzik, quant-ph/9912014.
- [83] M. Fleischhauer and T. Richter, *Phys. Rev. A* **51**, 2430 (1995).
- [84] L. Davidovich, *Rev. Mod. Phys.* **68**, 127 (1996).
- [85] M. Kitagawa and M. Ueda, *Phys. Rev. A* **47**, 5138 (1993).
- [86] H. Saito and M. Ueda, *Phys. Rev. A* **59**, 3959 (1999).
- [87] M. Ueda, T. Wakabayashi, and M. Kuwata-Gonokami, *Phys. Rev. Lett.* **76**, 2045 (1996).
- [88] I. Cirac, Private Communications, 1999.
- [89] G. F. Grom and A. M. Kuzmich, *JETP Lett.* **61**, 900 (1995).
- [90] A. Kuzmich, N. P. Bigelow, and L. Mandel, *Europhys. Lett.* **42**, 481 (1998).
- [91] Y. Takahashi, K. Honda, N. Tanaka, K. Toyoda, K. Ishikawa, and T. Yabuzaki, *Phys. Rev. A* **60**, 4974 (1999).
- [92] A. Kuzmich *et al.*, preprint (1999).
- [93] A. Sørensen and K. Mølmer, *Phys. Rev. Lett.* **83**, 2274 (1999).
- [94] P. R. Berman, *Phys. Rep.* **43**, 101 (1978).
- [95] P. W. Milonni and J. H. Eberly, *Lasers* (Wiley, New York, 1988).
- [96] P. R. Hemmer, B. W. Peuse, F. Y. Wu, J. E. Thomas, and S. Ezekiel, *Opt. Lett.* **6**, 531 (1981).
- [97] J. Dalibard and C. Cohen-Tannoudji, *J. Opt. Soc. Am. B* **2**, 1707 (1985).
- [98] E. B. Aleksandrov and A. B. Mamyurin, *Sov. Phys. JETP* **45(2)**, 247 (1977).
- [99] E. B. Aleksandrov and V. S. Zapasskii, *Sov. Phys. JETP* **54(1)**, 64 (1981).
- [100] A. M. Bacon, H. Z. Zhao, L. J. Wang, and J. E. Thomas, *Phys. Rev. Lett.* **75**, 1296 (1995).
- [101] H. Z. Zhao, Z. H. Lu, A. M. Bacon, L. J. Wang, and J. E. Thomas, *Phys. Rev. A* **57**, 1427 (1998).
- [102] A. M. Bacon, H. Z. Zhao, L. J. Wang, and J. E. Thomas, *Applied Optics* **34**, 5326 (1995).
- [103] E. Hagley, X. Maître, G. Nogues, C. Wunderlich, M. Brune, J. M. Raimond, and S. Haroche, *Phys. Rev. Lett.* **79**, 1 (1997).

- [104] Q. A. Turchette, C. S. Wood, B. E. King, C. J. Myatt, D. Leibfried, W. M. Itano, C. Monroe, and D. J. Wineland, *Phys. Rev. Lett.* **81**, 3631 (1998).
- [105] B. E. Cooper, *Statistics for Experimentalists* (Pergamon, Oxford, 1969).
- [106] N. C. Barford, *Experimental Measurements: Precision, Error and Thruth* (John Wiley, Chichester, 1990).
- [107] K. Szymaniec, H. J. Davies, and C. S. Adams, *Europhys. Lett.* **45**, 450 (1999).
- [108] A. Clairon, S. Ghezali, G. Santarelli, P. Laurent, S. N. Lea, M. Bahoura, E. Simon, S. Weyers, and K. Szymaniec, in *5th Symposium on Frequency Standard and Metrology*, edited by J. C. Berquist (World Scientific, Singapore, 1996), pp. 49–59.
- [109] P. Lemonde, Ph.D. thesis, École Normale Supérieure, 1997.
- [110] S. F. Huelga, P. L. Knight, C. Macchiavello, M. B. Plenio, and V. Vedral, *Appl. Phys. B* **67**, 723 (1998).
- [111] B. Peterson, *Spectrum Analysis - Application Note 150*, Hewlett Packard, <http://literature.hp.com/litweb/pdf/5952-0292.pdf>, 1989.